ÇUKUROVA UNIVERSITY
INSTITUTE OF NATURAL AND APPLIED SCIENCES

PhD THESIS

Funda AKSOY

AMBIENT PRESSURE X-RAY PHOTOELECTRON SPECTROSCOPY AND ITS APPLICATIONS

DEPARTMENT OF PHYSICS

ADANA, 2010

ÇUKUROVA UNIVERSITY
INSTITUTE OF NATURAL AND APPLIED SCIENCES

AMBIENT PRESSURE X-RAY PHOTOELECTRON SPECTROSCOPY AND ITS APPLICATIONS

Funda AKSOY

PhD THESIS

DEPARTMENT OF PHYSICS

We certify that the thesis titled above was reviewed and approved for the award of degree of the Doctor of Philosophy by the board of jury on 27/10/2010.

…….....	……..	…….....
Prof. Dr. Metin ÖZDEMİR	Prof. Dr. Ramazan ESEN	Prof. Dr. Sadullah SAKALLIOĞLU
Supervisor	Jury	Jury
…….....	……..	
Prof. Dr. Refik KAYALI	Assoc. Prof. Faruk KARADAĞ	
Jury	Jury	

This PhD Thesis is written at the Physics Department of Institute of Natural And Applied Sciences of Çukurova University.
Registration Number:

Prof.Dr. İlhami YEĞİNGİL
Director
Institute of Natural And Applied Sciences

This study was financially supported by the Research Fund of Çukurova University.
Project Number FEF2007D19

Not: The usage of the presented specific declerations, tables, figures, and photographs either in this thesis or in any other reference without citation is subject to "The law of Arts and Intellectual Products" number of 5846 of Turkish Republic.

ABSTRACT

PhD THESIS

AMBIENT PRESSURE X-RAY PHOTOELECTRON SPECTROSCOPY AND ITS APPLICATIONS

Funda AKSOY

ÇUKUROVA UNIVERSITY
INSTITUTE OF NATURAL AND APPLIED SCIENCES
DEPARTMENT OF PHYSICS

Supervisor :Prof. Dr. Metin ÖZDEMİR
Year: 2010, Pages: 197
Jury :Prof. Dr. Metin ÖZDEMİR
:Prof. Dr. Ramazan ESEN
:Prof. Dr. Sadullah SAKALLIOĞLU
:Prof. Dr. Refik KAYALI
:Assoc. Prof. Faruk KARADAĞ

During the past decade, the application of Ambient Pressure X-ray Photoelectron Spectroscopy (APXPS) has been recognized as an important in situ tool to study environmental and materials science, energy related science, and many other fields. Several APXPS endstations are currently under planning or development at the USA and international light sources, which will lead to a rapid expansion of this technique. The present work describes the design and performance of a new APXPS instrument at the Advanced Light Source beamline 9.3.2 at Lawrence Berkeley National Laboratory. This new instrument, Scienta R4000 HiPP, is a result of collaboration between Advanced Light Source and its industrial partner VG-Scienta. The R4000 HiPP provides superior electron transmission as well as spectromicroscopy modes with 16 µm spatial resolution in one dimension and angle-resolved modes with simulated 0.5° angular resolution at 24° acceptance.

Applications of APXPS have been also given in this work. In the first study the APXPS and mass spectrometry have been utilized to investigate the CO and O_2 co-adsorption and the catalytic oxidation of CO on a Pt(110) surface under various pressures of CO and O_2 (up to 250 mTorr). Studies suggest that there is no surface oxide formation on Pt under our reaction conditions. However, CO oxidation in this pressure (<500 mTorr), O_2 to CO ratio (<10), and temperature (150 °C) regime is consistent with the Langmuir–Hinshelwood reaction mechanism. Second work was to study early oxidation stages of NiTi shape memory alloys using APXPS and NEXAF. The role of the temperature on the formation of passivation layer on NiTi was pointed out.

Key Words: Ambient Pressure XPS, UHV, Catalyst, Pt(110), NiTi Shape Memory Alloy

ÖZ

DOKTORA TEZİ

YÜKSEK BASINÇ X-IŞINI FOTOELEKTRON SPEKTROSKOPİSİ VE UYGULAMALARI

Funda AKSOY

ÇUKUROVA ÜNİVERSİTESİ
FEN BİLİMLERİ ENSTİTÜSÜ
FİZİK ANABİLİM DALI

Danışman :Prof. Dr. Metin ÖZDEMİR
Yıl: 2010, Sayfa: 197
Jüri :Prof. Dr. Metin ÖZDEMİR
:Prof. Dr. Ramazan ESEN
:Prof. Dr. Sadullah SAKALLIOĞLU
:Prof. Dr. Refik KAYALI
:Doç. Dr. Faruk KARADAĞ

Son on yıllık zaman sürecinde, yüksek basınç fotoelektron spektrokopisi (APXPS)'nin uygulanması, çevre ve malzeme bilimi, enerji ve diğer birçok alandaki çalışmalarda önemli bir deneysel araç olarak kabul gördü. Bugünlerde, tekniğin hızlı bir şekilde yayılmasına öncülük eden Amerika ve diğer uluslararası sinkrotron merkezlerinde birçok APXPS sistemi kurulum aşamasındadır veya kurulumu planlanmaktadır. Bu tez çalışmasında, Lawrence Berkeley Ulusal Laboratuarı/ Advanced Light Source'da deney istasyonu 9.3.2'de kurulan yeni APXPS sisteminin tasarımı ve calışma performansı sunulmaktadır. Yeni sistem, Scienta R4000 HiPP, Advanced Light Source ve onun endüstriyel partneri olan VG-Scienta arasındaki işbirliği sonucu kurulmuştur. R4000 HiPP sistemi, üstün elektron iletimi ile birlikte 24° geliş açısı için simüle edilmiş-0.5° çözünümlü açı-çözünüm modu ve bir boyutta 16 μm uzamsal çözünümlü spektromikroskopik mod gibi özellikler sunmaktadır.

Bu tez çalışmasında APXPS'nin uygulamaları da verilmektedir. İlk uygulamada APXPS ve kütle spektrometresi, CO ve O_2 gazlarının Pt(110) yüzeyindeki adsorpsiyonunu ve katalitik oksidasyonunu incelemek üzere kullanılmıştır. Elde edilen sonuçlar, CO ve O_2 gazlarının 250 mTorr' a kadar çeşitli basınçlarda oluşturduğu reaksiyon şartları altında Pt üzerinde yüzey oksit oluşumunun gerçekleşmediğini göstermektedir. Bununla birlikte, belirtilen basınç değerindeki CO oksidasyonu, O_2/CO oranı ve sıcaklık rejimi Langmuir–Hinshelwood reaksiyon mekanizması ile uyumludur. İkinci uygulama NiTi şekil hafızalı alaşımların yüzey oksidasyon basamaklarının APXPS ve NEXAFS teknikleri kullanılarak çalışılmasıdır. Çalışmada sıcaklığın NiTi yüzeyindeki pasivasyon tabakasının oluşumu üzerine etkisi işaret edilmiştir.

Anahtar Kelimeler: Yüksek basınç XPS, Ultra-yüksek Vakum, Katalizör, Pt(110), NiTi Şekil Hafızalı Alaşım

ACKNOWLEDGMENTS

No one knows what the next in the life is. We just live the present time without knowing about even next minute. When my Ph. D. adventure began in 2005, I didn't realize that how long and how hard it was going to be. Now, I am almost at the end of this adventure with lots of knowledge, different experiences and feelings. I'm not only very happy that I will graduate soon; but also very sorry that not going to have advantage of being student any more.

This chapter of my life could not be completed without any support and help of many people. I would like to take the opportunity of writing a few sentences to express my appreciation and depth of gratitude to many people who have had important and unforgettable endeavors on me.

I would like to thank Prof. Dr.Yüksel Ufuktepe for his guidance, support and most importantly giving me the opportunity to go abroad for my Ph. D. study. It shouldn't be an easy decision to send an inexperienced student to one of the top research place in the world. For his confidence in me I'm much obliged. I am also grateful to my supervisor Prof. Dr. Metin Özdemir for his support during the last two months of my study.

I have had wonderful time in the last almost three years at ALS with all amazing people that I had the opportunity to interact with. It would have been absolutely impossible to accomplish this thesis work without great scientific/moral support and help from so many nice people. First and foremost, I would like to express my sincere gratitude to my host Dr. Zahid Hussain for providing me the chance and opportunity to work at ALS and my supervisor Dr. Zhi Liu for his effort and time, his active support. Zhi has always been a guide and very kind friend to me during my staying. Without his endless support and encourage, I could not even think to get this Ph. D. thesis done. I am greatly indebted to his generosity. I will never forget his help in my whole life. I wish to express my indebtedness to Asst. Prof. Bongjin Simon Mun who was beamline scientist at BL 9.3.2 before I joined Zhi Liu's group. I consider myself lucky because I could have had change to work with him many times when he had beamtime at ALS. Simon has been a very kind person

and guide to me over the last three years and I would always cherish all wonderful discussions that I have had with him.

One person that just thanking will be never enough is Dr. Michael Grass. Michael has been the practical advisor to me on a daily basis and it would better to say that I have basically learnt everything mostly from him. Michael is a very kind and generous friend, in addition to being an excellent scientist. I would like to express my sincere gratitude to Michael for supporting and guiding me through all the stages of my work at ALS and in daily life. From the beginning he has always been a brother to me throughout the time in Berkeley.

I would like to thank our collaborator Alan Pelton and Valeska Schroeder from NDC (Nitinol Devices and Components) for providing me NiTi samples. From the beginning I have been continually bothering them with so many questions related to this superior material. Their expert remarks, friendly approach, and above all their deep interest in research are unique. I have special thanks to Dr. Apurva Mehta and Dr. Yun Sun who are scientists at SSRL (Stanford Synchrotron Radiation Laboratory) for sharing their experimental expertise.

I also render my sincere indebtedness to the all reviewers of the examination committee for spending their valuable time to evaluate the thesis.

With deep regards and profound respect, I express my indebtedness to Prof. Dr. Refik Kayalı for inspiring me for research and boosting my morale constantly.

I sincerely indebted to all my friends, Shrawan Mishra, Naila Jabeen, Selva Raju, Nadeem Tahir, Sheraz Gul, Zulfiqar Ali, Paul Olalde Valesco, Jeng-Lung Chen, for sharing their unforgettable time with me. I would like to thank them all for their help, support and companionship. In ALS, I have also truly enjoyed the company of Gary Giangrasso and his team. I would like to thank them for being wonderful people to me since the time I joined ALS. Gary helped me a lot, not only in ALS but also beyond.

Many special thanks to Dr. Selma Erat for being a wonderful friend to me since the time I met with her at ALS.

A special thank goes to Ayşe Bozduman for her friendship and especially taking care of my all paperwork issues.

There are numerous more colleagues and friends who have inspired me, helped me out in hard times. I thank everyone who has helped me in this long journey.

I remember very well all those difficult days during my first year in ALS. Here, I would like to thank my fiancé, Güvenç Akgül, for giving me continuous moral support, help, and love in those days. He has been a great support for me especially at times when I was depressed or frustrated.

I would like to acknowledge the funding source for my thesis project. This work was supported by The Scientific and Technical Research Council of Turkey (TUBITAK), Scientific Human Resources Development (BAYG).

Last but not least, I express my devout obligation and gratitude to my beloved parents and other family members back home in Turkey, without their affection, and constant encouragement I cannot do anything at all.

Funda AKSOY

Fall 2010

CONTENTS **PAGE**

ABSTRACT I
ÖZ II
ACKNOWLEDGEMENTS III
CONTENTS VI
TABLES CAPTIONS XII
FIGURES CAPTIONS XIV
SYMBOLS AND ABBREVIATONS XXVI
1. INTRODUCTION 1
2. REVIEW OF LITERATURE 5
2.1. Synchrotron Radiation 5
2.1.1 Introduction 5
2.1.2 History of Synchrotron Radiation 5
2.1.3. Advantages of Synchrotron Generated Light 9
2.1.3.1. Brightness or Flux 10
2.1.3.2. In-Situ Experiments 11
2.1.3.3. Tunability (Ability to Select Specific Light) 11
2.1.3.4. Speed 12
2.1.4. Creation of Synchrotron Light 12
2.1.5. Advanced Light Source (ALS) 16
2.1.6. ALS Components 18
2.1.6.1. Linear Accerator (Linac) 21
2.1.6.1.(1). The Electron Gun 22
2.1.6.1.(2). The Buncher 22
2.1.6.1.(3). The Linac 23
2.1.6.2. Booster Synchrotron 23
2.1.6.3. Storage Ring 24
2.1.6.4. Undulators and Wigglers 25
2.1.6.5. Beamline 26
2.1.6.6. Experiment Station 27

2.1.6.7. RF System 27
2.1.6.7.(1). Klystrons 28
2.1.6.7.(2). Waveguide 29
2.1.6.7.(3). Radio Frequency (RF) Cavity 30
2.2. X-ray Photoelectron Spectroscopy (XPS) 32
2.2.1. Introduction 32
2.2.2. History of XPS 33
2.2.2.1. The Early Work 33
2.2.2.2. The Breakthrough Years 35
2.2.2.3. The Appreciation of Surface Sensitivity 37
2.2.2.4. Instrument Development 39
2.2.2.4.(1). Spectroscopy 39
2.2.2.4.(2). Imaging 40
2.2.2.4.(3). Other Aspects 44
2.3. Ambient Pressure X-ray Photoelectron Spectroscopy (APXPS) 45
2.3.1. Introduction 45
2.3.2. History of APXPS 47
2.3.3. Fundamentals of APXPS 51
2.3.3.1. Electron-Gas Interactions 51
2.3.3.2. Gas Flow and Differential Pumping 54
2.3.3.3 Transfer Electron Optics 57
3. THEORETICAL BACKGROUND 59
3.1. Basic Principles, Spectral Features and Qualitative Analysis of XPS 59
3.1.1. The XPS Experiment 61
3.1.1.1. The Principles 61
3.1.1.2. Aspects of Instrumentation 64
3.1.1.2.(1). X-ray Sources 64
3.1.1.2.(2). Control of Charging 66
3.1.2. The X-ray Photoelectron Spectrum 67
3.1.2.1. Primary Structure 67
3.1.2.1.(1). Core Levels 68

3.1.2.1.(2). Valence Levels 72
3.1.2.1.(3). Auger Series 74
3.1.2.1.(4). Information from Primary Structure 75
3.1.2.1.(4.a). Elemental Analysis 75
3.1.2.1.(4.b). Chemical State Analysis 77
3.1.2.1.(5). Energy Referencing 80
3.1.2.2. Secondary Structure 80
3.1.2.2.(1). Multiplet Splitting 80
3.1.2.2.(2). Shake-up Satellites 81
3.1.2.2.(3). Metal Core Level Asymmetry 82
3.1.2.2.(4). Vibrational Fine Structure 83
3.1.2.2.(5). Plasmon Loss Features 84
3.1.3. Surface Sensitivity 85
3.1.4. Angular Effects 88
3.1.5. Sample Damage 89
3. 2. Angle-Resolved Photoemission Spectroscopy (ARPES) 90
3. 3. Absorption Spectroscopy 91
3.3.1. X-ray Absorption Spectroscopy (XAS) 91
3.3.2. Near-Edge X-ray Absorption Fine Structure (NEXAFS) 94
4. EXPERIMENTAL RESULTS AND DISCUSSION 99
4.1. New Ambient Pressure XPS Endstation at ALS Beamline 9.3.2 99
4.1.1. System Design 99
4.1.1.1. APXPS System Considerations 99
4.1.1.2. General Design 101
4.1.1.3. Prelens Design 103
4.1.2. System Performance 105
4.1.2.1. Differential Pumping 105
4.1.2.2. Improved Transmission 107
4.1.2.3. Spatial Resolution 108
4.1.2.4. Angular Resolution 112

4.2. In-situ Study of the Catalytic Oxidation of CO on a Pt(110) Surface Using Ambient Pressure X-ray Photoelectron Spectroscopy 115
4.2.1. Introduction 115
4.2.2. Catalysts 117
4.2.3. Heterogeneous Catalysis 119
4.2.4. Classification of Reaction Mechanisms of CO Oxidation on Platinum Metals 122
4.2.4.1. Langmuir-Hinshelwood (L–H) Mechanism 124
4.2.4.2. Eley-Rideal (E–R) Mechanism 125
4.2.4.3. Mars-Van Krevelen (MvK) Mechanism 125
4.2.5. Crystal Structure of Clean Pt(110) 127
4.2.6. Experimental Procedure 127
4.2.7. Results and Discussion 128
4.3. Early Oxidation Stages of NiTi Shape Memory Alloys 133
4.3.1. Introduction 133
4.3.2. Fundamental Characteristics of Nitinol 133
4.3.2.1. Shape Memory Effect 133
4.3.2.3. Superelasticity 136
4.3.3. Objective of Work 137
4.3.4. Experimental Procedure 140
4.3.4.1. Cleaning of NiTi Surface 140
4.3.4.1.(1). Ar^+ Ion Sputtering 140
4.3.4.1.(2). Sample Preparation 142
4.3.4.1.(3). Results 143
4.3.4.2. Oxidation of NiTi Surface 150
4.3.5. Results 151
4.3.5.1. Oxidation at Low Dose of Oxygen 151
4.3.5.1.(1). XPS Spectra 151
4.3.5.1.(2). Atomic Ratio of Ti_{total}/Ni_{total} and Thickness 157
4.3.5.1.(3). Crystal Structure 158
4.3.5.2. Oxidation at High Pressure of Oxygen 161

4.3.5.2.(1). XPS Spectra 161
4.3.5.2.(2). Atomic Ratio of Ti_{total}/Ni_{total} and Thickness.....162
4.3.5.2.(3). Crystal Structure.....162
4.3.6. Discussion.....165
5. CONCLUSION 171
REFERENCES 175
CURRICULUM VITAE 191
APPENDIX 192

TABLE CAPTIONS **PAGE**

Table 2.1. History of synchrotron radiation research and sources 8
Table 2.2. Typical parameters for synchrotron radiation at ALS 20
Table 3.1. The spin-orbit splitting parameters 69

FIGURE CAPTIONS **PAGE**

Figure 2.1. (a) Early synchrotron radiation facilities were basically circular rings for bending magnet radiation, although some have been retrofitted with periodic magnetic structures (undulators or wigglers). (b) Modern storage rings are dedicated to broad scientific use optimized for high spectral brightness through the inclusion of many long straight sections for undulators and wigglers, as well as very tightly confined (spatial and angular extent) electron beams. Bending magnet radiation is also generated in turning from one straight section to the next 7

Figure 2.2. The evolution of spectral brightness (brilliance) of X-ray sources through time 9

Figure 2.3. Comparison of average brightness of synchrotron generated light to that of other light sources, such as sun and an incandescent light... 10

Figure 2.4. Wavelength range of synchrotron light 11

Figure 2.5. Bending magnet radiation occurs when a relativistic electron travels in a uniform magnetic field, executing a circular motion with acceleration directed toward the center. The radiation is directed tangentially outward in a narrow radiation cone, giving the appearance of a sweeping “searchlight”. The radiation spectrum is very broad, analogous to a “white light” X-ray light bulb. The emission angle is typically $1/\gamma$, where γ is the Lorentz contraction factor..... 13

Figure 2.6. Energy region of the spectrum at Advanced Light Source (ALS) covered by bending magnet 14

Figure 2.7. Undulator radiation is generated as a highly relativistic electron traverses a periodic magnetic field. In the undulator limit, the magnetic field is relatively weak and the resultant angular excursion of the electron are smaller than the angular width of the natural radiation cone, 1/γ, normally associated with synchrotron radiation. The frequency spread of undulator radiation can be very narrow, and the radiation can be extremely bright and partially coherent, under certain circumstances. The characteristic emission angle is narrowed by a factor $\sqrt{N}$, where N is the number of magnetic periods. Typically N is of order 100. Depending on the magnet strength, harmonic radiation may be generated 15

Figure 2.8. Wiggler radiation is also generated from a periodic magnet structure, but in the strong magnetic field limit where in at least one plane the angular excursions are significantly greater than the natural (1/γ) radiation cone. Because accelerations are stronger in this limit, the radiation generated peaks at higher photon energies and is more abundant (higher photon flux and more power). The radiation spectrum is very broad, similar to that of the bending magnet. Although more power is radiated, wiggler radiation is less bright because of the substantially increased radiation cone 16

Figure 2.9. Comparison of average brightness of bending magnet and undulator light from the Advanced Light Source (ALS) to that of other light sources, such as an X-ray tube and the sun..... 17

Figure 2.10. A schematic of components at Advanced Light Source (ALS). This sketch of an electron storage ring optimized for soft X-ray radiation shows a linear accelerator, linac, (1) and booster synchrotron (2) that brings electrons up to an energy matched to storage ring (3) magnet settings, an injection system, which directs electrons into the ring, and a radio frequency, RF, generator (7) to replenish the energy lost to synchrotron radiation as the electrons pass bending magnets, undulators, and wigglers (4). Straight sections for undulators and wigglers direct energy into beamlines (5) and end sections (6) for various scientific studies. Bending magnet radiation beamlines are located between straight sections 19
Figure 2.11. A photo of the ALS linac 21
Figure 2.12. A simplified drawing shows how a linear accelerator works..... 21
Figure 2.13. Buncher 23
Figure 2.14. Booster ring 24
Figure 2.15. Storage Ring 25
Figure 2.16. (a) Undulator, (b) ALS U5 undulator, beamline 7.0 (N = 89, λu = 50 mm)..... 26
Figure 2.17. Klystron 28
Figure 2.18. Diagram shows how klystron works 29
Figure 2.19. Waveguide 30
Figure 2.20. RF cavity..... 31
Figure 2.21. The basic principle of high-pressure X-ray Photoemission Spectroscopy 48
Figure 2.22. Electron-impact ionization cross-sections for molecular oxygen (O_2) as a function of kinetic energy. This figure was plotted from published data for oxygen. Dashed line demonstrates extrapolation of experimental data 52

Figure 2.23. Principle of APXPS. The sample is placed in a high-pressure chamber that is separated from the X-ray source by an X-ray transparent window. Electrons and gas escape through a differentially pumped aperture 54
Figure 2.24. Scheme for the Equation 2.4. 55
Figure 2.25. Principle of APXPS instruments. Electrons and gas molecules are transferred through first aperture of differentially pumping system. Electrostatic lenses refocus the photoelectrons into the apertures connecting the differential pumping stages. Electron trajectories in the "passive design" systems are illustrated by red color 57
Figure 3.1. General illustration of X-ray Photoelectron Spectroscopy technique .. 59
Figure 3.2. Inelastic mean free paths (IMFPs) for 41 elements, calculated using the TPP-2M formula: Li, Be, three forms of carbon (graphite, diamond, glassy C), Na, Mg, Al, Si, K, Sc, Ti, V, Cr, Fe, Co, Ni, Cu, Ge, Y, Nb, Mo, Ru, Rh, Pd, Ag, In, Sn, Cs, Gd, Tb, Dy, Hf, Ta, W, Re, Os, Ir, Pt, Au, and Bi. Five "outlier" elements are indicated to provide some idea of what electronic structure characteristics can give rise to deviations from the majority behavior: diamond and the alkali metals. The dashed straight line for higher energies represents a variation as $E_K^{0.78}$, and is a reasonable first approximation to the variation for all of the elements shown 60
Figure 3.3. Schematic of the processes involved in X-ray photoemission and Auger electron emission 62
Figure 3.4. X-ray photoelectron spectrum of a polystyrene sample previously exposed to nitrogen plasma. AlKα X-rays (1486.6 eV) were used to excite the photoemission. Note that the binding energy scale is drawn from right to left, so that the photoelectron kinetic energies measured by the spectrometer increase from left to right 62

Figure 3.5. X-ray emission spectrum from an aluminum target bombarded with 15 keV electrons, showing the characteristic Kα line at ~1.5 keV and the broad Bremsstrahlung radiation..... 65
Figure 3.6. Primary structures of $CuInS_2$ in the XPS survey spectrum..... 67
Figure 3.7. Spin orbit splitting in In 3d core levels 69
Figure 3.8. Calculated values of the photoemission cross-section, σ, for Al Kα radiation in terms of the C 1s cross-section..... 70
Figure 3.9. Schematic of the processes involved in X-ray photoemission and subsequent relaxation via X-ray fluorescence and Auger electron emission (in conventional AES the core hole is created by electron impact)..... 71
Figure 3.10. Valence band spectrum of CuInS2 obtained with X-rays and ultraviolet photons at high resolution..... 72
Figure 3.11. Schematic density of states for insulator (left) and a metal (right). The shading indicates the extent to which the energy levels are occupied..... 74
Figure 3.12. Si 2p photoelectron spectrum of a thin (5 Å) SiO_2 film on Si(100) showing all oxidation states of Si. Only the $2p_{3/2}$ component is shown..... 77
Figure 3.13. C 1s spectra of polystyrene, showing the low kinetic energy shake-up satellite..... 82
Figure 3.14. Core (4f) and valence level (VB) spectra of gold and platinum excited with monochromatic Al Kα radiation. Note the relationship between the degree of core level asymmetry and the density of states at the Fermi level (BE = 0)..... 83
Figure 3.15. The high resolution C 1s spectrum from hexatriacontane (n-$C_{36}H_{74}$) as a thin film on silicon. The intensities of four components represents the populations of the vibrational states of the core-ionized system, with the ground state having the lowest BE..... 84
Figure 3.16. Clean Aluminum spectrum showing plasmon resonance structures.... 85

Figure 3.17. The amount of information contributing to the XPS spectrum as a function of depth 87
Figure 3.18. Spectra from the surface of SiO_2 film on Si substrate taken at take-off angles of 0° and 75° with respect to the surface normal. At 0° spectrum is almost due to the silicone substrate (metallic silicone) 88
Figure 3.19. Photoemission geometry..... 90
Figure 3.20. Angle-scanned energy distribution curve from Cu(111)..... 91
Figure 3.21. Illustration of edges and the corresponding electronic transitions 92
Figure 3.22. An example of XAS spectrum 93
Figure 3.23. Schematic representation of the basic theory of NEXAFS. The target atom absorbs an X-ray photon and emits a core electron which propagates outwards to an unoccupied discrete level, thereby creating a core hole. An electron from a higher energy level fills the hole, releasing excess energy either by the radiation of fluorescence photons (bulk sensitive) or by the emission of Auger electrons (surface sensitive) 95
Figure 3.24. Two methods of recording X-ray absorption spectra 96
Figure 4.1. (a) Gas dynamic simulation of the complete prelens for P_0=10 mbar. (b) Pressure profile for P_0=1 mbar along the first 10 mm from the sample extending into the second differential pumping stage. Shown in black from left are the sample, first aperture (0 V), and second aperture (high voltage). Examples of extreme trajectories when the lens is set for high transmission are inserted. On the optical axis, and in the plane along the slit, take off angles of 23° will reach the detector. At a position 0.2 mm from the optical axis, and in the plane along the slit, take off angles of 28° will reach the detector 100
Figure 4.2. (a) Spectra of Au $4f_{7/2}$ recorded at 490 eV and a working distance of 1.9 mm with increasing pressure from 10^{-9} to 0.8 mbar O_2 and (b) the relative intensity of the integrated Au 4f signal as a function of pressure, indicating an effective path length of 2 mm 107

Figure 4.3. Ar spectra recorded at 500 eV and 0.25 mbar Ar using the old endstation at beamline 9.3.2 and the new Scienta R4000 HiPP, clearly demonstrating the enhanced signal to noise ratio of the new system due to optimized PE transmission 108
Figure 4.4. (a) CCD image of the Au $4f_{7/2}$ region of a 100 μm Au bar on SiO_2 shown in (b) (inset is an electron micrograph of the Au stripe). The image can be integrated across the x dispersion direction to yield PE spectra as shown in (c) or across the energy dispersion direction as shown in (d) to reveal spatial heterogeneity. The traces in (d) were used to calculate the spatial resolution as a function of working distance 110
Figure 4.5. Spatially resolved XPS spectra can be recorded with resolution better than 20 μm without sacrificing energy resolution. (a) The modeled PE trajectories from the sample to the front plane of the hemispherical analyzer agree well with (b) spectra from a 100 μm Au bar. The initial parts of the PE trajectories are shown in (c)..... 111
Figure 4.6. AP-ARPES of (a) HOPG, (b) HOPG in an atmosphere of 0.25 mbar CO, and (c) 0.25 mbar CO with no sample in front of the aperture. The sample was rotated 3° in theta between spectra (a) and (b). In both spectra, the Γ, M, and K points are clearly visible and in (b) and (c) the non-dispersive CO lines are also clearly observed..... 113
Figure 4.7. Schematic energy diagram for the oxidation of CO and a Pt catalyst. All energies are given in kJ mol^{-1}. For comparison, the heavy dashed lines show a non-catalytic route..... 121
Figure 4.8. A schematic diagram of synergic bonding of CO to a metal..... 123
Figure 4.9. Adsorption sites (a) top view (b) side view..... 124
Figure 4.10. Schematic representation of the Langmuir-Hinshelwood (L–H) mechanism 125
Figure 4.11. Schematic representation of the Eley-Rideal (E–R) mechanism..... 125

Figure 4.12. Schematic representation of the Mars-Van Krevelen (MvK) mechanism. The blue balls represent Pd atoms. Small red balls correspond to the oxygen atoms from the palladium oxide. (a) PdO_x and a CO molecule diffusing to the surface. (b) Reaction between the CO molecule and one oxygen atom from the palladium oxide, the formation of the CO_2 molecule and its diffusion in the gas phase. (c) Diffusion of the left coordinated Pd atom and refilling of the vacancy left by the oxygen atom, with oxygen from the gas phase..... 126

Figure 4.13. The plan and side view of the (100) surface of a platinum crystal, and the Pt(110)-(2 × 1) reconstructed surface represented as a ball model 127

Figure 4.14. The C1s, O1s and Pt4f core level spectra of the Pt(110) surface under various conditions. A: 200 mTorr CO at room temperature; B: 200 mTorr CO + 200 mTorr O_2 at room temperature; C: 200 mTorr CO + 200 mTorr O_2 at 100 °C; D: 200 mTorr CO + 200 mTorr O_2 at 150 °C 129

Figure 4.15. Partial pressures of CO, O_2, and CO_2 at constant temperature of 150 °C. We controlled the CO pressure to switch the reaction from a CO rich to oxygen rich environment and vise versa. Region A: 180 mTorr O_2; Region B: 140 mTorr O_2 + 230 mTorr CO; Region C: 150 mTorr O_2 + 14 mTorr–28 mTorr CO; Region D: 140 mTorr O_2 + 200 mTorr CO. These regions correspond to XPS spectra in Figure 3..... 130

Figure 4.16. XPS spectra at each region in Figure 2 (A–D): (a) C1s spectra recorded at 540 eV; (b) O1s spectra recorded at 800 eV; (c) Pt4f recorded at 340 eV 131

Figure 4.17. Schematic diagram of the shape memory effect. At high temperature (a), the material is fully austenite. Lowering the temperature below the M_f (b) without the addition of stress causes a phase transformation to twinned martensite. As the martensite is loaded, it begins to detwin (c), until full detwinning has occurred (d). Upon unloading to (e), the martensite elastically recovers, but does not return to a twinned state. Raising the temperature to the austenite start temperature, A_s (f), begins the reverse transformation from martensite to austenite, which is complete at A_f (a) 135

Figure 4.18. At temperatures above the austenite finish temperature, A_f, but below the martensite deformation temperature, M_d, the superelastic effect occurs in Nitinol as shown. Starting at (a) the material is fully austenite. The austenite is elastically loaded to point (b) at which time transformation to martensite occurs (the martensite forms in twins, and instantaneously detwins due to the high applied stresses). Further loading along a stress "plateau" to point (c) fully transforms the material to martensite. Continued loading to (d) requires increased stress and elastically deforms the martensite (note that the stress induced martensite (SIM) elastic modulus is lower than the austenite modulus of elasticity). Unloading back through point (c) recovers the elastic strains in the martensite, and continued unloading to (e) forces the onset of the reverse transformation to austenite, with full reverse transformation upon complete unloading to (a) (Robertson 2006) 137

Figure 4.19. SEM images of explanted Nitinol devices with different passivation layer (a) Mechanically polished Nitinol sample with thick thermal oxide layer after 9 months (Riepe 2000) (b) Electrically polished thin oxide layer after 12 months (Stoeckel et al. 2004) 139

Figure 4.20. Schematic diagram of a typical ion sputter gun used for sample cleaning. Such a gun can also be applied for sputter depth profiling, secondary ion mass spectrometry, and ion scattering spectrometry 141
Figure 4.21. The optical microscope images of a) unpolished and b) mechanically polished NiTi sample surface 143
Figure 4.22. XPS survey spectra of (a) mechanically polished and (b) Ar sputtered NiTi sample 144
Figure 4.23. C1s XPS spectra of the mechanically polished NiTi surface after different sputtering time: (a) 0 min, (b) 15 min, (c) 30 min, (d) 45 min, and (e) 60 min 145
Figure 4.24. O1s XPS spectra of the mechanically polished NiTi surface after different sputtering time: (a) 0 min, (b) 15 min, (c) 30 min, (d) 45 min, and (e) 60 min 145
Figure 4.25. Ni 3p XPS spectra of the mechanically polished NiTi surface after different sputtering time: (a) 0 min, (b) 15 min, (c) 30 min, (d) 45 min, and (e) 60 min 146
Figure 4.26. Ti 3p XPS spectra of the mechanically polished NiTi surface after different sputtering time: (a) 0 min, (b) 15 min, (c) 30 min, (d) 45 min, and (e) 60 min 147
Figure 4.27. Evolution of Ti species as a function of Ar^+ sputtering time 148
Figure 4.28. Evolution of Ti_{total} to Ni_{total} atomic ratio as a function of Ar^+ sputtering time 149
Figure 4.29. Deconvoluted XPS spectra of Ti 3p core level at 610 eV photon energy after (a) 1 L, (b) 19 L, (c) 159 L, and (d) 1559 L O_2 exposure at room temperature 152
Figure 4.30. Deconvoluted XPS spectra of Ti 3p core level at 610 eV photon energy after (a) 1 L, (b) 19 L, (c) 159 L, and (d) 1559 L O_2 exposure at 200 °C 153
Figure 4.31. Relative percentage of metallic and oxidized Ti as a function of oxygen dose at (a) room temperature and (b) 200 °C 154

Figure 4.32. Relative concentration of Ti^{+4}, Ti^{+3}, Ti^{+2}, and Ti^{0} states at (a) room temperature and (b) 200 °C as a function of oxygen exposure..... 155
Figure 4.33. Relative atomic concentration of (a) Ti^{+4} and (b) (Ti^{+3} + Ti^{+2}) as a function of oxygen dose 155
Figure 4.34. Calculated thickness of oxide (TiO_x) layer as a function of oxygen exposure (a) Linear scale and (b) Log scale 157
Figure 4.35. The Ti_{total}/Ni_{total} atomic ratio and oxide layer thickness as a function of oxygen dose at (a) room temperature and (b) 200 °C 158
Figure 4.36. Normalized Ti L-edge NEXAFS spectra as a function of oxygen exposure at (a) room temperature and (b) 200 °C..... 159
Figure 4.37. Deconvoluted Ti 3p XPS spectrum measured in presence of 100 mTorr oxygen at (a) room temperature and (b) 200 °C..... 162
Figure 4.38. Normalized Ti L-edge NEXAFS spectra measured under 100 mTorr oxygen at (a) room temperature and (b) 200 °C..... 164

SYMBOLS AND ABBREVIATIONS

Symbols

A	: Area
A	: Atomic mass
Å	: Angstrom
B	: Magnetic field
BE	: Binding energy
bcc	: Body centered cubic
c	: Velocity of light
D	: Crystalline size
d	: Distance
E	: Electric field
E	: Particle beam energy
E_B	: Binding energy
E_B^F	: Electron binding energy relative to the Fermi level
E_c	: Critical photon energy
E_F	: Fermi level
E_K	: Kinetic energy
E_e	: Storage ring energy
E_β	: Kinetic energies of the β-rays
e^-	: Electron
e-beam	: Electron beam
eV	: Electron volt
F	: Force
f	: Frequency
f	: X-ray flux
fcc	: Face centered cubic
fs	: Femtosecond
GeV	: Giga electron volt

g	: Degeneracy
H	: Hamiltonian
H	: Height
h	: Planck constant
hcp	: Hexagonal close packed
hυ	: X-ray energy
I	: Intensity
I_p	: Signal at pressure P
I_{vac}	: Signal in vacuum
J	: Total angular momentum quantum number
KE	: Kinetic energy
K	: Magnetic tuning
k	: Wavevector
k_B	: Boltzman constant
keV	: Kilo electron volt
l	: Orbital angular momentum quantum number
M	: Input lens magnification
MeV	: Mega electron volt
MHz	: Mega hertz
m	: Mass of the electron
mm	: Millimeter
n	: Principal quantum number
n	: An integer
n	: Atomic concentration
N	: Full cycles
N	: Number of neighboring atoms
N_{el}	: Number of electrons
P	: Pressure
Pa	: Pascal
p	: Momentum

R	: Radius
S	: Sensitivity factor
T	: Temperature
T	: Detection efficiency
t	: Thickness
V	: Voltage
V	: (unit cell) Volume
V	: Vertical
v	: Electron velocity
υ	: Frequency
ω	: Frequency
ω_b	: Bulk plasmon frequency
ω_s	: Surface plasmon frequenc
Z	: Atomic number
θ	: Angle
λ	: Wavelength
λ_e	: Electron mean-free path
μ	: Absorption coefficient
μ_o	: Permittivity
γ	: Lorentz contraction factor
σ	: Photoemission cross-section
$\Phi_{spec.}$	: Work function of the spectrometer
t	: Lifetime
σ_e	: Electron-gas scattering cross-section
λ_c	: Critical wavelength
θ	: Angular efficiency factor for the instrumental arrangement
ρ	: Radius in meters of the electron orbit at the bending magnet
μm	: Micrometer
2-D	: Two dimensional

Abbreviations

AES	: Auger Electron Spectroscopy
AEY	: Auger Electron Yield
ALS	: Advanced Light Source
AP-ARPES	: Ambient Pressure Angle Resolved Photoemission Spectroscopy
APS	: Advanced Photon Source
APXPS	: Ambient Pressure X-ray Photoelectron Spectroscopy
ARPES	: Angle Resolved Photoemission Spectroscopy
CB	: Conduction Band
CCD	: Charge-Coupled Device
CEMs	: Channel Electron Multipliers
DESY	: Deutsches Elektronen-Synchrotron
DFT	: Density Functional Theory
EXAFS	: Extended X-ray Absorption Fine Structure
FEL	: Free-Electron Laser
FWHM	: Full Width at Half Maximum
HAS	: Hemispherical Analyzer
HASYLAB	: Hamburger Synchrotronstrahlungslabor
HOPG	: Highly-Ordered Pyrolytic Graphite
H-P	: Hewlett-Packard
HP-STM	: High Pressure Scanning Tunneling Microscopy
IMFP	: Inelastic Mean Free Path
In	: Indium
IR	: Infrared
LEED	: Low Energy Electron Diffraction
MCPs	: Multichannel Plates
MES	: Molecular Environmental Science
Mo	: Molybdenum
NEXAFS	: Near-Edge X-ray Absorption Fine Structure
NiTi	: Nitinol

NMR	: Nuclear Magnetic Resonance
NSLS	: National Synchrotron Light Source
PE	: Photoelectron
PEs	: Photoelectrons
PEY	: Partial Electron Yield
PESM	: Photoelectron Spectromicroscopy
RF	: Radio-Frequency
RGA	: Residual Gas Analyzer
SLAC	: Stanford Linear Accelerator Center
SIM	: Stres Induced Martensite
SMA	: Shape Memory Alloy
SR	: Synchrotron Radiation
SSI	: Surface Science Instruments
TESLA-FEL	: 0.1 Å Free-Electron Laser
TEY	: Total Electron Yield
TTF-FEL	: Free Electron Laser of the Tesla Test Facility
UHV	: Ultra-High Vacuum
UPS	: Ultraviolet Photoelectron Spectroscopy
UV	: Ultraviolet
VB	: Valence Band
XPS	: X-ray Photoelectron Spectroscopy
XRF	: X-ray Fluorescence
XANES	: X-ray Absorption Near-Edge Structure
XAS	: X-ray Absorption Spectroscopy

1. INTRODUCTION

Development of new experimental techniques is often followed or paralleled by the progress in science. For instance, the optical microscope helped convert medicine and biology from a speculative activity in old times to today's sophisticated scientific disciplines. X-ray diffraction enabled the flourishing of solid state physics and materials science. Ambient Pressure X-ray Photoelectron Spectroscopy (APXPS), the object of present dissertation study, has also the potential of producing dramatic changes in the study of liquid and solid surfaces, particularly in areas such as atmospheric, environment and catalysis sciences. APXPS adds an important missing element to the host of techniques that give fundamental information, i.e., spectroscopy and microscopy, about surfaces in the presence of gases and vapors, as encountered in industrial catalysis and atmospheric environments. APXPS brings electron spectroscopy into the realm of techniques that can be used in practical environments.

Decades of surface science in ultra-high vacuum (UHV) has shown the power of electron spectroscopy in its various manifestations. Their unique property is the extremely short elastic mean free path of electrons as they travel through condensed matter, of the order of a few atomic distances in the energy range from a few eV to a few thousand eV. As a consequence of this the information obtained by analyzing electrons emitted or scattered from a surface refers to the top first few atomic layers, which is what surface science is all about. Low Energy Electron Diffraction (LEED), Auger Electron Spectroscopy (AES), X-ray Photoelectron Spectroscopy (XPS), Ultraviolet Photoelectron Spectroscopy (UPS), and other such techniques have been used for decades and provided some of the most fundamental knowledge about surface crystallography, composition and electronic structure available today. Unfortunately many of these surface sensitive techniques can not be applied under reaction conditions (***in situ***), usually between millibars and atmospheric pressures, due to the high interaction cross section of electrons with matter preventing them from traveling long distances unscattered in gas environments. Above the millibar

pressure range this distance is reduced to less than a millimeter. There is therefore a large gap of several orders of magnitude where information about surfaces is scarce because these powerful electron spectroscopies cannot operate.

One characteristic of surfaces in ambient pressure environments is that they are covered by dense layers of molecules, even when their binding energy is weak. Water for example is known to form layers several molecules thick at room temperature in humid environments. Metals readily form oxide films several layers thick in oxygen atmospheres. Dense layers of adsorbed molecules can also be produced in ultra high vacuum, often by the simple and expedient method of cooling the sample to cryogenic temperatures. A large amount of data has been obtained in the past in UHV by surface scientists using this method. While this has provided valuable information it begs the question of whether the structures formed in this manner represent equilibrium structures or metastable ones, kinetically trapped due to high activation energies that cannot be overcome at low temperature.

Even when cooling is not necessary, many surface treatments and most chemical reactions necessitate the presence of gases at pressures ranging from millibar to bars. What is the structure and chemical nature of the species formed on the surface in equilibrium with such gases? APXPS provides a much needed electron spectroscopy to analyze surface electronic structure and composition in equilibrium with gases.

The application of XPS as a tool for investigation of catalysis and environmental science has driven the advancement of XPS to function at higher pressure. While such systems have been developed for the past 30 years (Siegbahn et al. 1981, Ruppender et al. 1990, Joyner et al. 1979), there has been a resurgence of APXPS in the past decade due to advanced construction of electron analyzers combined with the exploitation of synchrotron facilities with high brilliance, tunable, monochromatic light with small spot size (Ogletree et al. 2002, Ogletree et al. 2009, Salmeron et al. 2008, Pantforder et al. 2005, Bluhm et al. 2007, Gates et al. 2009).

The first synchrotron based APXPS system to employ an electrostatically controlled and differentially pumped prelens system (an “active” APXPS lens system) was built at the Advanced Light Source (ALS) bending magnet beamline

9.3.2 (Ogletree et al. 2002). After this state of the art system was built, two additional second-generation systems were constructed jointly at ALS (Ogletree et al. 2009) and Die Berliner Elektronen-Speicherring Gesellschaft für Synchrotronstrahlung (Salmeron et al. 2008). These second-generation systems provided enhanced photoelectron (PE) transmission and utilized well focused undulator beamlines that provide better control of polarization of the X-ray. Advances in many fields, including the investigation of catalyst properties in relevant reaction conditions (Bluhm et al. 2004, Günther et al. 2008, Kovnir et al. 2007, Gabasch et al. 2007, Grass et al. 2008, Tao et all. 2008), surface interactions involving water at environmentally relevant humidity (Bluhm 2009, Ghosal et al. 2005) and oxidation of metals (Ketteler et al. 2005, Chung et al. 2009) have been pioneered utilizing these APXPS endstations.

Over the same period other photoelectron based techniques, such as PE microscopy (Casalis et al. 1995, Barinov et al. 2009, Bruche et al. 1932, Feng et al. 2008) and Angle Resolved Photoemission Spectroscopy (ARPES) (Damascelli et al. 2003, Libra et al. 2006) developed and become powerful tools in materials science and solid state physics over the same period. X-ray PE microscopy, which can be achieved either by focusing the X-ray beam or imaging PEs with a dispersive electron lens system, (Seah et al. 1988) provided spatial mapping of elemental composition as well as their chemical states (Günther et al. 2002, Barinov et al. 2009). ARPES has become an essential tool for investigation of electronic structure in modern condensed matter physics. This technique was very useful especially in the field of high temperature superconductors, to map band structures, which is the basis for understanding electron transport and surface reactivity (Damascelli et al. 2003). With similar rich phases and sensitive temperature dependence, catalysis is another example of complex phenomena in solids that can be explored using ARPES (Libra et al. 2006, Schneider et al. 1998).

The present work is devoted to describe the design and construction of a new APXPS system at the Advanced Light Source (ALS) bending magnet beamline 9.3.2 with high electron transmission and detection efficiency to reduce radiation exposure and data acquisition time. Two examples are also presented to demonstrate how this

technique can be used to investigate scientifically and commercially important materials under catalytically and environmentally relevant conditions.

The thesis consists of three main parts. The first part is about synchrotron light. History of synchrotron radiation and principles of creation of synchrotron light will be reviewed. In the second part XPS technique is discussed in the sense of its surface sensitivity. The physical basics, the features seen in the spectrum, and the qualitative interpretation of the results are also presented in that part. The third part describes the general design and construction of a high performance APXPS at the ALS system with the fundamentals of technique and details of the instrumentation. This section also includes the application of the APXPS technique. First, the catalytic oxidation of CO on a Pt(110) surface under various pressures of CO and O_2 gases will be given with a brief description of the basic reaction mechanisms behind the CO oxidation on Pt-group metals. XPS data will be presented and discussed from the viewpoints of the understanding the nature of the heterogeneous catalytic reactions. Second, the XPS results on the role of the temperature on the formation of passivation layer on NiTi shape memory alloys during the early stages of oxidation in pure O_2 gas environment will be introduced and discussed from the viewpoint of biocompatibility in the use of medical purposes. A conclusion and future outlook concludes the present work.

2. REVIEW OF LITERATURE

2.1. Synchrotron Radiation

2.1.1. Introduction

It is well known that an accelerated charged particle, such as one traveling on a curved trajectory, will emit radiation. When moving at relativistic speeds, this radiation is emitted as a narrow cone tangent to the path of the particle (Jackson 1962). Synchrotron radiation is generated when relativistic electrons (or positrons) are accelerated (undergo a change of direction) in a magnetic field. Synchrotron light is a source of brilliant light that scientists can use to gather information about the structural and chemical properties of materials at the molecular level. A synchrotron produces the light by using powerful electro-magnets and radio frequency waves to accelerate electrons to nearly the speed of light. Energy is added to the electrons as they accelerate so that, when the magnets alter their course, they naturally emit a very intense, bright, fully tunable, tightly focused, and highly polarized light, with a time structure useful for many types of dynamics experiments. Different spectra of light, such as Infrared, Ultraviolet, and X-rays, are directed down beamlines to experiment endstations where researchers choose the desired wavelength to study their samples. The researchers observe the interaction between the light and the matter in their sample at the endstations (small laboratories). This tool can be used to probe the matter and analyze a host of physical, chemical, geological, and biological processes.

2.1.2. History of Synchrotron Radiation

Historically, synchrotron light was first accidentally discovered in a General Electric electron synchrotron in 1947 (Elder et al. 1947). For a long time while it was considered just a nuisance to particle physics experiments since it is the major source of energy loss in all particle accelerators with the energy greater than ~200 MeV. In

the 1960's and early 70's pioneering use was made of the light in a parasitic mode so-called first-generation. In this mode, high-energy physics accelerators were used. The high-energy electrons were deflected by a magnetic field to keep them in the storage rings. The X-rays that were produced as such were considered a nuisance and were minimized. They could still be used for X-ray experiments. In the mid-1970's its unique properties and value were beginning to be appreciated and facilities totally dedicated to synchrotron light, such as the National Synchrotron Light Source (NSLS) were constructed. These early dedicated facilities, in which synchrotron light is produced at bending magnets, are called second-generation sources. In the last decade new ways of enhancing the yield, and particularly brightness of synchrotron light were developed. In this third-generation synchrotron sources a combination of focused electron beams and insertion devices (undulator and wiggler magnets) used. Figure 2.1 illustrates yesterday's and today's synchrotron radiation facilities.

The race to develop a new generation of synchrotron radiation sources with vastly enhanced performance has already begun, even as the third-generation facilities enter their prime, which takes us past the present into the future; namely, to the fourth generation. The candidate with the best scientific case for a fourth-generation source is the hard X-ray (wavelength less than 1Å) free-electron laser (FEL) based on a very long undulator in a high-energy electron linear accelerator. Such a device would have a peak brightness many orders of magnitude beyond that of the third-generation sources, as well as pulse lengths of 100 fs (femtosecond) or shorter, and would be fully coherent. Research and development on the many technical challenges that must be overcome are well under way at many laboratories around the world. In the United States, effort is centering around the multi-institutional "Linac Coherent Light Source" proposal to use 15-GeV electrons from the SLAC linac as the source for a 1.5 Å FEL, which if successful would lay the foundation for a later sub-angstrom X-ray FEL. In Europe, HASYLAB at DESY is hosting the two-phase TTF-FEL project culminating in a device operating at 6.4 Å several years from now. The project would pave the way to a still more ambitious 0.1 Å FEL (TESLA-FEL) farther in the future. The history of synchrotron radiation research and sources is summarized in Table 2.1 (Sham et al. 2002).

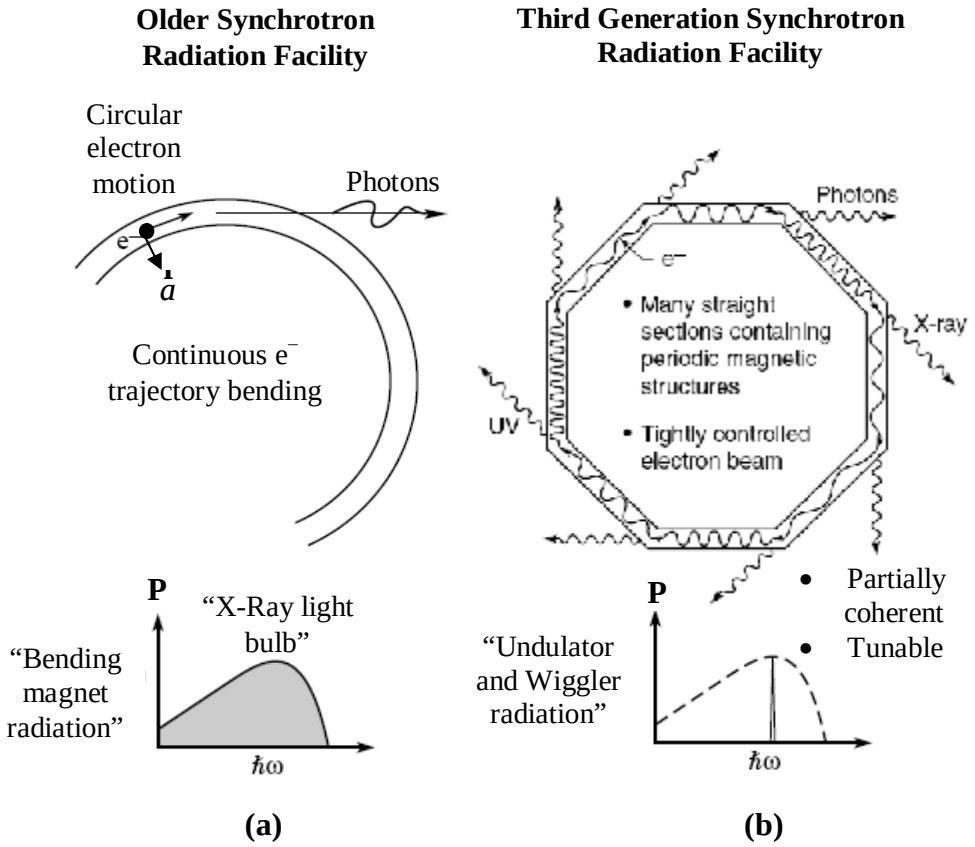

Figure 2.1. (a) Early synchrotron radiation facilities were basically circular rings for bending magnet radiation, although some have been retrofitted with periodic magnetic structures (undulators or wigglers). (b) Modern storage rings are dedicated to broad scientific use optimized for high spectral brightness through the inclusion of many long straight sections for undulators and wigglers, as well as very tightly confined (spatial and angular extent) electron beams. Bending magnet radiation is also generated in turning from one straight section to the next (Attwood 1999) (not shown)

Table 2.1. History of synchrotron radiation research and sources (Sham et al. 2002)

Period	Relevant Development
Pre-synchrotron era before 1947	Light emission by non-relativistic electrons (Larmor, 1897)
Birth and Infancy 1947	Principle of synchrotron (McMillian, Veksler, 1945)
Zero Generation 50's -60's	A few scattered experimenters used electron accelerators to perfom synchrotron radiation (SR) experiments, SR remained a nuisance for high energy physics, no users community
First Generation 60's-70's	Regular use of SR in research began (e.g. HASYLAB in Germany, Daresbury in UK and NBS in US). In late 60's, small synchrotron were built (e.g. Tantalus at Stoughton, DCI at Orsay, INS-SOR in Tokyo, SURF II at NBS). In early 70`s parasitic operation began and quickly expanded in high-energy facilities (e.g. SSRL at Stanford). User community emerged.
Second Generation late 70's-early 90's	SR research took off worldwide. Fully-dedicated Ultraviolet and X-ray rings were funded and built (NSLS, Photon factory, etc.). Most came on-line in mid 80`s. bending magnet (dipole) source was emphasized. User community expended to span a large number of disciplines. Demand of high quality SR (from R to hard X-rays) increased dramatically.

The rapid growth in the field of synchrotron radiation research over the last 25 years has been the most exciting period in the history of X-rays since the period immediately after they were discovered by Röntgen over 100 years ago. Figure 2.2 is a plot of the brilliance of X-ray beams versus time since their discovery in 1895 to the next-generation free-electron lasers (FELs). It can be seen from figure that unprecedented brilliance is being achieved today and even more brilliant machines are expected in the future. From the first generation of parasitic synchrotron facilities

to the third generation synchrotron X-ray research has enjoyed gains in beam brilliance that is 11 to 12 orders of magnitude greater than the standard laboratory X-ray tube.

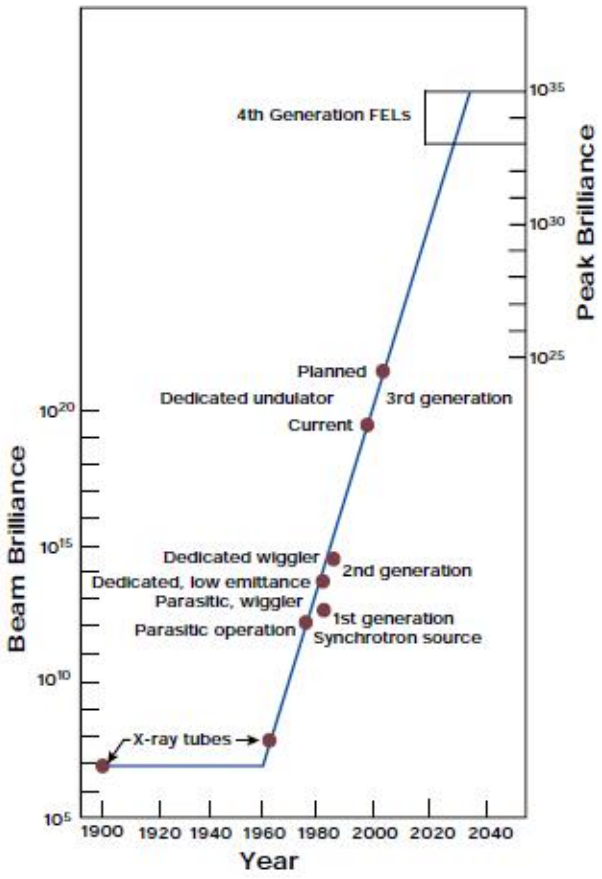

Figure 2.2. The evolution of spectral brightness (brilliance) of X-ray sources through time (Sham et al. 2002)

2.1.3. Advantages of Synchrotron Generated Light

A synchrotron is certainly not the only way to generate infrared (IR), ultraviolet (UV), or X-ray light and so many other techniques can also be used at other types of facilities. There are four general advantages to using synchrotron generated light.

2.1.3.1. Brightness or Flux

If we were to expose a 1mm^2 sample, similar to what a researcher might put under a regular light microscope, to a number of different light sources and measure the amount of energy the matter in that sample interacted with, we would find that the energy generated by a synchrotron using insertion devices is considerably higher than what is produced by other light sources. Generally speaking, synchrotron sources of light pack more photons into a smaller beam of light. Synchrotron radiation is orders of magnitude brighter than X-rays produced by a laboratory source and this brightness has opened up new fields of research and allowed investigation of previously un-measurable samples. More photons produce higher signals, which make it possible to measure a sample more rapidly or examine smaller, thinner, and lower density samples. This offers researchers more information about their sample and a greater variety of techniques to use to learn about their sample. A comparison of average brightness of synchrotron generated light with other light sources is shown in Figure 2.3.

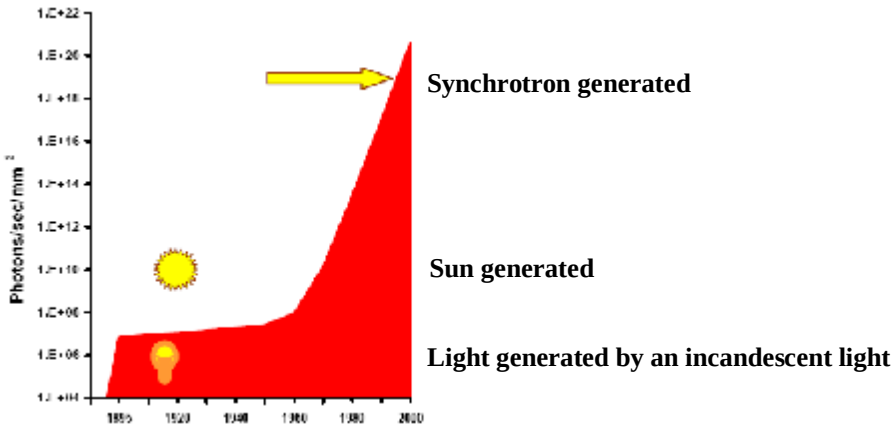

Figure 2.3. Comparison of average brightness of synchrotron generated light to that of other light sources, such as sun and an incandescent light (http://www.lightsource.ca/education/whatis.php)

2.1.3.2. In-Situ Experiments

Another advantage to some synchrotron techniques is the ability to conduct the experiments in situ, or as they are without treatment. There are a number of techniques that have been used in research that require the scientist to treat their sample (crush it; make a solution; slice it; etc). While this is also required for some synchrotron techniques, there are also some that allow for the sample to be analyzed without treatment or with less treatment, which can be a significant advantage.

2.1.3.3. Tunability (Ability to Select Specific Light)

By producing high flux light across a significant portion of the spectrum, a synchrotron offers many different techniques to researchers in one building. In order to gather information, the wavelength of the light has to be appropriate for the size of the matter of interest. Shorter wavelengths allow scientists to gather information about smaller things. In addition, each element absorbs energy at a known level. Thus, being able to select a specific wavelength, or range of wavelengths, allows researchers the flexibility to direct their research towards specific questions (Figure 2.4).

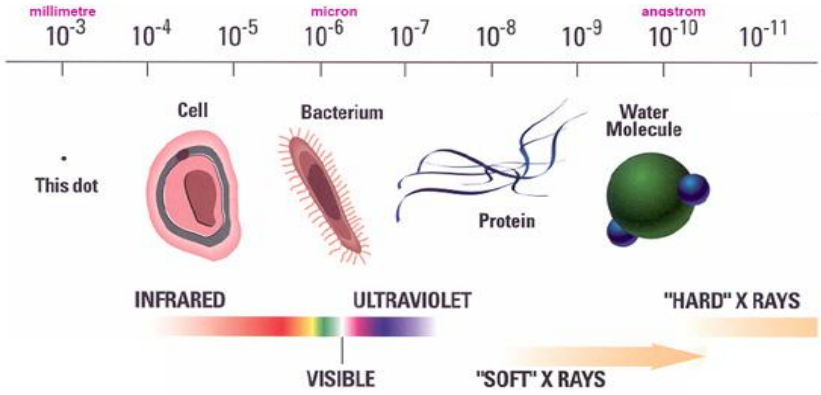

Figure 2.4. Wavelength range of synchrotron light (http://www.lightsource.ca/education/whatis.php)

2.1.3.4. Speed

Due to the extreme brightness of the light, it does not take as long to conduct the same experiment using a synchrotron source of light as it does with a “table top” source for some techniques.

2.1.4. Creation of Synchrotron Light

In a synchrotron, electrons are generated and accelerated to the desired energy before they are stored in a ring: the so-called storage ring. Without the presence of an external magnetic field, the electrons will travel in a straight line, but when a magnetic field is applied they will bend because of the Lorentz Force, which is proportional to the electron velocity and the magnetic field. This force causes an acceleration of the particles and therefore radiation is formed. This radiation is emitted in the direction of motion of the particle. Within the bending magnet, the electron changes direction and a radiation beam in between the original and the new electron direction is emitted. The creation of radiation will cause the velocity of the electrons to reduce and therefore the radius of the circular orbit will decrease. After a short period the electrons will have lost their energy and, in order to prevent this, the energy lost is compensated by a radio frequency cavity. During the bending of the electron beam, a wide spectrum of radiation is formed.

Between the magnets, the electrons follow a straight path without the formation of radiation. Magnetic structures (insertion devices) can be placed in the electron beam in order to produce radiation. There are three types of magnetic structures commonly used to produce synchrotron radiation: ***bending magnets, undulators,*** and ***wigglers***. Bending magnets cause a single curved trajectory as pictured in Figure 2.5. The result is a fan of radiation around the bend.

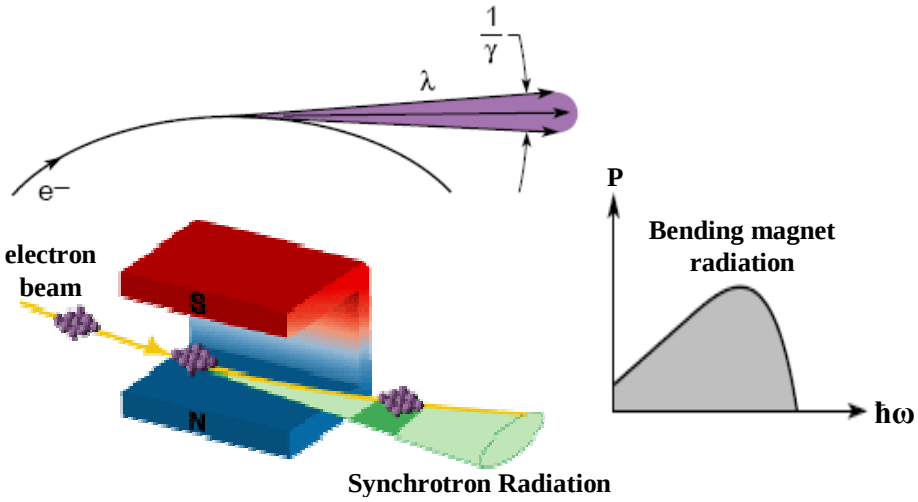

Figure 2.5. Bending magnet radiation occurs when a relativistic electron travels in a uniform magnetic field, executing a circular motion with acceleration directed toward the center. The radiation is directed tangentially outward in a narrow radiation cone, giving the appearance of a sweeping "searchlight". The radiation spectrum is very broad, analogous to a "white light" X-ray light bulb. The emission angle is typically 1/γ, where γ is the Lorentz contraction factor (Attwood 1999)

Bending magnets exhibits a continuum of radiation characterized by a critical photon energy E_c (keV) or critical wavelength λ_c (Å). By definition half of the radiated power is above E_c and half below. E_c is determined by the electron energy: the higher the electron energy, the higher the critical energy, with the relationship given by:

$$E_c = \frac{2.218E^3}{r} = 0.665E^2(GeV)B(T) \qquad (2.1.)$$

where ρ is the radius in meters of the electron orbit at the bending magnet, E is the particle beam energy in GeV, and B is the magnetic field in Tesla. To reach the ultraviolet/soft X-ray region, the electrons in a circular ring with conventional 1-Tesla bending magnets need to be accelerated up to about 1 GeV. More than 2 GeV is needed for hard X-rays (>5 keV). The critical photon energy is in fact a very useful parameter for characterizing synchrotron radiation from relativistic electrons as they traverse the fields of a bending magnet. For example two storage rings operating in

United States, the Advanced Light Source (ALS) at Lawrence Berkeley National Laboratory in California, with a beam energy of 1.9 GeV and a bending magnet field strength of 1.27 Tesla has a critical photon energy of 3.05 keV and a critical wavelength of 4.1 Å, while the Advanced Photon Source (APS) at Argonne National Laboratory in Illinois, with a beam energy of 7.0 GeV and a bending magnet field strength of 0.6 Tesla, has a critical photon energy of 19.5 keV and a critical wavelength of 0.64 Å.

Bending magnet radiation covers a broad region of the spectrum, including the primary absorption edges of most elements (Figure 2.6).

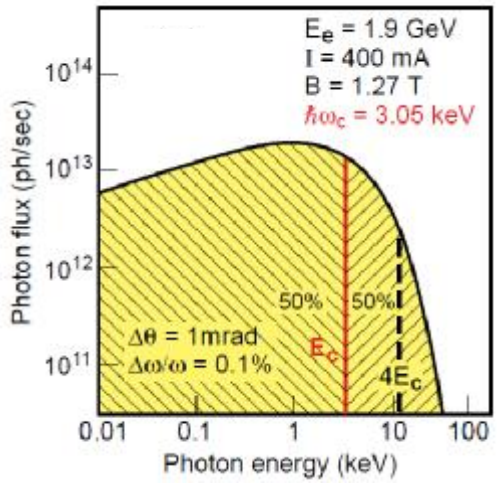

Figure 2.6. Energy region of the spectrum at Advanced Light Source (ALS) covered by bending magnet (Attwood 1999)

Undulators are periodic magnetic structures (with relatively weak magnetic fields) placed in straight sections which make wiggles (long period) in the charged particle trajectory which reinforces the light emitted by the accelerated electrons, much as multiple passes through a medium with a population inversion is the basis for the special properties of lasers. The periodicity causes the electron to experience a harmonic oscillation as it moves in the axial direction, resulting in a motion characterized by small angular excursions called undulations (Kim 1989, Kim 1995, Kim 1999, Attwood 1985), as shown in Figure 2.7. The weak magnetic fields cause the amplitude of this undulation to be small. Hence the resultant radiation cone is narrow. In combination with a tightly confined electron beam, this leads to radiation with small angular divergence and relatively narrow spectral width.

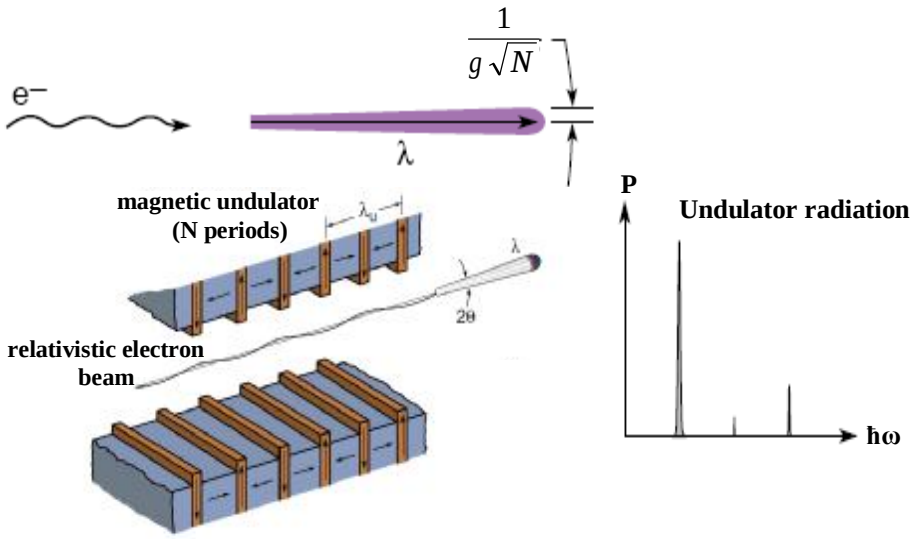

Figure 2.7. Undulator radiation is generated as a highly relativistic electron traverses a periodic magnetic field. In the undulator limit, the magnetic field is relatively weak and the resultant angular excursion of the electron are smaller than the angular width of the natural radiation cone, 1/γ, normally associated with synchrotron radiation. The frequency spread of undulator radiation can be very narrow, and the radiation can be extremely bright and partially coherent, under certain circumstances. The characteristic emission angle is narrowed by a factor $\sqrt{N}$, where N is the number of magnetic periods. Typically N is of order 100. Depending on the magnet strength, harmonic radiation may be generated (Attwood 1999)

Wigglers are strong magnetic field version of undulators. Due to the stronger fields, the oscillation amplitude and concomitant radiated power is larger. The radiation cone is broader in both space and angle. The radiation spectrum is similar to that of bending magnets, but characterized by a much larger photon flux and a shift to harder X-rays (shorter wavelengths) as seen in Figure 2.8.

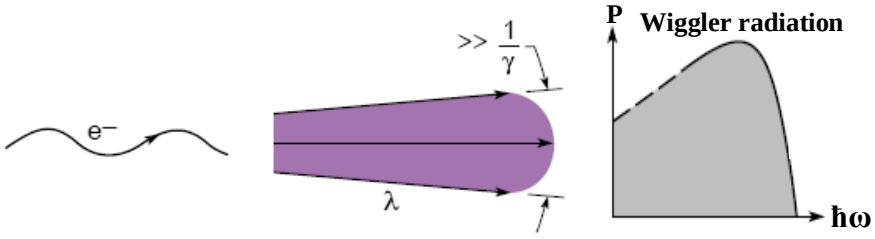

Figure 2.8. Wiggler radiation is also generated from a periodic magnet structure, but in the strong magnetic field limit where in at least one plane the angular excursions are significantly greater than the natural (1/γ) radiation cone. Because accelerations are stronger in this limit, the radiation generated peaks at higher photon energies and is more abundant (higher photon flux and more power). The radiation spectrum is very broad, similar to that of the bending magnet. Although more power is radiated, wiggler radiation is less bright because of the substantially increased radiation cone (Attwood 1999)

A wiggler generates a quasi continuum, with a flux higher than a bending magnet roughly in proportion to the number of wiggles. In an undulator the self-reinforcing aspect of the interaction of the electron beam with the magnetic structure leads to an N^2 gain in brightness, a highly collimated, partially coherent point source, and a very highly structured energy spectrum. It is the concentration of all of the emission into the narrow undulator lines that creates the many orders of magnitude higher brightness of undulators. The peak energy can be tuned by changing the gap between the magnet poles. Synchrotron light facilities which emphasize insertion devices, and have a high brightness electron beam (small, highly collimated) are called third generation sources. It is these sources that are creating tremendous excitement in many areas of science today.

2.1.5. Advanced Light Source (ALS)

The ALS is a research facility used by scientists to explore the properties of materials, analyze samples for trace elements, probe the structure of atoms and molecules, study biological specimens, investigate chemical reactions, and manufacture microscopic machines. The ALS produces light, in the far ultraviolet and soft X-ray regions of the electromagnetic spectrum, with special qualities. This

light has wavelengths from 0.0001 micrometer to 0.1 micrometer. Scientists use these X-rays as a tool to do their work. The nature of the particles in the storage ring at ALS is electrons with a nominal energy of 1.9 GeV. The size of the electron beam in the ring is ~0.20 mm x 0.02 mm (about the width of a human hair).

The ALS produces light in the X-ray region of the electromagnetic spectrum that is one billion times brighter than the sun (Figure 2.9). This extraordinary tool offers unprecedented opportunities for state-of-the art research in materials science, biology, chemistry, physics, and the environmental sciences. Ongoing research topics include the electronic structure of matter, protein crystallography, ozone photochemistry, x-ray microscopy of biological samples, and optics testing.

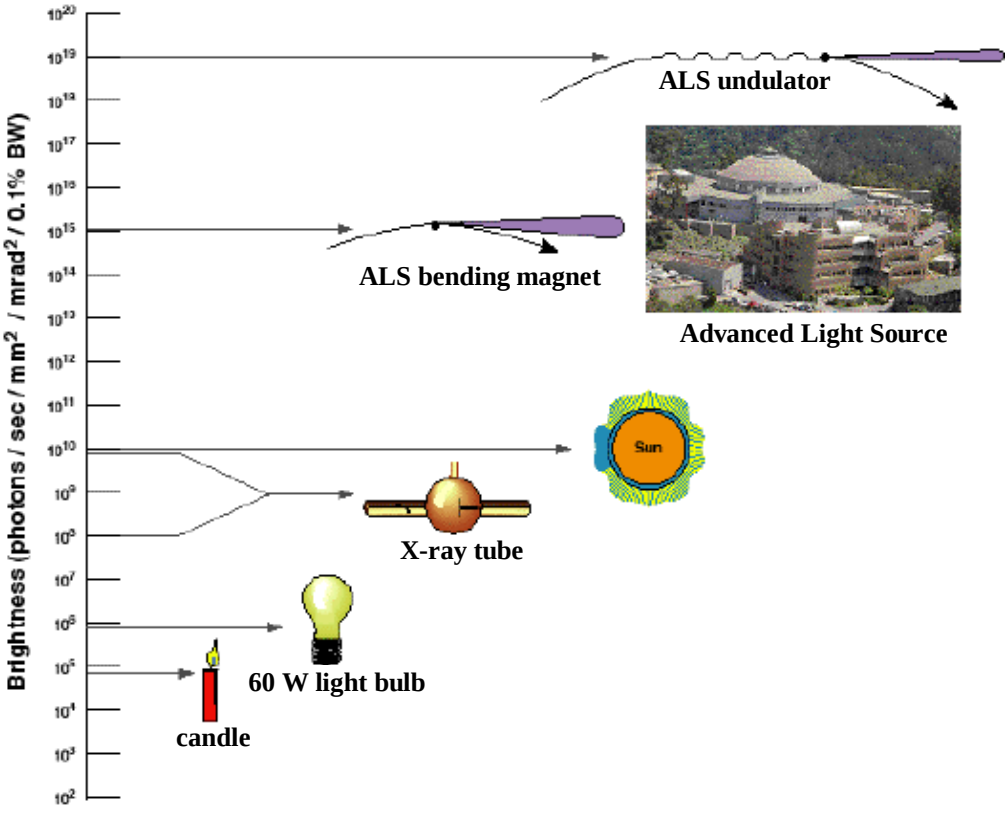

Figure 2.9. Comparison of average brightness of bending magnet and undulator light from the Advanced Light Source (ALS) to that of other light sources, such as an X-ray tube and the sun (http://unicorn.mcmaster.ca/research/synclight/overview.html)

The greatest advantage of the ALS is its brightness. The X-rays produced at ALS are a hundred million times brighter than those from the most powerful X-ray

tube. A higher concentration of photons on a smaller area allows scientists to increase the specificity of their experiments. They can study smaller objects or choose more specific photon energies (down to tenths of electron volts) to study a very specific target. To produce light of the wavelengths and brightness that scientists want, the ALS designers had to create a large machine. Its largest component, the storage ring, has a diameter two-thirds the length of a football field. The storage ring is a tubular vacuum chamber made to hold an electron beam travelling through it at nearly the speed of light and maintain the high energy of the electron beam. As the electrons circle the ring, they give off light. The ring must be as big as it is to maintain the electron beam at 1.5-1.9 billion electron volts, the energy required to produce light of the desired wavelengths and brightness. Besides their brightness, X-rays from the ALS have other useful characteristics such as tunability, near-coherence, pulsed nature, and polarization.

2.1.6. ALS Components

Figure 2.10 is a simple schematic of components at ALS. The relativistic electrons are injected into the ring from a linear accelerator and (energy) booster synchrotron. Various magnetic lenses keep the electrons traveling along the desired trajectory. Synchrotron radiation is produced as the electrons pass through the bending magnets, undulators, and wigglers. Electron beam energy lost to synchrotron radiation is replenished with a radiofrequency accelerator (a cavity with an axial electric field oscillating) at the frequency of arrival of sequential electron bunches). Typical parameters characterizing synchrotron radiation from ALS storage ring optimized for the generation of soft X-rays is given in Table 2.2.

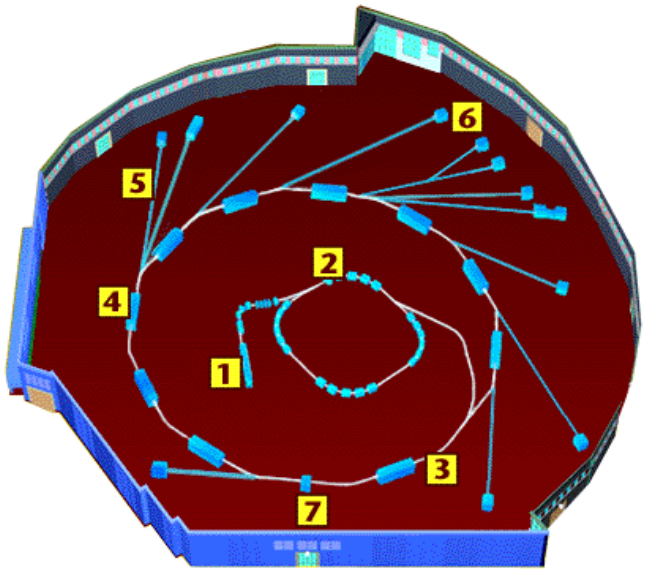

Figure 2.10. A schematic of components at Advanced Light Source (ALS). This sketch of an electron storage ring optimized for soft X-ray radiation shows a linear accelerator, linac, (1) and booster synchrotron (2) that brings electrons up to an energy matched to storage ring (3) magnet settings, an injection system, which directs electrons into the ring, and a radio frequency, RF, generator (7) to replenish the energy lost to synchrotron radiation as the electrons pass bending magnets, undulators, and wigglers (4). Straight sections for undulators and wigglers direct energy into beamlines (5) and end sections (6) for various scientific studies. Bending magnet radiation beamlines are located between straight sections (http://www.lbl.gov/MicroWorlds/ALSTool/ALS_Components/)

Table 2.2. Typical parameters for synchrotron radiation at ALS (Attwood 1999)

Typical Parameters of Advanced Light Source	
Electron energy (GeV)	1.90
γ	3720
Current (mA)	500
Circumference (m)	197
RF frequency (MHz)	500
Pulse Duration (FWHM) (ps)	35-100
Bending Magnet Radiation:	
Bending magnet field (T)	1.27
Critical photon energy (keV)	3.05
Critical photon wavelength (nm)	0.407
Bending magnet sources	24
Undulator Radiation:	
Number of straight sections	12
Typical undulator period (cm)	5.00
Number of periods	89
Photon energy (K=1, n=1) (eV)	457
Photon wavelength (K=1, n=1) (nm)	2.71
Tuning range (n=1) (nm)	2.0-5.4
Tuning range (n=3) (nm)	0.68-1.8
Central cone half-angle (K=1) (μrad)	35
Power in central cone (K=1, n=1) (W)	2.3
Flux in central cone (photon/s)	3.1×10^{16}
σ_x, σ_y (μm)	260, 16
σ'_x, σ'_y (μrad)	23, 3.9
Brightness (K=1, n=1) ((photons/s)/mm^2.mrad^2.(0.1%BW)	2.3×10^{19}
Total power (K=1, all n, all θ) (W)	187
Other undulator periods (cm)	3.65, 8.00, 10.0
Wiggler Radiation:	
Typical wiggler period (cm)	16.0
Number of periods	19
Maximum magnetic field (T)	2.1
K (maximum)	32
Critical photon energy (keV)	5.1
Critical photon wavelength (nm)	0.24
Total power (max. K) (kW)	13

2.1.6.1. Linear Accelerator (Linac)

The linear accelerator, or linac, is the electromagnetic catapult that brings electrons from a standing start to relativistic velocity, a velocity near the speed of light.

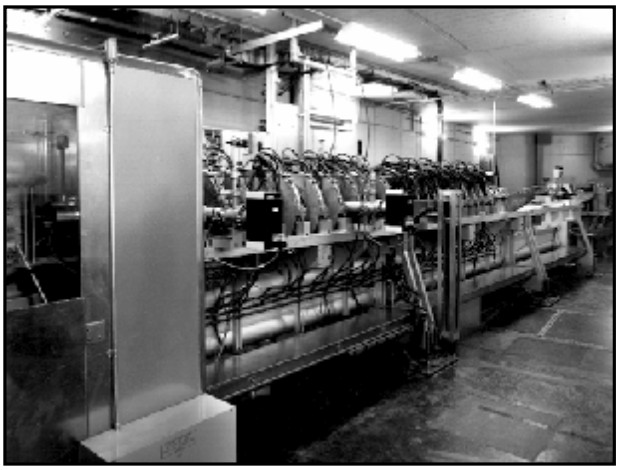

Figure 2.11. A photo of the ALS linac
(http://www.lbl.gov/MicroWorlds/ALSTool/ALS_Components/Linac/)

The linac is four meters long. A simplified drawing that shows how a linear accelerator works is shown in Figure 2.12. The major parts of a linear accelerator are:

a) The Electron Gun

b) The Buncher

c) The Linac (itself)

Each part is responsible for a stage in the acceleration of the electrons.

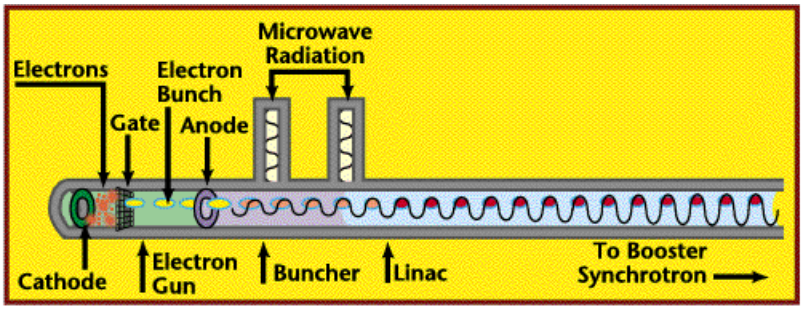

Figure 2.12. A simplified drawing shows how a linear accelerator works
(http://www.lbl.gov/MicroWorlds/ALSTool/ALS_Components/Linac/)

2.1.6.1.(1). The Electron Gun

The electron gun is where electron acceleration begins. The electrons start out attached to the molecules in a one-cubic-centimeter chunk of barium aluminate. This is the cathode of the electron gun. A cathode is a surface that has a negative electrical charge. In linac electron guns this charge is usually created by heating the cathode. Barium aluminate is a “thermionic” material; this means that its electrons tend to break free of their atoms when heated. These electrons "boil" near the surface of the cathode.

The gate is like a switch. It consists of a copper screen, or grid, and is an anode. An anode is a surface with a positive electrical charge. Every 500 millionth of a second the gate is given a strong positive charge that causes electrons to fly toward it from the cathode in tremendous numbers. As these electrons reach the gate, they become attracted even more strongly by the main anode, and pass through the gate. Because the gate is pulsing at a rate of 500 million times per second (500 MHz), the electrons arrive at the anode in loose bunches, a 500 millionth of a second apart. The anode is a torus (a doughnut) shaped to create an electromagnetic field that guides most of the electrons through the hole into the next part of the accelerator, called the buncher.

2.1.6.1.(2). The Buncher

The purpose of the buncher is to accelerate the pulsing electrons as they come out of the electron gun and pack them into bunches. To do this the buncher receives powerful microwave radiation from the klystron. The microwaves accelerate the electrons in somewhat the same way that ocean waves accelerate surfers on surfboards. In Figure 2.13, the red disks are electrons in the buncher. The curve is the microwave radiation in the buncher. The electrons receive more energy from the wave (more acceleration) depending on how near they are to the crest of the wave, so the electrons riding higher on the wave catch up with the slower ones riding lower. The right-hand wave shows the same group of electrons a split second later. On the

front of the wave, the two faster electrons have almost caught up with the slower electron. They won't pass it though, because they are now lower on the wave and therefore receive less acceleration.

The higher electron on the back of the wave gets just enough acceleration to match the speed of the wave, and is in the same position as it was on the left-hand wave. This represents the last electron in the bunch. The lower electron on the back of the wave gets too little energy to keep up with the bunch and ends up even lower on the right-hand wave. Eventually it will fall back to the electron bunch forming one wave behind.

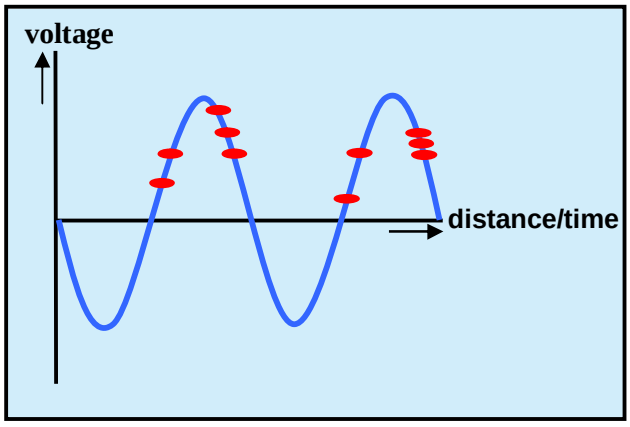

Figure 2.13. Buncher
(http://www.lbl.gov/MicroWorlds/ALSTool/ALS_Components/Linac/)

2.1.6.1.(3). The Linac

The linac itself is just an extension of the buncher. It receives additional Radio Frequency (RF) power to continue accelerating the electrons and compact them into tighter bunches. Electrons enter the linac from the buncher at a velocity of 0.6 *c*, that's 60% of the speed of light. By the time the electrons leave the linac, they are traveling very close to the speed of light.

2.1.6.2. Booster Synchrotron

A linac long enough to accelerate electrons to the energy needed by the ALS would not fit inside the building. Instead, a circular booster synchrotron is used in

which the electrons receive a "boost" from an accelerating chamber (RF cavity) each time they go around. In less than one second inside the booster, the electrons make 1,300,000 revolutions (and travel 98,000 kilometers), reach 99.999994% of the speed of light, attain their target energy (usually 1.5×10^9 eV), and are ready to be transported to the storage ring.



Figure 2.14. Booster ring
(http://www.lbl.gov/MicroWorlds/ALSTool/ALS_Components/Booster/)

2.1.6.3. Storage Ring

Once the electrons reach their target energy in the booster synchrotron, an injection system transfers them from the booster to the storage ring where they circulate for hours. The electrons travel in an aluminum vacuum chamber with fewer atoms per unit volume than outer space (the pressure is about one trillionth that of the atmosphere), so there are almost no collisions to slow them down.

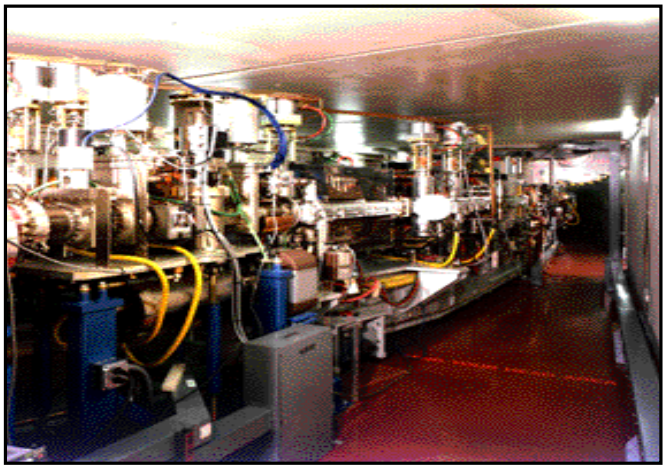

Figure 2.15. Storage Ring (http://www.lbl.gov/MicroWorlds/ALSTool/ALS_Components/StorageRing/)

The storage ring is roughly circular with 12 arc-shaped sections (about 10 meters long) joined by 12 straight sections (about 6 meters long). Hundreds of precision electromagnets focus and bend the electron beam as it circles the storage ring more than a million times a second. Electrons curving through the ring's 12 arc sections emit fanlike beams of photons, like cars rounding a bend at night. Between these curves are straight sections where multi-magnet devices, undulators and wigglers, wiggle the electrons back and forth to form a narrow beam of light 100 million times brighter than conventional X-ray sources. The synchrotron light emitted by the electrons is directed to beamlines through the round beam ports.

2.1.6.4. Undulators and Wigglers

The brightest synchrotron light at the ALS comes from undulators (located in the straight sections of the storage ring) that contain over one hundred magnetic poles lined up in rows above and below the electron beam. The magnets force the electrons into a snake-like path, so that the light from all the curves adds together. Although they are about 4.5 meters long and weigh about 40,000 pounds, the undulators have to be built to extreme precision. Many of the design tolerances are approximately 50 microns, less than the width of a human hair. Wigglers are similar to undulators but have fewer magnetic poles. Figure 2.16(a) shows one undulator

installed in a straight section of the storage ring (lower left), and another undulator being moved above the storage ring shielding to its final location in another part of the ring. The booster synchrotron to storage ring transfer line is visible in the lower right. Figure 2.16(b) is a close up photo of ALS U5 undulator.

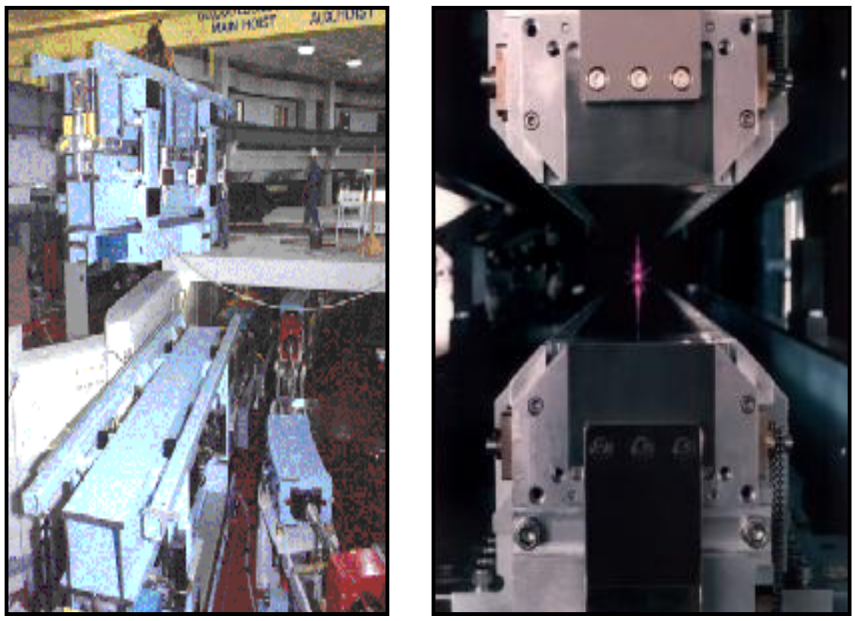

(a) **(b)**

Figure 2.16. (a) Undulator, (b) ALS U5 undulator, beamline 7.0 (N = 89, λu = 50 mm) (http://www.lbl.gov/MicroWorlds/ALSTool/ALS_Components/UndulatorWigs/)

2.1.6.5. Beamline

As the electrons travel in their circular orbit in the storage ring, they emit synchrotron light in the ultraviolet and X-ray range of the electromagnetic spectrum. The beamlines deliver the light down an optical obstacle course from the storage ring to the experiment stations.

Beamline mirrors steer and focus a thin beam of light (photons) down meters of vacuum pipe to the target, a sample of interest inside an experiment chamber. Some experiments use all the available photons, but the storage ring produces so many photons that scientists can afford to be choosy about which ones they use. Scientists who want to select only photons with certain wavelengths use beamlines with monochromators which act like prisms, spreading the thin photon beam into a

spectrum of different wavelengths so that only the desired ones can be selected. The beamline transfers the photons from the storage ring to the experiment chamber.

2.1.6.6. Experiment Station

At the experiment station, researchers make observations by using the synchrotron light (photons) to produce small changes in their samples, while a variety of instruments record the results. Computers help convert the instruments' readings into images, graphs, or even three-dimensional models, making new information available for advancing science and technology.

As a national user facility, the ALS is available to researchers from universities, industry, and government laboratories. Each year, over 100 scientists from around the world come to the ALS to conduct experiments

2.1.6.7. RF System

The radio-frequency system, or RF system, supplies power to the ALS in the form of microwaves. Microwaves are radio waves with a wavelength between about one meter and one millimeter, which are the wavelengths used for radio and television broadcasts as well as radar and microwave ovens. Most parts of the RF system supply microwave radiation with a wavelength of about 0.6 meter. Microwave power is used to energize electrons, keeping them whirling around the ALS storage ring at almost the speed of light. Eventually, the electrons release this energy as X-rays and ultraviolet light. Scientists use this light to carry out experiments at the ALS. All the energy released as synchrotron radiation originates as RF power.

The basic components of the RF system include klystrons, waveguides, and RF cavities.

2.1.6.7.(1). Klystrons

A klystron is very powerful type of microwave amplifier. Radar installations and television broadcast stations use klystrons to generate their broadcast signals. The klystrons at the ALS "broadcast" down special tubes and cables, called waveguides, which lead to the linac, booster synchrotron, and storage ring.

The ALS has four klystrons, two to accelerate electrons in the linac, one to power the RF cavity of the booster synchrotron, and one to maintain the energy of electrons in the storage ring. The klystron for the ALS booster ring (Figure 2.17) is a commercial model like those used in television broadcasting. As a TV transmitter it would broadcast on channel 18, which corresponds to a frequency of roughly 500 MHz.

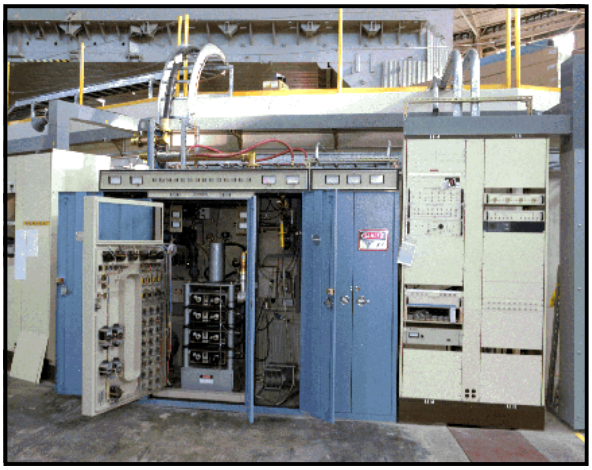

Figure 2.17. Klystron (http://www.lbl.gov/MicroWorlds/ALSTool/ALS_Components/RFSystem/)

Figure 2.18 illustrates how a klystron works. An electron gun produces an intense flow of electrons into the klystron. A low-energy microwave signal intersects this continuous electron beam, breaking it up into a pulsed beam consisting of separate "bunches" of electrons. The pulsed electron beam passes through a tuned waveguide, inducing a powerful high-energy microwave signal. High-energy microwave power travels along the waveguide to the linac, booster synchrotron, or storage ring, where it passes its energy to electrons, accelerating them to relativistic velocity.

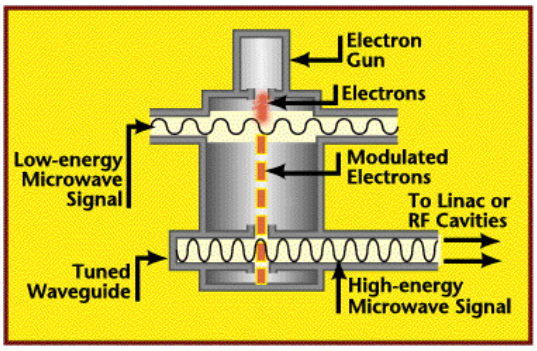

Figure 2.18. Diagram shows how klystron works (http://www.lbl.gov/MicroWorlds/ ALSTool/ALS_Components/RFSystem/)

In the same way that a radio broadcast signal induces an electrical current in a portable radio antenna, the low-energy microwave signal (let's say 500 MHz) causes the electrons in the electron beam to speed up or slow down at the point where the two intersect. When the microwave is near its crest (peak power) as it intersects the beam, it makes the electrons in that part of the beam at that moment speed up, just as a surfer speeds up when she catches a wave. When the microwave is near its trough as it meets the beam, the electrons in that part of the beam at that moment slow down. The result is an electron beam that is broken into pulses that have the same frequency as the low-energy microwaves: 500 MHz.

The pulsing electron beam interacts with the tuned waveguide (a very carefully constructed and adjusted hollow copper tube) causing it to resonate like a bell at 500 MHz, transmitting microwave radiation down its entire length, which extends either to the linac, the RF cavity on the booster synchrotron, or the RF cavities on the storage ring.

2.1.6.7.(2). Waveguide

A waveguide is a conduit for efficiently transmitting electromagnetic radiation. The coaxial cable used for cable television, the optical fiber used in telecommunications, and the linac are other examples of waveguides. The large box-like structures in Figure 2.19 are waveguides attached to the top of the storage ring.



Figure 2.19. Waveguide
(http://www.lbl.gov/MicroWorlds/ALS_Components/RFSystem/)

2.1.6.7.(3). Radio Frequency (RF) Cavity

Radio frequency cavities, or RF cavities, receive RF energy from a klystron and transfer it to electrons as they pass through the cavities on their way around the booster synchrotron and storage ring. Just as in the klystron, RF radiation interacts with electrons, adding energy to increase or maintain their speed. In the booster ring this energy increases the speed of the electrons to 99.999996 percent of the speed of light. In the storage ring two RF cavities resupply the electrons with the energy that they lose in emitting synchrotron light, about 100 MeV for every turn around the storage ring. Two photographs of an RF cavity during installation at the ALS booster synchrotron are shown in Figure 2.20.

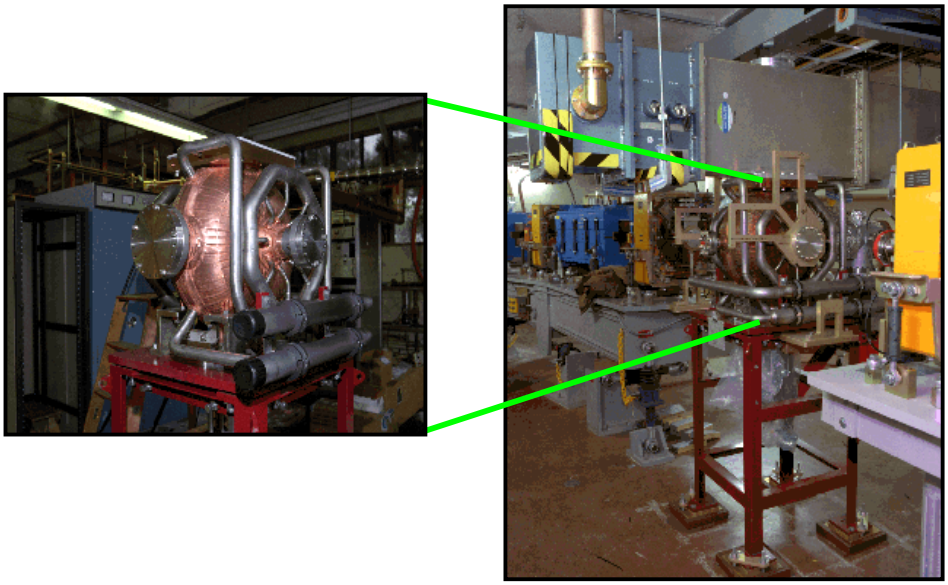

Figure 2.20. RF cavity
(http://www.lbl.gov/MicroWorlds/ALS_Components/RFSystem/)

The microwaves in the cavity are synchronized to crest just as each bunch of electrons enters the cavity (every 2 billionths of a second), so that the bunch is accelerated by a wave that is approaching peak amplitude. This synchronization takes into account the time it takes the control signal (travelling at the speed of light) to reach the controls for the klystron and the time it takes the microwave radiation to reach the RF cavity.

2.2. X-Ray Photoelectron Spectroscopy (XPS)

2.2.1. Introduction

During the last forty years or so, a very large number of techniques have been developed which probe the surfaces of materials. The catalyst for much of this activity was the availability, during the early 1960's, of stainless steel vacuum systems capable of routine operation under ultra-high vacuum (UHV) conditions, i.e. base pressures after bake-out of 10^{-10} Torr, thereby allowing clean surfaces to be generated ***in situ*** and maintained for periods up to an hour or more. A small number of these characterization methods are analytical, in the sense that they provide information on chemical composition. X-ray Photoelectron spectroscopy (XPS) is one of techniques that have achieved the status of widespread application with the commitment of commercial manufacturers to on-going improvement in performance. XPS involves the energy analysis of electrons emitted from the surface of a material by X-ray (photon) excitation. XPS is inherently quantitative, i.e. intensities of peaks which allow element identification are directly related to the atomic concentration within the samples volume. Furthermore, important information about the chemical state of surface atoms can be obtained. These fundamental attributes have ensured the usefulness of XPS for practical surface chemical analysis from the very beginning.

XPS has fascinating history dating back almost a century. This is chronicled in the next section as the milestones in the development of commercial instruments during the last 30 years. The following part provides an introduction to XPS. It covers the physical principles, the features seen in the spectrum, and the information they carry, the types of the experiment which can be performed and the qualitative interpretation of the results.

2.2.2. History of XPS

2.2.1.1. The Early Work

The emission of electrons from a metal surface under ultraviolet photon irradiation known as the photoelectric effect was discovered by Hertz in 1887. Subsequent research, in which the photon energy was extended into the X-ray regime, represents the beginnings of XPS. Innes, for example, reports in 1907 the use of a **Röntgen** (discharge) tube fitted with a Pt anticathode (generating Pt X-rays) to irradiate several metals in vacuum (Innes 1907). The emitted electrons were velocity selected using a magnetic field from two Helmholtz coils before detection on a photographic plate. This work was directed at understanding the photoelectric effect.

The field was first developed by Rutherford`s group in Manchester who had appropriate expertise in both the magnetic analysis of electron energies, from their β-ray spectroscopy studies of radioactive materials, and the application of X-ray spectroscopy to understanding the electronic structure of atoms. In 1911, Rutherford had introduced the nuclear atom model and in 1913, Moseley had used X-ray spectroscopy to establish the importance of atomic number. Also in 1913, Bohr had described the quantized motions of the atomic electrons. Rutherford was, therefore, ideally placed to understand the potential of the early XPS experiments for atomic structure studies and to encourage his junior colleagues in this direction. In a move that was to be repeated later in the evaluation of the technique, the key experimental development was the replacement of the radioactive sample in a β-ray spectrometer by a sample which could be irradiated by X-rays. The early experiments were carried out by Moseley (who designed the X-ray source), Rawlinson, and Robinson. As World War I intervened in 1914, some preliminary results were published (Robinson et al. 1914) and Rutherford tentatively attempted (Rutherford 1914) to relate the kinetic energies of the β-rays (E_β) to the X-ray energy ($h\upsilon$). However, there were to be several developments in thinking and understanding before the basic XPS equation could be expressed in terms of the atomic electron binding energies (E_B) as $E_b = hn - E_B$.

After World War I, in which Moseley was tragically lost, Robinson continued the work and Maurice de Broglie started research in France. By the early 1920s, the photoelectron spectra of many elements had been obtained, using a variety of high-energy X-rays for excitation, together with magnetic analysis of electrons emerging from thin foils, and photographic detection. The spectra consisted of bands with a more-or-less well-defined edge (from which the electron binding energy could be estimated) with a long tail of electrons which had suffered energy loss. The separation of the edges corresponded to the separation of lines in the X-ray emission spectrum. Anomalous band, seemingly due to emission caused by fluorescence X-rays characteristic of the element under study, were only understood in 1925 when Auger demonstrated the radiationless electron emission process (which bears his name) in completely unrelated cloud-chamber experiments. The growing superiority, in terms of accuracy, of X-ray spectroscopic techniques for studies of the electronic structure of atoms then lead to the demise of XPS activity. Robinson continued research through the 1930s, but without significant advances in technique, until World War II brought his long contribution to an end.

The technique was revived after World War II by Steinhardt, (A PhD student) and Serfaas (his supervisor) at Lehigh University, who take the credit for concerning XPS as a potential analytical tool, particularly for studying surface chemical phenomena such as corrosion and catalysis. Steinhardt's 1950 thesis (Steinhardt et al. 1951) bore the rather prophetic title "An X-ray Photoelectron Spectrometer for Chemical Analysis". A comparison of the spectra of metals and their binary alloys showed that "peak" intensities could be used for quantitative analysis. After completing his doctoral research, Steinhardt constructed several new instruments, including Geiger-Muller counting and a 127° electrostatic analyzer, but without a significant improvement in performance. Despite the use of very high energy X-rays, (Mo Kα at 17.5 keV) surface effects were discerned, for example, by depositing barium stearate layers onto a gold surface (Steinhardt et al. 1953). Similar experiments, again without improvements in resolution, were also carried out by Henke, several years later, using an instrument with a hemispherical electrostatic analyzer and, for the first time, soft X-rays (Al Kα at 1486.7 eV) for excitations

(Henke 1962, Henke 1963). Hence also designed the first indirectly-excited "XPS-type" X-ray source (as opposed to the type used in X-ray diffraction which has several disadvantages for XPS application) (Henke 1961). A detailed history of the period 1910-1960 has been published by workers at LaTrobe University (Jenkin et al. 1977, Jenkin et al. 1978).

2.2.2.2. The Breakthrough Years

In 1951, Kai Siegbahn then at Stockholm University initiated a programme to study X-ray photoelectrons at much higher energy resolution, in order to effectively compete with X-ray emission spectroscopy in the study of the electronic structure of atoms. This work built on his development, during the 1940s, of magnetic analyzers for high-resolution nuclear β-ray spectroscopy and the realization that XPS might be performed in a similar instrument if the radioactive source were to be replaced by an X-ray tube, he knew that a new spectrometer design was required in order to accurately measure electron energies at the lower energies involved (in the extreme, a few hundred eV for soft X-ray excitation compared with the several tens of keV for β-rays). Furthermore, the absolute energy resolution would have to be 1 eV or better to approach the natural line widths of the atomic levels. Shortly after moving to Uppsala in 1954, a new iron-free double-focusing magnetic β-ray spectrometer was tested and found to have the required precision in momentum measurement of 1:10 (Steinhardt et al. 1953). A Cu Kα X-ray source (8048.0 eV) was installed and the first photoelectron spectra followed once it was realized that the samples must be free of major surface contamination. For the first time, a sharp peak was now resolved at the high kinetic energy "edge" seen by all previous workers, corresponding to electrons emerging from the surface without energy loss. Accurate measurement of this peak position in kinetic energy (E_K), therefore, allowed the core level binding energy (E_B) to be accurately determined for the first time, since the energy of the exciting X-ray photon was also accurately known.

Chemical effects in X-ray spectroscopy had been appreciated since the 1920s, but, being difficult to measure accurately, they were not pursued. Seegbahn's group

published on chemical shifts in the spectra of copper and its oxides in 1957 (Sieghbeln et al. 1957) to 1958 (Sokolowski et al. 1958, Nordling et al. 1958). With the equipment then available, these small shifts were also difficult to measure and work in this area was not emphasized initially. The development of softer X-ray sources (Al Kα and Mg Kα) for studying the lighter elements significantly improved resolution in two ways: the exciting X-ray linewidth was reduced to 1 eV or less and, since the analyzer relative resolution was constant, the lowered photoelectron kinetic energies meant an increased absolute energy resolution. Then, the observation of two well-resolved peaks of equal intensity in the sulphur core level spectra from sodium thiosulphate, $(Na^{+})_2\,(S\text{-}SO_3)^{2-}$, provided the impetus to study chemical shifts in detail. This first clear association of core level binding energy shift with chemical state variation was published in 1964 (Hagstöm et al. 1964).

The majority of papers published by the group as they developed the subject during the period 1955-1965 appeared in Arkiv Fysik, the journal of the Uppsala Physics Institute, and they did not arouse much general interest. Then, having a wealth of accumulated material, they presented a major paper to the Royal Society of Sciences of Uppsala in December 1965. This was eventually published in a complete volume of the Siciety journal (Siegbahn et al. 1967a) in 1967 and in a book form, entitled *ESCA: Atomic, Molecular and Solid State Structure by Means of Electron Spectroscopy*, by the journal publishers Almqvist and Wiksells (Siegbahn et al. 1967b). This publication covered all aspects of Electron Spectroscopy for Chemical Analysis (ESCA was the term coined by Siegbahn to describe his technique) in considerable detail: the physical principles; the latest instrumental design and construction details; a huge collection of data on core levels, valance bands and Auger series together with underpinning theoretical calculations; description of experiments involving excitation with X-rays, electrons and UV, and studies of gases, frozen liquids and solids. The book brought large-scale awareness of the potential of XPS and immediately excited the interest of several instrument manufacturers. Some years later (in 1981), Siegbahn was awarded the Noble Prize for Physics.

As a result of a collaboration between J. M. Hollander of the then Lawrence

Radiation Laboratory (now the Lawrence Berkeley National Laboratory) and the Uppsala Group, one of the two high-resolution magnetic β-ray spectrometers at Uppsala was purchased and installed at Berkeley in the early 1960s. After being used for work in nuclear physics for which it was designed, the instrument was converted, in 1965, for XPS work within D. A. Shirley's group by C. S. Fadley (who was then commencing his PhD work) and S. B. M. Hagström (who had recently completed his PhD in Siegbahn's group). This led to the first high-resolution XPS work outside Sweden and to independent publications on chemical shifts and their quantitative interpretation using the charge potential model (Fadley et al. 1967, Fadley et al. 1968), with the first of these papers predating the appearance of the ESCA paper (Siegbahn et al. 1967a)/book (Siegbahn et al. 1967b) which included similar work.

2.2.2.3. The Appreciation of Surface Sensitivity

The potential of XPS as a surface analytical method did not feature significantly in the ESCA book (Siegbahn et al. 1967b), with only two pages being devoted to a discussion of this issue. Deliberate experiments to investigate the sampling depth were restricted to Langmiur-Blodgett multilayers of stearic acid and its α-iodo- and bromo-derivatives. These experiments demonstrated the sensitivity of XPS to a single monolayer and gave a qualitative indication that the average sampling depth, using Al Kα radiation, was around 100 Å. The comment was made that the information was not limited to "the first few Ångstroms as is, for example, the LEED method". However, the authors added "These features of ESCA are obviously of special interest in the physics and chemistry of surfaces". Elsewhere in the book, the core level spectra of several air-exposed evaporated metal film surfaces illustrated the simultaneous observation of metal and oxide overlayer components.

The major application sections of the book, regarding to elemental sensitivity (only H and He being non-detectable), chemical shifts and correlations of core level binding energies with valency or atomic charge distribution, were echoed in many of the early publications as commercial instruments appeared. XPS was initially hailed as the "NMR of the periodic table". Indeed, even in those situations where surface

analysis was the final goal, it was generally a prerequisite that the chemical shifts range/relationship to chemical state for the elements involved be researched through the study of reference compounds. Since the Uppsala group had only studied chemical shifts in N and S and, to a limited extend, C, most of the periodic table was still to be investigated. The petrochemicals industry was the first to grasp the potential of XPS as a surface analysis tool and to invest in equipment. In particular, it anticipated breakthroughs in the understanding of heterogeneous catalysts (typically, finely divided metals dispersed on porous ceramic supports, doped with "promoters") where elemental sensitivity, chemical state identification and surface specificity were all required whilst dealing with insulating samples in a variety of forms. Thus, one of the author's (David Briggs) career commenced in September 1970 with the then ICI "Petrochemical and Polymer Laboratory", with a PhD project on XPS studies of catalytic and related systems. This was carried out at the University of Durham in D. T. Clark's group, using a newly-delivered AEI ES100 instrument (the first in the UK). Meanwhile, the Durham group's main research interest was the use of XPS-derived atomic charge distribution in organic molecules to calibrate the predictions of theoretical calculations of different types.

Surface scientists had been using Low Energy Electron Diffraction (LEED) for single crystal surface and adsorption studies in UHV for some time before it was demonstrated, around 1967, that their instruments could be easily modified to do Auger Electron Spectroscopy (AES). From AES studies of deposited layers on substrates, a rapid appreciation of the kinetic energy dependence of the electron inelastic mean free path (and attenuation length) and, hence, the information depth, was gained. Researchers in this field saw the analytical potential of XPS for their work whilst, at the same time, the photoelectron spectroscopy pioneers discussed the need for UHV-compatible XPS instrumentation. Roberts and Brundle first brought these two themes together and commissioned Vacuum Generators to build a system for UHV XPS (and UPS/AES) studies. Preliminary results for the adsorption of water, carbon dioxide and mercury onto gold clearly demonstrated that Siegbahn`s estimate (Siegbahn et al. 1967a) of the XPS information depth was pessimistic from the viewpoint of surface sensitivity (Brundle et al. 1972). That same year (1972),

Seah pointed out that the electron mean free paths emerging from AES studies must also apply to photoelectrons having the same energies (Seah 1972). By 1974, compilations of such data (Powell 1974) produced the first so-called “universal curve” which allowed electron mean-free paths to be estimated for any combination of X-ray photon energy and core-level binding energy (i.e. from the kinetic energy of the resulting electron).

2.2.2.4. Instrument Development

2.2.2.4.(1). Spectroscopy

At the time of the ESCA book’s appearance, the Uppsala group had developed the double-focusing spherical electrostatic analyzer (originally described by Purcell in 1938 (Purcell 1938) and first used for XPS by Henke (Hence 1962, Henke 1963)). They had also introduced channel electron multipliers (CEMs) (and even multidetection using an array of four CEMs placed in the analyzer focal plane). In an addition to the book at the proof stage, they further proposed the monochromation of Al Kα by diffraction from quartz crystals and the use of a high-power rotating anode to counter the consequent reduction in photon flux.

The first commercial instruments, which appeared from Varian, AEI, VG and McPherson, starting in 1969, did not use all of this technology. All used a spherical sector electrostatic analyzer and offered single-target (Mg or Al) X-ray sources with different degrees of sophistication. Some had electrostatic lenses to retard the electrons prior to analysis, thereby increasing transmission (for single-channel detection (Helmer et al. 1968)) and introducing this now much-used concept. Initially, the vacuum systems were not UHV compatible. In 1972, Hewlett-Packard (H-P) launched an instrument which promised significantly improved performance. It offered a three-crystal (confocal) monochromated Al Kα source with a low-energy electron source for charge neutralization, a sophisticated input lens and a 2-D multi-detector with 200 effective channels (Kelly et al. 1973). The dispersion compensation system employed (invented by Siegbahn), whereby the energy

dispersion of the crystal monochromator was compensated by the dispersion of the electron optical system, avoided intensity-reducing slits but worked optimally (energy resolution ~0.6 eV) only for planar samples and a certain emission angle. H-P stopped production for strategic commercial reasons after only four years. Some of the H-P team eventually set up Surface Science Instruments (SSI) and, in 1982, launched the next fundamentally different design (the X-probe). This offered a small spot X-ray probe via a toroidally-bent, single-crystal monochromator (Chaney 1977). The smallest spot size was ~100μm. This instrument, therefore, provided the first degree of spatial resolution, albeit usable only for selected–area analysis (or crude mapping by stepping the stage under computer control), all previous instruments collecting photoelectrons from an area of several mm^2.

Meanwhile, instrumentation development had continued at Uppsala University (as foreshadowed in the ESCA book (Siegbahn et al. 1967b)) and a spin-off company, Scienta AB, was formed around 1984 to commercialize their latest technology. The ESCA300 which emerged in 1989 represented a step-change in performance. Its high-power, rotating anode and seven, individually adjusted, toroidally-bent quartz monochromator crystal produced a (line-focussed) X-ray flux of some $10\times$ that of a conventional non-monochromated source operating at 600 W and a markedly improved energy resolution of ~0.28 eV. Count rates were also increased by the use of a large hemispherical analyser (300 mm mean radius with 100 mm between the hemispheres), a high-transmission, five-element input lens and a microchannel plate detector (Gelius et al. 1990). Amongst several other design innovations, this instrument also provided two-dimensional imaging in the E_K-x imaging mode.

2.2.2.4.(2). Imaging

In contrast to AES, where the use of a focused electron beam was straightforwardly adapted from electron microscopy practice, the development of imaging in XPS was much more challenging. In addition to the problems associated with the difficulty of focusing X-rays, the cross-sections for X-ray photoelectron

emission tend to be less favorable relative to those for electron-induced Auger emission. Consequently, several approaches to solving these problems have evolved.

The first practical approach (i.e. one applicable to all samples and using a conventional instrument) was proposed by Gurker et al. (Gurker et al. 1983). This method, which came to be known simple as E-x imaging, makes use of the double-focusing properties of the spherical sector analyzer. If a narrow strip of the sample is illuminated by the X-rays (or defined by a slit between sample and analyzer), then mono-energetic photoelectrons emitted at points along this line form an image in the detector plane. If the points emit an energy spectrum, then the spectrum is dispersed along an orthogonal line in the same plane. The energy resolution and the detected energy range are defined by the chosen analyzer pass energy. Thus a 2-D multichannel detector will capture an E-x image. In the x-direction the spatial resolution is defined by the spherical aberration of the input lens and the ratio of the detector resolution (pixel size) to the input lens magnification (M), whilst in the y-direction it is determined, additionally by the ratio w/M where w is the width of the analyzer entrance slit. Adding a series of these lines together, by stepping the sample stage along the y-axis, allows an x-y image set to be acquired, form which a conventional image, based on intensity within an energy window, can be extracted. Gurker et al. used computer simulations to demonstrate the principles in 1983 and subsequently verified the method experimentally in 1987 (on an early McPherson instrument), achieving the expected spatial resolution of about 300 μm (Gurker et al. 1987). This approach was adopted on the Scienta ESCA300 (with its line X-ray source) to give a spatial resolution of the order of 10 μm in 1990.

In the early 1980s, as sensitivity improved, it became possible (on instruments without focusing monochromators) to sacrifice some intensity for area restriction. Selected area analysis was achieved by the use of a magnifying input lens, whereby a virtual image of the input aperture of the spherical sector analyzer defined the reduced acceptance region at the sample surface. In 1988, Seah and Smith described a pre-lens rastering technique to turn this approach into an imaging method (Seah et al. 1988). X, Y scan plates, placed between the sample and the input lens, and screened by an earthed enclosure, raster the area on the sample from which

the photoelectrons are accepted. The raster voltages are scaled with the voltage used to retard the electrons to the analyzer pass energy so that, as the energy spectrum is acquired, the viewed are remains stationary. Images with 150 µm resolution were demonstrated, but Seah and Smith estimated that, at the limits of current technology, an image of 10 µm resolution with 256×256 pixels might be acquired in about 10 h. This spatial resolution, but with more acceptable acquisition times, was subsequently achieved by Kratos on their AXIS-HS instrument. In addition to the conventional electrostatic lens, this instrument employed a single pole-piece magnetic "snorkel" lens placed beneath the sample (Robinson et al. 1993). This greatly improved sensitivity by allowing acceptance angles to be increased to up to ± 25°.

A parallel imaging method was devised by VG Scientific in the late 1980s and incorporated into their ESCASCOPE instrument (Coxon et al. 1990). A series of two electrostatic lenses, combined with an intermediate field aperture, form a magnified image of a variable field of view in the objective plane of a third lens which has its back focal plane coincident with the entrance plane of a hemispherical analyzer (HSA). Spatial information carried by the photoelectrons is converted into angular information at the HAS entrance. The parallel beams are energy-analyzed and six-channel electron multipliers in the exit plane in the exit plane collect spectroscopic information as usual. However, the channel electron multipliers are symmetrically positioned about a hole through which electrons can pass into a final lens, which exactly reverses the role of the third input lens, onto a 2-D position sensitive detector. Therefore, an image corresponding to any chosen electron energy (window) can be registered in parallel by arranging the lens/HAS voltages so that these electrons pass through the hole. The inherent resolution of the ESCASCOPE optics was about 5 µm, but to realize this performance required the use of very small acceptance angle, with loss of sensitivity and long acquisition times. In the later 220iXL model, the use of a magnetic immersion lens in addition to the electrostatic objective lens improved sensitivity and the ultimate spatial resolution. Additionally, the use of a small-spot monochromator also increased sensitivity and energy resolution to the point that chemically-shifted components of a single core line could be imaged, with a spatial resolution approaching 1 µm in favorable cases (Forsyth et

al. 1994). A different parallel imaging approach, giving similar performance, has recently been introduced by Kratos in their AXIS Ultra and Nova instruments, based on a concept first proposed by Sar-El (Sar-El 1996). Another recent innovation in the Thermo VG Scientific Theta Probe instrument is a transport lens/2-D detector combination which allows parallel acquisition of angle-resolved data without having to tilt the sample. In this model of operation, spectra in up to 112 energy channels are collected for up to 96 angle channels simultaneously (E-θ on the detector). With small area irradiation, this provides parallel depth information for localized regions of thin film systems.

Although never fully commercialized, a different parallel imaging approach was developed during the 1980s. Originally pioneered by Turner et al. at Oxford for low-energy (UV) photoelectron spectromicroscopy (PESM) (Beamson et al. 1981), this method involves irradiation of the sample with X-rays whilst placed in a strong magnetic field (~7 Tesla). Emitted photoelectrons are trapped into helical trajectories around magnetic field lines, which diverge from the sample down a drift tube as the field decays in a controlled manner. About 1.5 m from the sample, the field lines are almost parallel and, at this point, they intersect the plane of the position-sensitive detector, where a magnitified image of the sample results. Virtually all the emitted electrons are detected. The spatial resolution is approximately twice the maximum radius of the electron spiral (cyclotron radius), namely ~10 and 30 μm for 100 and 1000 eV electrons, respectively. A number of approaches to combining energy analysis or energy filtering and selected area analysis with this imaging method have been described (Keenlyside et al. 1990, Knapp et al. 1990). A final development, again by Turner, was of an ingenious imaging band-pass analyzer operating in the magnetic field between the sample and imaging detector, thus optimizing the parallel detection advantage (Turner et al. 1986). However the high costs of producing the strong magnetic field (using a superconducting solenoid) and the problems associated with insulator charging in a magnetic field, eventually led to the abandonment of this approach as a commercial proposition.

A scanning beam approach was developed by Physical Electronics for the Quantum 2000 instrument, which was launched in 1994. A scanning Al Kα X-ray

probe is produced via an ellipsoidal quartz crystal monochromator. The X-rays are generated at one of the focal of the ellipsoid by bombarding an Al anode with electrons from a variable spot size electron gun. The sample is placed at the other focal point. When the electron beam scans the anode, the monochromated X-ray probe of similar spot size scans the sample. Photoelectrons are collected by an input lens with a high solid angle of acceptance, the deflection plates within the lens are programmed to follow the X-ray beam so that collection efficiency is relatively unaffected by the emission point within the scanned area. The minimum probe size was ~10 μm and the maximum field of view 1.5 mm square. Another innovation was the use of a 16-channel multidetector in the analyzer detector plane, which, when the analyzer was operated at an appropriate pass energy, allowed mixed chemical states to be imaged simultaneously and separated by post acquisition processing.

2.2.2.4.(3). Other Aspects

One of the early instruments, developed within DuPont's analytical facilities and then marketed by their Scientific Instruments Division, had a radically different analyzer designed by Lee (Lee 1972, Lee 1973) (an electrostatic dispersing stage followed by low-energy-pass and high-energy-pass filters). This was an efficient, very compact instrument (aimed at the perceived applied surface analysis market) and of lower cost then contemporary instruments. DuPont stopped production in 1976, but Shimadzu took over the design and their instrument sold wall in Japan (it was upgraded and relaunched as the Amicus by Kratos in 1998). However, in the 30+ years of commercial XPS, a significant market for low-cost instruments suitable for undemanding, routine analysis has consistently failed to materialize outside Japan.

At the other extreme of cost and accessibility is the use of synchrotron radiation for photoelectron spectroscopy, which has opened up many possibilities since the early 1970s, including much higher energy and spatial resolution compared with commercial systems.

2.3 Ambient Pressure X-ray Photoelectron Spectroscopy (APXPS)

2.3.1. Introduction

Surface science is defined as the study of physical and chemical phenomena that occur at the interface of two phases, including liquid-solid, gas-solid, vacuum-solid, and gas-liquid interfaces. Over the past decades, surface science has gathered an unprecedented wealth of information about the structural and electronic properties of surfaces, the dynamics of clean and adsorbate covered surfaces and surface processes. Chemical processes at gas-solid and gas-liquid interfaces play a major role in environmental and atmospheric science, and heterogeneous catalysis. Thus, interactions of gas molecules with surfaces have been one of the mostly concerned topics.

Detailed studies on kinetics and dynamics of gas-surface interactions have mainly been done in ultra-high vacuum (UHV) conditions. However, results obtained from UHV experiments are not realistic. There are a few examples, where kinetic models derived from UHV experiments could be directly used to understand realistic reaction conditions. In an approach so-called single crystal approach, results from single crystal (ideal surfaces) experiments in UHV are simply extrapolated to industrial catalysts (real conditions). However, technologically important and interesting process in heterogeneous catalysis usually takes place at pressures of 1 bar and higher and elevated temperatures. Therefore resulting profound understanding of surfaces and surface processes does not automatically translate into an equally good understanding of heterogeneous catalysis as one might perhaps expect. The more than 13 orders of magnitude in pressure between UHV experiments and typical industrial applications and the difference in complexity and morphology between single crystal surfaces and catalysts used in so-called "real catalysis" cannot be easily bridged. Progress in the field has been limited mainly by two obstacles termed as "pressure gap" and "material gap".

Molecular Environmental Science (MES) is an expanding field that studies, on a molecular level, chemical and biological processes occurring at environmentally

relevant surfaces and interfaces. Fundamental understanding of these processes is necessary to solve important problems in environmental science related to the speciation, distribution, reactivity, transformations, mobility, and potential bioavailability of pollutants and contaminants in the environment. One characteristic of the surfaces under ambient pressure is the coverage by dense layers of molecules. Water, for example, is known to form layers several molecules thick at room temperature in humid environment. Interaction of water with surfaces starts from the adsorption of monomers, to the formation of monolayers and eventually the presence of bulk water and its reaction with the surface. Dense layers of adsorbed molecules can also be formed in UHV by simply cooling to low pressures to maintain a high surface coverage. But, decreased kinetics (by orders of magnitude) at reduced temperatures often makes it impossible to reach thermodynamic equilibrium state. Therefore, a high-pressure environment is necessary to be able to study these processes. While method has provided valuable information there is always an open question that whether the structures formed in this manner shows equilibrium structures or meta-stables ones.

To develop the applications in the surface science fields, it is important to obtain detailed knowledge of the atomic scale geometrical and electronic structure of the interfaces as close as possible to real operating conditions of pressure and temperature. For instance, several layers thick of oxide films readily form on metal surfaces in oxygen atmosphere. The metal-oxygen phase diagram is well known for bulk materials, but it is unknown at the surfaces. Even the bulk material is in well-defined phase, strong interactions with the oxygen gas as well as impurity and contaminant gases can affect the surfaces stoichiometry and completely change it. Thus surface structures of materials over entire region of Pressure-Temperature (P-T) phase diagram are missed when experiments are not performed in equilibrium at relevant gas pressures.

Over the past decades a number of surface-sensitive techniques have been used under elevated pressures. X-ray Photoelectron Spectroscopy (XPS) is one of the most versatile analytical techniques to study the composition and electronic structure of surfaces. The application of XPS as a tool for investigation of catalysis and

environmental science has driven the advancement of XPS to function at higher pressure. While such systems have been developed for the past 30 years (Siegbahn et al. 1969, Siegbahn 1985, Siegbahn et al. 1973), there has been a resurgence of Ambient Pressure XPS (APXPS) in the past decade due to advanced construction of electron analyzers combined with the exploitation of synchrotron facilities with high brilliance, tunable, monochromatic light with small spot size (Feldegg et al. 1975, Siegbahn et al. 1981, Siegbahn et al. 1982, Moberg et al. 1991a, Moberg et al. 1991b, Joyner et al. 1979).

In the first part of this section, a brief history of APXPS has been reviewed. Then, fundamentals of technique have been discussed in detail.

2.3.2. History of APXPS

The history of ambient pressure XPS goes back to the beginning of the technique when electron spectroscopy was used to study the electronic structures of materials. In order to perform XPS experiments at high pressures, the attenuation of the electrons due to scattering by gas molecules can be reduced by minimizing the path length of the electrons in the high-pressure region. This can be achieved by placing the sample inside a reaction chamber and bringing the sample surface close to a differentially-pumped aperture, behind which the pressure drops by several orders of magnitude. This basic concept has been used in all ambient pressure XPS setups developed over the past 40 years, starting with the designs by K. Siegbahn and coworkers in 1969, for investigation of gases at pressures of up to a few tenths of a Torr (Siegbahn et al. 1969). The system was based on a magnetic-type electron energy analyzer with one differential pumping stage. In Figure 2.21, the basic principle of APXPS instrumentation proposed by H. Siegbahn (Siegbahn et al. 1969) is shown.

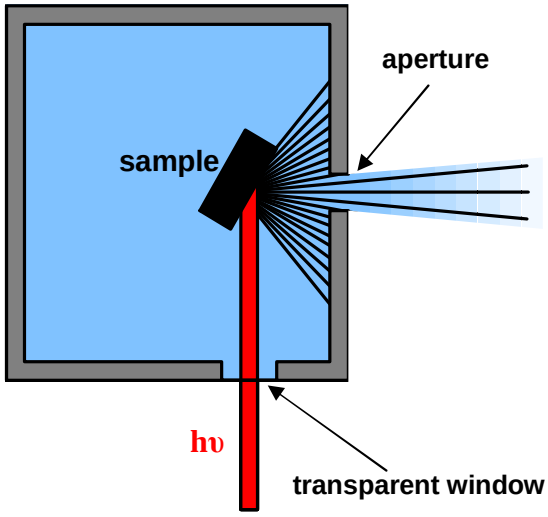

Figure 2.21. The basic principle of high-pressure X-ray Photoelectron Spectroscopy

During the following years a number of new setups were developed by K. Siegbahn and H. Siegbahn and coworkers (Uppsala group) (Siegbahn 1985), in particular for the investigation of liquid-vapor interfaces. In 1973, the first XPS experiment on liquids was reported by the same group (Siegbahn et al. 1973). The experimental system allowed investigations of liquid jet sources with a vapor pressure of less than 1 Torr and was also based on a magnetic-type electron energy analyzer with one differential pumping stage. Working with liquids poses additional challenges, because stable and clean liquid surfaces need to be prepared inside a vacuum chamber. This problem was achieved by using wires (Feldegg et al. 1975), rotating trundles (Siegbahn et al. 1981, Siegbahn et al. 1982) and disks (Moberg et al. 1991a, Moberg et al. 1991b) that continuously moved through a liquid reservoir and were coated by a thin liquid layer that was then investigated using XPS.

The first pioneering study of high pressure photoemission in gas-solid reactivity was made by R. W. Joyner et al. (Joyner et al. 1979a). In the study, a photoelectron spectrometer which permits the study of solids in the presence of gas at up to 1 Torr pressure has been developed and the main factors considered in its design and construction was reported. Silver was used to investigate performance of the spectrometer in the presence of argon at various pressures up to 1 Torr. The X-ray induced valence band spectrum of liquid mercury was also reported. In situ X-ray photoelectron spectroscopic observation of a silver foil at 473 K exposed to oxygen

at pressures up to 0.5 Torr was performed by the same group in the United Kingdom (Joyner et al. 1979b) and three species of oxygen was characterized by oxygen 1s core level spectrum. The first two were identified as due to atomic oxygen, respectively chemisorbed at the surface and incorporated into the bulk. The third species was tentatively assigned to molecular oxygen, probably as a surface peroxidic group. Although contamination problem caused by using oil diffusion pumps in the pumping system was a substantial disadvantage, several versions of this design were commercialized and are in use till now. But, new developments in the emerging field of interface science led to design of an improved version that overcomes sample contamination (Grunze et al. 1992).

A number of other instruments were designed in the 1970s for the investigation of liquids with low vapor pressures (<50 Pa) using ultraviolet photoelectron spectroscopy (UPS), e.g. Ballard et al. (Ballard et al. 1978, Ballard et al. 1979), Delahay et al. (Aulich et al. 1976, Nemec et al. 1977, Watanabe et al. 1980), and Roberts et al. (Joyner et al. 1979a). Grunze et al. (Ruppender et al. 1990) and Steinrück et al. (Pantförderr et al. 2005) developed APXPS instruments of vapor-solid surfaces, in particular for the investigation of heterogeneous catalytic reactions. All the aforementioned instruments used either X-ray cathodes or noble gas discharge lamps as photon sources, and are able to operate at pressures up to 100 Pa by using two or three differential pumping stages between the sample chamber and the electron analyzer. A different approach for the investigation of liquids with high vapor pressure was taken by Winter and Faubel et al. who perform XPS on liquid microjets with jet diameters below 10 mm (Winter et al. 2004, Winter et al. 2005). The jets were expanded into a measurement chamber with a working pressure of 10^{-3} Pa, where the scattering of electrons by gas-phase molecules was negligible. The limitation of this approach is that the liquid surface is not in equilibrium with its vapor.

Inelastic scattering of the electrons by gas molecules determines the pressure limit in APXPS experiments. The pressure difference between high-pressure region (sample or analysis chamber) and electron analyzer, which has to be kept under high vacuum, is also another factor that sets fundamental high-pressure limit for

photoemission. All of systems mentioned above were “passive designs” which referred that the emitted photoelectrons were accepted and spatially filtered through apertures separating the sample in the high-pressure environment from the electron analyzer at lower pressure. As will be discussed in detail below, by decreasing the size of the first aperture as well as reducing the path length of the electrons through the high-pressure region the upper pressure limit in APXPS experiments can be increased. Additionally, signal loss problem (higher noise to signal ratio) that is suffered in passive designs is accomplished by focusing the electrons onto the differentially-pumped apertures using electrostatic lenses in pumping stages. This principle of “active design” has been applied in a new generation of APXPS instruments that are based at third generation synchrotrons. A prototype instrument, developed at the Advanced Light Source (ALS) in Berkeley in 1999, operates at the bending magnet beamline 9.3.2 at the ALS (Ogletree et al. 2002). The spectrometer included a two-stage differential pumping combined with the first introduced electrostatic lens system for collection of photoelectrons. The system was used with a synchrotron X-ray source and allowed investigations at pressures of up to 7 mbar. This setup was applied to investigate heterogeneous catalytic systems under reaction conditions simultaneously with the monitoring of reaction products (Ogletree et al. 2002, Bluhm et al. 2004, Teschner et al. 2005) and to investigate of the process of ice premelting (Ogletree et al. 2002, Bluhm et al. 2002). In 2001, M.A. Kelly et al. reported construction of a high-pressure X-ray photoelectron spectrometer for monitoring of thin films synthesis (Kelly et al. 2001). The next generation of instruments was jointly developed a few years later by the Fritz Haber Institute (Berlin) and Lawrence Berkeley National Laboratory. These instruments, which have similar electrostatic lens systems, are running currently at the ISISS beamline at BESSY in Berlin (Bluhm et al. in preparation), and at beamline 11.0.2 at the ALS in Berkeley (Bluhm et al. 2006). The high brightness third generation synchrotrons provide firmly-focused, intense X-rays, which makes possible the use of small front aperture diameters (i.e. improved differential pumping) without loss of signal. The combination of a differentially-pumped electrostatic lens system with a synchrotron light source led to a significant increase of the pressure limit in APXPS. This novel

instrumentation made possible to study fluid and solid samples at higher pressures than ever before.

2.3.3. Fundamentals of APXPS

The development of APXPS has allowed investigation of samples at higher pressures. As mentioned before, to perform XPS experiments at high pressures ($>10^{-3}$ Pa), the attenuation of the electrons due to scattering by gas molecules has to be reduced to a minimum by bringing the sample surface close to a primary aperture of differential pump system, behind which the pressure drops by several orders of magnitude. The dimension of the aperture is one of the most important factors that set the fundamental scale of the experiment. If the aperture is too big, the sample has to be moved away while the gas environment on the surface of the sample is strongly perturbed. If the sample is placed too far away from the aperture, then the photoemission signal is reduced by electron-gas scattering.

2.3.3.1. Electron-Gas Interactions

Elastic and inelastic scattering of photoelectrons by gas molecules is the main obstacle in the photoemission spectroscopy at high pressures. When the emitted electrons travel in the gas environment they experience inelastic and elastic collisions with gas molecules. Elastically scattered electrons maintain their kinetic energy but they may be scattered out of the main aperture of the spectrometer. The effects of elastic scattering depend on the experimental geometry. If the aperture size is small compared to the area of the sample illuminated by X-rays, the net effect of elastic scattering will be small. Hence, the majority of the electrons will be scattered out of the spectrometer acceptance angle. On the other hand, if the X-ray spot small, then elastic scattering will reduce the intensity of the experimental spectrum without modifying the energy distribution.

Inelastic scattering of photoelectrons is mostly caused by the ionization of gas molecules as well as excitation of internal molecular states, e.g. rotational,

vibrational, or electronic. Inelastic scattering obscures the sample photoemission spectrum. In consequence of inelastic scattering, the original peaks are attenuated and the inelastically scattered background at lower kinetic energies increases.

To show the effect of inelastic scattering a compilation of literature values for electron impact ionization cross-section of molecular oxygen (O_2) as a function of kinetic energy is plotted (Figure 2.22) (Schram et al. 1965, Krishnakumar et al. 1992). In figure, the ionization cross-section rises rapidly, with a plateau between a few tens and a few hundreds of eV. This region is the most interesting energy region for synchrotron APXPS studies. Scattering is strongest around the kinetic energy of 100 eV, similar to the "universal curve" for the inelastic mean free path in solids (Seah et al. 1979). This means that strongest attenuation of the photoelectrons by gas molecules will take place in the most surface-sensitive XPS experiments at kinetic energies in the minimum of the mean free path curve.

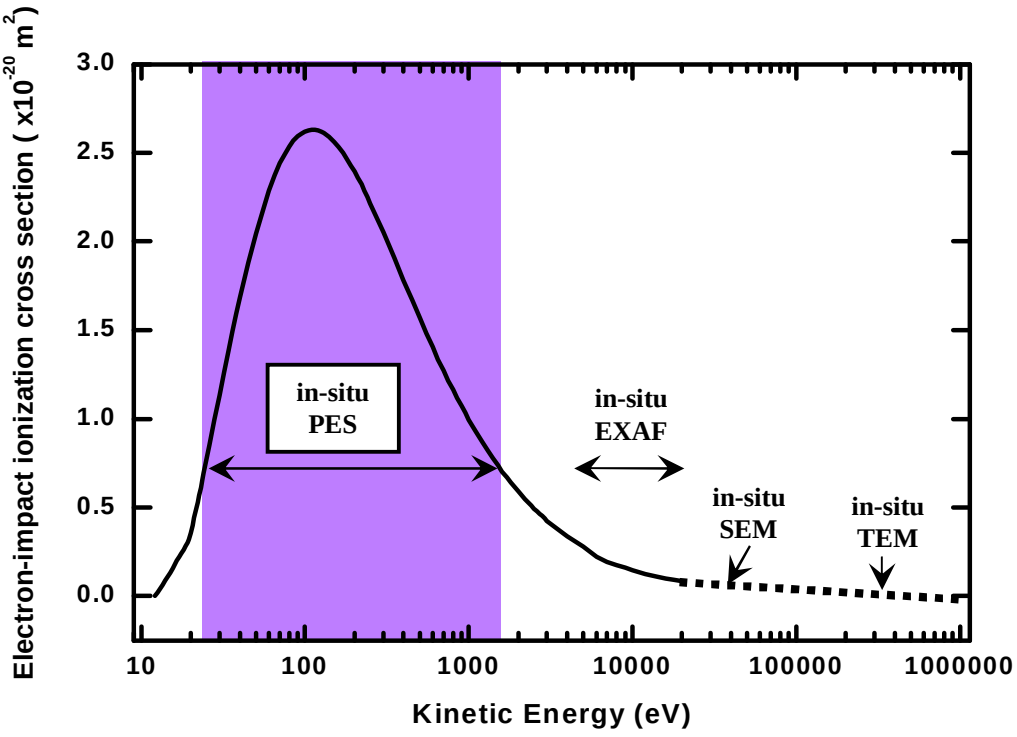

Figure 2.22. Electron-impact ionization cross-sections for molecular oxygen (O_2) as a function of kinetic energy. This figure was plotted from published data for oxygen (Schram et al. 1965, Krishnakumar et al. 1992). Dashed line demonstrates extrapolation of experimental data

The attenuation of the photoelectron signal in a gas environment depends on the gas species, gas pressure, and the kinetic energy of photoelectrons. For given pressure P, this attenuation is given as:

$$\frac{I_p}{I_{vac}} = \exp(-z / l_e(KE, P)) = \exp(-z \cdot P \cdot s_e(KE) / k_B T) \quad (2.2.)$$

where I_p is the signal at pressure P, I_{vac} is the signal in vacuum, λ_e(KE,P) is the electron mean-free path or average distance between collisions, k_B is the Boltzman constant, and z is the distance that electrons travel in a gas environment at temperature T and pressure P. The electron mean-free path in a gas atmosphere is:

$$l_e = k_B T / P \cdot s_e(KE) \quad (2.3.)$$

where σ_e is the electron-gas scattering cross-section and depends on the electron energy and gas composition. The mean free path of electrons with typical kinetic energies of a few hundred in eV is on the order of ~nm in a solid, ~µm in air, and ~mm in gas at 1 Torr. It means that electrons can travel ~mm in 1 Torr of gas without scattering. This is the fundamental limit of working distance in the basic concept of APXPS. All high-pressure XPS instruments are based on the idea, which is accomplished by bringing the sample surface close to a small aperture at a distance equal or less than mean free path of electrons, λ_e, to minimize the path length of electrons through the high-pressure region (Figure 2.23).

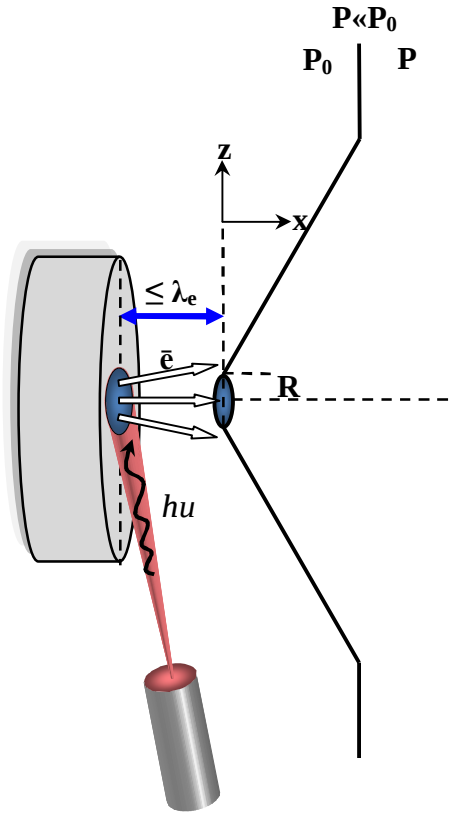

Figure 2.23. Principle of APXPS. The sample is placed in a high-pressure chamber that is separated from the X-ray source by an X-ray transparent window. Electrons and gas escape through a differentially pumped aperture

2.3.3.2. Gas Flow and Differential Pumping

Gas flow regimes described by the Knudsen number is the ratio of mean-free path for molecule-molecule collisions to the dimension of the system. In the case of APXPS, this ratio becomes larger meaning that molecule-molecule collisions can be ignored. Such a gas flow dynamic is defined as molecular flow which is typical case for high vacuum. In the simple ideal gas theory for molecular flow, a region with gas pressure of P_0 is separated by an aperture of radius R from another region that is at much lower pressure (The geometry is depicted in Figure 2.23). Because of the geometry, the gas flow through the aperture into the differential pumping system is not uniformly distributed. If we consider an electron at z position moving towards to aperture along a perpendicular axis, the effective pressure experienced by this

electron will be proportional to the included solid angle in the high-pressure side and it is given as:

$$P(z) = \frac{P_0}{2}(1 - \frac{z}{\sqrt{1+z^2}}) \qquad (2.4.)$$

where z is measured in R units. The pressure at the sample surface will be less than P_0 when the sample is placed close to the aperture, but it will increase rapidly away from the aperture. At $z = -2R$ the effective pressure is already 95 % of P_0 (very close to P_0), while at $z = +2R$ it is only 5% (Figure 2.24) (Ogletree. 2000). Therefore placing the sample at a distance greater than –2R (z≥–2R) ensures that the gas pressure at the sample is at least 95% of analysis chamber pressure.

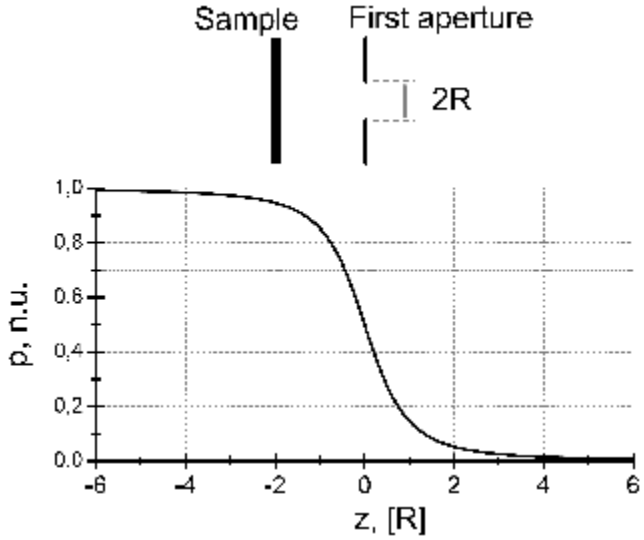

Figure 2.24. Scheme for the Equation (2.4.) (Kleimenov, 2005)

As mentioned earlier, the aperture size is one of the key factors that determine the maximum gas pressure in the APXPS experiments. Reducing the radius of the aperture increases the pressure on the sample surface, but it also reduces the photoemission signal. The size of the aperture not only determines the gas conductance but also sets the minimum distance between the sample and aperture. This minimum distance determines the upper limit of workable pressure.

Synchrotron based light source is ideal for APXPS experiments. Due to the high brilliance of third generation synchrotrons, the X-ray can be focused to a small

spot. Hence, smaller aperture can be used and higher maximum pressure can be achieved. The optimum aperture radius at a distance of $z = -2R$ for a given pressure can be derived through the optimization of the total electron counts since the total electron counts is proportional to the product of the usable aperture size (usable photon flux) and the attenuation ratio of photoelectrons given by Equation (2.2.):

$$pR^2 \cdot \exp(-2R / l_e) = pR^2 \cdot \exp(-2R \cdot P \cdot s_e / k_B T) \quad (2.5.)$$

The optimization of Equation (2.5.) results as:

$$R = k_B T / P \cdot s_e \quad (2.6.)$$

Attenuation of photoelectron signal due to the scattering by gas molecules is not only the parameter that limits the pressure, but also electron analyzer since electron analyzer has to maintain under high vacuum. To perform high-pressure experiments in the Torr range, several differential pumping stages are needed. The common approach to all APXPS is illustrated by Figure 2.25. Small apertures placed between pumping stages is used to improve differential pumping efficiency. But decreased effective solid angle is restricted transmission of photoelectrons into the analyzer through the differential pumping system.

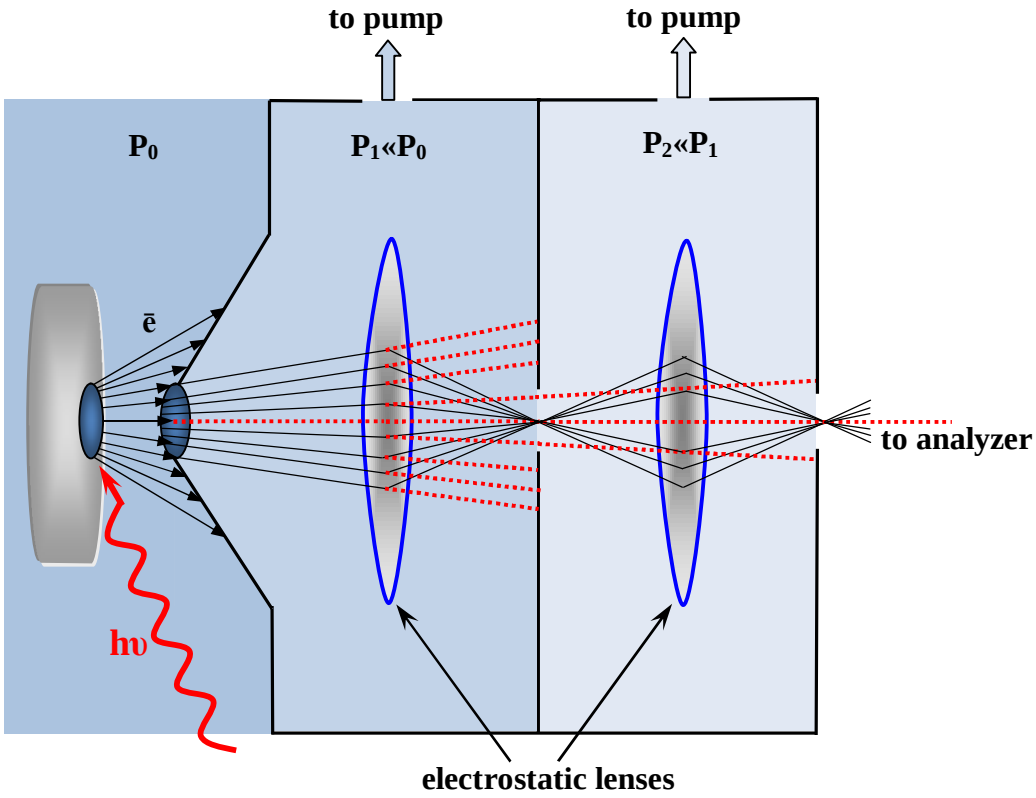

Figure 2.25. Principle of APXPS instruments. Electrons and gas molecules are transferred through first aperture of differentially pumping system. Electrostatic lenses refocus the photoelectrons into the apertures connecting the differential pumping stages. Electron trajectories in the "passive design" systems are illustrated by red color

2.3.3.3. Transfer Electron Optics

The electrostatic lens system is the key feature of the improved version of high-pressure photoelectron spectrometers. Emitted photoelectrons through main aperture extend in different directions due to diverging nature of their trajectories and in all "passive design" systems the small solid angle captured by apertures separating the pumping systems are not able to admit all of the photoelectrons. Hence, a significant amount of signal has to be lost. In new design systems, small apertures are placed at the focal or crossover points of electrostatic lenses to focus the photoelectrons into the differential pumping system, as displayed in Figure 2.25, and electron transmission through the differential pumping system is enhanced.

3. THEORETICAL BACKGROUND

3.1. Basic Principles, Spectral Features and Qualitative Analysis of XPS

X-ray Photoelectron Spectroscopy (XPS) is one of surface analytical techniques that bombard the sample with photons, electrons or ions in order to excite the emission of photons, electrons or ions. In XPS, the sample is irradiated with low-energy X-rays (~1.5 keV), in order to provoke the photoelectric effect. The energy spectrum of the emitted photoelectrons is determined by means of a high-resolution electron spectrometer (Figure 3.1).

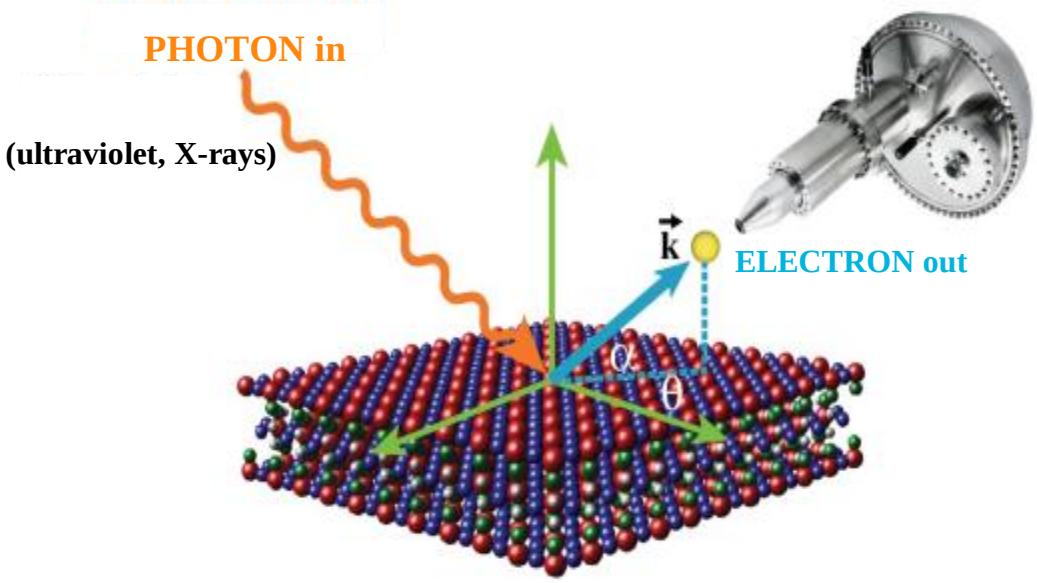

Figure 3.1. General illustration of X-ray Photoelectron Spectroscopy technique (http://www.ccmr.cornell.edu/igert/modular/docs/IGERT_Lecture1.pdf)

The sample analysis is conducted in a vacuum chamber, under the best vacuum conditions achievable, typically ~10^{-10} Torr. This facilitates the transmission of the photoelectrons to the analyzer but more importantly minimizes the re-contamination rate of a freshly cleaned sample. This is crucial because XPS is very surface-sensitive, with a typical ***"sampling depth"*** of only a few nanometers. The necessity for such ultra-high vacuum (UHV) conditions for the study of solid surfaces can be judged from the ***"universal curve"*** of the inelastic mean free path (IMFP) of

electrons. As a useful summary of the variation of IMFP with kinetic energy, Figure 3.2 shows a recent compilation of values calculated using the TPP-2M formula for 41 elemental solids (Fadley 2020). One sees that in the kinetic energy range of interest, between about 10 and 2000 eV, the IMFP is only of the order of a few Å. This means that any spectroscopy of a solid surface involving electrons samples only electrons from a very thin layer of the sample.

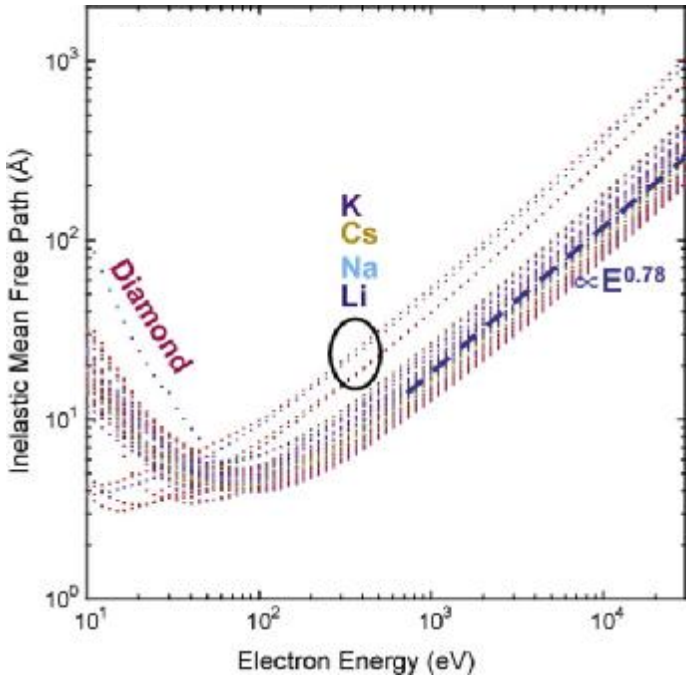

Figure 3.2. Inelastic mean free paths (IMFPs) for 41 elements, calculated using the TPP-2M formula: Li, Be, three forms of carbon (graphite, diamond, glassy C), Na, Mg, Al, Si, K, Sc, Ti, V, Cr, Fe, Co, Ni, Cu, Ge, Y, Nb, Mo, Ru, Rh, Pd, Ag, In, Sn, Cs, Gd, Tb, Dy, Hf, Ta, W, Re, Os, Ir, Pt, Au, and Bi. Five "outlier" elements are indicated to provide some idea of what electronic structure characteristics can give rise to deviations from the majority behavior: diamond and the alkali metals. The dashed straight line for higher energies represents a variation as $E_K^{0.78}$, and is a reasonable first approximation to the variation for all of the elements shown (from ref. (Fadley 2010))

The well-known form of curves in Figure 3.2, with a minimum between roughly 20 and 100 eV, a general increase on going above this to higher energies, and a less pronounced increase on going to energies below the minimum, is a critical ingredient in the analysis of XPS data. The IMFP increases above 1 keV roughly as $E_K^{0.75-1.10}$ over a variety of elements and compounds, but with the majority of

elements in Figure 3.2 suggesting $E_K^{0.78}$ as a convenient estimation formula.

3.1.1. The XPS Experiment

3.1.1.1. The Principles

The basic experiment involves the bombardment of a material in vacuum with (usually) soft X-rays, capable of penetrating many micrometers into the bulk. X-ray absorption by an atom in the solid leads to ejection of an electron (photoionization) either from a tightly-bound core level or from the weakly-bound valence levels (or molecular orbitals). A fraction of these electrons, generated close to the surface, escape into the vacuum system (photoemission) (Figure 3.3). The overall process is known as the ***photoelectric effect***. The photoelectron emission is energy analyzed to produce a spectrum of electron intensity as a function of energy: the X-ray photoelectron spectrum. A spectrum for a polystyrene sample previously exposed to nitrogen plasma is shown in Figure 3.4. Such a spectrum, typically from BE ~1100 eV, is a ***"survey scan"***, or ***"wide scan"*** spectrum, obtained at low resolution and covering the entire useful range of binding energies accessible with the X-ray source employed.

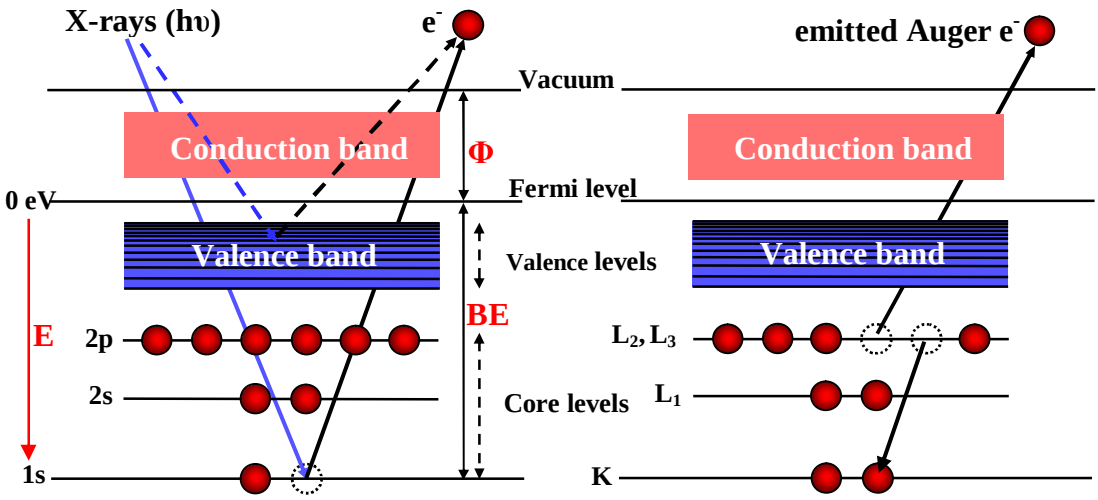

Figure 3.3. Schematic of the processes involved in X-ray photoemission and Auger electron emission

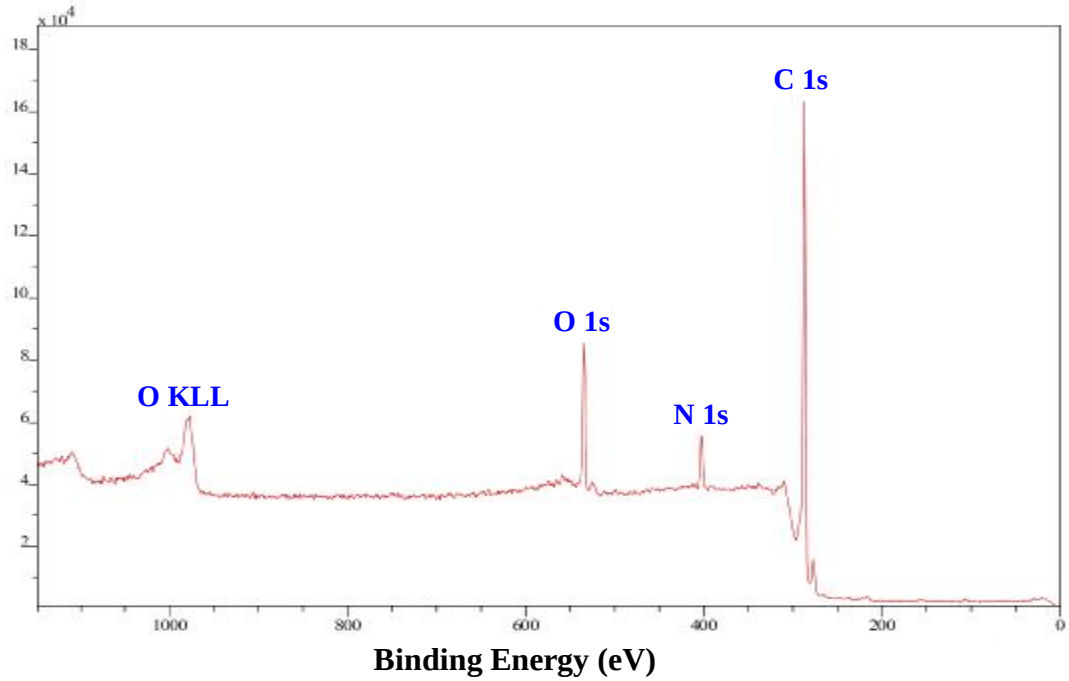

Figure 3.4. X-ray photoelectron spectrum of a polystyrene sample previously exposed to nitrogen plasma. AlKα X-rays (1486.6 eV) were used to excite the photoemission. Note that the binding energy scale is drawn from right to left, so that the photoelectron kinetic energies measured by the spectrometer increase from left to right (http://csacs.mcgill.ca/francais/docs/CHEM634/XPS_Paynter_t.pdf)

The survey spectrum in Figure 3.4 is dominated by three photoelectron peaks, corresponding to electrons originating in the 1s orbitals of the carbon, nitrogen and

oxygen atoms in the sample surface. The background on which these peaks sit comes from electrons excited by the X-ray Bremsstrahlung radiation at low binding energy, and from inelastically scattered photoelectrons at higher binding energy (essentially to the right and left of the C1s peak respectively). The "O KLL" structure results from the excitation of Auger electron emission. Auger electrons are emitted with a kinetic energy that is independent of the X-ray energy, so in cases where Auger peaks are superimposed on photoelectron peaks, the Auger peaks can be displaced elsewhere on the binding energy scale by changing the X-ray photon energy, by switching to a MgKα source, for example.

For a conducting sample in electrical contact with the spectrometer, conservation of energy leads to the equation

$$E_K = hu - E_B^F - \Phi_{spec.} \qquad (3.1.)$$

where E_K is the measured kinetic energy of the emitted electron, hυ is the energy of the exciting X-ray photon, E_B^F is the electron binding energy (BE) relative to the Fermi level (E_F) of the sample (defined as $E_F = 0$) and $\Phi_{spec.}$ is the work function of the spectrometer (typically about 4.5 eV). Since the electron binding energy is the parameter of the fundamental interest, the spectrometer can be set up to record the spectrum on this energy scale directly, rather than on the measured kinetic energy scale. The spectrometer energy scale must be accurately linear and correctly calibrated. This is achieved using clean metal standards with traceable peak energies across the energy range.

For insulating sample which does not have a well-defined Fermi level and which can not be in electrical contact with the spectrometer Equation (3.1.) does not apply. Additionally, the surface potential of the sample may be uncertain because of charging. A modified version of:

$$E_K = hu - E_B - \Phi \qquad (3.2.)$$

is used in this case where Φ is now a term which capture these uncertainties relating to surface potential and the actual reference point for E_B. The clear implication is that for BEs from different insulating samples to be meaningfully compared, a common reference point needs to be established.

3.1.1.2. Aspects of Instrumentation

3.1.1.2.(1). X-ray Sources

Two types of X-ray source are in common usage. Non-monochromated sources utilize the Kα radiation form Al or Mg. These materials (as thin films deposited onto water-cooled copper target) are bombarded with electrons up to 15 keV in energy. The X-ray output consists of a continuous energy distribution extending up to the incident electron energy (Bremsstrahlung), with much higher intensity at the characteristic Kα energy (Figure 3.5). This line, actually an unresolved doublet ($K\alpha_{1,2}$) results from the transitions $2p_{3/2} \rightarrow 1s$ and $2p_{1/2} \rightarrow 1s$ in the ionized target atom. Weaker satellite lines also result from valence band $\rightarrow$1s (Kβ) transitions and transitions involving multiply-charged atoms (for example, $K\alpha_3$, $K\alpha_4$). All these photons excite peaks in the photoelectron spectrum according to Equation (3.1.). The characteristic energies and widths of the principal lines are 1253.6 (0.70) eV for Mg Kα and 1486.6 (0.85) eV for Al Kα. Old and damaged targets may also produce Cu Kα from the exposed copper base and/or O Kα from heavy target (anode) oxidation. Al and Mg targets are usually included in a single dual-anode source for easy switching between photon sources, but filament misalignments can give rise to additional ghost peaks.

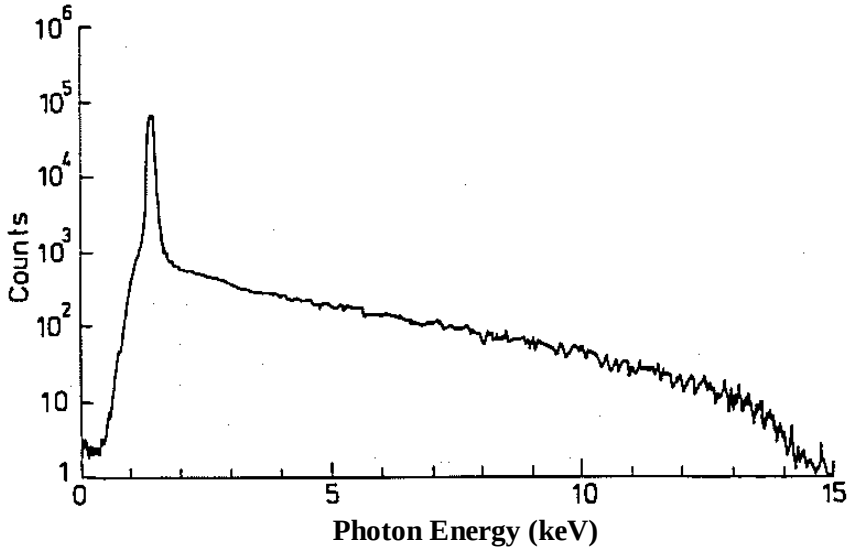

Figure 3.5. X-ray emission spectrum from an aluminum target bombarded with 15 keV electrons, showing the characteristic Kα line at ~1.5 keV and the broad Bremsstrahlung radiation (Briggs et al. 2003)

Al Kα radiation can be monochromated by first-order diffraction using α-quartz crystals. This allows the energy spread of the exciting radiation to be significantly reduced, typically to just under 0.3 eV. At the same time, all satellite lines and the Bremsstralung radiation are removed, producing a cleaner spectrum with reduced background intensity, particularly in the low BE region. The same monochromator, with slight adjustments to the geometry can be used to monochromate Ag Lα (2984.3 eV) and Cr Kβ (5946.7 eV); these have almost exact multiples of the Al Kα energy and can be monochromated using second-order and fourth-order diffraction respectively.

Synchrotron is another type of X-ray source. When electrons are accelerated, they radiate energy in the form of photon (It was discussed in the previous chapter in detail.). In a synchrotron, electrons are constrained to move in a circular path by a magnetic field, and are accelerated by the centripetal force acting at right angles to the direction of motion. The photons are emitted as a continuous spectrum with an intensity maximum at critical wavelength, λ_c (of order 0.1-0.4 nm, energy 1-10 keV), which is directly proportional to the path radius and inversely proportional to the cube of the electron energy. Beam energies are several GeV and path radii many meters.

In the simplest synchrotron source, a storage ring, the electrons are injected into the torus form a linear accelerator at energies close to the operating energy and the energy lost in the synchrotron radiation is continually replenished by pulses of rf power. The photons are emitted in a very narrow cone tangential to the electron path, making them highly suitable for extraction, and passage into a monochromator, at ports stationed around the circumference of the ring.

The advantages of synchrotron radiation are the high photon intensity (orders of magnitude greater than characteristic X-ray sources at the same energies), the ability to "tune" (select or scan) the excitation energy and the fact that the radiation can be almost 100% plane polarized.

3.1.1.2.(2). Control of Charging

Photoemission from an insulating materials leads to the build-up of a positive charge unless this can be dissipated in some way. Non-monochromated X-ray sources produce a broad, diverging X-ray beam which illuminates the sample holder and other parts of the analysis chamber, generating low-energy electrons. Bremsstrahlung excited low-energy electrons also emerge from the front face of the aluminum window, separating the X-ray source from the analysis chamber, which is close to the sample. A sufficient flux of these low-energy electrons is attracted to the sample surface to "neutralize" the charge build-up, in fact, an equilibrium surface potential is established, essentially instantaneously when the X-ray source is switched on, which is usually a few eV positive.

This fortuitous situation does not apply with a monochromated X-ray source, which produced a focused beam illuminating only part of the sample. Any vacuum-separating window is well removed from the sample and, of course, the Bremsstrahlung radiation has been eliminated. An external source of low-energy electrons is, therefore required in the form of electron "flood gun". The introduction of highly-focused X-ray sources led to more severe differential charging problems, whereby lineshapes are broadened and distorted. This negated the improved resolution achieved by X-ray monochromation and generated the need for a better

understanding of the phenomena involved.

3.1.2. The X-ray Photoelectron Spectrum

3.1.2.1. Primary Structure

Figure 3.6 displays all the aspects of primary structure in the XPS spectrum.

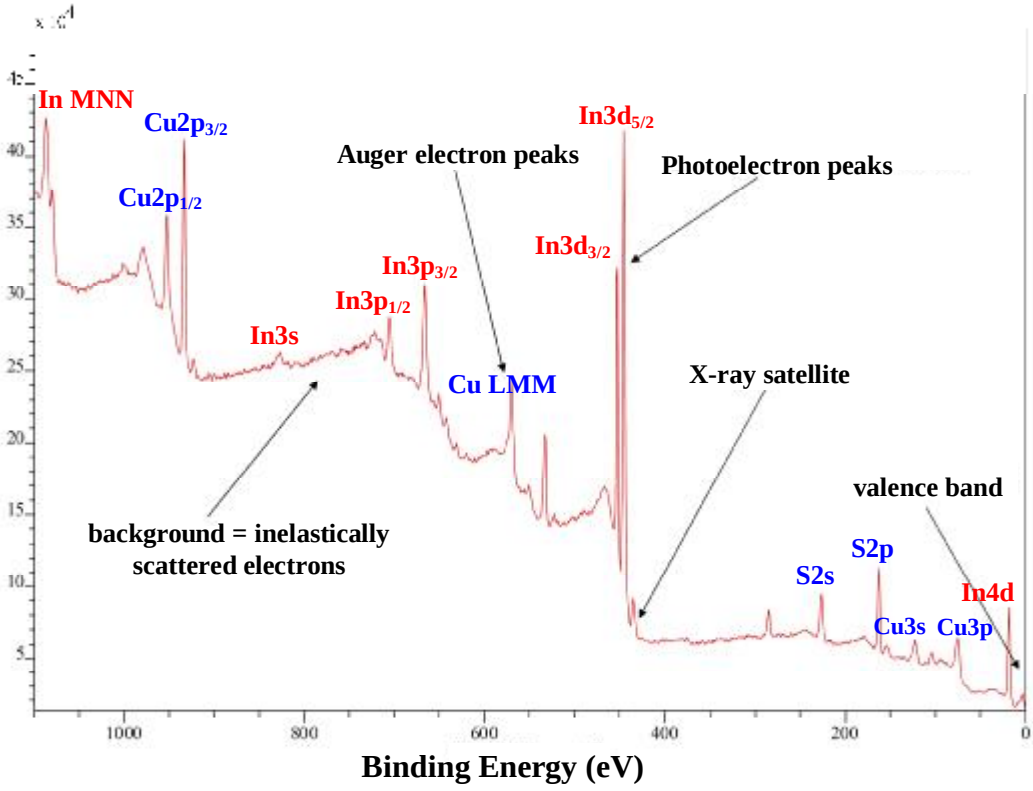

Figure 3.6. Primary structures of $CuInS_2$ in the XPS survey spectrum (http://csacs.mcgill.ca/francais/docs/CHEM634/XPS_Paynter_t.pdf)

Elastic photoemission, in which a photoelectron is ejected from an atom in the solid and escapes from the surface without suffering energy loss, gives rise to discrete peaks whose energies obey Equation (3.1.) or (3.2.) and which reflect the shell structure of the atomic electrons. Thus, at BE close to zero, the closely-spaced valence band levels, labeled indium (In) 4d, appear and with increasing BE the increasingly tightly-bound core levels (4p, 4s, 3d, 3p, 3s, 2p). The next core level, for example In 2p, has a BE (> 3keV) which is higher than the energy of Mg Kα

radiation and so it can not be photoionized by the characteristic radiation. Finally, the decay of the core holes resulting from photoemission can give rise to Auger electron emission and the appearance of Auger peaks (series), the In MNN and Cu LMM series in the case of copper indium sulphide ($CuInS_2$).

The peaks sit on the background which rises with BE. At low BE, the background is dominated by emission due to the continuous Bremsstrahlung radiation (for a non-monochromatic source), whilst with increasing BE (or, more appropriately, decreasing kinetic energy, KE) the background is dominated by the electrons resulting from inelastic scattering. The background is seen to have a step-like character, with increases on the low KE side of each peak, due to electrons which have suffered some energy loss during their escape. The structure of the background in the region of each peak carries information about surface morphology.

3.1.2.1.(1). Core Levels

The nomenclature for core levels is *nlj* where *n* is the principal quantum number, *l* is the orbital angular momentum quantum number, and *j* is the total angular momentum quantum number, $j = (l + s)$ where s is the spin angular momentum quantum number ($\pm 1/2$). Thus s levels $(l = 0)$ are singlets but all other levels (l >0) give rise to doublets. The two possible states are different in energy because the unpaired electron left in an orbital following photoionozation can have its spin and orbital angular momentum vectors either parallel or anti-parallel. This is known as ***spin-orbit (j-j) coupling***. The difference in energy between the doublet components, ΔE_j, is proportional to the spin-orbit coupling constant which depends on the expectation value $<1/r^3>$ of the orbital involved, r being the average radius. The separation, which can be many electron volts, therefore increases with atomic number, Z, for a given subshell (constant *n, l*) and decreases as l increases for constant n (thus Figure 3.6 shows splitting of In 3p > 3d). The relative intensities of the components are given by the ratio of their degeneracies g = (2j + 1), as shown in Table 3.1.

Table 3.1. The spin-orbit splitting parameters

Subshell	Total angular momentum j = (l + s)	Area ratio (degeneracies) g = (2j +1)
s	**1/2**	**—**
p	**1/2, 3/2**	**1:2**
d	**3/2, 5/2**	**2:3**
f	**5/2, 7/2**	**3:4**

The anti-parallel alignment is more “favourable”, has a lower energy and therefore appears at higher binding energy. In the case of the In 3d orbital (Figure 3.7), the orbital angular momentum quantum number l = 2 and the electron spin quantum number s = ± 1/2 so the total angular momentum j is either 3/2 (higher binding energy) or 5/2 (lower binding energy).

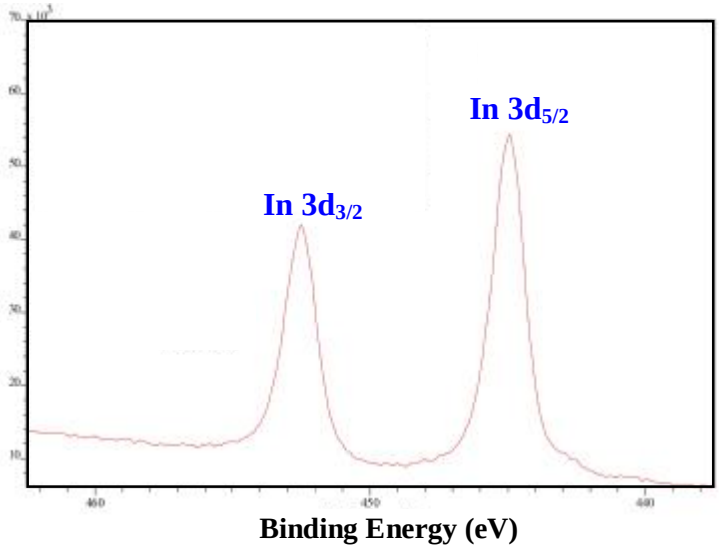

Figure 3.7. Spin orbit splitting in In 3d core levels
(http://csacs.mcgill.ca/francais/docs/CHEM634/XPS_Paynter_t.pdf)

The relative intensity of a core-level peak is fundamentally determined by the atomic photoemission cross-section, σ, which depends on the atomic number, quantum numbers *n*, *l*, and *j* and on the proximity of the photon energy to the photoemission threshold. However, for the two common X-ray sources, Al Kα and Mg Kσ, the effect of this final factor on relative cross-sections is very small. Values of σ have been derived from X-ray mass absorption coefficients and also calculated,

those of Scofield for Al Kα being illustrated in Figure 3.8 to show the trends. Relative intensities across the spectrum are also a function of the spectrometer (lens/analyzer combination) and the mode of operation, which define the "transmission function".

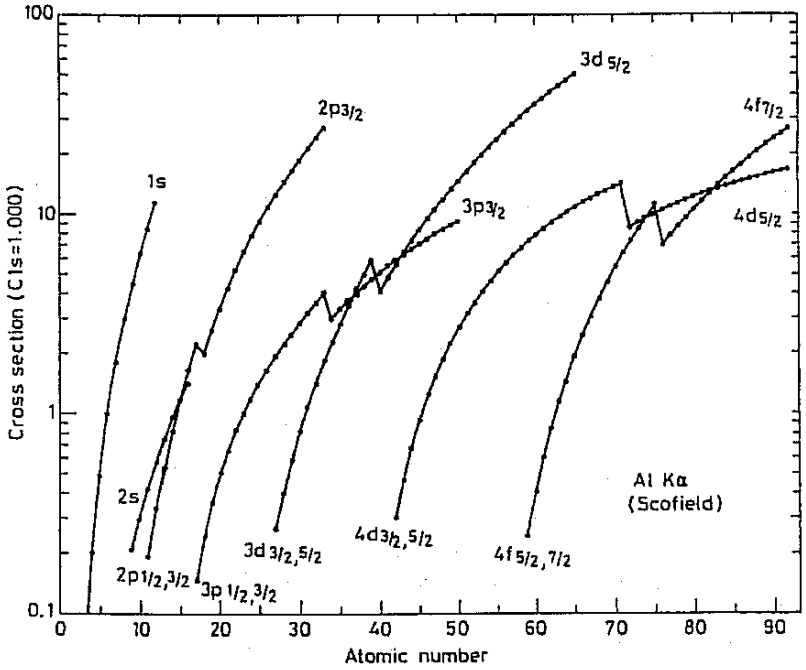

Figure 3.8. Calculated values of the photoemission cross-section, σ, for Al Kα radiation in terms of the C 1s cross-section (after Schofield (Schofiled 1976))

Figure 3.6 demonstrates that core level peak widths vary greatly. The peak width ΔE, defined as the full-width-at-half-maximum (FWHM) has several contributions. To a first approximation, assuming that the components are all of Gaussian form, these can be convoluted such that

$$\Delta E = (\Delta E_n^2 + \Delta_p^2 + \Delta E_a^2)^{1/2} \qquad (3.3.)$$

where ΔE_n is the natural linewidth, ΔE_p is the width of the excitation (photon) source and ΔE_a is the analyzer resolution, all expressed as FWHM. Working in the constant analyzer energy mode and with low pass energy, ΔE_a is constant for all peaks and can be made negligible relative to ΔE_p. ΔE_p itself can be reduced to about 0.27 eV with a good monochromator. Under these conditions narrow core lines, such as the

Ag $3d_{5/2}$ from metallic silver or the C 1s from highly-ordered pyrolytic graphite (HOPG), can have a measured FWHM of ~0.45 eV, from which (using Equation 3.3.) ΔE_n must be ~0.36 eV.

The natural linewidth is a direct reflection of the lifetime of core-hole state resulting from the emission of the photoelectron under consideration. From the Uncertainty Principle:

$$\Delta E_n = \frac{h}{t} = \frac{4.1\times10^{-15}}{t} eV \qquad (3.4.)$$

when Planck`s constant (h) is expressed in eV seconds and the lifetime (τ) in seconds. Thus the lifetime of the Ag $3d_{5/2}$ core-hole is of order 10^{-14} s.

Core-hole lifetimes are governed by the processes that follow photoemission, by which the excess energy of the ion state decays. The possible decay mechanisms are (Figure 3.9): emission of an X-ray photon (X-ray fluorescence); emission of a second electron yielding a doubly-charged ion via an Auger process and emission of a second electron via the related Coster-Kronig process. Coster-Kronig processes are very fast, of the order of 10^{-15} s, producing the broadest peaks with FWHM of several eV (for example In 3s in Figure 3.6).

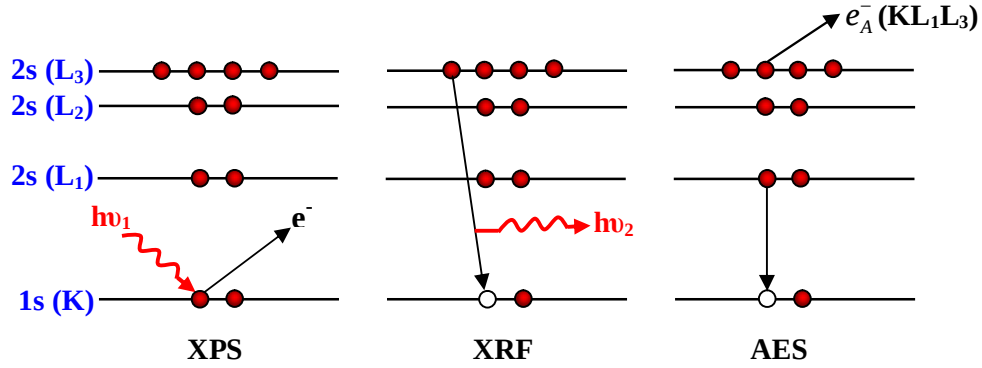

Figure 3.9. Schematic of the processes involved in X-ray photoemission and subsequent relaxation via X-ray fluorescence and Auger electron emission (in conventional AES the core hole is created by electron impact)

3.1.2.1.(2). Valence Levels

Valence levels are those occupied by electrons with low BE (0-15 eV) which are involved in delocalized or bonding orbitals. The spectrum in this region consists of many closely-spaced energy levels, producing a band structure. Hence, this region is usually referred to as the valence band. The valence band spectrum obtained from a solid sample tends to be a lumpy, continuous envelope in which the peaks are less specific to atoms and more characteristic of the bonds they form. Figure 3.10 shows the valence band spectrum of $CuInS_2$ obtained with X-rays (on the right) and ultraviolet photons (on the left) at high resolution.

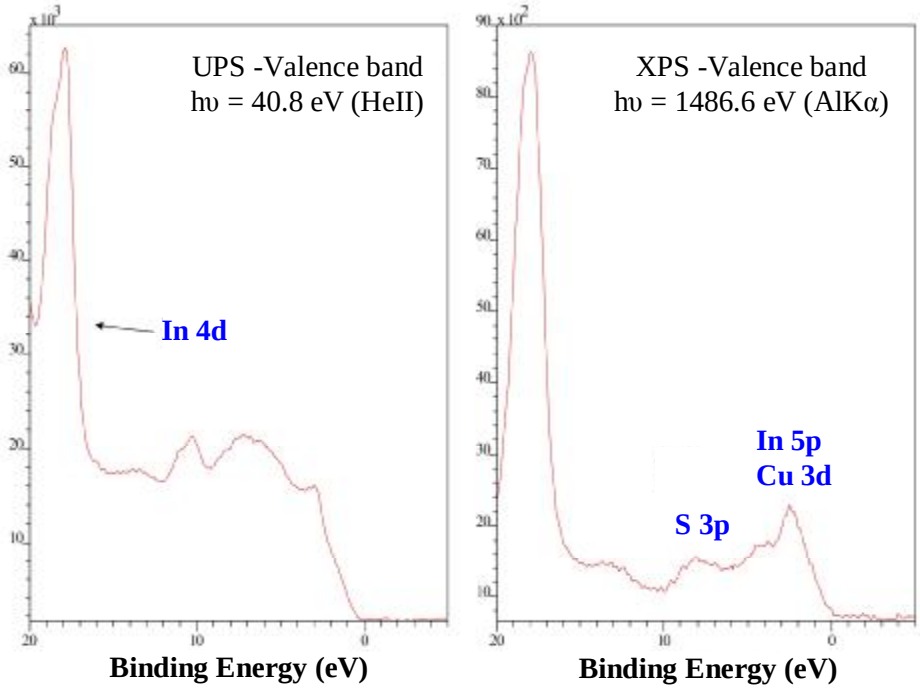

Figure 3.10. Valence band spectrum of $CuInS_2$ obtained with X-rays and ultraviolet photons at high resolution (http://csacs.mcgill.ca/francais/docs/CHEM634/XPS_Paynter_t.pdf)

On the right is the valence band spectrum of $CuInS_2$ obtained with X-rays, on the left the spectrum obtained with ultraviolet photons. Ultraviolet Photoelectron Spectroscopy (UPS), because of the much lower photon energy, probes just the valence band and is used to study bonding, especially in gas phase molecules, which exhibit much narrower peaks in which vibrational fine structure can be discerned. In

solid state studies, the interpretation of valence band spectra is usually attempted in concert with quantum chemical calculations. The two spectra in Figure 3.10, taken on the same sample, look different for several reasons. First, the cross-sections for photoemission are different for the two radiations. Second, UPS is even more surface sensitive than XPS, due to the lower kinetic energies of the photoelectrons produced. Third, whereas XPS samples the occupied valence band states, UPS convolutes this information with a sampling of the unoccupied "antibonding" states.

Figure 3.11 distinguishes the situation for conductors and insulators, where the density of electron states (per unit energy in unit volume) is plotted. In the case of insulators, the occupied valence band is separated from the empty conduction band, whilst for metallic conductors these bands overlap and the highest occupied state is termed the Fermi level, E_F. This energy-density diagram also illustrates the difference between XPS and UPS in valence band studies. The kinetic energy of the valence photoelectrons in XPS is well over 1 keV, which means that the final states occupy a flat continuum. As a result, the measured valence band is a close match to the initial density of states which is the focus of interest in studies of the electronic structures of materials. This contrasts with the situation in UPS where the kinetic energy are low, such that the final states are just above E_F and structured (as shown in Figure 3.11). The measured valence band is then a complex convolution of initial and final densities of states. Valence bands are an important source of information on both electronic and chemical structure, although theoretical calculations are required to fully exploit their potential.

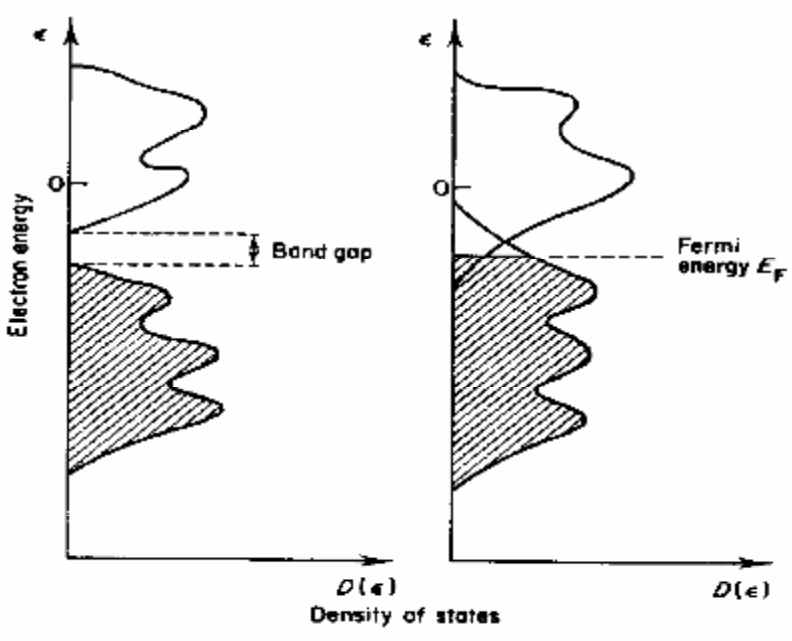

Figure 3.11. Schematic density of states for insulator (left) and a metal (right). The shading indicates the extent to which the energy levels are occupied (after Orchard (Orchard 1977))

3.1.2.1.(3). Auger Series

Auger electrons arising form the de-excitation of core holes resulting from photoemission can lead to dominant peak (or, more usually, series of peaks) in the "photoelectron spectrum", as seen in Figure 3.6. An Auger electron is given approximately by

$$E_{ABC} = E_A - E_B - E_C^* \tag{3.5.}$$

where E_A is the BE of the photoionized level (A), E_B the BE of the level (B) from which an electron moves to fill the hole created and E_C^* the BE of the level (C) from which the Auger electron is emitted (* indicates that level C is in the presence of a hole in level B, so E_C^* is not the same as E_C, the ground state BE).

Overlaps between Auger and photoelectron peaks can be serious. The kinetic energy of the Auger electron is, to a first approximation, a function of the orbital energies themselves and not of the radiation responsible for the production of the

core hole, in contrast to the KE of a photoelectron. Conversely, for spectra plotted conventionally on the BE scale, only the Auger peak positions depend on the excitation energy. Thus by switching photon energy, overlaps between specific photoelectron and Auger peaks can be avoided.

3.1.2.1.(4). Information from Primary Structure

3.1.2.1.(4.a). Elemental Analysis

With Mg Kα or Al Kα excitation, at least one core level for each element of the periodic table is observed in the spectrum (except H where the 1s electron is always involved in bonding and He where the cross-section is very low). The peak positions on the BE scale are sufficiently unique for element identification. There are only a small amount of series overlaps, with those involving first row elements (which have only the 1s level) being most problematic, especially C 1s/Ru 3d and O 1s/Sb 3d. Al 2s/Cu 3s and Al 2p/Cu 3p is an unfortunate double overlap as far as Al is concerned, but Cu would normally be identified through the stronger 2p signals.

A single survey scan acquired under appropriate conditions (resolutions, channel width and signal to noise ratio) allows a complete elemental analysis. XPS is inherently quantitative: i.e. the intensity of a peak is directly proportional to the density of the atom from which it derives (under fixed experimental conditions) within the sampled volume.

The stoichiometry of the sample surface can be estimated from the area ratio of XPS peaks. The general formula for the XPS peak area (Chastain 1992) is

$$I = n.f.\sigma.\theta.y.\lambda.A.T \qquad (3.6.)$$

where n is the atomic concentration of the element, f is the X-ray flux, σ is the photoemission cross-section for the atomic orbital of interest, θ is the angular efficiency factor for the instrumental arrangement, y is the efficiency in the photoelectronic process for formation of photoelectrons of the normal photoelectron

energy, λ is the mean free path of the photoelectrons in the sample, A is the area of the sample from which photoelectrons are detected, T is the detection efficiency for electrons emitted from the sample.

In the case of a laboratory X-ray tube the stoichiometric ratio of two elements A and B in a homogeneous solid, or at least homogeneous within the sampling depth, could be determined from the peak areas:

$$\frac{n_A}{n_B} = \frac{I_A / s_A \cdot y_A \cdot l_A \cdot T_A}{I_B / s_B \cdot y_B \cdot l_B \cdot T_B} = \frac{I_A / S_A}{I_B / S_B} \tag{3.7.}$$

where S_A and S_B are the sensitivity factors for the elements, which are tabulated and listed in literature (for example (Chastain 1992)).

If the X-ray source is a synchrotron, it is possible to set kinetic energies of photoelectrons from certain core levels of two different elements to the same value by use of two different excitation energies. The same information depth and the same analyzer transmission are achieved in this case and the formula for the stoichiometric ratio has the form:

$$\frac{n_A}{n_B} = \frac{I_A}{I_B} \cdot \frac{s_B}{s_A} \cdot \frac{f_B}{f_A} \tag{3.8.}$$

When the photoemission cross-section (σ) for the most intense core levels of each atom are compared (Figure 3.8), it is found that the variation across the periodic table is about a factor of 100, if Li and Be are excluded. The cross-section is the most important parameter influencing the relative sensitivity factor; hence, XPS does not suffer unduly from inherent sensitivity effects. Detection limits are typically 0.1 atomic % for elements with low cross-section core levels.

The cross-sections were calculated theoretically in (Yeh et al. 1985). An analytical formula for the photon-energy dependence was obtained on base of this data in (Verner et al. 1995). It should be noted that some disagreements were found for selected compounds between theoretical cross-section values and experimental

data (Coulston et al. 1996). As far as no other extended theoretical or experimental cross-section database is available, stoichiometric ratio estimations are desired to be proven by measurement of reference compounds.

3.1.2.1.(4.b). Chemical State Analysis

Although the core-level BEs of a given element are sufficiently unique to allow unambiguous identification in most instances, they are not fixed values. Indeed, the discovery that the same atom in different chemical environments can give rise to discrete core level components provided a major impetus to the development of XPS. These relative BE differences are called "***chemical shifts***". Figure 3.12 recalls that chemical shifts in the binding energy of the Si 2p core level allow it to separate Si atoms in different oxidation states (Himpsel et al. 1994).

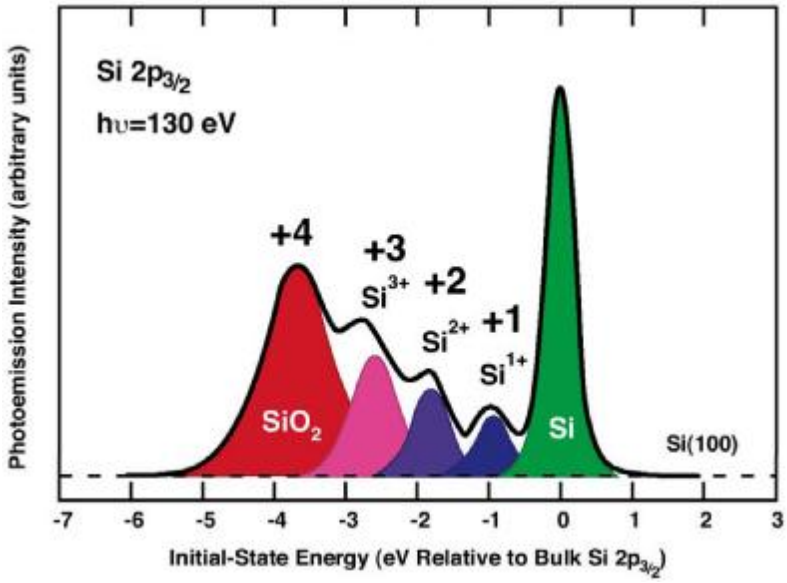

Figure 3.12. Si 2p photoelectron spectrum of a thin (5 Å) SiO_2 film on Si(100) showing all oxidation states of Si. Only the $2p_{3/2}$ component is shown (Himpsel et al. 1994)

A simple model which relates the BE to the atomic charge, the charge potential model, can be given here:

$$E_i = E_i^0 + kq_i + eV_i \tag{3.9.}$$

where E_i is the BE of the particular core level on atom *i*, E_i^0 is a reference energy, k is a constant, and q_i is the charge on atom *i*. V_i is defined as sums the potential at atom *i* due to point charges on atoms *j*:

$$V_i = \sum_{i \neq j} \frac{q_i}{r_{ij}} \tag{3.10.}$$

If the atom is considered to be a hollow sphere, on the surface of which the valence charge, q_i, resides, then inside the sphere, the classical potential is the same at all points and equal to q_i/r_v, where r_v is the average valence orbital radius. A change in the valence charge (density) of Δq_i changes this potential by $\Delta q_i/r_v$. Thus all core levels of the atom should experience the same BE shift and for equivalent compounds the shift will decrease as a column of the periodic table is descended, as observed to a first approximation in practice.

For two atoms in different chemical environments Equation (3.10.) gives

$$\Delta E_i = k\Delta q_i + e\Delta V_i \tag{3.11.}$$

In molecular solids, atoms *j* are essentially the atoms bound to atom *i* and ΔV_i is relatively small, thus electronegativity effects will dominate Δq_i. An increase in positive charge is therefore accompanied by an increase in BE. In ionic solids, however, V_i is summed over the whole solid and ΔV_i can be appreciable as well as being of opposite sign to Δq_i. This can result in very small shifts even for a change of oxidation state.

The major simplification of Equation (3.11.) is that it ignores final state effects. The measured BE is actually the difference between the final and initial state energies, so any chemical shifts must involve consideration of both of these. The core hole of the final state has a polarizing effect on surrounding electrons, both interatomic (on atom *i*) and extra-atomic (on atoms *j*). The electronic response is

referred to as relaxation. Again, in molecular solids, relaxation energies are fairly constant, so initial state (particularly electronegativity) effects tend to dominate.

The chemical shift range for any element is quite small, typically less than 10 eV, and, since peak widths are of the order of 1 eV, the dynamic range is rather poor. This has three consequences for data analysis. First, if the different chemical states are present in the same system, the core level components will likely overlap, probably severely. To accurately measure the components, BEs and quantify the intensities the components need to be resolved. This requires curve fitting and some understanding of appropriate lineshapes. Second, the choice of background (to fit or subtract) can have a significant effect on these results. Third, for insulating samples, the BE or chemical shifts needs to be established relative to a reference value. This might be an internal reference, i.e. the BE of a core level of an atom which is part of the same molecular species, or an external reference, typically the adsorbed carbonaceous contamination often observed on surfaces. This is often a non-trivial exercise involving inherent assumptions about the nature of the contamination, its thickness and electrical contact with the material (Swift 1987). The contamination of these three factors means that BE data may not be very accurate, as is evident from the range of BE values for the same compound measured by different workers in BE databases an uncertainty of ± 0.2 eV would be a good experimental result, but probably nor precise enough to unambiguously identify the species involved with a chemical shift range of only a few eV covering all candidate species.

A possible solution to this problem is to make use of the Auger peaks in the spectrum. For the Auger processes in which the final vacancies arise in core levels, it is clear from the above that a chemical change which gives rise to a shift in the photoelectron line will be accompanied by a shift in the Auger line(s). Indeed, such Auger shifts are usually larger than photoelectron shifts and multiple components can sometimes be observed in Auger peaks when only a single component is present in the photoelectron peak. That more information was available from the study of both Auger and photoelectron lines together, rather than separately, was recognized by Wagner, who introduced the concept of the Auger parameter, α. This was originally defined as the difference between the kinetic energies of the Auger and photoelectron

lines. This parameter is a chemical state fingerprint which is unaffected by charging and, therefore, does not require any energy reference.

3.1.2.1.(5). Energy Referencing

The obvious problem of BE referencing for insulating materials has been referred to in the previous section. However there are other areas in which this issue must be addressed. The conductivity of most semiconductors is sufficient to ensure that when they are in electrical contact with the spectrometer E_F is at zero BE, even though a Fermi level as such may not be observed in the spectrum. E_F can, in principle, occur anywhere in the bandgap so that any shift in E_F will lead to an equal shift in all core level BEs. E_F can be "pinned" by doping the bulk or surface layers (for example, n or p type), by creating surface states (for example, by metallization) or by creating defect states (for example, by ion etching). Thus core level shifts in semiconductor spectra must be interpreted with caution.

The reference level is also a particular problem in studies of the following types:

(a) Gas phase-condensed phase shifts (for example, in molecules adsorbing onto surfaces or atoms condensing onto surfaces, as in thin film growth)

(b) The growth of small metal clusters

(c) The alloying of metals

(d) Shifts in core levels between bulk and surface atoms in single crystals

3.1.2.2. Secondary Structure

3.1.2.2.(1). Multiplet Splitting

Multiplet splitting (also referred to as exchange splitting or electrostatic splitting) of core level peaks occurs when the system has unpaired electrons in the valence levels. As an example, consider the case of the 3s electron in the Mn^{2+} ion. In the ground state the five 3d electrons are all unpaired and have parallel spins

(^6S initial states). Following photoemission of a 3s electron, the remaining 3s electron is also unpaired. If the spin of this electron is parallel to that of the 3d electron (^7S final state) then exchange interaction can occur, resulting in a lower energy than for the case of anti-parallel spins (^5S final state). Thus the 3s level will be split and the doublet separation is exchange interaction energy:

$$E = (2S+1)K_{3s3d} \tag{3.12.}$$

where S is the total spin of the unpaired electrons in the valence levels (5/2 in this case) and K_{3s3d} is the 3s-3d exchange integral. The intensity ratio for the two components is given by

$$\frac{I(S+1/2)}{I(S-1/2)} = \frac{(S+1)}{S} \tag{3.13.}$$

For the 3s in Mn^{2+} this ratio is 1.4 and E is calculated to be ~13 eV. In the real case of MnF_2 the intensity ratio is ~1.8 and the separation ~6.5 eV. This discrepancy is due to relaxation and configuration interaction effects which complicate the simple model just described (Fadley 1978).

Multiplet splitting for non-s levels is more complex because of the additional involvement of orbital angular momentum coupling. Thus, in Mn^{2+}, the 3p level is split into four levels. Multiplet splitting is strongest when both levels involved are in the same shell (as with 3s/3p-3d) but the effects are still apparent in transition metal systems for the 2p-3d interaction.

3.1.2.2.(2). Shake-up Satellites

To the valence electrons, the loss of a core electron by photoemission is equivalent to an increase in the nuclear charge. This major perturbation gives rise to a substantial reorganization of the valence electrons (relaxation) which may lead to

an electronically-excited final state, i.e. a valence electron promoted to a higher unfilled level. The energy required for this transition is not available to the primary photoelectron and thus the two-electron process leads to discrete structures on the low KE side of the peak (shake-up satellites). Two situations can be distinguished in the solid state. Especially aromatic systems in organic materials show shake-up peaks with intensities of up to 5-10% of the main peak. In aromatic systems, the satellites are due to $\pi \rightarrow \pi^*$ transitions involving the two highest filled and the lowest unfilled valence levels. The satellite separations can be up to 15 eV (Figure 3.13).

In inorganic systems very strong satellites are observed for certain transitions metals and rare earths which have unpaired electrons in the 3d and 4f shells, respectively. Although referred to as shake-up, a preferable description is that strong configuration interaction takes place in the final state, involving significant ligand-metal charge transfer, so that an extra 3d or 4f electron is present relative to the initial state. The resulting spectra can be complex.

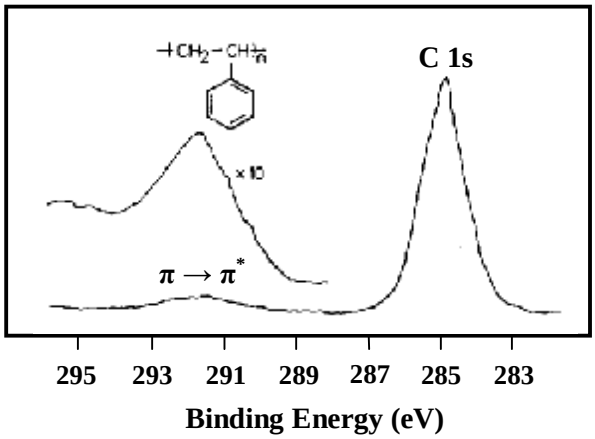

Figure 3.13. C 1s spectra of polystyrene, showing the low kinetic energy shake-up satellite (Clark et al. 1976)

3.1.2.2.(3). Metal Core Level Asymmetry

As Figure 3.11 shows, a solid metal has a distribution of unfilled one-electron levels above the Fermi level which are available for shake-up like events following core electron photoemission. In this case, instead of discrete satellites on the low KE side of the peak, the structure is a low KE tail on the peak itself. A high density of

states at the Fermi level produces the greatest effect, resulting in a high degree of

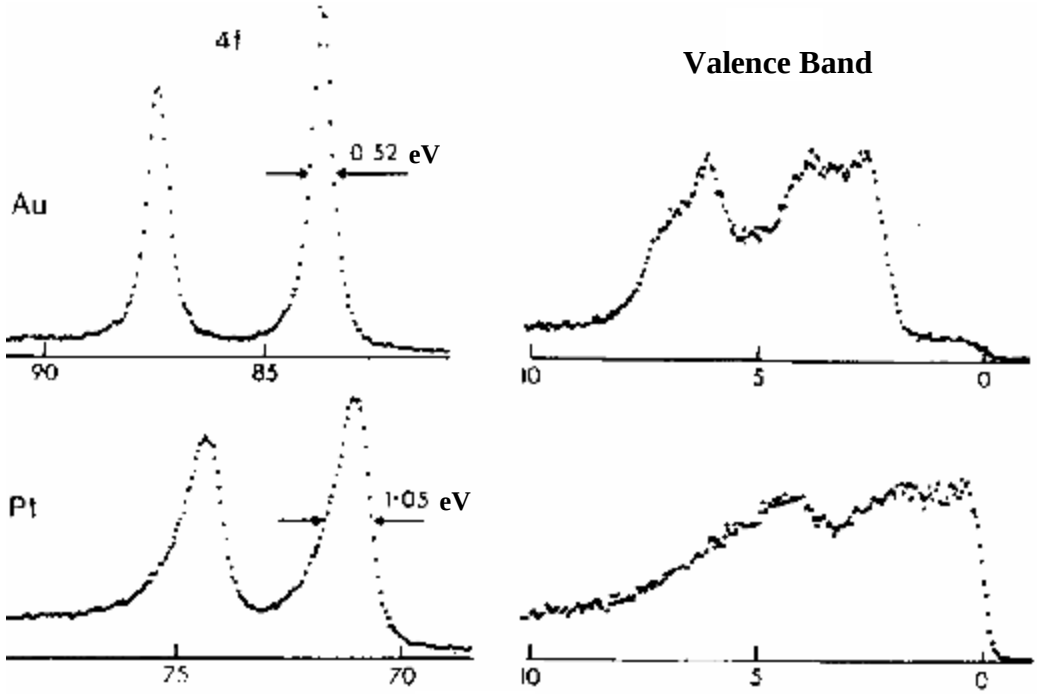

core level asymmetry, as shown in Figure 3.14.

Figure 3.14. Core (4f) and valence level (VB) spectra of gold and platinum excited with monochromatic Al Kα radiation. Note the relationship between the degree of core level asymmetry and the density of states at the Fermi level (BE = 0) (Barrie et al. 1976)

3.1.2.2.(4). Vibrational Fine Structure

This form of asymmetry is observed in the high resolution C 1s spectra from polymers which contain saturated hydrocarbon components. Final states in which the molecule is vibrationally excited are significant, with the C-H stretch vibration being the dominant contributor. The result, seen best in the spectrum of the linear hydrocarbon hexatriacontane, Figure 3.15, is a harmonic progression of lower KE peaks separated by the C–H stretch energy of 0.39 eV. An identical result, with slightly greater FWHM, is obtained from polyethylene (Beamson 1992).

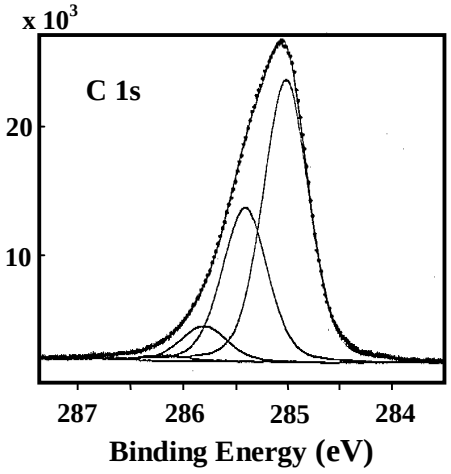

Figure 3.15**.** The high resolution C 1s spectrum from hexatriacontane (n-$C_{36}H_{74}$) as a thin film on silicon. The intensities of four components represents the populations of the vibrational states of the core-ionized system, with the ground state having the lowest BE (Beamson et al. 1992a)

The relative intensities of the components (and their separation) are the same as those seen in the gas-phase spectrum of methane, for which the components can be completely resolved. C 1s peaks due to functional groups which do not have C–H bonds (for example carboxyl or quaternary C) are narrower and more symmetrical. In the saturated hydrocarbon case, the relaxation mechanism is σ-inductive electron migration to the core hole, resulting in a shorter bond length for the molecular ion and vibrational excitation. This contrasts with the aromatic hydrocarbon where relaxation is via π electron excitation leading to shake-up satellites and essentially symmetric C 1s peaks as described above (Beamson et al. 1992b).

3.1.2.2.(5). Plasmon Loss Features

These features are of most importance for clean metal surfaces. Electrons passing through a solid may excite modes of collective oscillation of the conduction electrons, and in so-doing suffer a characteristic energy loss (plasmon loss). The most important plasmon frequency is that of the bulk plasmon, ω_b, and this is followed by higher harmonics. Plasmon losses at energies of $\hbar\omega_b$, $2\hbar\omega_b$ …. can be

seen on the low KE side of the metal core level peak with rapidly decreasing intensity. For very clean surfaces, a surface plasmon loss of lower energy ($\hbar\omega_s$) may also be observed along with lower intensity features representing coupling between surface and bulk plasmons, such as a ($\hbar\omega_b$+ $\hbar\omega_s$) energy loss. Loss peaks which involve the surface plasmon are rapidly attenuated when the surface becomes oxidized. Figure 3.16 illustrates these features.

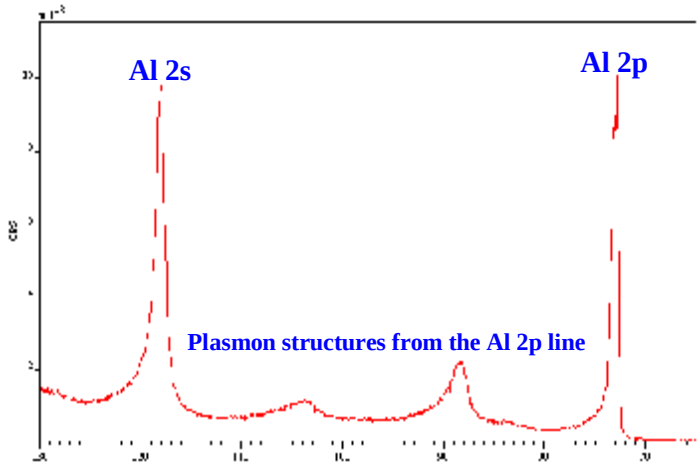

Figure 3.16. Clean Aluminum spectrum showing plasmon resonance structures (http://www.casaxps.com/help_manual/XPSInformation/Introductionto XPS.htm)

3.1.3. Surface Sensitivity

The surface sensitivity of XPS is due to the low probability that electrons generated below the surface will leave the solid with their original energy and contribute to the peaks which are described in terms of this energy by Equation (3.1.) or (3.2.). The depth of origin of these electrons and their attenuation during transport to the vacuum are therefore of fundamental importance. Understanding in this area has changed markedly in recent years.

Initially, it was believed that only inelastic scattering was responsible for electron attenuation and that this obeyed a Beer-Lambert law, so that:

$$I_z = I_0 \cdot e^{-z/l \sin q} \qquad (3.12.)$$

where I_z is the intensity emanating from the atoms at depth z, I_0 is the intensity from the surface atoms, θ is the electron "take-off angle" (with respect to the surface plane) and λ the electron inelastic mean free path (IMFP), the average distance travelled between inelastic collisions for an electron with the appropriate energy.

For a sample consisting of an overlayer of material A on a substrate of material B (both homogeneous), Equation (3.12.) leads to the expression:

$$I_A = I_A^{\infty}(1-e^{-d/l_A \sin q}) \tag{3.13.}$$

$$I_B = I_B^{\infty} \cdot e^{-d/l_B \sin q} \tag{3.14.}$$

where I_A and I_B are the measured intensities, I_A^{∞} and I_B^{∞} are the intensities from bulk A and B measured under the same conditions, λ_A and λ_B are the IMFPs for the core electrons representing A and B travelling through material A (these differ if the electrons have different kinetic energies).

These equations formed the basis for determinations of λ from overlayer deposition experiments with an independent measurement of film thickness. However, it was subsequently realized that elastic scattering, in which the electron trajectory is altered without any energy change, was also important during electron transport and that this would lead to significantly greater values for λ (better referred to as ***attenuation lengths***). Furthermore, it is also now known that electron attenuation in solids is not exponential and that attenuation lengths are dependent on the experimental geometry. These problems have led to a great deal of theoretical modeling of electron transport in solids.

Experimental electron attenuation lengths (λ_{AL}) show a general behavior when plotted as a function of kinetic energy. At vey low energy, λ_{AL} decreases rapidly as KE increases and minimizes in the region of ~20 keV. As KE increases further λ_{AL} slowly increases in a manner which can be modeled over quite large energy ranges by a power law of the form $\lambda_{AL} \propto (E_K)^x$ where, typically, $0.5 < x < 1$. Attenuation lengths are critical to any quantitative treatments of XPS data. IMFPs

can be calculated from experimental optical data and fitted with a modified form of the Bethe Equation for inelastic scattering.

Returning to definitions which assume an exponential attenuation, the ***escape length*** is defined as the depth, measured normal to the surface, at which the intensity drops to 1/e (36.8%) of its original value. 95% of the detected signal will then come from three times the escape depth. If the attenuation length is λ_{AL} then for a take-off angle of θ, the escape depth $d = \lambda_{AL} \sin\theta$ and 3d ($=3\lambda_{AL} \sin\theta$) is usually taken to be the ***sampling depth*** of XPS. The variation of this parameter with take-off angle is the basis of angle-resolved experiments for non-destructive depth profiling.

It can be also note at this point that at higher photoemission angles, the information is obtained from shallower depths than at lower photoemission angles (compare the 90° and 15 ° in Figure 3.17). The height of the dark orange cone in the figure is illustrative of the amount of information contributing to the XPS spectrum as a function of depth. By varying the photoemission angle, therefore, we vary the effective "sampling depth", because we oblige the emerging photoelectrons to travel through more material at the higher photoemission angles, so that only those photoelectrons originating from closer to the surface tend to escape with no energy loss. Whatever the photoemission angle, however, most of the information comes from the very surface of the sample, and so we must expect the quality of a reconstruction of the depth profile to degrade as a function of depth.

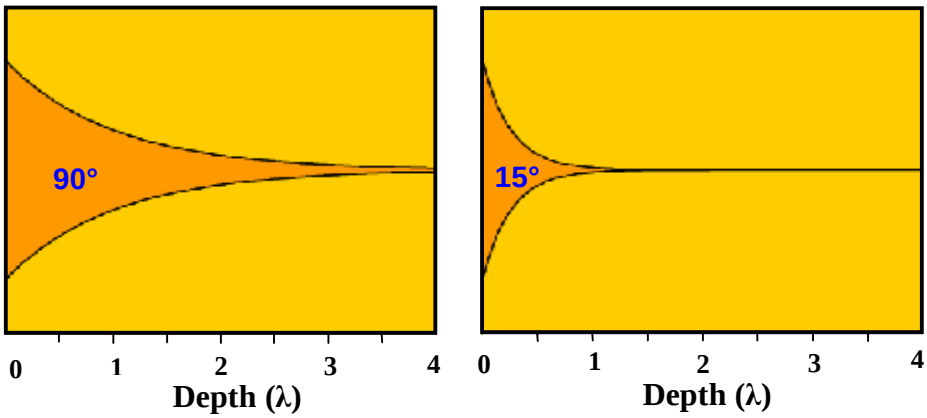

Figure 3.17. The amount of information contributing to the XPS spectrum as a function of depth (http://goliath.emt.inrs.ca/surfsci/arxps/samplingcss.html)

3.1.4. Angular Effects

Angle-resolved XPS experiments required the taking of data at series of angles in turn by changing the angle of detection relative to the surface plane. A simple example is given in Figure 3.18, which allows a rapid qualitative assessment of the relative vertical ordering of the species involved. However, the derivation of an accurate quantitative depth profile, i.e. the variation of atomic composition within the maximum sampled depth, from angle-intensity data is non-trivial exercise.

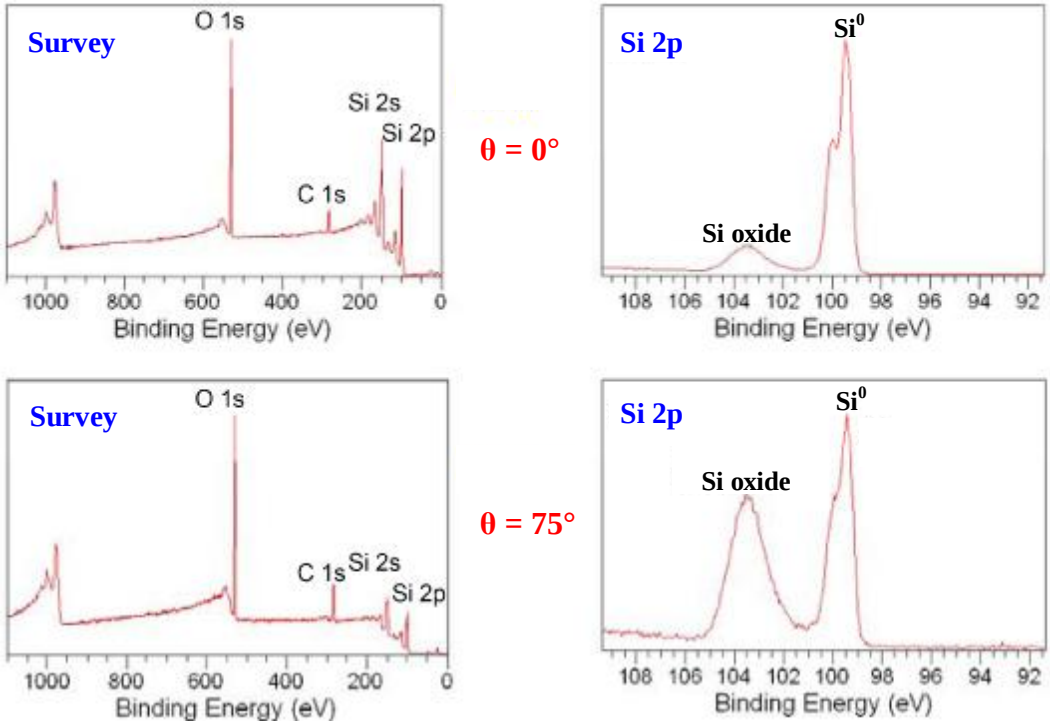

Figure 3.18. Spectra from the surface of SiO_2 film on Si substrate taken at take-off angles of 0° and 75° with respect to the surface normal. At 0° spectrum is almost due to the silicone substrate (metallic silicone) (http://cmm.mrl.uiuc.edu/Workshop2010/downloads/Workshop10_SurfaceAnalysisI)

Recent instrumental developments have transformed the prospects for this kind of experiments. The “radian lens”, introduced by Thermo VG Scientific, allows parallel acquisition of high resolution spectra over an angular range without tilting the sample. Moreover, with small area excitation and in situ sample visualization by both optical and photoelectron imaging, non-destructive depth profiling has become possible from well-defined (small) regions of specimen. Alternatively, with

automated sample movement, the variation in thickness of a thin film over a large area can be assessed (Seah et al. 2002).

A different angular effect is that of photoelectron diffraction (the interference between the various coherent components of the same photoelectron wave functions), observed for ordered materials such as single crystals and adsorbed or epi-layers on them, or materials with large grain sizes. This is largely, the result of forward-scattering of photoelectron, so that emission is enhanced along major inter-nuclear axes. The absolute intensity of a core-level peak is plotted as a function of take-off (polar) angle and the diffraction effects are seen as significant modulations of the expected smooth instrument response function. Similar modulations are observed when the intensity is plotted, at a fixed polar angle, as a function azimuthal angle (by rotating the crystal in the surface plane). These intensity modulations can then be related to surface structure.

3.1.5. Sample Damage

XPS is generally though to be the most benign surface analysis technique in terms of radiation damage potential. Additionally, there are many references in the literature which state or imply that damage potential is greatly reduced when a monochromatic X-ray source is used. However, as with all generalizations, these should be treated with caution. It is true that two sources of degradation present with non-monochromated sources are eliminated by monochromation, namely the thermal effects associated with having a hot source very close to the sample and the effects of the high-energy Bremsstrahlung. However, the characteristic photon themselves, or the photo- or secondary electrons generated within the sample are still capable of causing significant damage, particularly in the case of organic materials. The effect of charge compensating electrons may not be negligible. In experiments involving long exposures, it is always a good idea to check for time variation.

3.3. Angle-Resolved Photoemission Spectroscopy (ARPES)

Photoelectron spectroscopy is a general term which refers to all techniques based on the photoelectric effect originally observed by Hertz. This was later explained as a manifestation of the quantum nature of light by Einstein, who recognized that when light is incident on a sample; an electron can absorb a photon and escape from the material with a maximum kinetic energy, hυ-Φ where hυ is the light energy and Φ is the work-function of the material. The energy of an electron inside a solid can be obtained using photoelectron spectroscopy. The core electrons will have a lower kinetic energy than the valence electrons when absorbing the same photon energy. In principle, the momentum of the electrons can also be obtained. Different momentum electrons will escape at different angles from the surface of a material (Figure 3.19).

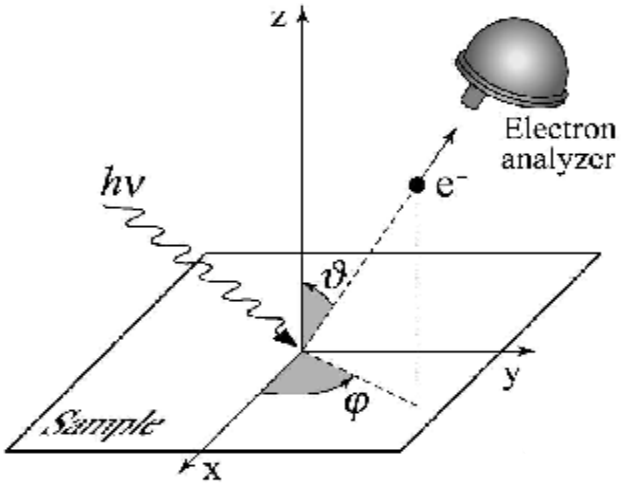

Figure 3.19 Photoemission geometry (http://www.ccmr.cornell.edu/igert/modular/docs/IGERT_Lecture1.pdf)

However, since the electrons are being projected through the surface, the momentum perpendicular to the surface is not conserved. Therefore, angle-resolved photoemission is ideal for 2D materials where the principle momentum directions of interest are parallel to the surface.

In practice, the electrons ejected from the material are collected using a hemispherical detector in which lens voltages direct the electron onto a two-dimensional (energy, momentum) multi-channel plate. The sample and the detector

are kept in an ultra-high vacuum (UHV) chamber in order to minimize surface contamination. Light sources are either synchrotron radiation at ~20-100eV, plasma Helium discharge at ~20eV, or more recently, modern-day lasers ~6 eV.

ARPES, with its unique capability to directly resolve in energy-momentum space and hence image electronic structures of materials, has been demonstrated to be a powerful experimental probe to study materials of a wide range of interesting properties (Figure 3.20). A major area of research in condensed matter physics is the science of emergence where complex quantum systems develop novel properties not pertinent to the individual constituencies on their own.

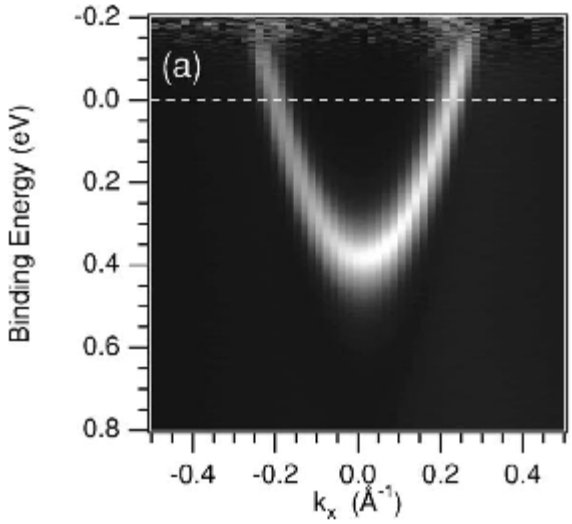

Figure 3.20 Angle-scanned energy distribution curve from Cu(111)(Baumberger et al. 2001)

3.2. Absorption Spectroscopy

3.2.1. X-ray Absorption Spectroscopy (XAS)

X-ray Absorption Spectroscopy (XAS) is a characterization technique used to determine structural information of a compound. It has become an important spectroscopic tool for the characterization of materials as well as for fundamental studies of atoms, molecules, adsorbates, surfaces, liquids and solids (Stöhr, 1992). The particular assets of XAS are its element specificity and the possibility to obtain

detailed information without the presence of any long-range order. XAS is able to provide a detailed picture of the local electronic structure of the element studied. The X-ray absorption spectrum in some cases is closely related to the empty density of states of a system.

In XAS, a core electron is excited into unoccupied atomic/molecular orbital or band above the Fermi level and therefore it mainly reflects the electronic structure of unoccupied states. The electron is considered a photoelectron and it is propagated as a spherical wave. The energy of this photoelectron is equal to the energy of the absorbed photon minus the binding energy of the electron to the atom. The energy at which these photoelectrons are absorbed is related to the edges seen in XAS, K, L, and M, which correspond to the particular electronic transitions, Figure 3.21. These edges are due to a drop in transmitted X-ray intensity as the amount of absorbed X-rays increases. This idea is shown in Equation 3.15:

$$I_t = I_0 e^{-\mu t} \qquad (3.15.)$$

where I_t is the intensity of X-rays transmitted through the sample, I_0 is the intensity of X-rays shined on the sample, μ is the absorption coefficient, and t is the thickness of the sample. Each element has known edge locations that are due to the individual binding energies of its electrons.

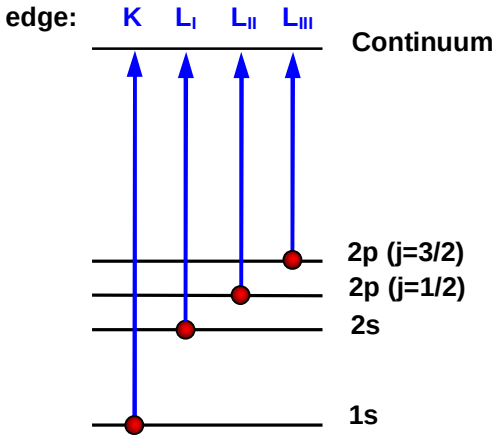

Figure 3.21 Illustration of edges and the corresponding electronic transitions

There are two main regions of an XAS spectrum from which one can get

information: X-ray Absorption Near-Edge Structure (XANES) for bound states and low energy resonances in the continuum, and Extended X-ray Absorption Fine Structure (EXAFS) when the outgoing electron is well above the ionization continuum (Figure 3.22). These transitions are caused by the absorption of an X-ray photon with energy tuned by means of synchrotron radiation to the ionization energy of the electron and lead to a pronounced fine structure in the XAS spectrum. The XAS spectra record the absorption intensity as a function of the incoming photon energy.

The X-ray Absorption Near-Edge Structure, XANES, is the part of the spectrum that gives qualitative data based on modeling and simulation. XANES is used to give information about the average oxidation state, local coordination geometry (local structure), Fermi energy, and density of states. By taking unknown data and fitting a linear combination of known data, one can get an estimate of what the unknown contains. This is called finger printing. XANES is controlled by bond lengths, symmetry, and the types of ligands. XANES spans a region of about 100 eV, and relates to Near-Edge X-ray Absorption Fine Structure, NEXAFS. NEXAFS is used at photon energy of less than 1000 eV, which is considered soft X-ray spectroscopy and is used for surface science.

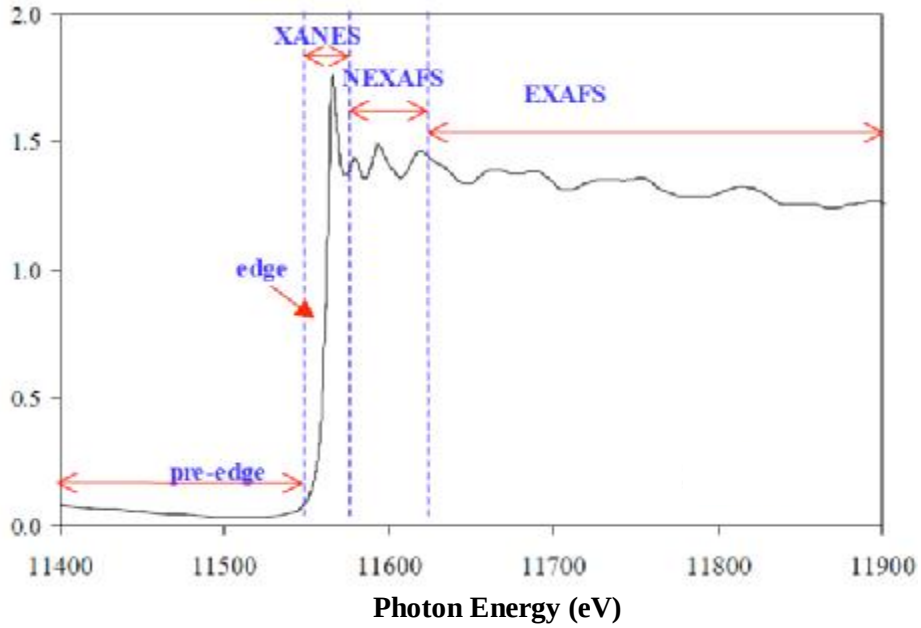

Figure 3.22 An example of XAS spectrum (http://.png.si/~arcon/xas/exafs/exafs.htm)

3.2.2. Near Edge X-ray Absorption Fine Structure (NEXAFS)

Near Edge X-Ray Absorption Fine Structure, NEXAFS, spectroscopy refers to the absorption fine structure close to an absorption edge, about the first 30eV above the actual edge. This region usually shows the largest variations in the X-ray absorption coefficient and is often dominated by intense, narrow resonances. Today, the term NEXAFS is typically used for soft X-ray absorption spectra and XANES for hard X-ray spectra.

NEXAFS involves the excitation of electrons from a core level to partially filled and empty states in the same system. The peak positions and spectral lineshape intensity are directly related to the nature of unoccupied electronic states. Probing the excitation of core electrons to unoccupied states, NEXAFS measurements provide direct information about the nature of the empty molecular orbitals. Since the number of empty molecular orbitals and their energy positions are characteristic of foe different classes of chemical species, NEXAFS spectra can be used as “fingerprints” for identifying molecular species. Because NEXAFS measurements involve dipole transitions from well-defined initial and final states, the application of the dipole selection rule often provides information about the local symmetry of the molecules (Stöhr, 1992). This picture is valid in the NEXAFS measurements of inorganic solids such as transition metal compounds, gas, as well as solution.

The decay of core hole states results in the emission of Auger electrons from valence molecular orbitals, resulting in a NEXAFS electron yield spectrum (Figure 3.23). Decay of core holes may also occur via the emission of fluorescent photons, which originate from the top 200 nm of the film as opposed to Auger electrons, which arise from the top 10 nm. Thus, this technique is both surface and bulk sensitive.

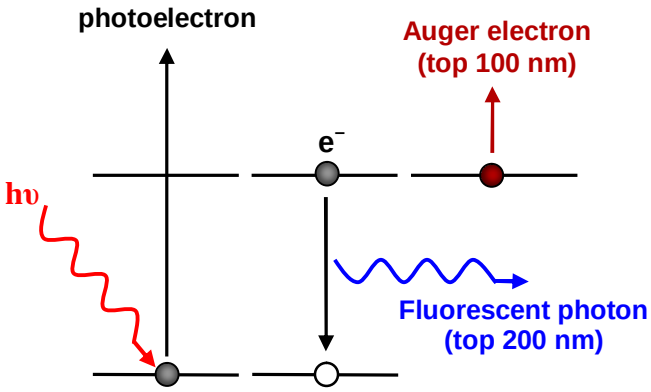

Figure 3.23 Schematic representation of the basic theory of NEXAFS. The target atom absorbs an X-ray photon and emits a core electron which propagates outwards to an unoccupied discrete level, thereby creating a core hole. An electron from a higher energy level fills the hole, releasing excess energy either by the radiation of fluorescence photons (bulk sensitive) or by the emission of Auger electrons (surface sensitive)

Opposite to the related XPS technique, where the photon energy is fixed and the electron intensity is measured as a function of electron kinetic energy, in NEXAFS the X-ray energy is scanned and the absorbed X-ray intensity is measured. As illustrated in the Figure 3.24 below, NEXAFS spectra can be recorded in different ways. The most common methods are transmission and electron yield measurements. Note that the absorption coefficient μ is obtained either as the logarithm or the direct ratio of the detected intensities I_t and I_e and incident intensity I_o, as indicated in the Figure 3.24. The transmission technique requires thin foils while the electron yield technique, often called Total Electron Yield (TEY) detection, can be used for conventional samples. The absorbed X-ray intensity is not measured directly in TEY measurements, but rather the photoelectrons that are created by the absorbed X-rays. X-rays are absorbed through excitations of core electrons to empty states above the vacuum or Fermi level. The created holes are then filled by Auger decay (dominant in the soft X-ray region over X-ray fluorescence). The intensity of the emitted primary Auger electrons is a direct measure of the X-ray absorption process and is used in so called Auger Electron Yield (AEY) measurements, which are highly surface sensitive, similar to XPS. As they leave the sample, the primary Auger electrons create scattered secondary electrons which dominate the total electron yield (TEY) intensity. The TEY cascade involves several scattering events and originates

from an average depth, the electron sampling depth. Electrons created deeper in the sample lose too much energy to overcome the work function of the sample and therefore do not contribute to the TEY. The sampling depth in TEY measurements is typically a few nanometers, while it is often less than 1 nm for AEY measurements.

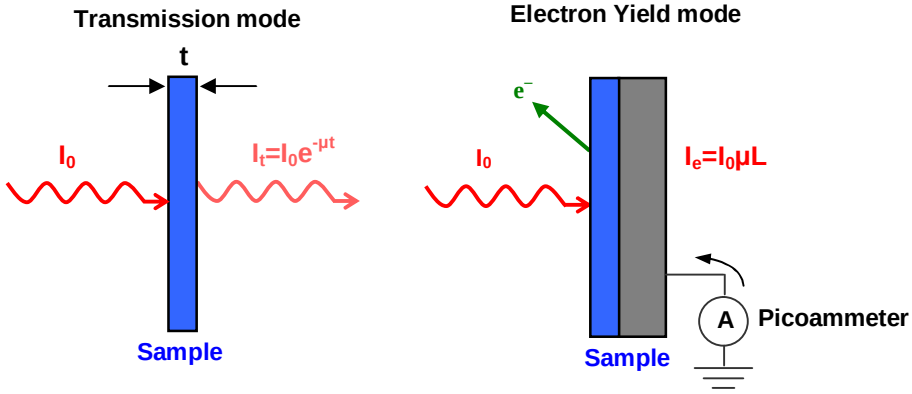

Figure 3.24 Two methods of recording X-ray absorption spectra (Stöhr, 1992)

NEXAFS is ***element specific*** because the X-ray absorption edges of different elements have different energies. NEXAFS is also very ***sensitive to the bonding environment*** of the absorbing atom. The NEXAFS spectrum exhibits considerable fine structure above each elemental absorption edge. This fine structure arises from excitations into unoccupied molecular orbitals. NEXAFS is dominated by multiple scattering of a low-energy photoelectron in the valence potential set up by the nearest neighbors. Often one can use a spectral “fingerprint” technique to identify the local bonding environment.

Another great asset of NEXAFS spectroscopy is its ***polarization dependence***. Linearly polarized X-rays are best suited for covalent systems like low-Z molecules, macromolecules and polymers, which possess directional bonds. In this case the directional electric field vector of the X-rays can be viewed as a “search light” that can look for the direction of chemical bonds of the atom selected by its absorption edge.

The remarkable capabilities of NEXAFS or the study of charge and spin phenomena in materials derive from the direct coupling of the X-ray electric field vector to the charge and the coupling of the X-ray angular momentum to the angular (orbital) momentum of the charge. The absorption processes are governed by electric dipole transitions that obey strict selection rules on angular momentum conservation

and couple different core shells to specific valence shells. In X-ray absorption, sensitivity to the spin arises indirectly from the coupling of the orbital moment to the spin moment in the valence shell through the spin-orbit coupling.

4. EXPERIMENTAL RESULTS AND DISCUSSION

4.1. New Ambient Pressure XPS Endstation at ALS Beamline 9.3.2

The design and construction of a new APXPS system at the Advanced Light Source (ALS) bending magnet beamline 9.3.2 with high electron transmission and detection efficiency to reduce radiation exposure and data acquisition time has been described in the first part of the presented section. Furthermore, the test results of one-dimensional imaging so called spectromicroscopy and angular modes have been demonstrated. These additional features enhance the ability of system to extract more information from detected PEs and study more complex materials under various catalytically and environmentally relevant conditions.

4.1.1. System Design

4.1.1.1. APXPS System Considerations

There are various multiple design criteria for an APXPS system in addition to those for XPS under ultrahigh vacuum (UHV) conditions. First and foremost, the UHV environment of the X-ray source must be separated from the elevated pressure of the analysis chamber. This is typically achieved by the use of a thin silicon nitride or aluminum window. Secondly, the analysis chamber must be separated from the electron detector, which operates in high vacuum. This can be accomplished by differential pumping through a series of apertures. The radius of the aperture between the analysis chamber and the first pumping section, R (Figure 4.1(b)), in large part defines the ultimate pressure limit of the system. R (typically 0.1–0.5 mm) determines the gas conductance from the analysis chamber into the analyzer lens column and also sets the minimum distance between the sample and aperture and therefore PE transmission through the gas. This minimum distance determines the upper limit of workable pressure.

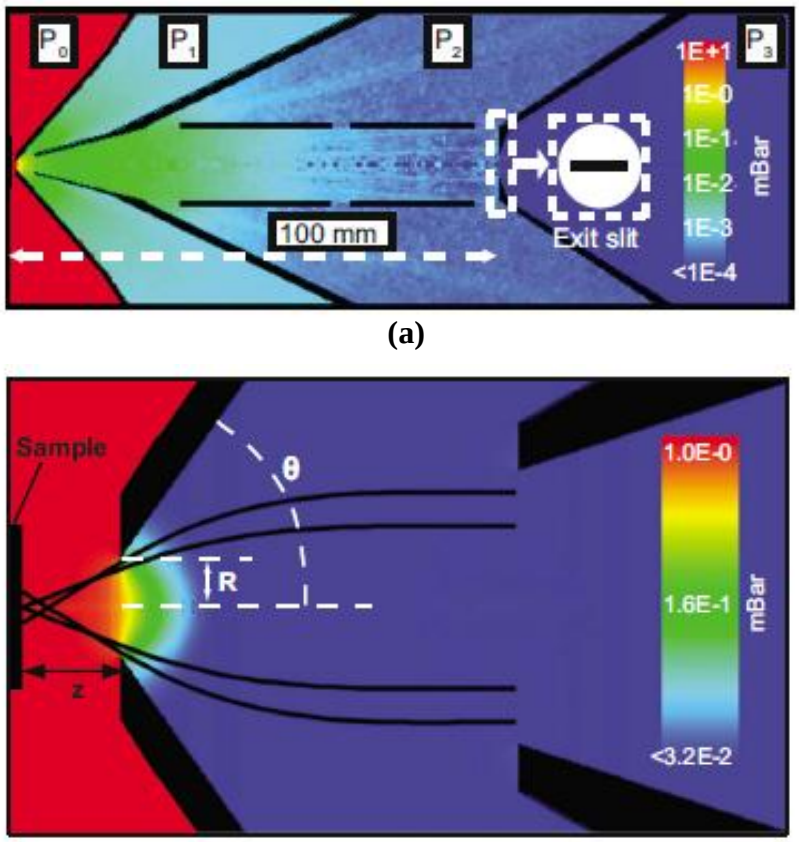

Figure 4.1. (a) Gas dynamic simulation of the complete prelens for P_0=10 mbar. (b) Pressure profile for P_0=1 mbar along the first 10 mm from the sample extending into the second differential pumping stage. Shown in black from left are the sample, first aperture (0 V), and second aperture (high voltage). Examples of extreme trajectories when the lens is set for high transmission are inserted. On the optical axis, and in the plane along the slit, take off angles of 23° will reach the detector. At a position 0.2 mm from the optical axis, and in the plane along the slit, take off angles of 28° will reach the detector

During the experiments, damage of samples resulting from irradiation must be considered for XPS and related spectromicroscopy techniques (Gregoratti et al. 2009). Decomposition of organic materials (Zubavichus et al. 2004), reduction of oxides (Ramsier et al. 1991), and charging of insulators and semiconductors lead to unwanted artifacts (Cazaux et al. 2009). APXPS introduces additional challenges when samples are analyzed in reactive gas environments: gas molecules and/or adsorbates are ionized by PEs and secondary electrons, inducing unwanted reactions and leading to surface modification. Additionally, APXPS experiments require

higher X-ray doses because of gas-phase PE scattering, so that optimized PE transmission is of even greater importance. Maximum PE transmission has been considered as a major design criterion of this endstation.

4.1.1.2. General Design

The R4000 HiPP system is based on a Scienta R4000 with a two-dimensional detector consisting of two multichannel plates (MCPs) coupled to a phosphor screen and charge-coupled device (CCD) camera. Furthermore, the electrostatic lens system is integrated to incorporate separated pumping sections within the lens housing. The outer stainless steel chamber extends from the fourth pumping stage to the port connecting the main analysis chamber with the preparation chamber. To enhance the energy and spatial/angular resolution, the system has μ-metal shielding from the analysis chamber to the entrance of the hemispherical analyzer to reduce the effects of external magnetic fields. The individual μ-metal sections are interconnected to form a closed shield. The shielding in the main chamber was Au coated to protect the Ni-rich alloy from corrosion by reactive gases. The first aperture is at the front end of a removable Au coated Ti cone with a radius of 0.425 mm. The size of the first aperture is a compromise between maximizing counts at low pressure (larger radius) and increasing the maximum pressure of the system (smaller radius). To match the spot size of beamline 9.3.2, a relatively large aperture size was selected. The typical X-ray spot size at beamline 9.3.2 is 0.5 mm(V)x1.5 mm(H), spreading out much further because of the 15° incident angle. As the X-ray spot size decreases with improved beamline refocusing optics, the aperture radius can be decreased, thereby increasing the pressure without sacrificing counts. The main chamber is equipped with a four-axis motor system for computer control of sample motion by step motors with submicron precision. The sample holder is a Thermionics STLC platen with a HeatWave ceramic coated button heater for oxidizing environments. A home-built manipulator is used in conjunction with VG Scienta Omniax xyz stages, and a Thermionics rotatable axis stage. The manipulator can be cooled by water, chiller fluid, or liquid nitrogen. The main chamber is also equipped to be backfilled with

gases to a few millibar during analysis. Sample cooling has been accomplished using a specially designed Peltier platen (Ogletree et al. 2009) and plans are currently underway to heat with a focused infrared laser to reduce background reactions during catalytic studies.

The system resides at bending magnet beamline 9.3.2 at the ALS. This beamline delivers soft X-ray light in the range 30–850 eV. The beamline, which must be maintained under UHV to avoid contamination of optical elements, is separated from the main chamber by a 2 mm x 2 mm x 100 nm thick Si_3N_4 window at a distance 3.0 cm from the sample. Usual operation of the storage ring at 500 mA and beamline exit slit at 30 μm, delivers a flux of $4.6x10^{10}$ photons s^{-1} at 500 eV using a 600 l/mm grating. A 100 l/mm grating provides light peaked at 100 eV. The energy resolution of the beamline is about $E/\Delta E$ = 3000 (Hussain et al. 1996).

For the preparation, cleaning, and study of well-defined samples, including single crystals and thin films, a preparation chamber has been built which includes ion sputtering (PHI 20-045), LEED (VG Microtech RVL900), and a thermal evaporator. Moreover, there are many ports on the preparation chamber that can be equipped with user-provided UHV equipment.

The pumping system of the APXPS endstation was designed to optimize the PE count rate while also providing the highest possible maximum pressure at the sample and a low pressure ($<3x10^{-6}$ mbar) at the detector. The system consists of five pumping systems separated by apertures and isolated using metallic C-ring seals.

The electron focusing of the spectrometer is achieved by using the Scienta R4000 spectrometer lenses as well as other additional lens elements in a prelens system. Using the current setup, the prelens has a working distance of 1 mm (maximum transmission mode) and focuses the PEs onto the focal plane of the R4000. The additional lens elements are controlled by the analyzer electronics and have been integrated into the lens tables of the R4000. Different lens tables have been developed to provide either: the largest energy range, highest transmission, optimal spatial resolution, or angular resolution.

4.1.1.3. Prelens Design

The first priority has been to develop a system for optimized PE transmission when the probed sample surface is at high pressure. The prelens geometry should therefore be able to lower the pressure over a very short distance while collecting a large fraction of the PEs. It is noteworthy that the optimal solution has to take into account the size of the excitation spot and the multidimensional geometry of the gas flow. Simultaneously, it is also important to design stable operating conditions, create flexibility in lens mode operation, maintain excellent energy resolution, and allow for the light beam to have an unimpeded path to the sample. The main objective has been to design a multifunctional system that is very flexible, gives a high experimental throughput, and maximum uptime.

We built and empirically tested the differential pumping performance of a number of simplified models of prelenses. Utilizing these models we have also been able to study the breakdown voltage for different pressures and gases. In addition, gas dynamic simulations based on Monte Carlo methods have been used to visualize the performance of the differential pumping system. These calculations have proven invaluable in guiding the prelens design. Figure 4.1(a) shows a gas dynamic simulation of the prelens geometry. To facilitate the calculations, a rotationally symmetric equivalent of the actual prelens geometry has been considered. The first aperture has a radius of 0.425 mm and the pressure behind the sample has been set to 10 mbar, which is higher than recommended for this aperture size. Moreover, some additional boundary conditions associated with the differential pumping have been set from empirical results. It has been found that a prelens geometry with a relatively large acceptance angle allows for attractive gas flow and optical properties. On the low pressure side of the first aperture, the gas can significantly expand in the radial direction, resulting in a steep pressure gradient of the gas expansion zone in the direction along the optical axis (Figure 4.1(b)). An open first cone also allows for the possibility to put a second conical lens element very close to the first aperture. There are several benefits of putting a lens element very close to the first aperture. Firstly, it allows the electron optics to control the trajectories very early in the path, making it

possible to keep the trajectories close to the optical axis. Secondly, a very efficient differential pumping stage is obtained which implies that most of the gas load is directed toward the first pump. Thirdly, this differential pumping stage has a high PE transmission without requiring a node of the electron trajectories. Because of the spherical aberrations inherent in electrostatic lens systems, good point-to-point imaging is limited to relatively small angular intervals. Furthermore, electrostatic lens systems inherently have strong chromatic aberrations. The position of a node will therefore be a function of the kinetic energy. This is especially important to consider when optimizing for high transmission with large pass energy, when a two-dimensional detector simultaneously collects over a large energy interval.

The second differential pumping stage consists of comprises additional lens elements and ends with an exit slit. The size of this slit is matched to the hemispherical analyzer entrance slit. The position of the exit slit is in the standard sample position of the R4000 lens. Under such scenario a well-matched exit slit gives sufficient differential pumping properties at this stage without reducing the electron throughput. Most importantly, the use of an exit slit provides the dynamical freedom necessary to operate complex lens modes stably and continuously over large energy ranges.

The prelens moves the effective source point of the R4000 lens 100 mm further from the analyzer and matches the size and angular divergence of the beam to the analyzer acceptance properties. In typical operation, a magnified image of the sample spot is created on the exit slit. Depending on the requirements of various experiments, magnifications ranging from two to six times can be achieved. The imaging properties of the prelens are best for a magnification of around five times. In the current design setup, the sample, first aperture, and exit slit of the prelens are all at ground potential, so that the prelens does not change the energy of the PEs. According to Liouville's theorem, the product of the spatial and angular lens magnifications is then unity. The R4000 lens will therefore receive PEs where the angular distribution has been compressed into a range that is well adapted to its normal operation parameters. For optimal transmission, the R4000 lens can be set to very efficiently focus such a distribution on the entrance slit of the hemispherical

analyzer using lens tables similar to those developed for large spots. Since the prelens can control the electron trajectories at such an early stage, a very large angular range can be transformed into a well collimated beam through the exit slit of the prelens (Figure 4.1(b)). Dependent of the chosen slit size and energy resolution, virtually all electrons that pass through the exit slit of the prelens will reach the detector. For kinetic energies below 500 eV and for spot sizes similar to the radius of the first aperture, the total transmission under UHV conditions of the system is not much different from that of a normal R4000 lens.

In order to calculate lens tables for more complex situations, the complete lens system must be treated by the optimization routines. Both imaging mode (with good linearity and constant magnification) and angular mode (with constant dispersion and good linearity of the dispersion) have been calculated to work over large energy ranges.

4.1.2. System Performance

4.1.2.1. Differential Pumping

Considered new APXPS endstation consists a differential pumping system that is different from the first prototype system (Ogletree et al. 2002) and qualitatively similar to those used in the second generation systems (Ogletree et al. 2002, Ogletree et al. 2009, Pantforder et al. 2005). In order to achieve the ideal gas pressure profile predicted by molecular flow through an aperture, the front aperture and first pumping stage have been specifically designed. Particularly, a Ti cone with 60° half-angle (θ, Figure 4.1(b)) and a thin aperture edge that causes rapid expansion of the gas after crossing the aperture plane has been selected. This profile has been modeled for 1 mbar gas at a sample surface 1 mm from the first aperture with R=0.425 mm as depicted in Figure 4.1(b).

The differential pumping system of the Scienta R4000 HiPP was testified with 250 l/s turbomolecular pumps on each of the first three pumping stages (since testing, a 250 l/s turbomolecular pump was added to the fourth stage). The pressure

was monitored in the first three pumping stages as well as near the detector, while N_2 was dosed into the main analysis chamber. When the pressure was approximately 8 mbar in the analysis chamber (P_0=8 mbar), the first and second stage pressures measured near the pump inlets were $P_1=2.9\times10^{-3}$ mbar and $P_2=4.4\times10^{-4}$ mbar, respectively. The pressure at the analyzer was $P_5=9.9\times10^{-6}$ mbar. A pressure drop of $\sim10^6$ between the main chamber and the analyzer is sufficient for pressures up to a few mbar.

Utilizing the nomenclature as proposed by Ogletree et al. (Ogletree et al. 2002), the maximum pressure for an APXPS system is when the effective path length for PEs through a pressure P_{max} is twice the electron mean free path ($\lambda_e=k_BT/P_{max.}\sigma_e$).Under these condition the measured intensity is roughly 13% of the intensity measured in vacuum (while this value is arbitrary, it serves as a good comparison between systems). It is important to note here that the gas pressure at the sample is at least 95 % of P_0, the sample must be at a distance greater than twice the first aperture radius ($z\geq-2R$). At this minimum distance, one obtains the expression $P_{max}\approx k_BT/R\ \sigma_e$. $P_{max}\approx2.3$ mbar can be achieved when R=0.425 mm for 400 eV PEs through oxygen gas at room temperature. When the system is used for spatial resolution, the optimum working distance is 1.9 mm=4.5R, which reduces the effective P_{max} to 0.9 mbar.

At a working distance of 1.9 mm, the effect of pressure on the PE count rate was determined by monitoring the Au 4f peak intensity of an Au thin film at incident photon energy 490 eV in an oxygen atmosphere over a range of pressures (Figure 4.2(a)). A fit of the data to

$$\ln(I/I_0) = -d_{eff}\,.\,\sigma_e\,.\,P_0/k_B\,.\,T \qquad (4.1.)$$

where $\sigma_e=4.3\times10^{-16}$ cm^2 for oxygen at 400 eV KE implies d_{eff}=2 mm (Figure 4.2(b)). This value can be compared with the effective path length under conditions of molecular flow for which

$$d_{eff} = (1/P_0)\int P(x)\,dx = \frac{1}{2}\left(\sqrt{1+z^2} - z\right) \qquad (4.2.)$$

where *z* is in units of R. At a working distance of 1.9 mm (z= −4.47R), d_{eff} (ideal)=1.92 mm (4.53R), which is within the uncertainty of the experimentally determined value of d_{eff}.

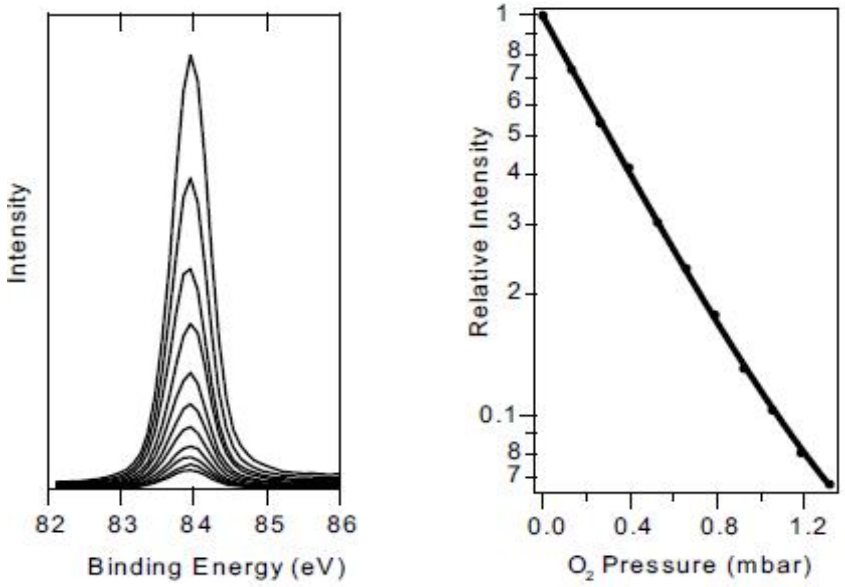

(a) **(b)**

Figure 4.2. (a) Spectra of Au $4f_{7/2}$ recorded at 490 eV and a working distance of 1.9 mm with increasing pressure from 10^{-9} to 0.8 mbar O_2 and (b) the relative intensity of the integrated Au 4f signal as a function of pressure, indicating an effective path length of 2 mm

4.1.2.2. Improved Transmission

The main objective of designing a new APXPS system to replace the old APXPS endstation at beamline 9.3.2 was to achieve an enhanced transmission and detection efficiency of PEs. Designing of new system has not only improved transmission and detection of PEs but also decrease data acquisition times. Above all it also alleviates problems associated with beam damage by decreasing the radiation exposure of a sample to achieve the same counting statistics. Additionally, faster acquisition time leads to improved temporal resolution for time-resolved studies.

In order to demonstrate above mentioned feature in designed new APXPS system, PE spectra of Ar 2p were recorded at a pressure of 0.25 mbar Ar with 100 meV steps and 200 ms dwell time. Figure 4.3 shows the comparison between three scans acquired using the high transmission mode with the new Scienta R4000 HiPP with an average of ten identical scans recorded with the old endstation at beamline 9.3.2 (Ogletree et al. 2002) (pass energy was set to achieve similar resolution). It can be clearly noticed that there is a significant improvement in detection efficiency and therefore counting statistics, providing faster acquisition times and decreased beam damage. Comparison suggests that even with only 30% of the counting time, the signal-to-noise is significantly improved. We estimate that the transmission of the R4000 HiPP endstation is well over an order of magnitude better than previously obtainable. For even faster acquisition times, the CCD detection can be utilized to record spectra in "fixed mode" rather than sweeping through an energy range.

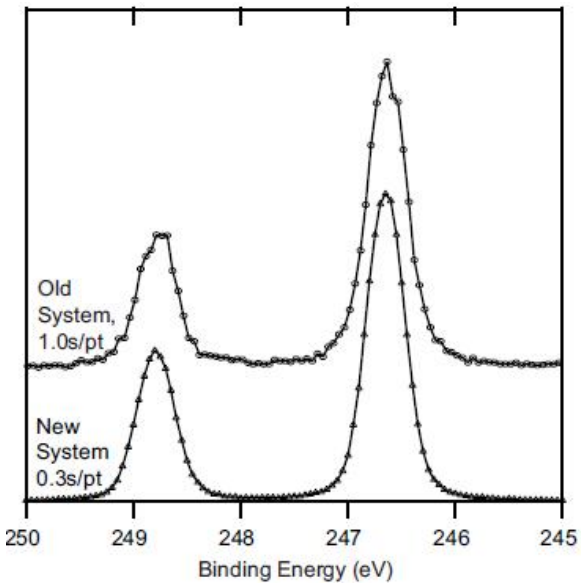

Figure 4.3. Ar spectra recorded at 500 eV and 0.25 mbar Ar using the old endstation at beamline 9.3.2 and the new Scienta R4000 HiPP, clearly demonstrating the enhanced signal to noise ratio of the new system due to optimized PE transmission

4.1.2.3. Spatial Resolution

In the present section, it has been described that using a dispersive hemispherical analyzer with two MCPs and CCD camera detector system, it is

possible to record data in two dimensions. One dimension represents the energy and the other may represent either spatial distribution or take-off angle. Within the field of view, electron counts can be averaged over a suitable energy range, while spatial or angular resolution can be obtained in the slit direction, depending on the lens table used for the spectrometer electrostatic lenses.

Lens tables has been developed in order to optimize the spatial resolution of the spectrometer and were verified by measuring a sample consisting of a 100 μm Au line that was e-beam deposited onto thermally grown SiO_2 on a Si wafer (Figure 4.4(b)). This particular sample was mounted in such a way that the Au line was perpendicular to the slit. Under such condition, the Au 4f photoemission lines appear only within a narrow range of the camera image (Figure 4.4(a)).

Experimental determination of the magnification was achieved by shifting the sample parallel to the slit with a calibrated step motor and recording the center of the Au 4f peak on the CCD camera (Figure 4.5). One camera pixel corresponds to ~1 μm, depending on the exact distance between the sample and first aperture; this agrees well with the calculated magnification of 34. After determining the magnification at each working distance, the spatial resolution of the spectrometer as a function of working distance (Figure 4.4(d)) and kinetic energy was determined. The best resolution achieved is ~16 μm. The estimation of the spatial resolution was performed at 100 eV pass energy.

The magnification and resolution of the electron lens system are determined by the electron lens table. Spatial resolution not being a primary design requirement of the prelens system, it is difficult to achieve good spatial resolution with a short working distance. The original calculation of the optimal resolution lens table led to a working distance of 3 mm. However, this distance is too far for the X-ray beam to reach the sample with the small Si_3N_4 window and the beam is cut off. Second obstacle with such a long working distance will greatly reduce the electron transmission when operating at elevated pressure. It has been found good imaging capabilities at a working distance of 1.9 mm through our experiments with the gold bar samples. The best resolution of ~16 μm was obtained at this distance (inset of Figure 4.4(d)) at photon energy of 450 eV (370 eV KE). The spatial resolution of the

system depends on the retardation ratio, and was determined to be 18, 16, and 28 µm at kinetic energy of 270, 370, and 570 eV, respectively. However, it is possible to improve the performance of this imaging mode by improving both the X-ray spot size and the electron lens table. We are currently working to obtain a shorter working distance, larger magnification, and smaller aberration. It seems that a smaller aperture size is essential requirement for any significant improvement.

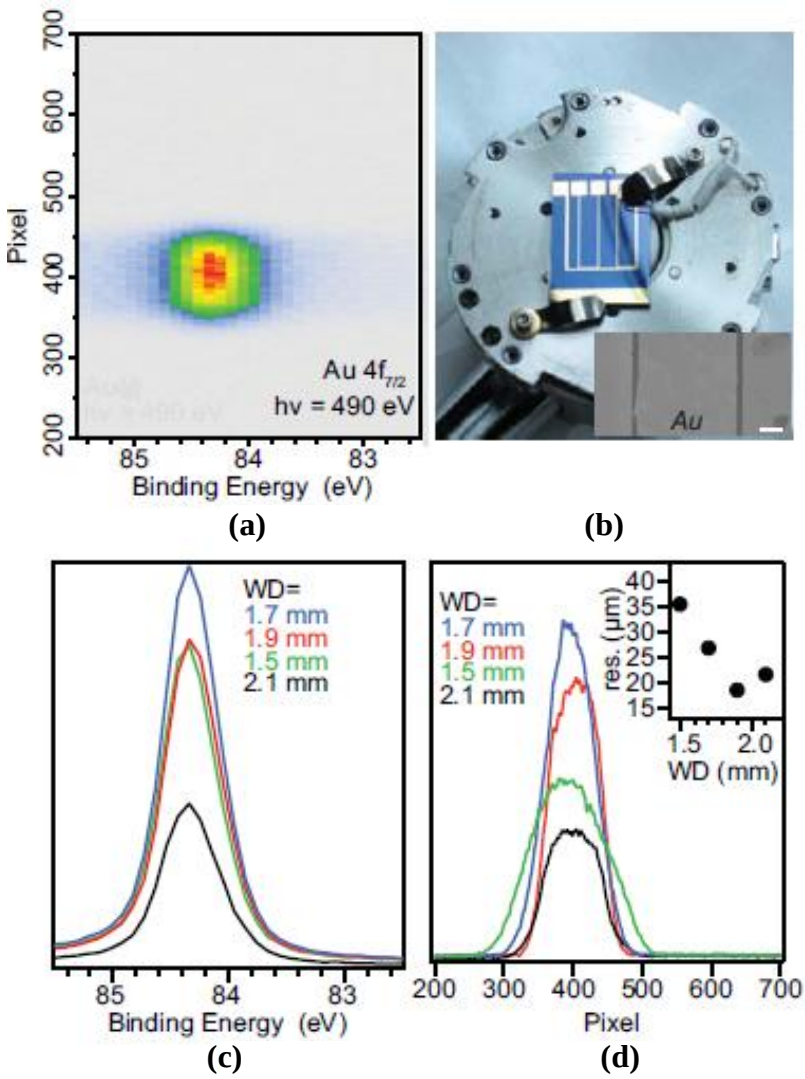

Figure 4.4. (a) CCD image of the Au $4f_{7/2}$ region of a 100 µm Au bar on SiO_2 shown in (b) (inset is an electron micrograph of the Au stripe). The image can be integrated across the x dispersion direction to yield PE spectra as shown in (c) or across the energy dispersion direction as shown in (d) to reveal spatial heterogeneity. The traces in (d) were used to calculate the spatial resolution as a function of working distance (see inset)

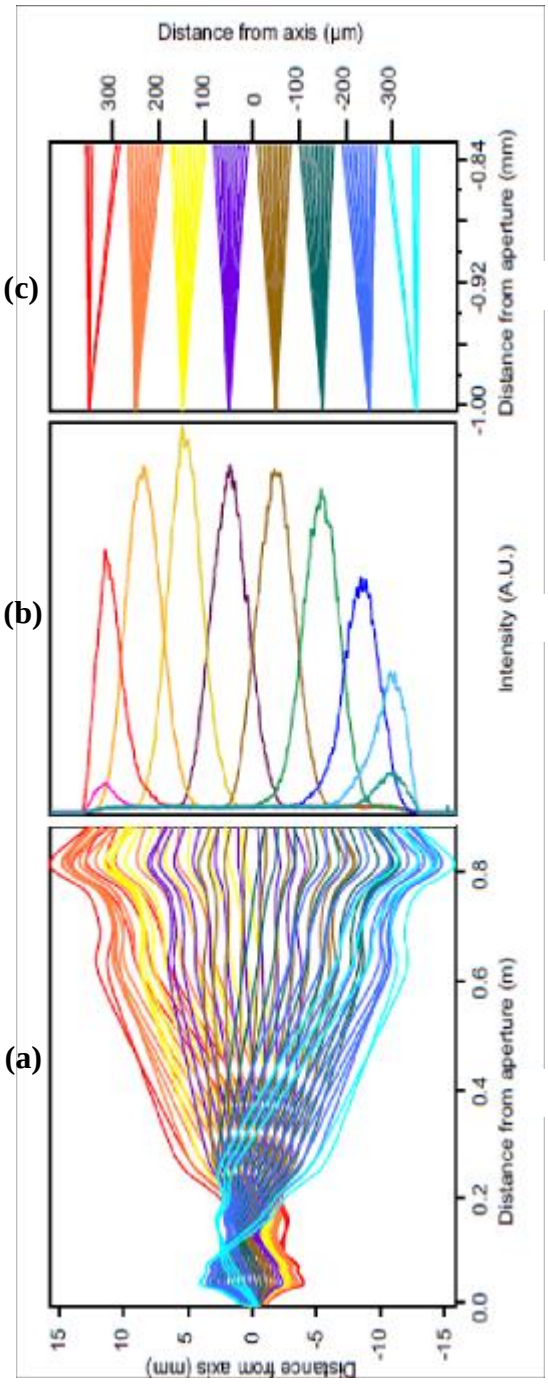

Figure 4.5. Spatially resolved XPS spectra can be recorded with resolution better than 20 µm without sacrificing energy resolution. (a) The modeled PE trajectories from the sample to the front plane of the hemispherical analyzer agree well with (b) spectra from a 100 µm Au bar. The initial parts of the PE trajectories are shown in (c)

4.1.2.4. Angular Resolution

Considering a novel design of the prelens system combined with numerical simulations and experimental testing of the electron lens table, the resulting ambient pressure ARPES (AP-ARPES) capabilities are promising.

Due to the limitation of azimuthal rotational degree of freedom of present manipulator attached to the system, the first AP-ARPES experiment on highly oriented pyrolytic graphite (HOPG) has been performed. It has been observed that azimuthally disordered HOPG graphite that sharp quasiparticle dispersions along the radial direction can coexist with a complete lack of dispersion along the azimuthal direction.

ARPES data were collected using the wide angular mode with acceptance angle of 25° and theoretical angular resolution of 0.5°. The sample used was a grade ZYA HOPG, obtained commercially from Structure Probe Inc. Prior to measurements, the HOPG sample was cleaved in air and transferred to the load lock. The sample was then transferred into the high pressure chamber under UHV.

Figure 4.6 shows an UHV ARPES intensity map taken at 120 eV photon energy as a function of binding energy and angle (in-plane momentum k), corresponding to a momentum cut along a random azimuthal direction through the point on the Fermi intensity map. Due to the azimuthal disorder of HOPG, the Fermi intensity map has a perfect circular pattern. A well-defined dispersions in excellent agreement with data collected using the Scienta R4000 at the same photon energy has been observed (Zhou et al. 2005), except with higher background intensity. This characteristic is mainly due to the large photon spot size (~500 μm×1.5 mm) and possible surface contamination from cleavage in air. Upon sample rotation in the theta direction, all these features in the intensity map shifted accordingly. This clearly demonstrates the linearity of the lens table over a large acceptance angle of +/−12° (comparison of Figures 4.6(a) and 4.6(b)).

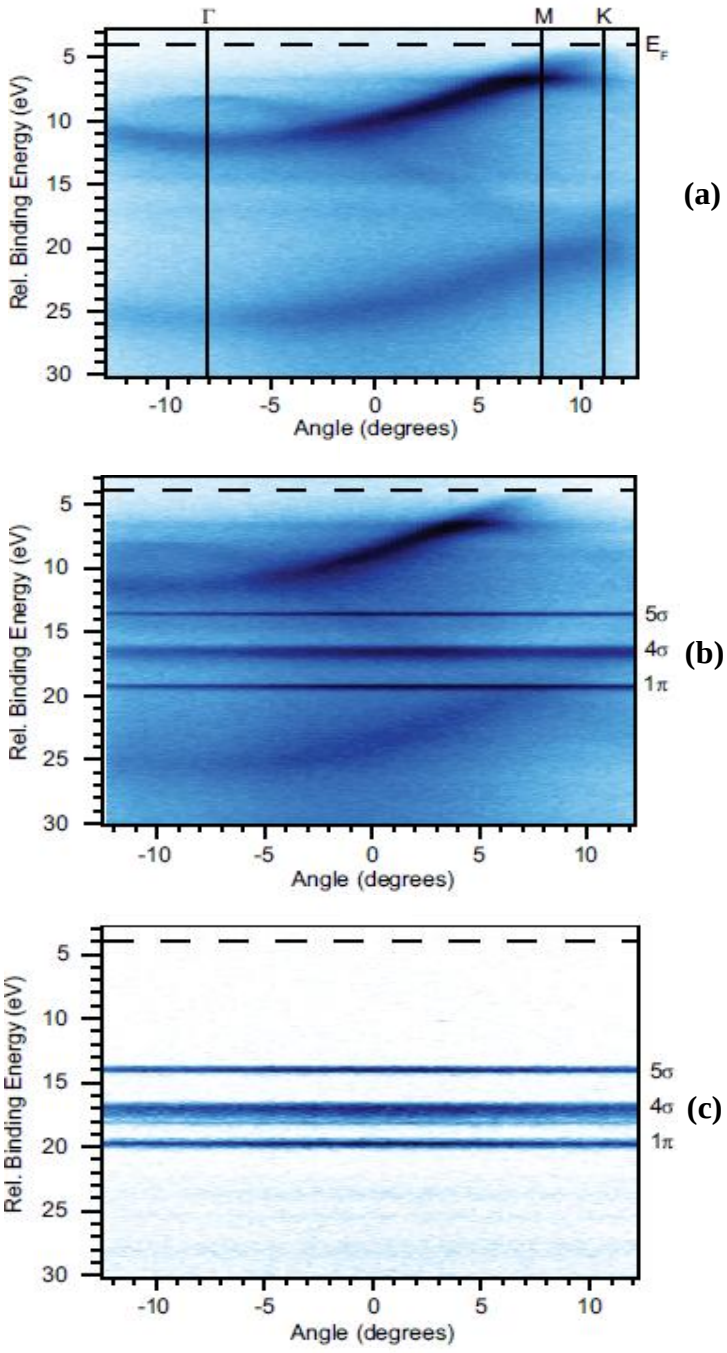

Figure 4.6. AP-ARPES of (a) HOPG, (b) HOPG in an atmosphere of 0.25 mbar CO, and (c) 0.25 mbar CO with no sample in front of the aperture. The sample was rotated 3° in theta between spectra (a) and (b). In both spectra, the Γ, M, and K points are clearly visible and in (b) and (c) the non-dispersive CO lines are also clearly observed

Figure 4.6(b) illustrates the same ARPES intensity map in a 0.25 mbar CO gas environments. It can be noticed that there is an increase in background noise, but

the energy dispersion of HOPG is still clearly visible. A direct comparison between Figures 4.6(a) and 4.6(b) suggests no significant pressure dependence modification of the HOPG dispersion. Three major non-dispersive features appear at 9.5, 12.5, and 15.3 eV (referenced to the Fermi level) due to 5σ, 1π, and 4σ PEs from gas phase CO.

4.2. In-situ Study of the Catalytic Oxidation of CO on a Pt(110) Surface Using Ambient Pressure X-ray Photoelectron Spectroscopy

In this section, we present Ambient Pressure X-ray Photoelectron Spectroscopy (APXPS) and Mass Spectrometry experiments on CO and O_2 co-adsorption and the catalytic oxidation of CO over a Pt(110) surface under various pressures of CO and O_2 (up to 250 mTorr). We observe that there is no surface oxide formation on Pt under our reaction conditions. However, CO oxidation in this pressure (<500 mTorr), O_2 to CO ratio (<10), and temperature (150 °C) regime is consistent with the Langmuir–Hinshelwood reaction mechanism. Our experimental findings provide in-situ surface chemical composition data of the catalytic oxidation of CO on Pt (110) at total pressures below 1 Torr.

4.2.1. Introduction

Platinum based catalysts have many applications. As a catalyst in the chemical reactions platinum has been employed since the early 1800s, when platinum powder was used to catalyze the ignition of hydrogen. The most important application of platinum is in automobiles as a catalytic converter, which allows the complete combustion of low concentrations of unburned hydrocarbon from the exhaust into carbon dioxide and water vapor. Platinum is also used in the petroleum industry as a catalyst in a number of separate processes, but especially in catalytic reforming of straight runflammable liquid mixtures of hydrocarbons (i.e. a distillation product from petroleum or coal tar boiling in a certain range and containing certain hydrocarbons) into higher-octane gasoline which becomes rich in aromatic compounds. PtO_2, also known as Adams' catalyst, is used as a hydrogenation catalyst, specifically for vegetable oils (Krebs 1998). Platinum metal also strongly catalyzes the decomposition of hydrogen peroxide into water and oxygen gas (Petrucci 2007). Platinum is a good catalyst for the production sulphuric acid and for the production of nitric acid via NH_3 oxidation to NO_2. Another application is the conversion of alcohol to formaldehyde. Moreover platinum is a

catalyst in the production of biodegradable elements for household detergents. It is also one of the most used materials in electrocatalysis. Additionally, platinum is used to make jewelries, electrodes, noncorrosive laboratory containers, medical instruments, dental prostheses, electrical contacts, and thermocouples.

In the past, the formation of oxides on transition metal surfaces has been actively investigated because of its importance in exploring the heterogeneous catalytic reactions on metal surfaces (Ertl 1994, Somorjai 1994). Various high vacuum ($<10^{-6}$ Torr) surface science techniques are utilized to explore the mechanism and kinetics of oxidation and heterogeneous catalysis on model surfaces. It has been reported that low pressure results can often be extrapolated across a wide pressure range (Stoltze et al.1985). However, few cases exist where violation of such an extrapolation is observed. Recently, the development of advanced ***in situ*** surface science techniques, such as synchrotron based APXPS (Ogletree et al. 2002, Ketteler et al. 2005, Salmeron et al. 2008), high pressure scanning tunneling microscopy (HP-STM) (Österlund et al. 2001, Hendriksen et al. 2002), surface X-ray diffraction (Ackermann et al. 2005), sum frequency generation spectroscopy (Su et al. 1996, Rupprechter et al. 2008) and other optical imaging techniques (Rotermund et al. 1995), has rejuvenated research in this field. Particularly, the study of surface oxides on Pt(110) (Hendriksen et al. 2002, Ackermann et al. 2005, Rotermund et al. 1995, Salmeron et al. 1981, Chen et al. 2007) has received much attention due to its unique oscillatory behavior of surface morphology under CO oxidation reaction conditions (Rotermund et al. 1995). Utilizing a combined HP-STM and mass spectrometer, Hendriksen and Frenken (Hendriksen et al. 2002) demonstrated the existence of roughening of the Pt(110) surface during CO oxidation at 425 K, pressures near 0.5 bar and an O_2/CO ratio >45. The formation of surface roughening, assumed to be Pt oxide, is observed when the reaction rate is enhanced. Later, using high pressure X-ray diffraction and density functional theory (DFT) model calculation, Ackermann et al. (Ackermann et al. 2005) proposed that the surface oxide formed on the Pt(110) is stabilized by carbonate species. One important conclusion drawn from these studies is that CO oxidation under high pressure (~1 bar) and at a high O_2/CO ratio may follow the Mars–Van Krevelen mechanism (Mars et al. 1954) rather than the

Langmuir–Hinshelwood (L–H) mechanism (Campbell et al. 1980). Furthermore, the characteristics of Pt oxide were also explored with DFT calculations under elevated pressure. Wang et al. (Wang et al. 2005) reported the importance of a phase boundary between metal and gas during CO oxidation. It was predicted that the surface oxides provide lower activation barriers for the CO redox process, which favors the Mars–Van Krevelen mechanism under highly reactive conditions.

This part of dissertation deals with the study of the catalytic oxidation of CO on a Pt(110) surface under various pressures of CO and O_2 gases (10–250 mTorr) at 150–200 °C using APXPS, a technique which is highly sensitive to the chemical state of catalysts and platinum surface atoms and surface adsorbates. We will start this section with a brief description of catalyst and heterogeneous catalysis. Then, we discuss the CO interaction with platinum group metals surfaces and describe the basic reaction mechanisms behind the CO oxidation on Pt-group metals.

4.2.2. Catalysts

Catalysis is a term coined by Baron J. J. Berzelius in 1836 to describe the property of substances that causes or increases the rate of the reaction at which a chemical system approaches equilibrium, without itself being substantially consumed in the process. A broad definition of catalysis also allows for materials that slow the rate of a reaction. Whereas catalysts can greatly affect the rate of a reaction, the equilibrium composition of reactants and products is still determined solely by thermodynamics. Most chemical reactions used in today's chemical plants would proceed slowly without catalysts. Such slow reactions could not be detected even when the reaction conditions (such as temperature and pressure) make them thermodynamically favorable. Catalysts play important role in the chemical and petrochemical industry to protect our environment by converting polluting waste gases into less harmful products. In the human body, enzymes are naturally occurring catalysts responsible for many essential biochemical reactions.

A catalyst produces its effect by changing activation barriers. It changes neither the thermodynamics of the reaction nor the equilibrium composition. Because

of the kinetics of a reaction is determined by the relative heights of activation barriers, the equilibrium constants are determined by the relative energetic positions of the initial and final states. The acceleration of reactions is not the only key factor in catalytic activity. If catalysts only accelerated reactions, they would not be nearly as important or as effective as they actually are. Catalysts can be designed not only to accelerate reactions. The best of them can also perform this task *selectively*. In other words it is important for catalysts to speed up the right reactions, not simply every reaction. The reaction with a solid catalyst generally occurs at, or within several atomic distances of the catalysts surface. The catalyst surface can play several important roles in order to accelerate the reaction (Ackermann, 2007). These are:

(a) The surface offers a two dimensional (2D) matrix of adsorption sites which acts as a simple trap where the chance for the different species from the gas phase to come into contact with each other is much greater than in the gas phase.

(b) The catalyst surface alters (lowers) the energetic barrier that must be overcome to go from the reactants to the reaction product. This effectively lowers the temperature at which the reaction will run, or equivalently accelerates the reaction at a given temperature, as long as the original energetic barrier was larger or in the order of kT.

(c) The catalyst surface alters one or more of the reactants, creating an intermediate species which is necessary for the reaction to run. This is for example the case with dissociative adsorption: where atomic oxygen is virtually absent in the gas phase at 500 K in 1 bar of O_2, it is present due to dissociative adsorption on the surface of catalysts employed for CO oxidation in these conditions.

In all cases one or more species from the gas phase adsorb onto the catalyst surface, diffuse on the surface, react, and leave the surface in the form of the reaction product. All three processes just mentioned depend strongly on the interaction between the molecules and the surface, which is determined by the specific adsorption energy of a certain molecule or atom with a specific surface. In the combination of adsorption and subsequent desorption of the molecules lies a balance

between high and low adsorption energy. For very high adsorption energies, the surface will accumulate many reactants, but might be very slow in releasing the reaction product, effectively blocking the surface for the adsorption of new reactants. For very low adsorption energies, the reactants might adsorb and desorb so rapidly that they will leave the surface before reacting to the reaction product. This effect is often plotted in so called 'volcano plots' where the reactivity is plotted versus the binding energy of different catalyst. The optimal catalyst, at the top of the volcano curve, is the one with the correct balance between adsorption and desorption for the reactants and reaction product (Ertl et al. 1997, Somorjai 1994).

4.2.3. Heterogeneous Catalysis

One of the great motivations for studying chemical reactions on surfaces is the will to understand heterogeneous catalytic reactions. Heterogeneous catalysis is the basis of the chemical industry. Heterogeneous catalysis is involved in literally billions of pounds worth of economic activity. Neither the chemical industry nor civilization would exist, as we know them today, if it was not for the successful implementation of heterogeneous catalysis.

Heterogeneous catalysts are distinguished from ***homogeneous catalysts*** by the different phases present during reaction. Homogeneous catalysts are present in the same phase as reactants and products, usually liquid, while heterogeneous catalysts are present in a different phase, usually solid. Heterogeneous reactions occur in systems in which two or more phases are present, for instance, solids and liquids or gases and solids. The reactions occur at the interface between these phases. The interfaces are where the two phases meet. Liquid/solid and gas/solid are of particular interest because the surface of a solid gives us a place to deposit and immobilize a catalytic substance. By immobilizing the catalyst, we can ensure that it is not washed away and lost in the stream of products that are made. However, surfaces are of particular interest not only because they are where phases meet and because they give us a place to put catalysts. The surface of a solid is inherently different from in the bulk. Therefore we should expect the chemistry of the surface to

be unique.

The most common reactions within heterogeneous catalysis involves adsorption of reactants from a gas phase onto a solid surface, surface reaction of adsorbed species, and desorption of products into the gas phase. Due to the slow mass transport processes in the solid phase, the chemical reaction usually takes place at the surface of the solid catalyst (at the gas/solid interface). Clearly, the presence of a catalyst provides an alternative sequence of elementary steps to accomplish the desired chemical reaction from that in its absence. If the energy barriers of the catalytic path are much lower than the barrier(s) of the non-catalytic path, significant enhancements in the reaction rate can be realized by use of a catalyst.

In Figure 4.7, a proposed thermochemical kinetic profile for the platinum-catalyzed oxidation of carbon monoxide is depicted. The first step in the profile represents the adsorption of carbon monoxide and O_2 onto the catalyst. In this case, adsorption of oxygen molecule involves dissociation into individual oxygen atoms on the Pt surface. The product is formed by addition of an adsorbed oxygen atom (O_{ads}) to an adsorbed carbon monoxide molecule (CO_{ads}). The final step in the catalytic reaction is desorption of adsorbed carbon dioxide (CO_{2ads}) into the gas phase. The Pt catalyst facilitates the reaction by providing a low energy path to dissociate O_2 and form the product. The non-catalytic route shown in Figure 4.7 is extremely slow at normal temperatures due to the stability of O_2 molecules.

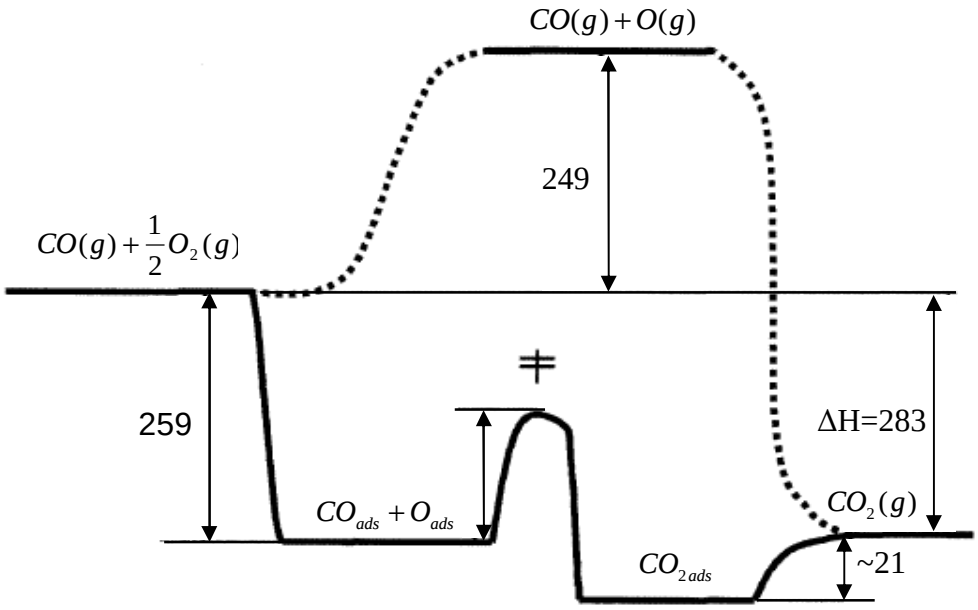

Figure 4.7. Schematic energy diagram for the oxidation of CO and a Pt catalyst (Ertl 1983). All energies are given in kJ mol^{-1}. For comparison, the heavy dashed lines show a non-catalytic route

The main advantage of using a heterogeneous catalyst is the relative ease of catalyst separation from the product stream that aids in the creation of continuous chemical processes. Additionally, heterogeneous catalysts are typically more tolerant of extreme operating conditions than their homogeneous analogues. Heterogeneous catalysis plays a key role in the large-scale production of liquid fuels, pharmaceuticals, plastics, and many other chemicals. Another important application is pollution control, particularly in the automotive industry. The main emissions of a car engine are nitrogen gas (N_2), carbon dioxide (CO_2) and water vapor (H_2O). These emissions are mostly benign, although carbon dioxide emissions are believed to contribute to global warming. Because the combustion process is never perfect, some smaller amounts of more harmful emissions are also produced in car engines.

The three-way catalyst used to efficiently remove harmful components from the exhaust gas of car engines is one of the best-known important applications of heterogeneous catalysis. Most modern cars are equipped with three-way catalytic converters that refer to the three regulated emissions it helps to reduce. This catalyst exhibits high rates for the conversion of gases such as carbon monoxide CO, nitrogen oxides NO_x, and hydrocarbons or volatile organic compounds. These gases cause

harmful effects for human health as well as environment. The main reactions involved in these three gases can be given as follows:

$$CO + \frac{1}{2}O_2 \rightarrow CO_2 \quad (4.3.)$$

$$NO + H_2 \rightarrow \frac{1}{2}N_2 + H_2O \quad (4.4.)$$

$$NO + CO \rightarrow \frac{1}{2}N_2 + CO_2 \quad (4.5.)$$

$$H_2 + \frac{1}{2}O_2 \rightarrow H_2O \quad (4.6.)$$

$$Hydrocarbons + O_2 \rightarrow H_2O + CO_2 \quad (4.7.)$$

The final products on the basis of reactions given above should be harmless. These reaction products are thermodynamically favored at typical exhaust temperatures, e.g. 770 K. The noble metals such as platinum, rhodium, and specially palladium are the three-way catalysts. Among them, platinum is used in the second stage of the catalytic converter as an oxidation catalyst to reduce the unburned hydrocarbons and carbon monoxide by burning (oxidizing) them.

4.2.4. Classification of Reaction Mechanisms of CO Oxidation on Platinum Metals

The interaction of CO with platinum group metals has been intensively studied in the last decades. The general consent is that carbon monoxide adsorbs as a molecule on such a metal with the carbon atom directed towards the surface and it can coordinate several geometries. The Blyholder model that invokes donor-acceptor mechanism (Blyholder 1964) describes the CO bonding to metal surfaces. In this model, the bonding occurs through an electron transfer from the highest filled molecular orbital of CO (5σ) to unoccupied metal orbitals, essentially d orbitals, with back-donation occurring from occupied metal orbitals to the lowest unfilled (2π)

orbital of CO. In Figure 4.8, a schematic diagram of CO bonding to a metal is shown (Bobaru 2006). In CO the molecular orbitals are: $1\sigma^2\ 2\sigma^2\ 3\sigma^2\ 4\sigma^2\ 1\pi^4\ 5\sigma^2\ 2\pi^*$. The 4σ orbital is localized on the oxygen atom while the 5σ orbital is localized on the carbon atom and both of these orbitals are non-bonding. The empty 2π* anti-bonding orbital is also available to take parting the interaction with the surface. This combination of σ and π orbitals of CO in the interaction with the surface is called synergic bonding. In the case of molecularly chemisorption of CO, a covalent bond is form by donation of electrons from the 5σ orbital to a vacant metal d orbital (Figure 4.8(a)). At the same time, the full d orbitals are able to donate electron density into the vacant 2π* orbitals (Figure 4.8(b)). On adsorption the situation is analogous (Figure 4.8(c)).

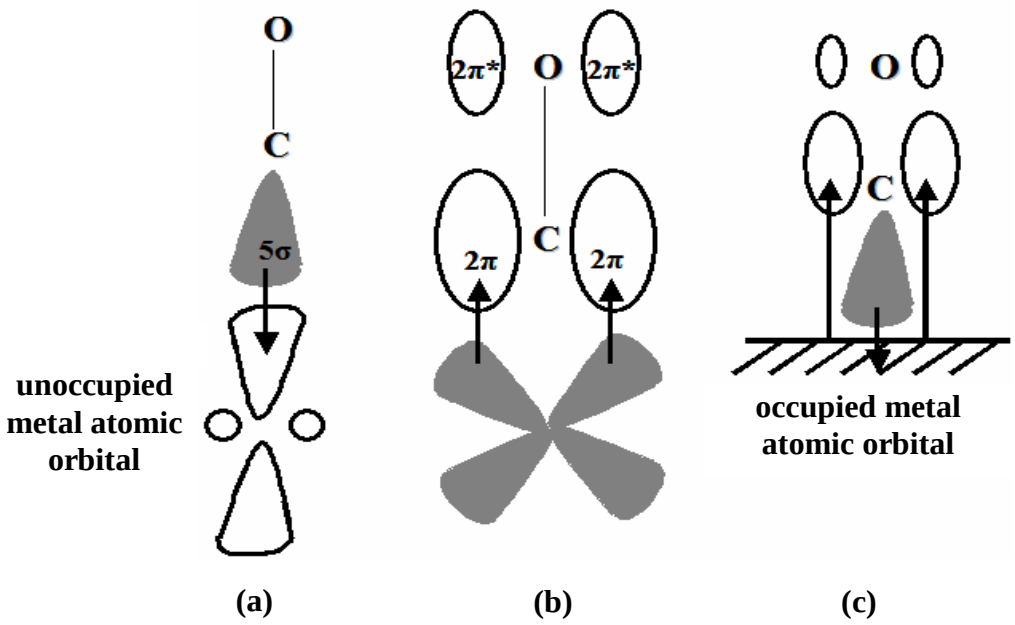

Figure 4.8. A schematic diagram of synergic bonding of CO to a metal (adapted after reference (McCash 2002))

The strength of the CO-metal bond depends on the nature of the adsorbent metal, the crystallographic orientation of the surface, and the geometric location of the adsorbed molecule on a given single crystal plane (Boudart et al. 1984, Nieuwenhuys et al. 1993).

Three typical adsorption positions for CO molecules are usually considered on a metal surface: on-top, bridge-bonded, and threefold-coordinated. Figure 4.9 illustrates several adsorption positions. CO molecule on platinum metals adsorbs more strongly in the on-top position than in the bridge position.

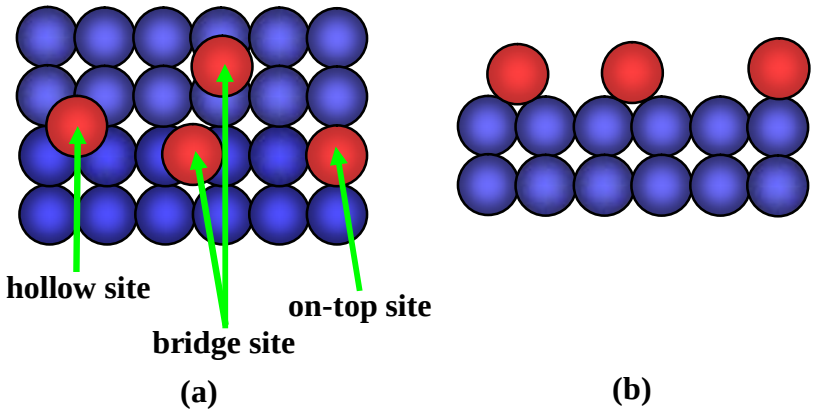

Figure 4.9. Adsorption sites (a) top view (b) side view

Much of the present-day fundamental understanding of heterogeneous catalysis has been obtained by studying simplified model catalysts. One of the most studied subjects in surface chemistry as a model system of heterogeneously catalysed reactions is CO oxidation on platinum metal surfaces. Several mechanisms that one can imagine for CO oxidation on a metal surface are proposed. Here, three most popular ones are briefly discussed.

4.2.4.1. Langmuir-Hinshelwood (L–H) Mechanism

L–H mechanism is the most common surface reaction mechanism for CO oxidation over platinum group metal catalysts. In this reaction scheme four different elementary reaction steps are concerned. First, both reactants (CO and O_2) from the gas phase are adsorbed on the surface of the catalyst which is assumed to be a perfectly flat isotropic surface, consisting of fully equivalent adsorption sites for both reactants. Then O_2 dissociates on the surface. In the third step, an oxygen atom recombines with CO to produce CO_2. In final step, the CO_2 molecule desorbs to the gas phase. The mechanism is explained in Figure 4.10.

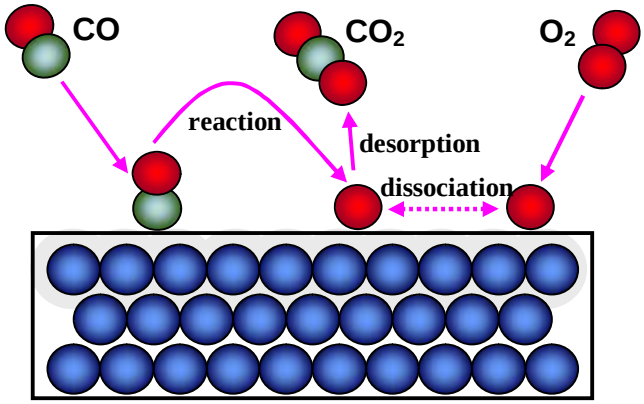

Figure 4.10. Schematic representation of the Langmuir-Hinshelwood (L–H) mechanism

4.2.4.2. Eley-Rideal (E–R) Mechanism

E–R mechanism is another common surface reaction proposed for catalytic CO oxidation. In this mechanism, surface reaction does not involve two adsorbed surface species. Only one of both species is adsorbed on the surface. If a gas molecule strikes a previously adsorbed molecule there is a possibility that a surface reaction takes place and the product escapes directly into the gas phase (Figure 4.11).

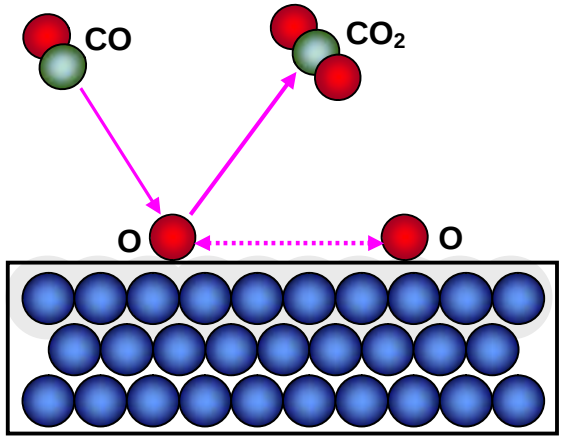

Figure 4.11. Schematic representation of the Eley-Rideal (E–R) mechanism

4.2.4.3. Mars-Van Krevelen (MvK) Mechanism

MvK mechanism is a last class of reaction for CO oxidation which is similar to the E–R mechanism. In this mechanism, one of the species forms a compound

with the catalyst, which then acts as a source for the other species to react with. The catalyst itself participates more actively in the reaction, playing the role of intermediate product rather than merely a suitable substrate. Hendriksen and Frenken have provided direct evidence that the Mars-Van Krevelen mechanism is responsible for the oxidation of CO over the (110) orientation of platinum at atmospheric pressure (Hendriksen et al. 2002). In later publications, it has been shown that the same mechanism is also active in the CO oxidation over the (110) surface of palladium (Hendriksen et al. 2004). In the mechanism, the following steps take place (Figure 4.12): First, the metal will oxidize in an oxygen rich environment, i.e. at a high partial pressure of O_2, and at elevated temperatures. After the oxide has been formed at the surface, CO molecules adsorbed on the oxide from the gas phase will react with oxygen atoms from the oxide to produce CO_2. The resulting oxygen vacancies are refilled rapidly by oxygen from the gas phase.

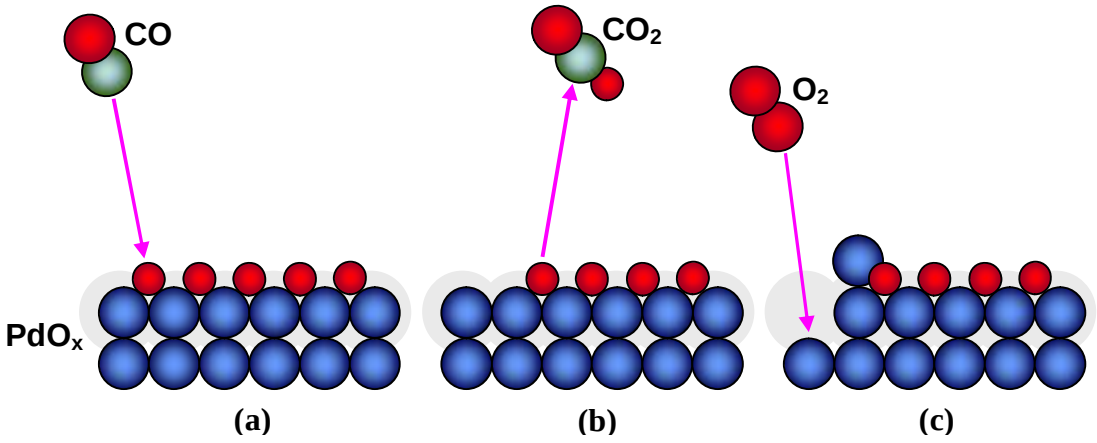

Figure 4.12. Schematic representation of the Mars-Van Krevelen (MvK) mechanism. The blue balls represent Pd atoms. Small red balls correspond to the oxygen atoms from the palladium oxide. (a) PdO_x and a CO molecule diffusing to the surface. (b) Reaction between the CO molecule and one oxygen atom from the palladium oxide, the formation of the CO_2 molecule and its diffusion in the gas phase. (c) Diffusion of the left coordinated Pd atom and refilling of the vacancy left by the oxygen atom, with oxygen from the gas phase (Bobaru 2006)

4.2.5. Crystal Structure of Clean Pt(110)

Much of the present-day fundamental understanding of heterogeneous catalysis has been obtained by studying simplified model catalysts at well-defined conditions. The most thoroughly studied system is CO oxidation on platinum (Pt). The crystal structure of Pt is face-centred cubic with a lattice parameter at 20°C of 3.92 Å. Among the low- index surfaces of platinum, the (110) plane is the most thoroughly studied system for CO oxidation. Surface atoms on (110) are seven-coordinate while atoms of the second layer have 11 nearest neighbors. Figure 4.13 shows a ball model of unreconstructed and (2 × 1) reconstructed Pt (110) surface.

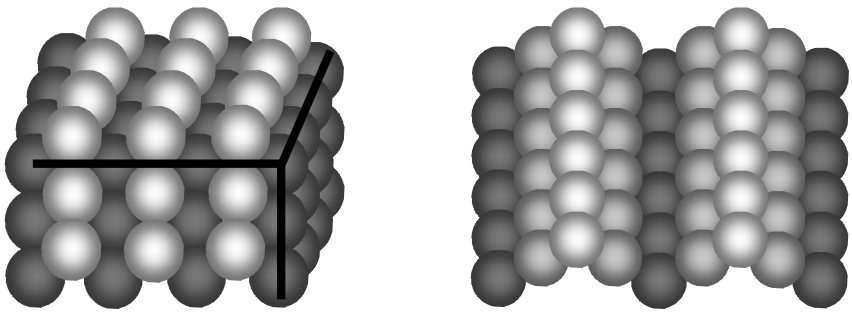

Figure 4.13. The plan and side view of the (110) surface of a platinum crystal, and the Pt(110)-(2 × 1) reconstructed surface represented as a ball model

4.2.6. Experimental Procedure

APXPS experiments were performed at Beamline 9.3.2 at the Advanced Light Source. The apparatus (Ogletree et al. 2002) consists of two connected vacuum chambers: one for sample preparation and other for analysis. The design of the spectrometer consists of a chamber with a differentially pumped electrostatic lens system that focuses the electrons emitted from the sample onto the focal plane of a hemispherical PHI-360 SCA electron energy analyzer (Ogletree et al. 2002, Salmeron et al. 2008).

A Pt(110) single crystal from Matek, polished on both sides, was used in present study. After repeated cycles of Ar^+ sputtering and oxygen annealing, and a final annealing above 750 °C in vacuum in the sample preparation chamber, the sample was transferred in vacuum to the high pressure cell in the analysis chamber.

The sample surface was checked with XPS to confirm the absence of contaminants. The (2 × 1) reconstruction of the surface was observed with low energy electron diffraction (LEED) and STM in a separate UHV system after identical sample preparation. Photoelectron spectra of the C1s, O1s and Pt4f core levels were recorded at photon energies of 540, 800 and 340 eV, respectively, corresponding to approximately the same photoelectron kinetic energy (~270 eV) to ensure the same probe depth sensitivities.

CO (Air Gas, UHP) and O_2 (Air Gas, UHP) are connected to a gas manifold via UHV leak valves. The gases are premixed in the manifold and delivered to the high pressure cell through a vacuum gate valve. Calibrated Baratron and Convectron gauges are used to monitor the total pressures inside of the high pressure cell and the gas manifold, respectively. During the reaction, XPS has been used to determine the chemical composition of the Pt(110) surface. Simultaneously, using an Ametek Dycor LC100 residual gas analyzer (RGA) reactivity of the reaction has been monitored. The RGA is attached to the second differential pumping stage behind the front nozzle (Ogletree et al. 2002). RGA signals are proportional to the gas pressures in the high pressure cell (Vass et al. 2008); thus one can calibrate the RGA signals with the Baratron readings in the high pressure cell to obtain the partial pressure of each gas.

4.2.7. Results and Discussion

The C1s, O1s and Pt4f spectra of the Pt(110) surface under different CO and O_2 pressures and at different temperatures is shown in Figure 4.14. Using different photon energies to ensure the same surface sensitivity, each core levels have been analyzed. When 200 mTorr CO was added to the high pressure cell, a broad peak that can be de-convoluted into two peaks (Ertl 1994) appeared in the C1s spectrum (Spectrum A) with binding energies of 286.0 ± 0.1 and 286.7 ± 0.1 eV. And two distinct peaks (Ertl 1994) appeared in the O1s spectrum (Spectrum A), with binding energies of 531.0 ± 0.1 and 532.7 ± 0.1 eV. We assigned these peaks to CO molecules adsorbed on bridge sites and on-top sites, respectively. These binding

energies are in good agreement with CO adsorption experiments under UHV conditions (Björneholm et al. 1994).

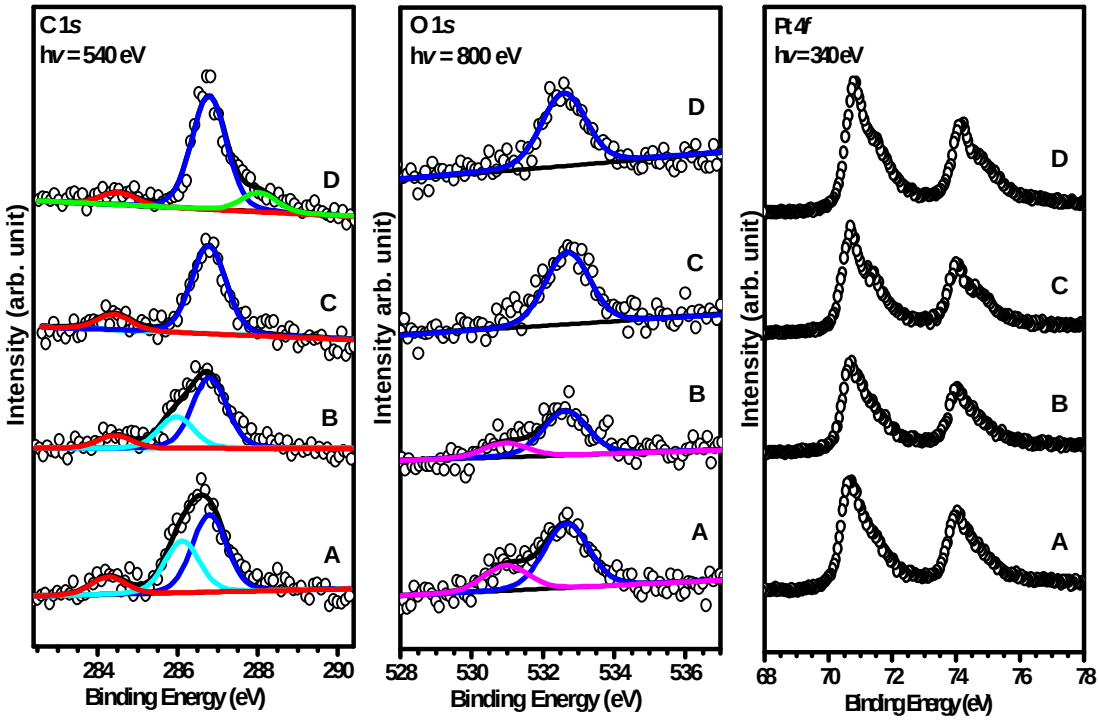

Figure 4.14. The C1s, O1s and Pt4f core level spectra of the Pt(110) surface under various conditions. A: 200 mTorr CO at room temperature; B: 200 mTorr CO + 200 mTorr O_2 at room temperature; C: 200 mTorr CO + 200 mTorr O_2 at 100 °C; D: 200 mTorr CO + 200 mTorr O_2 at 150 °C

The Pt4f peak of the CO covered surface is broader compared to the clean Pt surface due to CO adsorption. Upon addition of 200 mTorr O_2, the population of CO on bridge sites decreased (Figure 4.14, Spectra B). The area ratio between on-top and bridge sites changed from 2.5:1 to 3.1:1 without the appearance of additional peaks. This is consistent with asymmetric inhibition of CO and O_2 on Pt(110) (Krischer et al. 1997). Thereafter, the sample was subsequently heated to 150 °C under the same CO and O_2 pressure. Most bridge site CO molecules were removed above 100 °C and only on-top CO remained (Spectra C). Upon further heating, CO_2 was first detected at 120 °C. At 150 °C, the surface was still CO covered. However, a new peak at 287.9 eV appeared in the C1s spectrum at the high binding energy side of the on-top CO peak. This peak was only observed during CO oxidation (i.e. when CO_2

formation was observed). The origin of such a characteristic is not completely known, though it may belong to an intermediate reaction (Ackermann et al. 2005). Although it is similar to the CO vibrational fine structure, the intensity is much larger than what has been reported earlier (Fohlisch et al. 1998).

The sample temperature was maintained at 150 °C during the entire CO oxidation experiment. Figure 4.15 illustrates the reaction data, i.e., the partial pressures of CO, O_2, and CO_2 gases during CO oxidation. By controlling the CO pressure, we can switch the reaction conditions from a CO rich to an O_2 rich environment and vice versa. In each region, XPS data (Figure 4.16) was collected after the pressure stabilized. First, we introduced 180 mTorr O_2 into the high pressure cell (Region A), creating a Pt surface that is covered with chemisorbed atomic oxygen (Li et al. 2004). Only one O1s peak at 529.7 eV, belonging to chemisorbed oxygen, is observed (Freyer et al. 1986). A corresponding high binding energy shoulder also appears in the Pt4f spectrum (Wang et al. 2005, Björneholm et al. 1994).

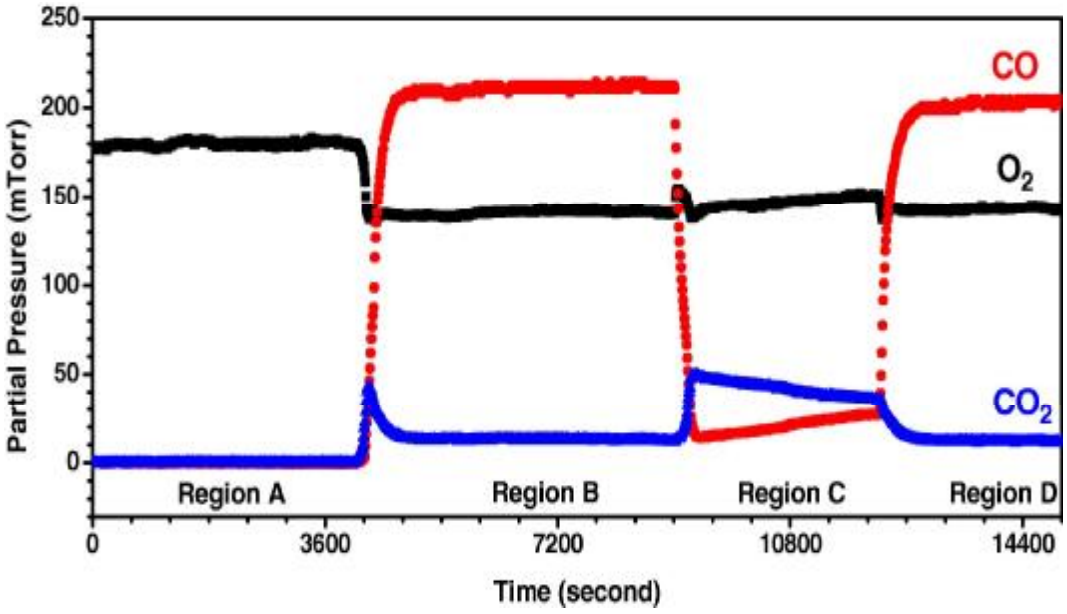

Figure 4.15. Partial pressures of CO, O_2, and CO_2 at constant temperature of 150 °C. We controlled the CO pressure to switch the reaction from a CO rich to oxygen rich environment and vise versa. Region A: 180 mTorr O_2; Region B: 140 mTorr O_2 + 230 mTorr CO; Region C: 150 mTorr O_2 + 14 mTorr–28 mTorr CO; Region D: 140 mTorr O_2 + 200 mTorr CO. These regions correspond to XPS spectra in Figure 4.16

At t = 4200 s (start of Region B), CO was introduced at 230 mTorr. Simultaneously, the O_2 partial pressure dropped to 140 mTorr. This drop is partly due to the consumption of O_2 by the reaction, but the major reason is the gas delivery system, i.e., a decrease of the pressure difference between the gas manifold and the high pressure cell. As soon as CO is introduced, a sharp increase in CO_2 production is observed in Region B of Figure 4.15, which is then followed by a decrease to a steady state value of ~14 mTorr. The abrupt enhance in CO_2 production results from reaction between CO gas and chemisorbed oxygen on the Pt surface. However, this chemisorbed oxygen is not stable under such reaction conditions and disappears immediately. Due to the limited flow rate of the chamber, the CO_2 decreases slowly to a steady state value, 14 mTorr. O1s spectra taken after the pressure stabilized clearly show that the chemisorbed oxygen on the surface is completely removed. The main peak at 532.7 eV in the O1s spectrum results from on-top site CO molecules on the Pt surface.

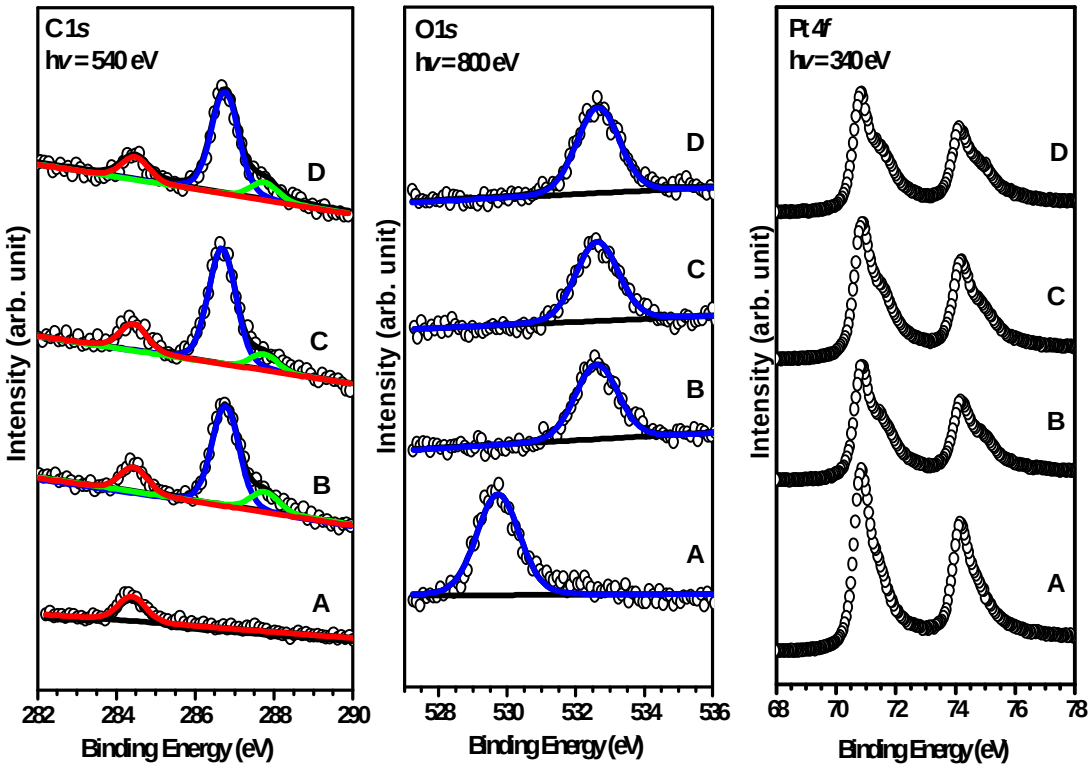

Figure 4.16. XPS spectra at each region in Figure 4.15 (A–D): (a) C1s spectra recorded at 540 eV; (b) O1s spectra recorded at 800 eV; (c) Pt4f recorded at 340 eV

This is also supported by the corresponding C1s peak and Pt4f spectrum (Figure 4.16(a), (c) Spectrum B). The main peak at 532.7 eV in the O1s spectrum results from on-top site CO molecules on the Pt surface. This is also supported by the corresponding C1s peak and Pt4f spectrum (Figure 4.16(a),(c) Spectrum B). Furthermore, the new peak observed in Figure 4.14(a) (Spectrum D) at 287.8 ± 0.1 eV is present in the C1s spectrum. The rapid increase and decay of the CO_2 signal in the early stage of Region B clearly demonstrates that the oxygen covered Pt(110) surface has a higher reaction rate than that of the CO covered surface. However, this surface is not stable under CO rich conditions.

In order to achieve an O_2 rich condition, we reduce CO pressure (Region C). The formation of CO_2 starts to increase as the CO pressure decreases. The CO_2 production reaches a maximum when the CO pressure reaches a minimum at 14 mTorr. The O1s, C1s and Pt4f core level spectra recorded in this region are almost identical to those of Region B, except for a slight decrease of the high BE shoulder of the Pt4f peaks. This shows that the Pt surface is still CO covered, but with lower CO coverage. There is no chemisorbed oxygen or oxide formation on the Pt surface. Furthermore, the CO_2 pressure decreases from 50 to 36 mTorr as the CO pressure increases from 14 to 28 mTorr in Region C, a negative order in CO. This result is consistent with the classical L–H mechanism. Because of the asymmetric adsorption of CO and O_2 on the Pt surface, a state with low (high) CO coverage exhibits a high (low) rate of CO_2 production (Krischer et al. 1992). This high reaction rate region is different from the high reaction rate region observed by Hendriksen (Hendriksen et al. 2002), where the Mars–Van Krevelen mechanism is proposed. In their experiment which was performed under higher pressures and higher O_2/CO ratio, the CO_2 pressure increases as the pressure of CO increases in the high reaction rate region.

To have a comprehensive understanding in this study, we then enhanced the CO pressure back to 200 mTorr to reproduce a CO rich condition similar to Region B. Both reaction data in Figure 4.15 (Region D) and XPS data in Figure 4.16 shows identical results as those obtained in Region B. The production of CO_2 decreases again when the CO pressure increases, which is consistent with the L–H mechanism.

4.3. Early Oxidation Stages of NiTi Shape Memory Alloys

4.3.1. Introduction

Nickel titanium (chemical symbol NiTi), also known as Nitinol, is a metal alloy of nickel and titanium with an elemental ratio near unity. Nitinol derives its name from its chemical composition and its place of discovery, (***Ni***ckel ***Ti***tanium ***N***aval ***O***rdnance ***L***aboratory). The shape memory effect of Nitinol was discovered by Buehler et al. (Buehler 1965) during research at the Naval Ordnance Laboratory in the early 1960s. Since that time, intensive metallurgical investigations have been made to explore the mechanics of its basic behavior.

The use of NiTi for medical purposes was first reported in the early 1970s. In the early 1980s, this idea got more attention and some orthodontic and experimental orthopedic applications were released. It was only in the mid-1990s, however, that the first widespread commercial stent applications made their breakthrough in medicine. Currently, NiTi produces significant interest in the medical and commercial sectors.

Nitinol has good biocompatibility (response is similar to stainless steel), making it ideally suited for design of biomedical implantable devices. Nitinol has two characteristics that make it extraordinarily unique and potentially very useful in surgical applications. Thermal shape memory and superelasticity make it possible for such alloys to behave differently compared to other bioengineering metallic alloys. When used in surgical implants, these extraordinary properties make the implants self-locking, self-expanding and self-compressing all activated at body temperature.

4.3.2. Fundamental Characteristics of Nitinol

4.3.2.1. Shape Memory Effect

NiTi, a shape memory metal alloy, can exist in two different temperature-dependent crystal structures (phases) called martensite (lower temperature) and

austenite (higher temperature or parent phase). Several properties of austenite NiTi and martensite NiTi are notably different.

When austenite NiTi is cooled, it begins to change onto (twinned) martensite. The temperature at which this phenomenon starts is called martensite start temperature (M_s). The temperature at which the entire material is in the martensite phase is called martensite finish temperature (M_f). While in this phase, the twinned martensite is deformed which causes non-plastic detwinning, all while still maintaining a martensite crystal structure. Upon removal of the load, the martensite elastically recovers, but retains some permanent deformation (strain). When martensite NiTi is heated, it begins to change into the austenite phase. The temperature at which this phenomenon starts is called austenite start temperature (A_s). The temperature at which this phenomenon is complete is called austenite finish temperature (A_f). A schematic diagram of the phase transformation is show in Figure 4.17.

Composition and metallurgical treatments have dramatic impacts on the above transition temperatures. From the point of view of practical applications, NiTi can have three different forms: martensite, stress-induced martensite (superelastic), and austenite. When the material is in its martensite form, it is soft and ductile and can be easily deformed (somewhat like soft pewter). Superelastic NiTi is highly elastic (rubber-like), while austenitic NiTi is quite strong and hard (similar to titanium). NiTi has all these properties, their specific expression depending on the temperature in which it is used.

NiTi can sense a change in ambient temperature and is able to convert its shape to a preprogrammed structure. Shape-memory is the ability of Nitinol to remember its shape following a deformation. This phenomenon utilizes the temperature effects on the phase transformation. While NiTi is soft and easily deformable in its lower temperature form (martensite), it resumes its original shape and rigidity when heated to its higher temperature form (austenite). This is called as one-way shape memory effect.

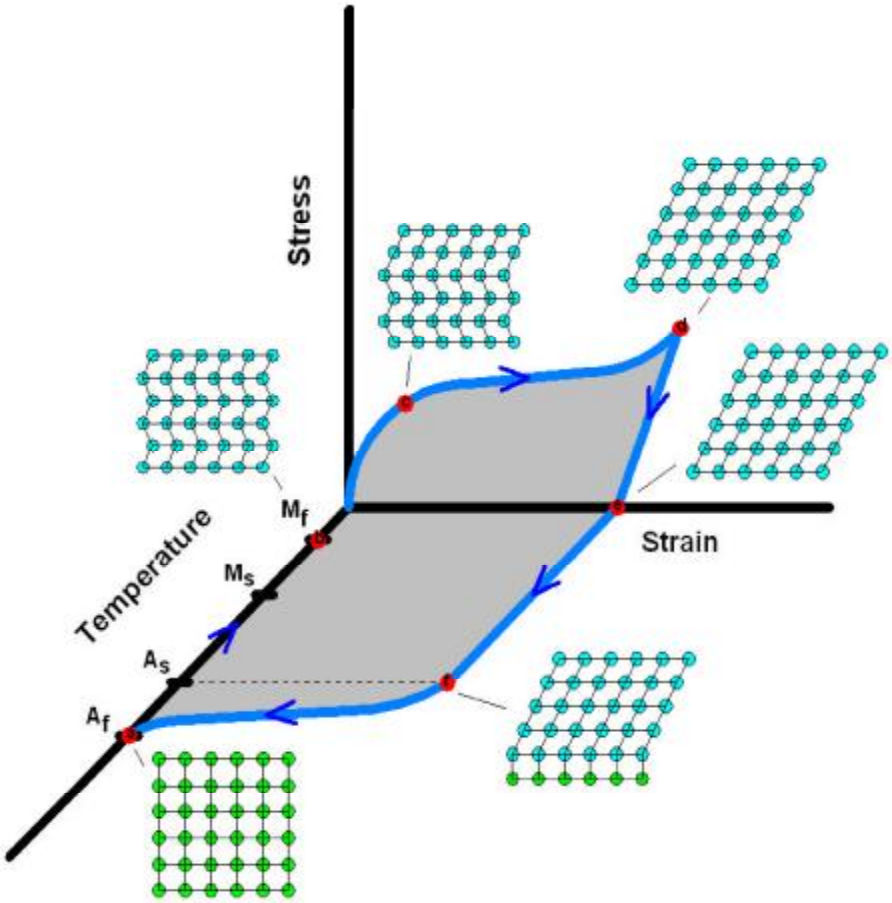

Figure 4.17. Schematic diagram of the shape memory effect. At high temperature (a), the material is fully austenite. Lowering the temperature below the M_f (b) without the addition of stress causes a phase transformation to twinned martensite. As the martensite is loaded, it begins to detwin (c), until full detwinning occurs (d). Upon unloading to (e), the martensite elastically recovers, but does not return to a twinned state. Raising the temperature to the austenite start temperature, A_s (f), begins the reverse transformation from martensite to austenite, which is complete at A_f (a) (Robertson 2006)

The ability of shape memory alloys to recover a preset shape upon heating above the transformation temperatures and to return to a certain alternate shape upon cooling is known as the two-way shape memory effect. Two-way memory is an exceptional case.

4.3.2.3. Superelasticity

Superelasticity (or pseudoelasticity) is the ability to elastically deform to higher than normal levels when mechanically deformed (Figure 4.18). This is based on stress-induced martensite formation.

The application of an outer stress causes martensite to form at temperatures higher than M_s. The macroscopic deformation is accommodated by the formation of martensite. When the stress is released, the martensite transforms back into austenite and the specimen returns back to its original shape.

Nitinol can elastically deform to nearly 11% strain, whereas most metals only have the ability to elastically deform to less than 1% strain. While in this temperature range, Nitinol deformation above ~1% results in a phase transformation from austenite to detwinned martensite. An additional forward strain is required, typically at a relatively constant stress “plateau”, to fully transform all of the austenite phase to martensite. Upon unloading, the martensite phase becomes unstable and transforms back to its original austenite phase, resulting in full strain-recovery upon the removal of load.

Superelastic NiTi can be strained several times more than ordinary metal alloys without being plastically deformed, which reflects its rubberlike behavior. It is, however, only observed over a specific temperature range. Above the martensite deformation temperature, Md, austentite cannot be transformed to martensite via stress. Above M_d, NiTi alloy is deformed like ordinary materials by slipping. Below A_s, the material is martensitic and does not recover. Thus, superelasticity appears in a temperature range from near A_f and up to M_d. The largest ability to recover occurs close to A_f.

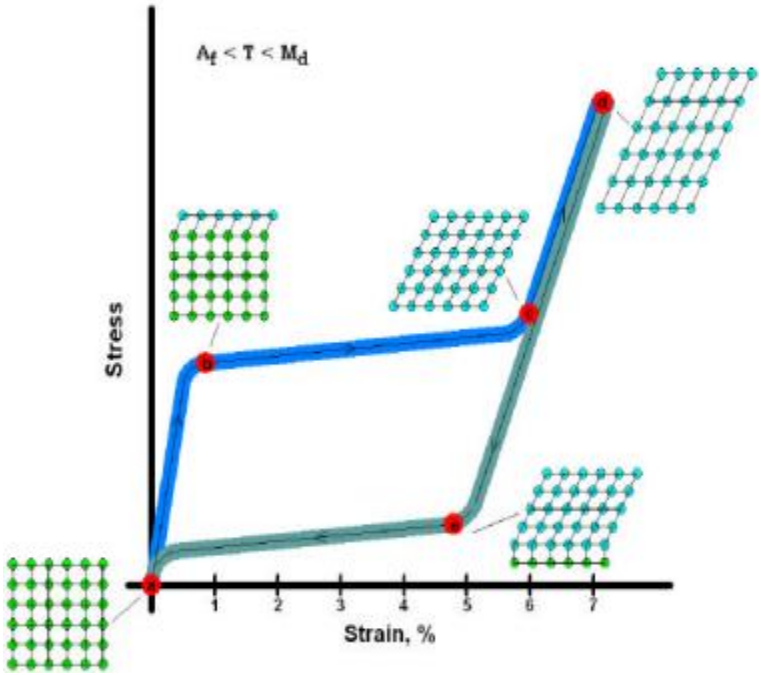

Figure 4.18. At temperatures above the austenite finish temperature, A_f, but below the martensite deformation temperature, M_d, the superelastic effect occurs in Nitinol as shown. Starting at (a) the material is fully austenite. The austenite is elastically loaded to point (b) at which time transformation to martensite occurs (the martensite forms in twins, and instantaneously detwins due to the high applied stresses). Further loading along a stress "plateau" to point (c) fully transforms the material to martensite. Continued loading to (d) requires increased stress and elastically deforms the martensite (note that the stress induced martensite (SIM) elastic modulus is lower than the austenite modulus of elasticity). Unloading back through point (c) recovers the elastic strains in the martensite, and continued unloading to (e) forces the onset of the reverse transformation to austenite, with full reverse transformation upon complete unloading to (a) (Robertson 2006)

4.3.3. Objective of Work

Nitinol (Ni-Ti) is an equiatomic nickel-titanium intermetallic which is known for its technologically significant attributes of "shape memory" and "superelasticity". Through a well-characterized martensitic phase transformation, the alloy can recover deformation strains as high as 11%, compared to typical elastic (recoverable) strains of 0.5% for other metals. By simply changing its temperature or by removing an applied stress, Nitinol will return to its original state. Because of these

characteristics, Nitinol is being used in biomedical implants and devices such as orthodontic wires, expanding cardiovascular and urological stents, spine correction rods, bone fraction fixation plate and staples, and so on. (Shabalovskaya 2002, Yeung et al. 2006, Duerig et al. 1999, Widu et al. 1999, Gil et al. 1996).

Nitinol is one of many titanium-based alloys that have been successfully used *in vivo*. The biocompatibility of these alloys has been attributed to a predominantly TiO_2 passive surface film. Likewise, the surface film on Nitinol appears to be titanium and oxygen-based (Zhu et al. 2003), possibly TiO_2 (Shabalovskaya et al. 1995). Ti is considered an element of low toxicity because it does not modify any essential physiological functions in humans and has a low solubility *in vivo* (Seiler et al. 1988). TiO_2 is even less soluble and more biologically inert (Seiler et al. 1988). Ni and Ni oxides, on the other hand, have very poor biocompatibility. Nickel may dissolve more easily than titanium because its oxide is less stable. Nickel has apparently dissolved from stainless steel orthopaedic implants into the extracellular fluids and has been implicated in cell death, inflammation, allergic reactions, and increased susceptibility to infection (Seiler et al. 1988, Brown et al. 1985). There are similar concerns about Ni poisoning from Nitinol devices. Depending on the structure and composition of the surface film, Nitinol devices have either released high concentration of Ni *in vivo* (Gimenez et al. 2000), or have demonstrated very high corrosion resistance and biocompatibility (Venugopalan et al. 2000, Trepanier et al. 1998). In fact, severe localized corrosion has been observed in certain explanted Nitinol devices (Riepe 2000). It has been reported that corrosion causes out-diffusion of nickel ions that may induce hypersensitive reactions and tissue necrosis (Shevchenko et al. 2004, Jia et al. 1999).

When Nitinol shape memory alloys are subject to the physiological environment, the corrosion behaviour affects not only their biocompatibility but also long-term implementation safety in the human body. The human body in a corrosive environment; the presence of ionic salts in body fluids can corrode NiTi alloy surfaces and further accelerate Ni diffusion from the substrate. A good passivation film on Nitinol can prevent significant release of nickel ions into the body. Many device manufacturers have achieved such a protective passivation film using a

variety of surface treatments such as mechanical polishing (Shabalovskaya et al. 2008, Trigwell et al. 1998), electropolishing and chemical polishing (Shabalovskaya et al. 2008, Trigwell et al. 1998, Chu et al. 2008), polymeric coatings (Tepe et al. 2006), and so on. These treatments aim to remove any nickel-rich phases from the surface and create a biocompatible TiO_2 layer. MP surfaces typically are less resistant to localized corrosion than chemically passivated or EP surfaces (Figure 4.19). These differences in localized corrosion behavior suggest that each treatment method may lead to different passivation layer.

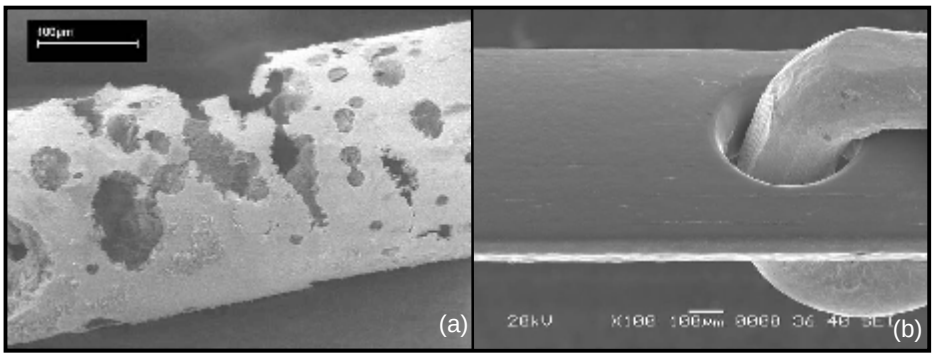

Figure 4.19. SEM images of explanted Nitinol devices with different passivation layer (a) Mechanically polished Nitinol sample with thick thermal oxide layer after 9 months (Riepe 2000) (b) Electrically polished thin oxide layer after 12 months (Stoeckel et al. 2004)

Heat treatment, as one of the surface preparation methods of Nitinol, results in the oxidation of NiTi and the formation of a titanium oxide layer on its surface in the oxygen containing environment. Several reports on oxidation treatments and the oxidation behaviour of Nitinol at high temperature have been published in the literature (Armitage et al. 2003, Firstov et al. 2002, Xu et al. 2004, Chu et al. 1996, Chan et al. 1990). For instance, the surface oxidation of NiTi shape memory alloy (SMA) subjected to heat treatment in air from 300 to 800 °C was reported by Firstov et al. (Firstov et al. 2002). Xu et al. studied the isothermal oxidation behavior of NiTi in pure oxygen over the temperature range 450–750 °C (Xu et al. 2004). The isothermal oxidation behavior of NiTi in dry air from 550 to 1000 °C (Chu et al. 1996) was investigated by Chu et al. Chan et al. (Chan et al. 1990) studied the oxidation behavior of NiTi at 400 °C at an oxygen pressure of 10^{-4} Torr and in air.

Since its discovery nearly a half century ago, much research has been

conducted on Nitinol due to its enormous variety of applications, from catalysis to medicine. However, there is a dearth of information in the literature regarding the initial oxidation mechanism of NiTi. The primary goal of this investigation is to determine the role of temperature on the formation of the NiTi passivation layer during initial oxidation. In-situ X-ray Photoelectron Spectroscopy (XPS) and Near-edge X-ray Absorption Fine Structure (NEXAFS) spectroscopy have been used to investigate variations in the composition of the outermost layer (or oxide layer) and its structure, caused by exposure to pure O_2 at two temperatures, room temperature and 200 °C.

4.3.4. Experimental Procedure

4.3.4.1. Cleaning of NiTi Surface

The cleaning procedure of NiTi surfaces is discussed in this section. The surface morphology was observed by optical microscopy. The surface composition and chemical alterations in the near-surface region have been examined using X-ray Photoelectron Spectroscopy (XPS). In the following sections, first Ar^+ ion sputtering method is explained. Then, the results obtained from optical microscopy and XPS will be presented and discussed.

4.3.4.1.(1). Ar^+ Ion Sputtering

Various cleaning treatments such as mechanical polishing, chemical etching, rinsing in acetone or ethanol, etc. constitute a pretreatment stage. For an atomically clean surface, an in-situ final preparation in the UHV chamber is needed. One of the most common and effective in-situ surface cleaning methods is ion sputtering. Due to its many advantages, e.g. practicability and easy incorporation into ultra high vacuum systems, it has become a widely used standard procedure for surface cleaning. The idea is to remove enough atomic layers from the surface by ion bombardment so that a clean, ideally undisturbed surface of the material under

investigation is exposed. Surface contaminants can be sputtered off together with the substrate top layer by bombardment of the surface by noble gas ions. Ar^+ ion beams of 1-5 keV energy are the most commonly used species for sputter cleaning. Ar^+ is chosen because it is a heavier ion and an inert gas, thereby eliminating chemical effects. In general, surface cleaning means removal of "natural" contaminants, i.e. mostly O, C, and H containing species which form surface layers less than a few nanometers thickness. Ideally for surface cleaning the sputtering process would remove the topmost atomic layer of a solid and consequently the surface would be eroded layer-by-layer by ion bombardment. To produce an ion beam, Ar gas is admitted through a leak valve directly into the ion gun (Figure 4.20) or into the UHV chamber as a whole. Ionization of the gas atoms proceeds via electron impact in the ionizer of the ion gun. Electrons are emitted from the cathode. The ions are extracted from the ionizer, accelerated to the desired energy (typically 0.5-5.0 keV) and directed toward the sample, typically at ground potential.

Ion sputtering is a very effective cleaning technique. The side effect of ion bombardment is the degradation of the surface structure. Therefore, subsequent annealing is required to restore the surface crystallography and to remove embedded and adsorbed Ar atoms. In practice, several ion bombardment/annealing cycles are required to prepare a well-ordered atomically clean surface.

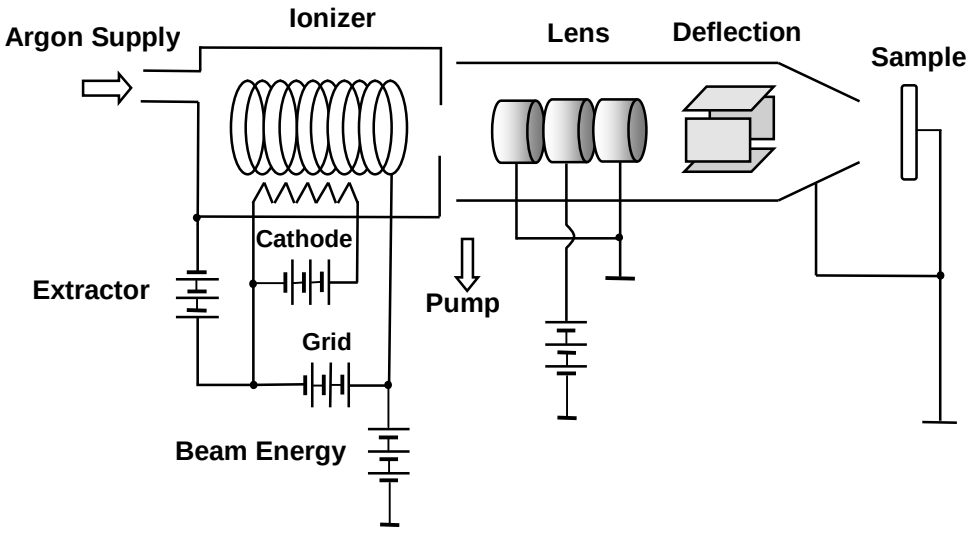

Figure 4.20. Schematic diagram of a typical ion sputter gun used for sample cleaning. Such a gun can also be applied for sputter depth profiling, secondary ion mass spectrometry, and ion scattering spectrometry

4.3.4.1.(2). Sample Preparation

The material used in this study was a commercially available superelastic Nitinol disc (Nitinol Device & Components, Fremont, Ca) for medical application with nearly equiatomic ratio of Ni and Ti (50.8 at % Ni and 49.2 at. % Ti). The sample was ~10 mm in diameter and ~2 mm in thickness. The experiments were carried out at Beamline (BL) 9.3.2 at Advanced Light Source (ALS). In-situ X-ray Photoelectron Spectroscopy (XPS) measurement was performed in an ultra-high vacuum system equipped with Scienta R4000 HiPP analyzer, with a base pressure of 10^{-10} Torr. Prior to the oxidation experiment, the specimen was mechanically polished progressively with 320, 400, 600, and 1200 grit SiC emery papers to remove macro-level surface contamination as well as any native oxide layer. An Al_2O_3 suspension was used for the final polishing to achieve a mirror finish. Polishing was followed by cleaning with acetone (15 minutes), and then ethanol (15 minutes) in an ultrasonically agitated bath.

Mechanically polished NiTi sample was inserted into the load lock immediately right after the ultrasonic bath to avoid oxidation in air. The sample was then transferred to the preparation chamber. The duration between ultrasonic cleaning and loading was less than 15 minutes. The sample was maintained in the preparation chamber overnight at room temperature for the purpose of outgassing. The base pressure of the preparation chamber was less than 10^{-9} Torr.

The final preparation of the sample was done by sputtering with an Ar^+ ion beam in the preparation chamber in order to remove surface contamination by carbon-containing or water molecules adsorbed from the environment as well as the oxide layer formed on the NiTi surface. The ion source used in this study was a PHI Model 04-16 Sputter Ion Gun with a PHI Model 20-045 Sputter Ion Gun Control. The ion source was operated at a primary beam energy of 2.0 keV with an emission current of 15 mA. The source was operated within a high vacuum chamber backfilled to a pressure of 1×10^{-5} Torr Ar. The sample was exposed at normal angle and a distance of ~10 cm from the source (ion gun).

Ion bombardment was carried out until nearly steady state compositional changes had been achieved. Total sputtering interval was 1 hour. At 15 minutes intervals of sputtering, the chemical composition of the surface was checked using X-ray Photoelectron Spectroscopy (XPS) since XPS is the most suitable technique to study the chemical composition of surfaces due to its surface sensitivity. Survey scans were measured for element species on the surface over a binding energy range of 0-550 eV at an energy step of 0.5 eV. High-resolution core-level XPS spectra over the O1s, Ti2p, Ti3p, Ni3p and C1s ranges were recorded at 610 eV photon energy using constant pass energy of 100 eV to determine the chemical states and concentrations. The binding energies were referenced to the Fermi edge of the valance band. Curve fitting was performed using the CASA-XPS after a Shirley background subtraction.

4.3.4.1.(3). Results

The surface morphology of the mechanically polished NiTi sample was examined by optical microscopy. Figure 4.21 shows optical microscope images of the surface of the NiTi specimen before and after polishing. As shown in Figure 4.21(a), a very rough and porous surface is observed for the unpolished sample. In contrast, polished surface is smooth and no scratches are left except pits on the surface. Mechanical polishing visibly improves the surface quality.

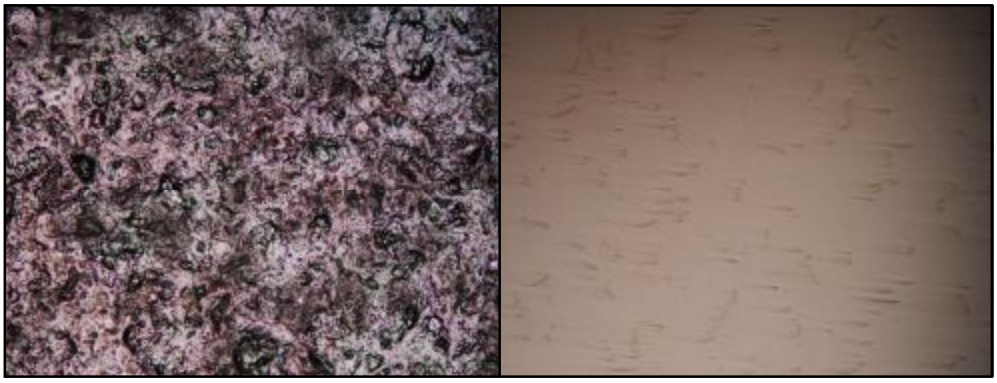

(a) **(b)**

Figure 4.21. The optical microscope images of a) unpolished and b) mechanically polished NiTi sample surface

Figure 4.22 displays XPS survey spectra collected at 610 eV before and after Ar^+ ion sputtering. The results recorded for the mechanically polished NiTi sample show that the dominant surface elements are C, O, and Ti which suggests that a titanium oxide film was formed on the surface during polishing in air. Carbon contamination may be from the SiC emery paper used for polishing and/or hydrocarbons in the atmosphere.

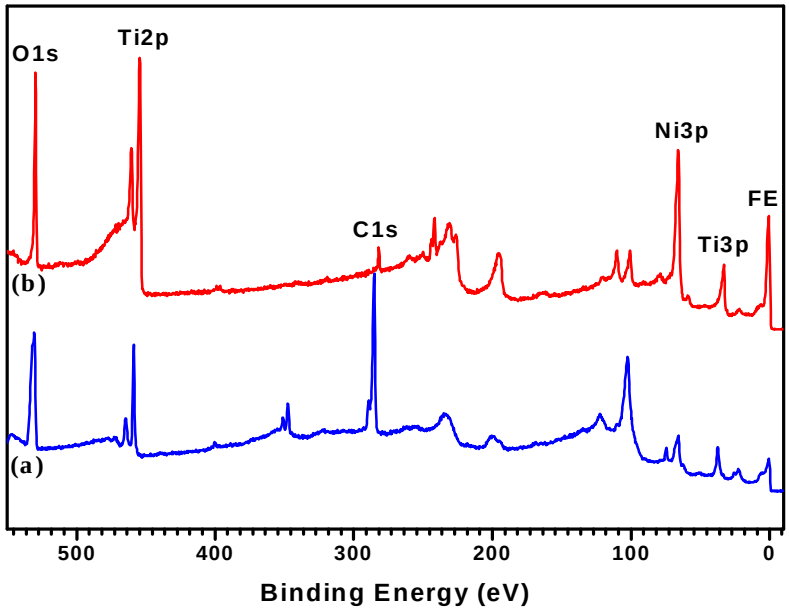

Figure 4.22. XPS survey spectra of (a) mechanically polished and (b) Ar sputtered NiTi sample

After 1 hour exposure to 2.0 keV Ar^+ ions, significant changes are apparent in the survey spectra (Figure 4.21(b)). On the basis of the high resolution C 1s XPS spectra shown in Figure 4.23, hydrocarbon species at binding energy 284.5 eV have been removed after 15 minutes of sputtering, and a new structure emerges on the lower binding energy side after sputtering. The C1s peak of the mechanically polished NiTi surface (Figure 4.23(a)) can be deconvoluted into three main peaks with contributions from the C–C (285.48 eV), C–O (286.97 eV), and COOH or carbon compounds with nitrogen, oxygen and hydrogen (O=C–N–H) (289.49 eV) (Schier et al. 1993, Shabalovskaya et al. 2009). The smaller peak (indicated by arrow in figure) at 283.37 eV is indicative of a carbide, probably some type of Ti–C bond (Muller et al. 1996). As the sputtering process proceeds, a new peak evolves at

282.15 eV. This feature can be assigned to titanium carbide (TiC) (Schier et al. 1993).

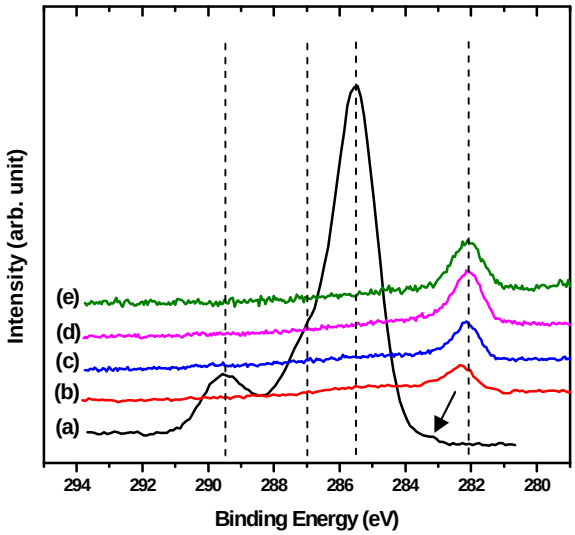

Figure 4.23. C1s XPS spectra of the mechanically polished NiTi surface after different sputtering time: (a) 0 min, (b) 15 min, (c) 30 min, (d) 45 min, and (e) 60 min

Figure 4.24 depicts the O 1s XPS spectra of the NiTi surface after different sputtering time.

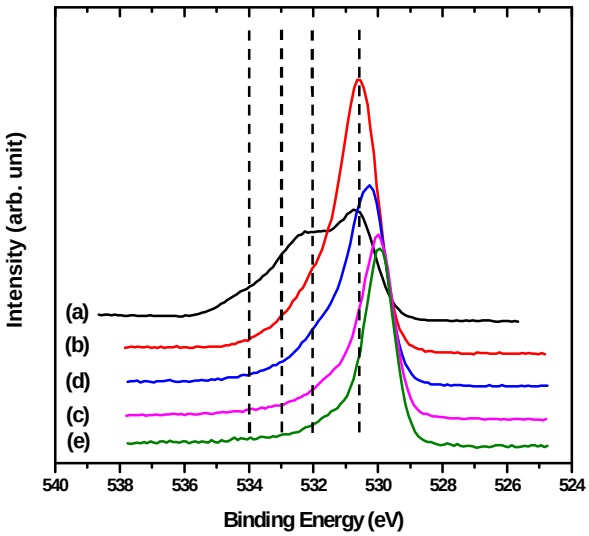

Figure 4.24. O1s XPS spectra of the mechanically polished NiTi surface after different sputtering time: (a) 0 min, (b) 15 min, (c) 30 min, (d) 45 min, and (e) 60 min

The mechanically polished sample exhibits a broader O 1s spectrum with a main peak at 530.54 eV, which is assigned to the oxygen present in metal oxides

(Shabalovskayaet al. 1995). Other oxygen states present in adsorbed water (532.89 eV), OH^- (531.95 eV) and carbon single bond (C–O) (534.17 eV) could also be found (Wang et al. 2007). The intensity of the metal oxide peak increases after 15 minutes of sputtering with the removal of adsorption layers by argon ion bombardment. Further argon sputtering reduces the intensity of this dominant peak with a slight shift in the binding energy. A new peak arises around 530 eV. With the combination of the results obtained from the XPS analysis of Ti 3p, it is clear that the surface of the as-received NiTi sample is mainly covered by titanium dioxide (TiO_2). The observed energy shift with sputtering indicates a reduction of the main TiO_2 phase to titanium suboxides in the oxide layer.

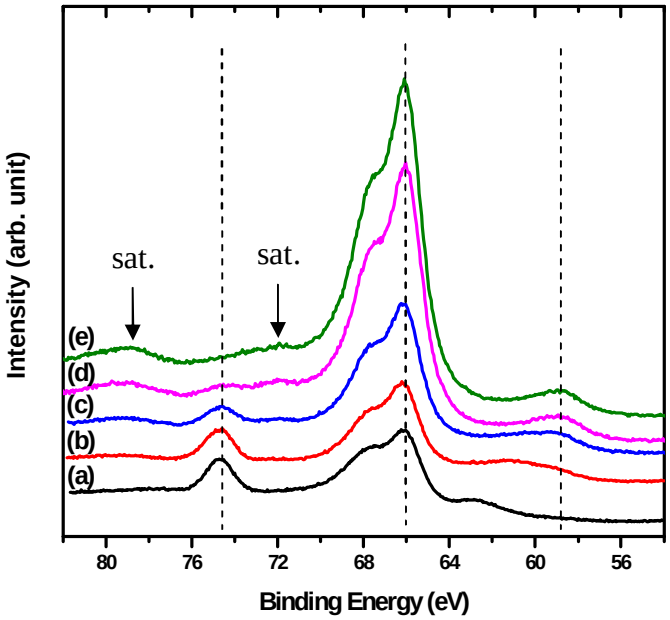

Figure 4.25. Ni 3p XPS spectra of the mechanically polished NiTi surface after different sputtering time: (a) 0 min, (b) 15 min, (c) 30 min, (d) 45 min, and (e) 60 min

Ni 3p XPS spectra of the NiTi sample after different Ar^+ sputtering time are displayed in Figure 4.25. Generally, the Ni 3p peak for the intermetallic NiTi state is a doublet consisting of $2p_{1/2}$ and $2p_{3/2}$ peaks whose energies are ~66 eV and ~67.8 eV, respectively (NIST database). Figure 4.25 reveals that Ni in the intermetallic NiTi state is present before sputtering, but its intensity significantly increases with sputtering time. It is also found that the as-received mechanically polished NiTi surface has some aluminum oxide (at 74.7 eV), most probably Al_2O_3, and its

intensity decreases upon sputtering. With argon ion sputtering, a new feature at 58.56 eV appears and two additional satellite structures become more apparent. The satellite peaks are separated from the main peak of Ni in intermetallic state by ~6 eV and ~14 eV, respectively. These the 6-eV and 14-eV satellites can be assigned to the $3p^5d^9$ final-state configuration with the main line associated with the $3p^5d^{10}$ configuration (Sacchi et al. 1998). The observed peak at 58.56 eV is attributed to Ti 3s (NIST database).

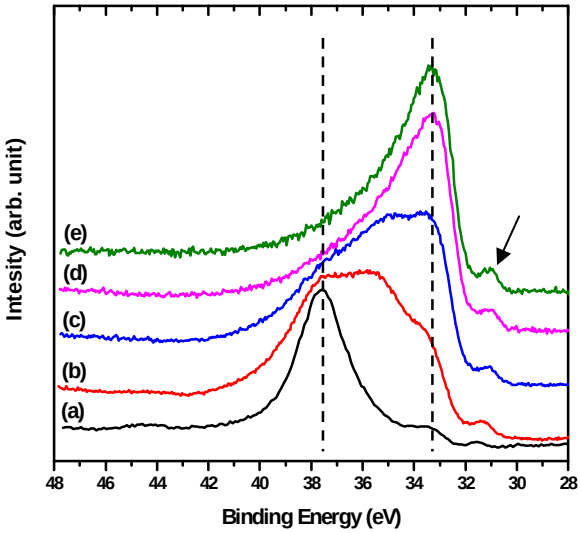

Figure 4.26. Ti 3p XPS spectra of the mechanically polished NiTi surface after different sputtering time: (a) 0 min, (b) 15 min, (c) 30 min, (d) 45 min, and (e) 60 min

Ti 3p XPS spectra of the surface of mechanically polished Nitinol for different durations of argon ion bombardment are shown in Figure 4.26. It can be seen that the overall shape of the Ti 3p peak changes with sputtering time. The mechanically polished sample can be deconvoluted into four peaks. The deconvoluted peaks correspond to four chemical states of Ti which are Ti^{+4} (TiO_2), Ti^{+3} (Ti_2O_3), Ti^{+2} (TiO), and Ti^0 (intermetallic state of Ti or metallic Ti). The dominant peak at 37.67 eV can be identified as Ti^{+4} (TiO_2). X-ray Photoelectron Spectroscopy carried out after 15 min Ar^+ sputtering looks very different. Widening of the Ti 3p peak is caused by the reduction of TiO_2 to Ti_2O_3 and TiO as well as to the fully reduced intermetallic state of NiTi. After 1 hour Ar^+ sputtering, metallic Ti at 33.1 eV is the predominant peak we observe. In addition to the Ti species, there is

a peak at 31.52 eV as indicated by Figure 4.26. This small peak may be attributed to surface contamination associated with sodium (Na) (NIST database).

To obtain detailed information on the constituents of the sputter-induced titanium oxide layer on the NiTi, the relative amounts of the titanium compounds in Ti^{+4}, Ti^{+3}, Ti^{+2}, and Ti^{0} (intermetallic Ti) states are calculated as a function of sputtering time and shown in Figure 4. 27. As can be seen, the atomic percentages of Ti species change with the sputtering time. As discussed above, oxygen and carbon are the dominant surface elements found on the surface of the mechanically polished sample before sputtering. It can clearly be observed that there is little Ti^{0} (metallic titanium) from the intermetallic NiTi state, indicating the surface of the mechanically polished sample is mainly titanium oxides. After a 15 min. sputtering, the amount of surface hydroxyl concentration decreases and the hydrocarbon peak disappears as well as other surface contaminations, and a considerable decrease is observed in the Ti^{+4} states. Further ion bombardment cause a gradual increase in the metallic state of titanium in contrast to Ti subspecies due to the preferential sputtering of the oxygen atoms. After sputtering for 60 minutes, most of the Ti is metallic.

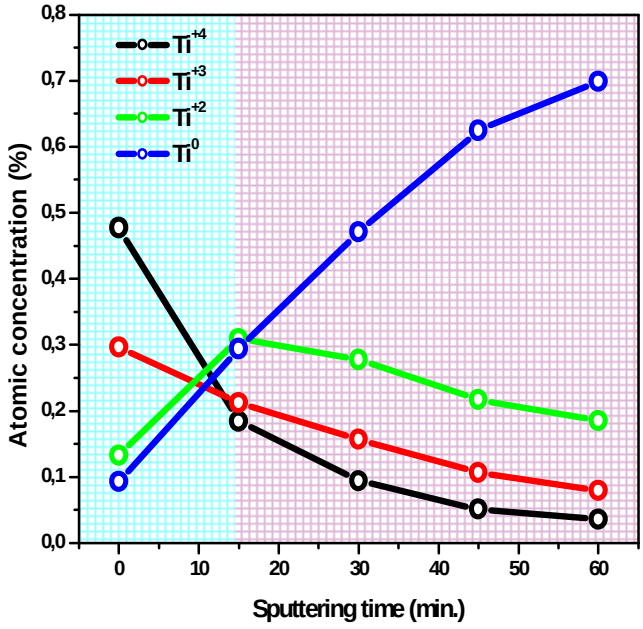

Figure 4. 27. Evolution of Ti species as a function of Ar^{+} sputtering time

The evolution of Ti_{tot} to Ni_{tot} atomic ratio as a function of the sputtering time is displayed in Figure 4.28. A maximum value determined after 15 minutes sputtering time is followed by decreasing gradually to a nearly steady- state value of about 0.72. The inconsistency of the steady-state value of Ti_{tot}/Ni_{tot} ratio in the sample after the sputtering of Ar^+ ion beam with the untreated Nitinol (Ti/Ni is about 1, 50.8 at %Ni) may be due to the preferential sputtering of Ti (Firstov et al. 2002).

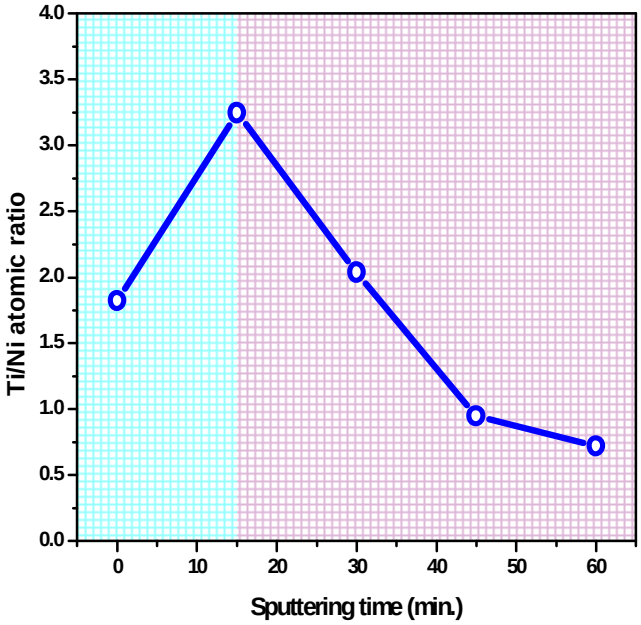

Figure 4.28. Evolution of Ti_{total} to Ni_{total} atomic ratio as a function of Ar^+ sputtering time

A number of key features from the sputtering profiles are determined. Firstly, the surface of the mechanically polished NiTi sample is mainly composed of TiO_2 with a small amount of metallic titanium. Secondly, aluminum (Al) contamination detected on the surface of mechanically polished sample is most likely caused by the Al_2O_3 suspension used for final polishing to achieve a mirror finish. To avoid this contamination, the NiTi sample was mechanically polished progressively with SiC emery papers without any final polishing. Thirdly and most importantly, sputtering did an oxygen-free surface. The lowest level of oxygen on the surface was found after 1 hour Ar^+ ion sputtering. Hence, the surface of mechanically polished NiTi sample was only sputtered 1 hour prior to oxidation experiments.

4.3.4.2. Oxidation of NiTi Surface

The Nitinol sample investigated in this study was consisting of 50.8 at%Ni-49.2 at%Ti. The experiments were carried out at Beamline (BL) 9.3.2 at Advanced Light Source (ALS). In-situ X-ray Photoelectron Spectroscopy (XPS) and Near-edge X-ray Absorption Fine Structure (NEXAFS) measurements were performed in ultra-high vacuum system equipped with Scienta R4000 HiPP analyzer, with a base pressure in the 10^{-10} Torr range. The incoming photon energy was set to 610 eV. The radiation was incident at 15° with respect to the surface, and the photoelectrons were emitted normal to surface. The detailed information about endstation which experiments are done in this study can be found in previous published paper (Grass et al. 2010). NiTi sample was mechanically polished and cleaned by an ultrasonic bath in ethanol and acetone each for 15 min after polishing. Prior to the oxidation measurements, mechanically polished NiTi sample was cleaned by repeated cycles of 2kV Ar^+ ion sputtering with 15 mA emission current at room temperature Sample cleanliness was verified by XPS checking the carbon and oxygen level after repeated cycles of Ar^+ cleaning. Oxygen adsorption was performed at room temperature (300 K) and 200 °C (473 K). Ultra high purity oxygen (99.997%) was dosed by means of a molecular leak valve. Initially, pure oxygen was dosed in sequence at the doses of 1L, 3L, 5L, 10L, 40L, 100 L, 400 L, 1000 L, 2500 L, 5000 L (1 L = 10^{-6} Torr·s) at room temperature. Finally, we exposed the sample at a constant pressure of 100 mTorr of oxygen after the oxygen dose of 5000 L. XPS spectra of the Ti3p, Ni3p, O1s, C1s, and valance band regions were obtained after each exposure. All exposures are shown in Langmuir units. The measured XPS data were calibrated using the Fermi Edge position as zero eV binding energy, and were analyzed by using CASA XPS. Subsequently, the same experiments repeated on sample on sample at 200 °C. Sample temperatures were measured through a chromel-alumel thermocouple attached to the sample. The NEXAFS signal was measured in the Partial Electron Yield (PEY) mode as a function of the incident X-ray photon energy in the vicinity of Ti L-edge region.

4.3.5. Results

4.3.5.1. Oxidation at Low Dose of Oxygen

4.3.5.1.(1). XPS Spectra

The survey spectrum measured after the repeated cycles of Ar^+ sputtering shown that our NiTi sample still exhibited a significant level of oxygen. Further Ar^+ sputtering did not remove this residual oxygen and oxygen was always present on the surface. We haven't detected pure metallic Ti on Ar^+ sputtered NiTi surface, yet these surfaces are highly reactive. So, once the lowest level of oxygen was achieved, as verified by survey XPS spectra, the oxidation experiment was initialized. To analyze XPS spectra of Ti 3p and Ni 3p core levels recorded for all oxygen doses, intensities and binding energies were obtained by deconvolution of the spectra (into GL(10)T(1) line shapes for Ti 3p and GL(70) line shapes for Ni) after a Shirley background (Shirley 1972) subtraction due to inelastic scattering. Ti 3p core-level spectra exhibited a bulk-titanium component (Ti^0) and various oxide components. Each Ti 3p spectrum was devoncoluted into four peaks corresponding to four chemical states of the titanium, TiO_2 (Ti^{+4}), Ti_2O_3 (Ti^{+3}), TiO (Ti^{+2}), and Ti or NiTi (Ti^0-metallic Ti) (Tollefsen et al. 2009).

Figures 4.29(a)-(d) shows deconvoluted Ti 3p XPS spectra for the sample at room temperature after various O_2 exposures. From the figure it is remarkable that a progression of discrete oxidation states of Ti is observed. One goes from the most metal-rich configuration to a more oxygen rich species as the oxygen exposure increases. Three different oxidation states of Ti are identified by different core level binding energies, and we assign them to the formation Ti^{+4}, Ti^{+3}, and Ti^{+2} oxide species that may resemble TiO_2, Ti_2O_3, and TiO, respectively.

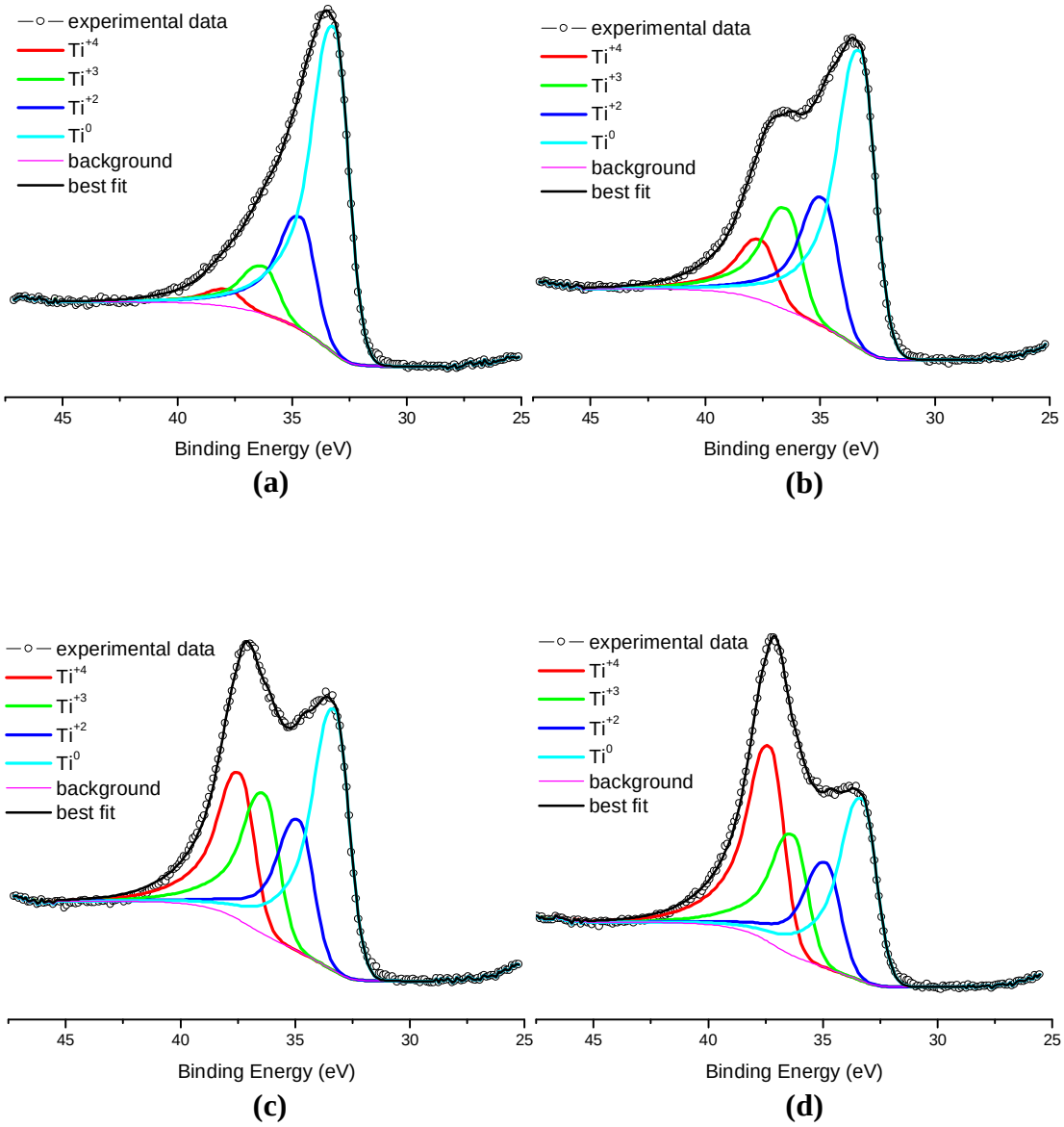

Figure 4.29. Deconvoluted XPS spectra of Ti 3p core level at 610 eV photon energy after (a) 1 L, (b) 19 L, (c) 159 L, and (d) 1559 L O_2 exposure at room temperature

In Figure 4.30, we show the evolution of Ti 3p XPS from clean NiTi substrate up to oxygen dose of 1559 L at 200 °C. The same trend is observed as in Figure 4.29 emphasizing the different oxidation states of Ti develop sequentially with the lower oxidation states.

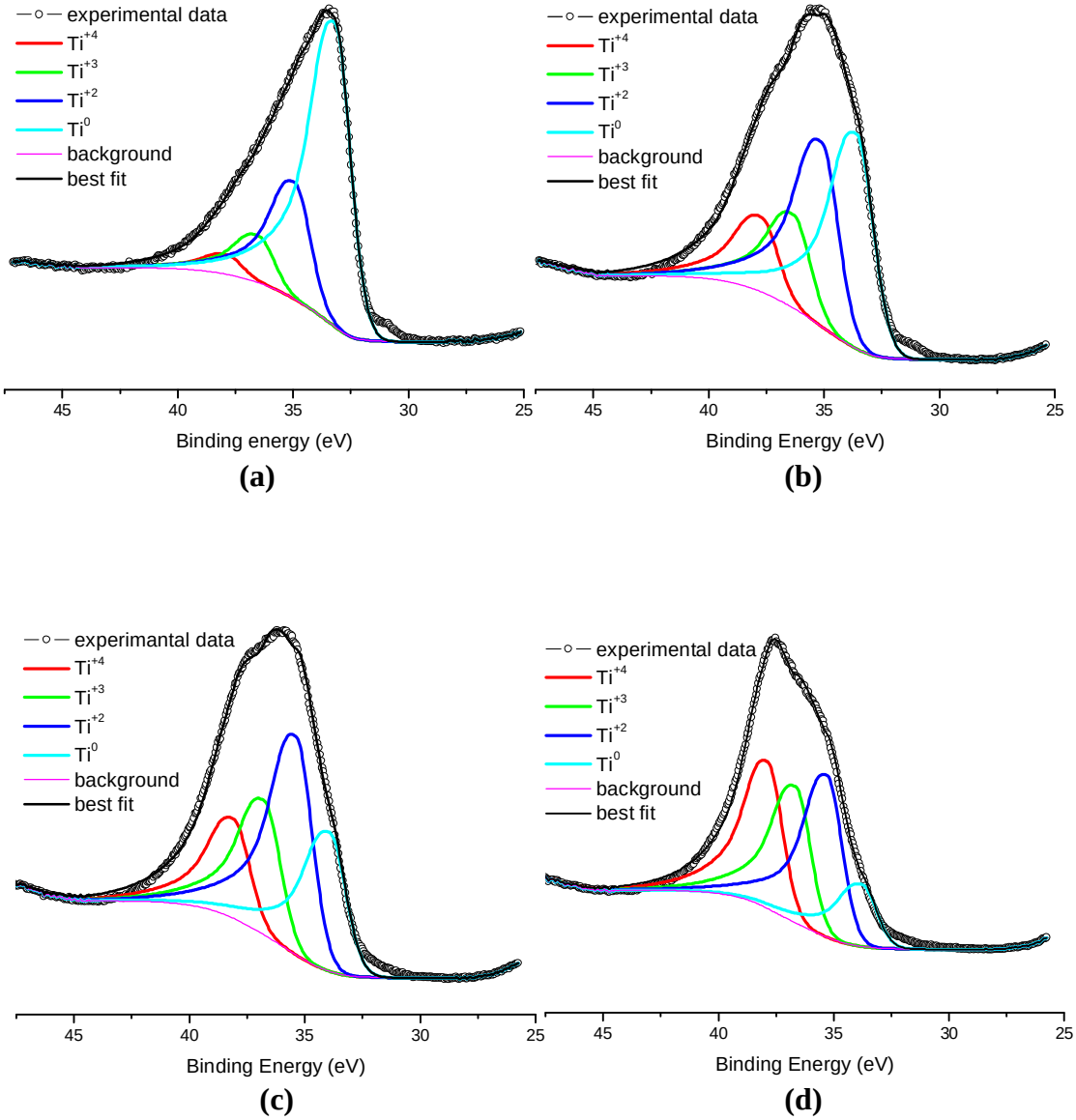

Figure 4.30. Deconvoluted XPS specta of Ti 3p core level at 610 eV photon energy after (a) 1 L, (b) 19 L, (c) 159 L, and (d) 1559 L O_2 exposure at 200 °C

At the next stage of our study, we calculated the relative atomic concentration of Ti species within the sampling depth of XPS to investigate the changes in the surface composition as a function of oxygen dose. Figure 4.31 presents the evolution of the total oxide states (Ti^{+4} + Ti^{+3} + Ti^{+2}) versus metallic titanium within the near surface region upon dosing of oxygen for room temperature and 200 °C. The concentration of the total oxide states equals the metallic state after an oxygen dose of 19 L at room temperature. After the dosing of 9059 L oxygen, 26% of titanium in the examined layer remains in the metallic state. On the other hand, an oxygen dose

of 9 L is enough to oxidize the half amount of Ti (50%) at 200 °C. At this temperature, 0.98% of Ti is in metallic state after the dosing 9059 L oxygen. Apparently the NiTi sample at 200 °C oxidizes more rapidly than the sample at room temperature starting from the first oxygen dose (1 L).

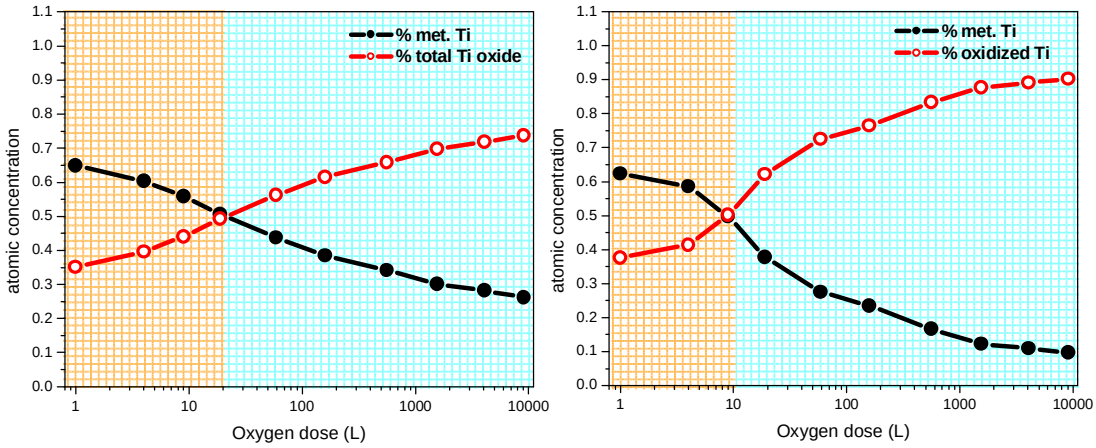

(a) **(b)**

Figure 4.31. Relative percentage of metallic and oxidized Ti as a function of oxygen dose at (a) room temperature and (b) 200 °C

The relative atomic concentration of each Ti species at the two temperatures is presented in Figure 4.32 as a function of oxygen dose. At both temperatures, the concentration of metallic Ti dramatically decreases in favor of $Ti^{+2,}$ Ti^{+3}, and Ti^{+4} with oxygen exposure. After 9059 L of dosing, NiTi sample at 200 °C present less metallic Ti. Figure 4.32 indicates that high temperature during oxidation enhances the formation of Ti^{+2} and Ti^{+3} states. The relative concentration of Ti^{+3} and Ti^{+2} at room temperature is significantly less as compared to the sample oxidized at 200 °C.

Figure 4.32 demonstrates that high temperature increases the formation of Ti^{+3} and Ti^{+2} at the expense of Ti^{+4} formation.

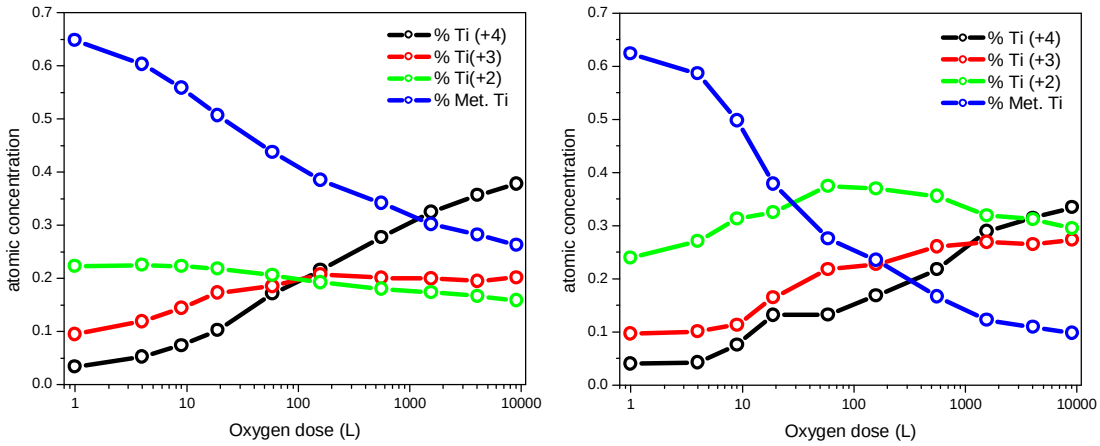

(a) **(b)**

Figure 4.32. Relative concentration of Ti^{+4}, Ti^{+3}, Ti^{+2}, and Ti^{0} states at (a) room temperature and (b) 200 °C as a function of oxygen exposure

In order to emphasize changes in Ti^{+4} and (Ti^{+3} + Ti^{+2}) as a function of oxygen dose and temperature, we plot Figure 4.33. In figure 4.33(a), three regimes can be clearly seen. In the first regime (1–9 L), the increase in Ti^{+4} is roughly equal at both temperatures. More Ti^{+4} forms at room temperature in the second regime (9-59 L) and then the formation rate is temperature independent again in the third regime. Figure 4.33(b) shows that the relative concentration of (Ti^{+3} + Ti^{+2}) is higher at the higher temperature from the beginning of oxygen dosing. This result illustrates the enrichment in Ti^{+3} and Ti^{+2} states on the surface at high temperature compared to room temperature.

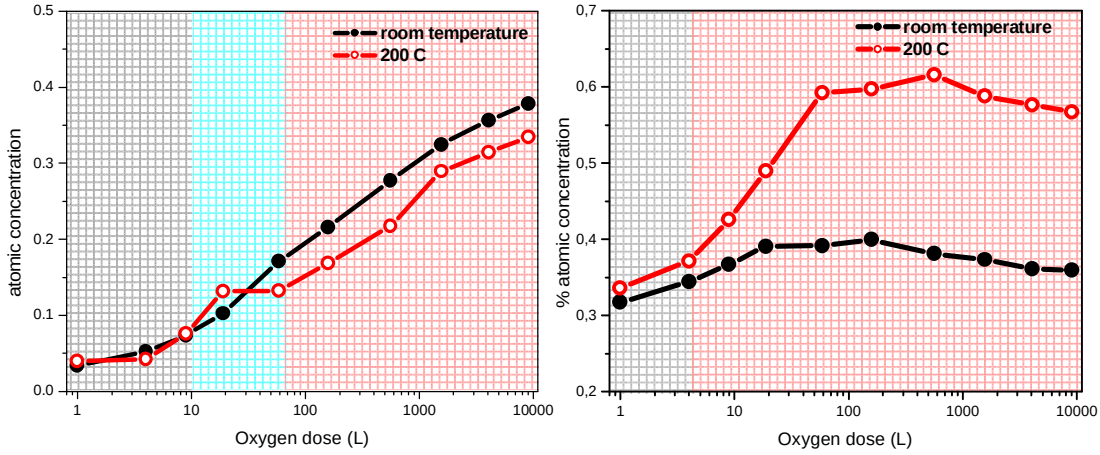

(a) **(b)**

Figure 4.33. Relative atomic concentration of (a) Ti^{+4} and (b) (Ti^{+3} + Ti^{+2}) as a function of oxygen dose

In this study, the oxide thickness and hence the oxidation rate was estimated using XPS. The thickness of the TiO_2 layer was calculated using the equation given by Carlson and McGuire (Massies et al. 1985, Carlson et al 1972/1973):

$$R_{ov} = \frac{I_{ov}}{T_{sub}} = \frac{D_{ov}}{D_{sub}} \frac{l_{ov}}{l_{sub}} \frac{1 - \exp(-d_{ov} / l_{ov} \cos q)}{\exp(-d_{ov} / l_{sub} \cos q)} \tag{4.8.}$$

where I_{ov} and I_{sub} are the intensities of photoelectrons coming from the same atomic shell, D_{ov} and D_{sub} the densities of the overlayer and substrate, λ_{ov} and λ_{sub} the mean-free path of electrons in the overlayer and substrate, d_{ov} the thickness of the overlayer, and a the emission angle of electrons relative to the surface normal (θ is equal to 0 in our case). It is assumed that λ_{ov} is equal to λ_{sub}, and λ_{sub} is taken as 12.35 Å for Ti 3p (KE ~ 577 eV) according to the calculation by Tanuma, Powell and Penn (Tanuma et al. 1994). Under this assumption, the oxide layer thickness can be given as:

$$d_{ov} = l_{sub} \ln\left(\frac{R_{ov} D_{sub}}{D_{ov}} + 1 \right) \tag{4.9.}$$

Figure 4.34 shows the growth of the TiO_x layer as a function of oxygen exposure measured at oxidation temperatures of room temperature and 200 °C. The curves in the Figure 4.34(a) show that the oxidation starts with a very rapid rate at the beginning of oxidation and an oxide layer of ~14–22 Å very quickly forms. Both curves exhibit a thickness regime above ~17–30 Å in which the rate is much slower and the thickness achieves an approximate saturation value. As the temperature increases, the slope of the rapid regime is steeper, indicating a faster growth of the oxide layer at high substrate temperature. The oxide thickness at the break point dividing the rapid and slow regimes strongly depends on the oxidation temperature. The thickness becomes larger as the temperature is increased, ~17 Å at room temperature, and ~30 Å at 200 °C. It is also observed that oxidation rate at room temperature is slower. Figure 4.34(b) shows the evolution of oxide thickness with the

oxygen dose pressures in log scale. The oxide thickness is observed to be independent of temperature for oxygen doses up to 4 L, whereas for higher doses of oxygen the change in thickness increases with temperature. Upon altering the exposure dose, faster oxidation was observed at high temperature. Near linear relationships were observed between the oxide thickness and the logarithm of the oxygen dose for measurements at room temperature and 200 °C indicating a parabolic growth of the oxide layer (Pelton et al. 2005).

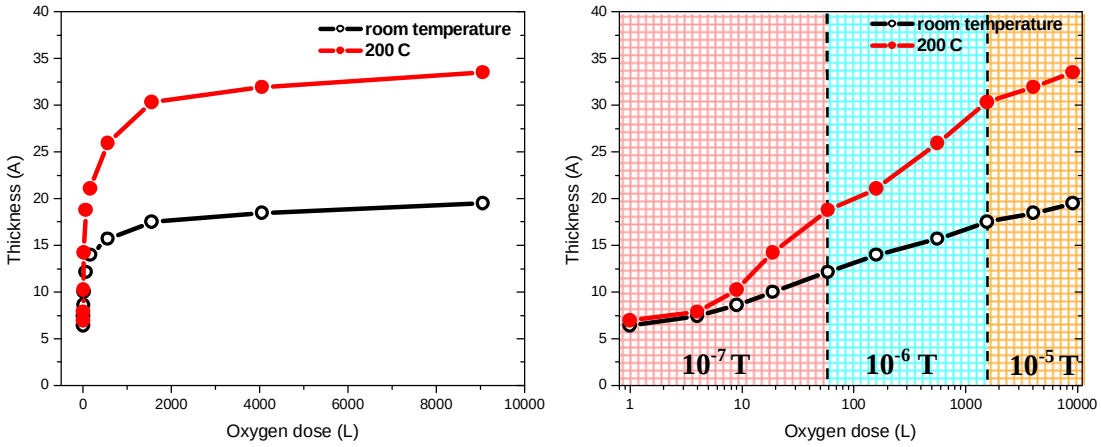

Figure 4.34. Calculated thickness of oxide (TiO_x) layer as a function of oxygen exposure (a) Linear scale and (b) Log scale

4.3.5.1.(2). Atomic Ratio of Ti_{total}/Ni_{total} and Thickness

We have determined the thickness of the oxide layer and the elemental atomic ratio of Ti_{total} to Ni_{total}. The ratios were calculated using the area of the Ti 3p and Ni 3p core level XPS spectra obtained from deconvolution of each peak and atomic cross sections.

Figure 4.35 shows the ratio and thickness of the oxide layer as a function of oxygen exposure at room temperature and 200°C. A gradual increase in the thickness and Ti_{total}/Ni_{total} ratio are observed at room temperature throughout the oxygen dose. After 9059 L O_2, the calculated oxide thickness and atomic ratio are 19.5 Å and 1.07, respectively. Oxidation at 200°C proceeds much differently (Figure 4.35(b)). In the figure, a progressive increase in the Ti/Ni ratio up to 19 L is followed by a rapid rise until 159 L after which no Ni is observed under these conditions. The estimated ratio

is 243.59 after 159 L oxygen. An oxide thickness of 33.52 Å at 200 °C is determined after the dose of 9059 L and no Ni 3p is detectable.

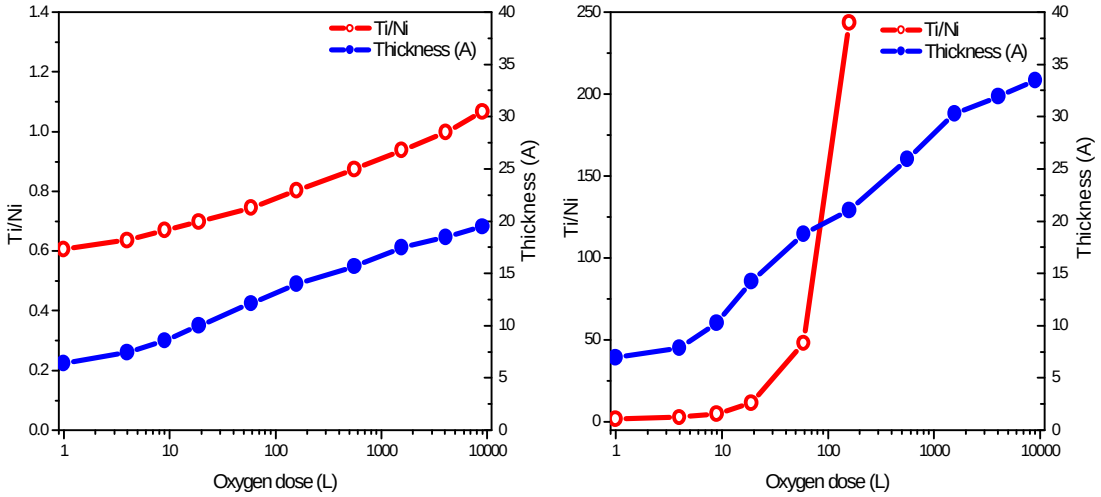

Figure 4.35. The Ti_{total}/Ni_{total} atomic ratio and oxide layer thickness as a function of oxygen dose at (a) room temperature and (b) 200 °C

4.3.5.1.(3). Crystal Structure

The Near-edge X-ray Absorption Fine Structure (NEXAFS) technique has been applied to characterize the oxidation states of the Ar^+ sputtered Nitinol surface oxidized by exposure to pure oxygen at two different temperatures. NEXAFS is ideally suited to this study due to the sensitivity of the Ti L-edge features to local bonding environment. Therefore, NEXAFS has provided crucial information about crystal structure and oxidation states of various forms of titanium oxides and complements the XPS data during the initial oxidation stages.

The electron-yield NEXAFS spectra of the Ti L-edge of NiTi as a function of oxygen exposure are shown in Figure 4.36. In the figure, spectra have been normalized to give the same height of the most intense peak. From the Ti L-edge spectrum measured after repeated cycles of Ar^+ bombardment, it is apparent that pure metallic Ti is not formed by sputtering the NiTi surface. We suggest here that reduction to pure metallic Ti is not favored with a bulk composition of NiTi.

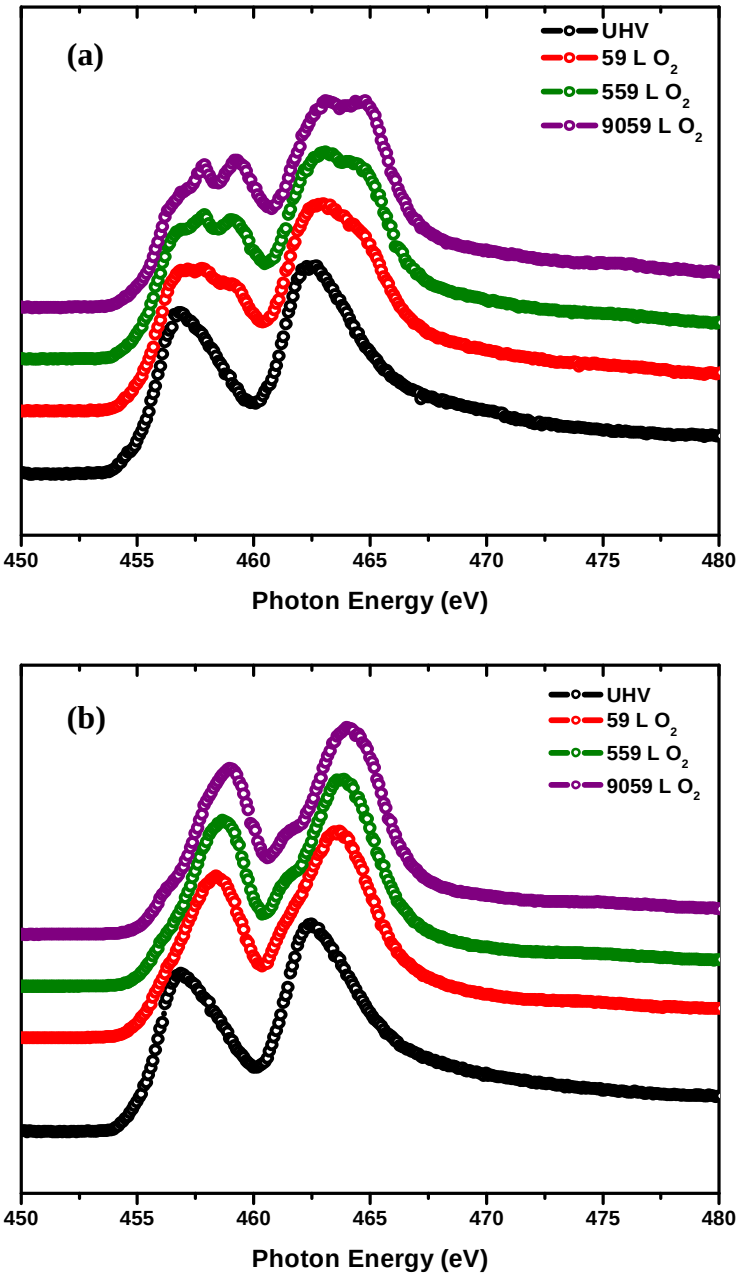

Figure 4.36. Normalized Ti L-edge NEXAFS spectra as a function of oxygen exposure at (a) room temperature and (b) 200 °C

Previous studies on single crystal (Lusvardi et al. 1998) and polycrystalline (Soriano et al. 1993) TiO_2 have shown that Ar^+ sputtering produces a partial reduction of Ti ions and generates a surface which contains a combination of reduced cations, including Ti_2O_3 (Ti^{+3}) and TiO (Ti^{+2}). One can compare the Ti L-edge of Ti metal, which has a prominent feature at 455 eV (Soriano et al. 1993), with our results shown in Figure 4.36. This comparison confirms that metallic Ti (Ti^0) is also present

in the altered layer of NiTi. Also, a detailed analysis of deconvoluted Ti 3p XPS spectra verifies the presence of metallic Ti. Hence, our clean NiTi surface after Ar^+ sputtering is oxygen deficient and compromised of a mixture of Ti species (Ti^{+4}, Ti^{+3}, Ti^{+2}, and Ti^0). The Ti L-edge spectrum of clean NiTi has two broad main structures observed between 450 and 470 eV.

Dosing 59 L oxygen at room temperature produces prominent changes in the spectrum. Broad features of the Ar^+ cleaned sample consist of a single doublet. Increasing the oxygen exposure to 559 L results in the appearance of a second doublet at 457 - 461 eV and 464 eV. The second doublet becomes more pronounced upon dosing to 9059 L of oxygen. A gradual decrease in intensity and a shift to higher energy for the leading (first) peak at 457 eV and the appearance of second doublet upon oxygen exposure is associated with a progressive transition to TiO_2, supporting the observed trend in the XPS spectra. Lusvardi et al. (Lusvardi et al. 1998) observed an energy shift to higher photon energy in the Ti L-edge from TiO to Ti_2O_3 to TiO_2; consistent with the results of Soriano et al. (Soriano et al. 1993), and thus the comparison with these early studies confirms the gradual transform to TiO_2.

Oxidation at 200 °C produces a different trend in the Ti L-edge features (Figure 4.36(b)). The changes on the NEXAFS spectra at 200 °C were less pronounced than in the case of room temperature. On dosing, there is a dramatic change on the spectra with no resolved doublets. A sharp transition was observed with the oxygen dose of 59 L. This big difference on the Ti L-edge spectra at two different temperatures can be attributed to the different concentrations of Ti states in the oxide layer. As we have discussed earlier, the quantitative analysis of XPS spectra yield that the relative % atomic concentration of Ti^{+3} and Ti^{+2} species is explicitly higher at 200 °C. Since the spectral region in the Ti L-edge spectra is very sensitive to the local environment, and therefore changes in the surface composition at 200 °C result significant difference in the absorption spectra.

4.3.5.2. Oxidation at High Pressure of Oxygen

4.3.5.2.(1). XPS Spectra

In order to see the changes in the chemical states of Ti under high pressure, we introduced 100 mTorr of oxygen after the final dose (9059 L). Figure 4.37 shows the Ti 3p core level XPS spectra of the NiTi alloy after the oxygen exposure. Photoemission spectra collected at room temperature in the presence of 100 mTorr oxygen indicate that various states of Ti (Ti^{+3}, and Ti^{+2}) are still present in the oxide layer with the dominant contribution from Ti^{+4}. However, Ti^{+4} cations were the only species detected at 200 °C suggesting that a complete oxidation of Ti took place. At this point, the Ti 3p spectrum consists of pure Ti^{+4} states. This observation is consistent with NEXAFS spectra (Figure 4.38). Although the high amount of oxygen is provided, the surface at room temperature does not tend to be oxidized due to the less amount of Ti atom provided by bulk material. It is interesting to note that Ni remained in metallic state even after high pressure of oxygen.

The thickness of the TiO_2 layer at room temperature was determined to be about 19.5 Å after the oxygen dose of 9059 L. After exposing 100 mTorr of oxygen, the thickness increased to 27.6 Å. With the sample at 200 °C, the thickness was 33.52 Å after 9059 L and after exposing 100 mTorr of oxygen we could not determine the thickness because the metallic Ti contribution top the Ti 3p core level was below our detection limit. At higher oxygen exposure Nitinol is fully oxidized at 200 °C, but four components of Ti (Ti^{+4}, Ti^{+3}, Ti^{+1}, Ti^{0}) have been observed at room temperature. For 200 °C, only one phase of Ti (TiO_2) is detected. High temperature increased the TiO_2 by lowering in three Ti_2O_3, TiO, and Ti contents. From the comparison of Ti 3p XPS spectra obtained at room temperature and 200 °C, we conclude that the process does not involve the complete oxidation of Ti even for the depth of the order of the XPS escape depth (~50 Å).

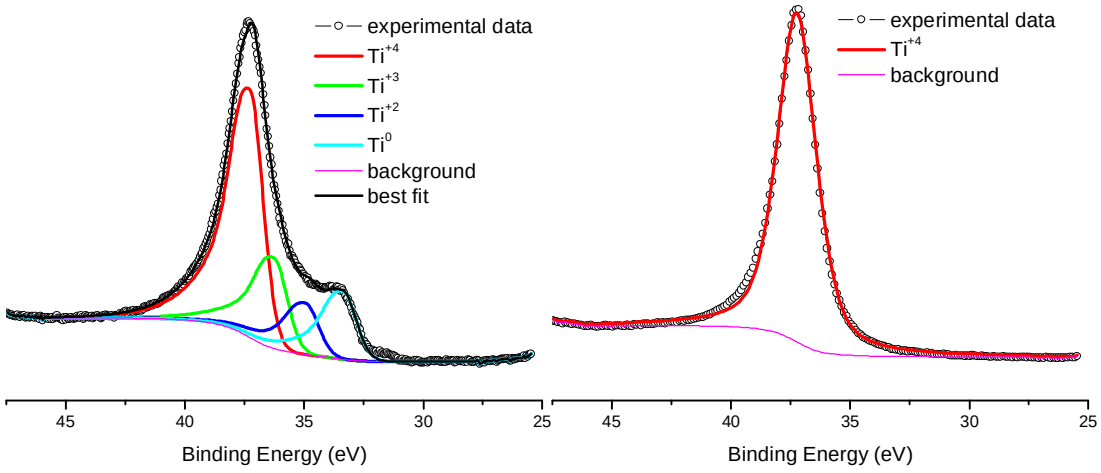

(a) **(b)**

Figure 4.37. Deconvoluted Ti 3p XPS spectrum measured in presence of 100 mTorr oxygen at (a) room temperature and (b) 200 °C

4.3.5.2.(2). Atomic Ratio of Ti_{total}/Ni_{total} and Thickness

The Ti_{total}/Ni_{total} atomic ratio for room temperature increased to 1.72 after exposing of 100 mTorr oxygen. However, due to a complete formation of TiO_2 surface layer in the case of 200 °C, the signal of metallic Ti coming from the bulk material was totally attenuated. At this point, we could not be able to determine the oxide thickness.

4.3.5.2.(3). Crystal Structure

Figure 4.38 shows the Ti 2p NEXAFS spectra of Nitinol measured under the 100 mTorr oxygen. In the figure, the two doublets become well resolved at both temperatures and new peaks develop (insets in Figure 4.38). In particular, it is apparent that in the high photon energy range, new features are more structured at 200 °C, in contrast to room temperature. The shape of the observed spectra at both temperatures are similar to the spectrum of Ti^{+4} (TiO_2) reported in the literature (Lusvardi et al. 1998). The main structures of the spectra are the two doublets, observed between 455 and 470 eV. The presence of two doublets arises from the spin-orbit interaction of Ti 2p core-level which splits the core-level into a lower and

higher energy level, $2p_{3/2}$ and $2p_{1/2}$, respectively (Soriano et al. 1993, van der Laan 1990). Two doublets observed in the spectrum originate primarily from an electron transfer from the Ti $2p_{3/2}$ or Ti $2p_{1/2}$ core levels to the Ti 3d orbitals in TiO_2, which split into t_{2g} and e_g orbitals in the octahedral symmetry (Soriano et al. 1993, Van der Laan 1990). The first peak in the doublet has been assigned to transition to the t_{2g} orbital and the second one to the e_g orbital of TiO_2.

Well-resolved prominent features in the Ti L-edge spectra (Figure 4.38) are labeled a, b, c, and d. The most striking observations from two spectra are: the difference in the dip between the peaks b and c, the sharpness of peak a, and the shoulder on the low energy side of peak a. For the room temperature spectrum, the first doublet (peaks a and b) is less separated than in the spectrum taken at 200 °C. Feature a, centered around 458 eV, has sharp structure for both temperatures. The energy difference between the peaks a and c, which is due to spin-orbit splitting, is 5.30 eV for room temperature and 5.41 eV for 200 °C. The energy separation of peaks c and d is 1.71 eV for room temperature, and 1.94 eV for 200 °C. Brydson et al. (Brydson et al. 1989) have investigated the Ti 2p edge of two TiO_2 crystallographic phases rutile and anatase. In the study, the obtained spin-orbit splitting is 5.4 eV for both phases, and the energy difference between peaks c and d is reported as 2.45 and 1.97 eV for rutile and anatase respectively. Although the peak energy positions are almost the same for rutile and anatase, the shapes of these peaks are different for the two crystallographic phases depending on the ligand coordination (Soriano et al. 1993). We can derive that NEXAFS spectra measured at both temperatures have similar features as TiO_2, i.e. the pure Ti^{+4} oxidation state is the most likely to occur under the high oxygen pressure.

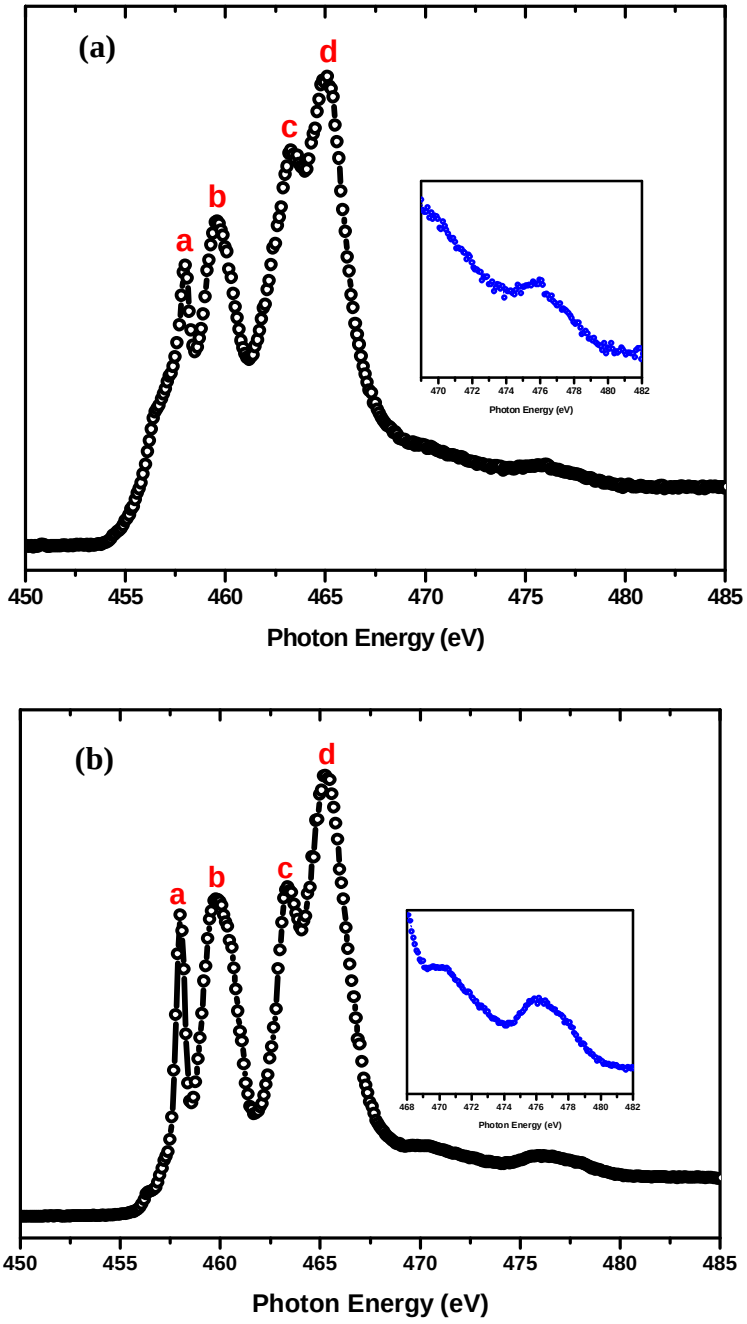

Figure 4.38. Normalized Ti L-edge NEXAFS spectra measured under 100 mTorr oxygen at (a) room temperature and (b) 200 °C

4.3.6. Discussion

Calculations based on the analysis of the Ti 3p core level XPS spectra show that an oxide layer about 19.5 Å in thickness forms on the NiTi sample upon oxidation at room temperature, whereas for the case of sample oxidation at 200 °C, an oxide layer about 33.52 Å in thickness forms for initial oxidation up to oxygen exposure of 9059 L. For both temperatures, the oxide layer was mainly composed of TiO_2. Depending on the temperature, different relative concentrations of TiO_2 (Ti^{+4}), Ti_2O_3 (Ti^{+3}), and TiO (Ti^{+2}) was found in the oxide layer indicating that the composition of oxide layer and its stability depend on the oxidation temperature. High temperature increased the concentrations of lower oxides and reduced the concentration of TiO_2 in the initial oxidation phase. Higher relative concentration of lower oxidation states of titanium (Ti^{+3} and Ti^{+2}) are formed at 200 °C and this finding is consistent with the previous studies on pure Ti (Vaquila et al. 1996). In this study, the formation of lower oxidation states of titanium at temperatures above 350 °C was reported. Other studies on the oxidation of Ti at temperatures below 200 °C concluded that the initial fast-linear oxidation was followed by a slow-logarithmic oxide growth (Vergara et al. 2002, Vaquila et al. 1997). The rapid initial oxidation was explained by the formation of oxide layer by virtue of dissociation of oxygen and site exchange. The followed slow oxidation was associated with a slowing down in the oxygen migration capability due to the passivating TiO_2 film formed at the surface. The TiO_2 oxide film limits the free oxygen diffusion to the bulk facilitating further oxidation.

The observed structure of thickness curves as a function of oxygen dose indicates that the oxide growth in the initial phases of oxidation is approximately logarithmic for both temperatures (Figure 4.34(a)). The oxide growth rate increases at 200 °C and this finding shows that the oxide growth is dependent on temperature. Depending on the strength of the oxide bond, metal oxides are classified as network modifiers, intermediates, and network formers (Fehlner et al. 1970, Jacobsen et al. 1995). Titanium is categorized as a network former. Network-forming oxides allow anion migration. Hence, TiO_2 is an anion conductor and the oxide layer grows by

migration of oxygen ions. In this class of oxides, the number of ions and the reaction rate is sensitive to oxygen pressure. In the case of NiTi, no distinct effect of oxygen exposure pressure on the oxide growth for pressures of 10^{-7}, 10^{-6}, and 10^{-5} T was observed (Figure 4.34(b). Therefore, the oxide growth is found to be relatively insensitive to oxygen partial pressure, indicating that incorporation of oxygen atoms at the surface does not limit the oxidation process in this low pressure regime.

The oxide growth on a clean metallic surface begins with chemisorption of oxygen and the first layer is formed by dissociative chemisorption of oxygen molecules. This is followed by a fast oxidation in the early stages which is promoted by electron tunneling from the metal to form oxygen ions on the initial oxide surface leading to an electric field across the growing oxide film which in turn assists ionic motion at or below room temperature (Fehlner et al. 1970, Jacobsen et al. 1995). The oxygen ions formed on the oxide surface set up a potential (Mott potential) across the oxide film (Mott 1939a, Mott 1939b, Mott 1947, Cabrera et al. 1948). This potential provides a driving force for continued oxidation. The effect of the built up field across the oxide is to lower the activation energy sufficiently for further oxidation. Hence, ion migration can occur. For the case of NiTi sample at 200 °C, our results show that the oxide layer growth increases with temperature, and at this point thermally activated processes limit the oxidation.

Core-level XPS in conjunction with NEXAFS forms a powerful tool to elucidate changes in the electronic and geometric structure under different conditions. Especially, NEXAFS provides a clear fingerprint for titanium oxides. Depending on the crystallographic structures as well as Ti reduction, the spectrum shows significant differences (Lusvardi et al. 1998, Soriano et al. 1993, Ruus et al. 1997, Groot et al. 1989). In particular, TiO_2 single crystals exhibit well-resolved peaks in the energy range between 455 and 470 eV corresponding to the various transitions from Ti 2p to Ti 3d levels (Lusvardi et al. 1998, Soriano et al. 1993, Diebold 2003). The Ti L-edge shows two groups of peaks arising from the spin-orbit splitting of the Ti 2p core level into $2p_{3/2}$ and $2p_{1/2}$ levels with ~6 eV energy separations. These levels are further split due to crystal-field effects (Lusvardi et al. 1998). This rich structure is absent in the case of Ti_2O_3 and TiO (Lusvardi et al.

1998). Their spectra present broader features, and the splitting due to crystal-field effects is quenched by the fact that the Ti 3d spectral weight is redistributed by the influence of the core hole. An analogous behavior is seen in the spectra of metallic Ti (Soriano et al. 1993). Comparing our results measured at low oxygen exposures with the NEXAFS spectra of TiO, TiO_2, and Ti_2O_3 (Lusvardi et al. 1998), as well as of metallic Ti (Soriano et al. 1993), we can conclude that the spectral features of the oxidation layer of NiTi at room temperature and 200 °C have strong contributions from Ti^{3+} and Ti^{2+} suboxides as well as metallic Ti. On the other hand, oxidation under high pressure produced significant changes in the NEXAFS spectra relative to room temperature. At 200 °C, lower states of Ti were completely oxidized to Ti^{+4}. This result suggests that significant rearrangement of the surface occurs at this temperature. The NiTi surface at room temperature is an intermediate surface between sputtered and the fully oxidized surfaces. Even at high oxygen pressure, it still contains the lower states of Ti with the Ti^{+4} cations (54% of the overall Ti concentration). On the contrary, the near surface region of the NiTi can be completely oxidized by dosing 100 mTorr oxygen at 200 °C. The measured NEXAFS spectrum at this temperature is consistent with the structure of amorphous TiO_2 (Kucheyev et al. 2004). It is also interesting to note that the spectrum has a typical TiO_2 pre-edge feature which may be assigned to a spin-orbit forbidden transition ($p_{3/2} \rightarrow d_{3/2}$) as in the single crystal case (Brydson et al. 1989). Thus, this finding leads a conclusion that the surface of NiTi may consist of a mixture of various crystalline and amorphous phases at the higher temperature. The Ti 2p spectrum collected at room temperature can not be uniquely interpreted since the spin-orbit splitting as well as spectral shape does not agree with those reported for rutile, anatase, or amorphous TiO_2 (Brydson et al. 1989, Kucheyev et al. 2004). But combining with the XPS results it is clear that the oxide layer formed at room temperature has a high degree of disorder.

According to our XPS results, oxidation of Ni was not observed at room temperature (or 200 °C) even under 100 mTorr of oxygen in spite of the fact that NiTi contains a large amount of Ni. The reason is that the difference in the oxygen affinity between Ti and Ni. The free energy of formation ΔG of TiO, TiO_2, and NiO

at room temperature is -118.3, -212.6, and -50.6 kcal mol^{-1}, respectively, and these thermodynamic data strongly imply that the oxidation of Ti is a much more favorable process than the oxidation of Ni (Chan et al. 1990). The growth of TiO_2 is the primary contributor to the oxide thickness during the initial stages of oxidation at both temperatures and therefore a fast oxide formation occurs. A progressive formation of a stoichiometric TiO_2 layer is observed with suboxides (Ti_2O_3 and TiO) appearing underneath at the TiO_2-NiTi interface. Ni remains in its metallic state even under high pressure of oxygen. Due to the evoluation of oxide layer, Ni atoms are liberated from the Ni-Ti interatomic bonds. These Ni atoms are lattice defects, intersititial atoms in the structure of the Ti-surface oxides (Shabalovskaya et al. 2009). The sites of the missing oxygen atoms in the non-stoichiometric Ti-surface oxides can present structural oxygen vacancies that can be used by Ni atoms to migrate through the Ti oxides (Shabalovskaya et al. 2009). Thus, the diffusion of Ni atoms through surface oxides can occur effectively at low temperatures (60-160°C) (Shabalovskaya et al. 2009). Furthermore, the smaller size of Ni atoms, as compared with Ti and oxygen atoms, also helps the diffusion of the Ni through an interstitial path (Shabalovskaya et al. 2009). A vacancy mediated diffusion mechanism has been suggested to provide diffusion of Ni in NiTi (Divinski et al. 2009). In that situation, it has been shown that metallic Ni may interact with Ti suboxides ions and thus providing a driving force for the diffusion of nickel through oxide layer (Espinos et al. 1993). A migration of metallic Ni occurs in the deeper layers leading to its disappearance from the surface. In our study, no Ni signal was detected at 200 °C after the oxygen dose of 159 L. The absence of Ni in the analyzed layer suggests that a nickel-rich phase might be formed underneath the oxide layer. Earlier investigations on NiTi oxidation regarding the formation of a Ni-rich layer support this claim (Pelton et al. 2005, Tiana et al. 2009). In these studies, it has been shown that at high temperatures a Ni-rich layer forms at the bulk-oxide interface and this layer was identified as Ni_3Ti using various analysis methods (Pelton et al. 2005, Shabalovskaya et al. 2009, Tian et al. 20092). Pelton at al. (Pelton et al. 2005), it has been also pointed out that continued oxide growth involved simultaneous nucleation and growth of TiO_2 and Ni-rich phases. Therefore, our findings are good agreement

with the results in the literature. It can be concluded that the preferential oxidation of Ti at high temperature creates a Ni-rich region between the oxide layer and NiTi bulk material. Accumulation of a higher density of Ni atoms in such a layer can be a potential reservoir for enhanced and lasting release that inevitably could affect the biological performance of implant devices made of NiTi. In the view of biocompatibility, the formation of a Ni-rich layer underneath the TiO_2 surface leads to poor corrosion (Trépanier et al. 2003). At high temperature, the oxide layer is thicker. This thick layer can easily form cracks in vivo and harmful Ni ions which can create inflammation or stimulate intimal hyperplasia (Franca et al. 2008) can release to surrounding living cells.

5. CONCLUSION

The presented studies in this thesis can be grouped into three parts.

In the first part of work (section 4.1), the design and construction of a new Ambient Pressure X-ray Photoelectron Spectroscopy (APXPS) endstation at beamline 9.3.2 of the Advanced Light Source (ALS) is described. The mission of beamline 9.3.2 is to provide state-of-the-art ***in situ*** characterization for catalysis and materials science using X-ray Photoelectron Spectroscopy, which will be greatly served by this new endstation. This new endstation provides a manyfold enhancement in photoelectron (PE) transmission, therefore a better signal-to-noise ratio and decreased acquisition time. Additionally, an imaging mode and an angle resolved mode has been developed. By recording spatial and angular information, one can obtain detailed insights from each collected PE. Improved spatial resolution up to ~16 μm provides the ability to study structured materials with junctions on the scale of tens to hundreds of microns, such as batteries, solid oxide electrochemical cells, gas sensors, etc. On the other side, angle resolved APXPS offers the possibility of directly mapping the electronic structure of catalysts under relevant operating conditions. The measured electronic structure of model catalysts under reaction condition can be directly compared with theoretical calculations. With many additional APXPS systems in development or being planned at synchrotron facilities around the world, this technique is poised to reveal new insights into the structure of catalysts, the mechanisms of corrosion, and many other important industrial and environmental processes.

Looking ahead concerning APXPS, much higher pressures (15-20 Torr regime), better energy resolutions, and shorter timescales (millisecond range) can be expected with a combination of brighter X-ray sources, better differential pumping systems, more efficient detectors, and higher throughput spectrometers. Being able to collect data under operating conditions would open up numerous applications in biological and environmental science.

In the second part (section 4.2), a systematic investigation of the CO and O_2 co-adsorption and catalytic oxidation of CO on a Pt(110) surface using APXPS at

various temperatures and pressures was presented. Experimental findings suggest that the CO molecules occupy both bridge and on-top sites at room temperature. As the temperature increases, the number of the bridge site CO molecules is reduced and completely disappeared above 100 °C and only CO molecules absorbed at on-top site remain. We also observe a reaction peak in the C1s spectra that is associated with CO oxidation. During CO oxidation, the surface chemical composition and surface reactivity under both O_2 rich and CO rich environments have been monitored. No surface oxides were detected under either experimental condition; the chemisorbed oxygen surface formed under 200 mTorr O_2 can lead to a high reaction rate, but it is not stable under the reaction conditions described here. At given temperature and pressure, the high reaction rate observed in Region C (O_2 rich) can be explained by the Langmuir–Hinshelwood mechanism.

The surface characterization of NiTi shape memory alloy was reported in the last part (section 4.3), in particular the initial oxidation results. Although much research has been conducted on Nitinol there is a dearth of information in the literature regarding the initial oxidation mechanism of NiTi. The primary goal of this part of study is to determine the role of the temperature on the formation of passivation layer on NiTi during initial oxidation. In-situ X-ray Photoelectron Spectroscopy (XPS) and Near Edge X-ray Absorption Fine Structure (NEXAFS) spectroscopy has been used to investigate variations in the composition of the outermost layer (or oxide layer) and its structure, caused by exposure of pure O_2 at two temperatures (room temperature or 300 K and 200 °C or 473 K) and two pressure regimes. It was found that, the oxidation process at low temperature is dominated by diffusion of the oxygen flux. The surface is dominated by the TiO_2 phase. At elevated temperatures (200 °C), Ti atoms in the NiTi alloy start to move. Due to the free energy and mobility difference, there is an effective movement of Ti atoms towards the surface to react with oxygen. For a given dosage of oxygen, there can be too many Ti atoms move to the near surface region to form stoichiometric TiO_2. Therefore, more TiO and Ti_2O_3 phase are found at 200 °C. Because of such a Ti movement, Ni atoms are driven inward. This is observed through the sudden disappearance of Ni signal from the surface. The Ni concentration below the Ti oxide

layer will increase accordingly. Therefore it is not a surprise that $TiNi_3$ phase was observed underneath the Ti oxide layer. As the oxidation continues, more Ni atoms will cluster together to convert $TiNi_3$ layer into larger Ni clusters, which will limit the movement of Ni atoms further. As the oxide front moving inwards, such a process will repeat itself again and again at different depths. This result explains why layers of Ni cluster embedded in the thick TiO_2 have observed at high temperature. At room temperature, the oxidation is dominated by the diffusion of oxygen. Very small cluster of Ni or Ni rich alloy cluster will be formed. TiO_2 tends to be amorphous. At high temperature, both oxygen diffusion and Ti and Ni movements play important roles. The chemical composition of the surface oxides depend on the exact temperature and oxygen pressure. In general, the Ni will form large clusters inside Ti oxide layer. TiO_2 layer will be thicker and tends to be polycrystalline at high temperature. All these will contribute to the biocompatibility of TiO_2 passivation film.

REFERENCES

ACKERMANN, M. D., PEDERSEN, T. M., HENDRIKSEN, B. L. M., ROBACH, O., BOBARU, S. C., POPA, I., QUIROS, C., KIM, H., HAMMER, B., FERRER S., FRENKEN, J. W. M., 2005. Phys. Rev. Lett. 9, 255505.

ACKERMANN, M. D., 2007. Operando SXRD: A new view on catalysis, Ph.D. Thesis Leiden University, Netherlands.

ARMITAGE, D. A., and GRANT, D. M., 2003. Mater. Sci. Eng. A349, 89.

ATTWOOD, D. T., HALBACH, K., and KIM, K.-J., 1985. Tunable Coherent Radiation. Science 228, 1265.

ATTWOOD, D., 1999. Soft X-rays and Extreme Ultraviolet Radiation Principles and Applications. Cambridge University Press, Cambridge, New York.

AULICH, H., NEMEC, L., CHIA, L., DELAHAY, P., 1976. J. Electron Spectrosc. Relat. Phenom. 8, 271.

BALLARD, R. E., BARKER, S. L., GUNNELL, G. G., HAGAN, W. H., PEARCE, S. J., WEST, R. H., 1978. J. Electron Spectrosc. Relat. Phenom. 14, 331.

BALLARD, R. E., GUNNELL, G. G., HAGAN, W. H., 1979. J. Electron Spectrosc. Relat. Phenom. 16, 435.

BARINOV, A., DUDIN, P., GREGORATTI, L., LOCATELLI, A., MENTES, T. O., NINO, M. A., and KISKINOVA, M., 2009. Nucl. Instrum. Methods Phys. Res., Sect. A 601, 195-202.

BARRIE, A., SWIFT, P. W., and BRIGGS, D., 1976. preprints ,27th Pittsburgh Conference on Analytical Chemistry and Applied Spectroscopy, Cleveland, USA.

BAUMBERGER, F., GREBER, T., and OSTERWALDER, J., 2001. Physical Review B 64, 195411.

BEAMSON, G., PORTER, H. A., and TURNER, D. W., 1981. Nature 290, 556.

BEAMSON, G., and BRIGGS, D., 1992a, High Resolution XPS of Organic Polymers. John Wiley and Sons, Chichester, UK.

BEAMSON, G., and BRIGGS, D., 1992b. Mol.Phys.76 , 919.

BJÖRNEHOLM, O., NILSSON, A., TILLBORG, H., BENNICH, P., SANDELL, A., HERNNAS, B., PUGLIA, C., MARTENSSON, N., 1994. Surf. Sci. 315, L983.

BLUHM, H., OGLETREE, D. F., FADLEY, C. S., HUSSAIN, Z., SALMERON, M., 2002. J. Phys. Cond. Matter. 14, L227-L233.

BLUHM, H., HAVECKER, M., KNOP-GERICKE, A., KLEIMENOV, E., SCHLÖGL, R., TESCHNER, D., BUKHTIYAROV, V. I., OGLETREE, D. F., and SALMERON, M., 2004. J. Phys. Chem. B 108, 14340-14347.

BLUHM, H., ANDERSSON, K., ARAKI, T., BENZERARA, K., BROWN, G. E., DYNES, J. J., GHOSAL, S., GILLES, M. K., HANSEN, H.-Ch., HEMMINGER, J. C., HITCHCOCK, A. P., KETTELER, G., KILCOYNE, A. L. D., KNEEDLER, E., LAWRENCE, J. R., LEPPARD, G. G., MAJZLAM, J., MUN, B. S., MYNENI, S. C. B., NILSSON, A., OGASAWARA, H., OGLETREE, D. F., PECHER, K., SALMERON, M., SHUH, D. K., TONNER, B., TYLISZCZAK, T., WARWICK, T., YOON, T.H., 2006. J. Electron, Spectrosc. Relat. Phenom. 150, 86.

BLUHM, H., HAVECKER, M., KNOP-GERICKE, A., KISHINOVA, M., SCHLÖGL, R., and SALMERON, M., 2007. MRS Bull. 32, 1022-1030.

BLUHM, H., 2009. J. Electron Spectrosc. Relat. Phenom. 177, 71-84.

BLUHM, H., HAVECKER, M., IHMANN, K., KLEIMENOV, E., TESCHNER, D., OGLETREE, D. F., SALMERON, M., KNOP-GERICKE, A., SCHLÖGL, R., in preparation.

BLYHOLDER, G., 1964. J. of Chem. Phys. 68, 2772.

BOBARU, S. C., 2006. High-pressure STM studies of oxidation catalysis, Ph.D. Thesis, Leiden University, Netherlands.

BOUDART, M., and DJEGA-MARIADASSOU, G., 1984. 1984. Kinetics of Heterogeneous Catalytic Reactions, Princeton University Press, Princeton, NJ.

BRIGGS, D., and GRANT J. T., 2003. Surface Analysis by Auger and X-ray Photoelectron Spectroscopy, IM Publications.

BROWN, S. S., and SUNDERMAN, F. W., 1985. Progress in Nickel Toxicology. Blackwell, Ltd, 1- 244

BRUCHE, E., and JOHANNSON, H., 1932. Ann. Phys. 15, 145-166.

BRUNDLE, C. R., and ROBERTS, M. W., 1972. Proc. Roy. Soc. A 331, 383.

BRYDSON, R., SAUER, H., ENGEL, W., THOMAS, J. M., ZEITLER, E., KOSUGI, N., and KURODA, H., 1989. J. Phys. Condens. Mat. 1, 797.

BUEHLER, W. J., WILEY, R. C., 1965. Nickel-Based Alloys. USA Patent No. 3,147,851.

CABRERA, N., and MOTT, N. F., 1948. Rep. Prog. Phys. 12, 163.

CAMPBELL, C.T., ERTL, G., KUIPERS, H., SEGNER, J., 1980. J. Chem. Phys. 73, 5862.

CARLSON, T. A., and MCGURIE, G. E., 1972/1973. J. Electron Spectrosc. Relat. Phenom. 1, 161.

CASALIS, L., JARK W., KISKINOVA, M., LONZA, D., MELPIGNANO, P., MORRIS, D., ROSEI, R., SAVOIA, A., ABRAMI, A., FAVA, C., FURLAN, P., PUGLIESE, R., VIVODA, D., SANDRIN, G., WEI, F.-Q., CONTARINI, S., DEANGELIS, L., GARIAZZO, C., NATALETTI, P., and MORRISON, G. R., 1995. Rev. Sci. Instrum**.** 66, 4870-4875.

CAZAUX, J., doi:10.1016/j.elspec.2009.03.007. J. Electron Spectrosc. Relat. Phenom.

CHANEY, R. L., 1977. Surf. Interface Anal. 10, 36.

CHAN, C.M., TRIGWELL, S., and DUERIG, T., 1990. Surf. Interface Anal. 15, 349-354.

CHASTAIN, Ed. J., 1992. Handbook of X-ray photoelectron spectroscopy, Perkin-Elmer Corporation.

CHEN, M. S., CAI, Y. YAN, Z., GATH, K. K., AXNANDA, S., GOODMAN, D. W., 2007. Surf. Sci. 601, 5326.

CHU, C. L., WU, S. K., and YEN, Y. C., 1996. Mater. Sci. Eng. A216, 193.

CHU, C. L., WANG, R., HU, M. T., YIN, L. H., PU, Y. P., and LIN, P. H., 2008. Mater Sci Eng, C C28, 1430–1434.

CHUNG, J. Y., AKSOY, F., GRASS, M. E., KONDOH, H., ROSS, P., LIU, Z., and MUN, B. S., 2009. Surf. Sci. 603, L35-L38.

CLARK, D. T., and DILKS, A., 1976. ESCA studies of polymers. VII. Shake-up phenomena in some alkane-styrene copolymers Journal of Polymer Science Polymer Chemistry Edition Vol. 14, 533-542.

COULSTON, G. W., THOMPSON, E. A., and HERRON, N., 1996. Journal of Catalysis 163, 122-129.

COXON, P., KRISEK, J., HUPHERSON, M., and WARDELL, I. R. M., 1990. J. Electron Spectrosc. Relat. Phenom. 52, 821.

DAMASCELLI, A., HUSSAIN, Z., and SHEN, Z. X., 2003. Rev. Mod. Phys. 75, 473.

DE GROOT, F. M. F., GRIONI, M., FUGGLE, J. F., GHIJSEN, J., SAWATZKY, G. A., and PETERSEN, H., 1989. Phys. Rev. B 40, 5715.

DIEBOLD, U., 2003. Surf. Sci. Rep. 48, 53.

DIVINSKI, S. V., STLOUKAL, I., KRAL, L., and HERZIG, Chr., 2009. Defects and Diffusion Forum, Vols. 289-292, 377-382.

DUERIG, T., PELTON, A., and STOCKEL, D., 1999. Mater. Sci. Eng., A 273–275, 149.

ELDER, F. R., GUREWITSCH, A. M., LANGMUIR, A. M., POLLOCK, H. C., 1947. Phys Rev 71:829-830.

ERTL, G., 1983. Catalysis: Science and Technology, vol. 4, Springer-Verlag, Berlin, 245.

ERTL, G., 1994. Surf. Sci. 299/300, 742.

ERTL, G., KNÖZINGER, H., and WEITKAMP, J., 1997. Handbook of Heterogeneous Catalysis, Wiley, New York,

ESPINOS, J. P., FERNANDEZ, A., GONZALEZ-ELIPE, A. R., 1993. Surf. Sci., 295: 402–410.

FADLEY, C. S., HAGSTROM, S. B. M., HOLLANDER, J. M., KLEIN, M. K., and SHIRLEY, D. A., 1967. Science 157, 1571.

FADLEY, C. S., HAGSTROM, S. B. M., HALLANDER J. M., KLEIN, M. K., and SHIRLEY, D. A., 1968. J. Chem. Phys. 48, 3779.

FADLEY, C. S., 1978. Electron Spectroscopy: Theory , Techniques and Applications, Vol.2, Academic Press, London ,UK, p. 99.

FADLEY, C. S., 2010. Electron Spectrosc. Relat. Phenom. 178–179, 2–32.

FEHLNER, F. P., and MOTT, N. F., 1970. Oxidation of Metals, Vol. 2, No.1.

FELDEGG, H. F., SIEGBAHN, H., ASPLUND, L., KELFVE, P., SIEGBAHN, K., 1975. J. Electron Spectrosc. Relat. Phenom. 7, 421.

FENG, J., and SCHOLL, A., 2008. Science of Microscopy, Springer, pp. 657-695.

FIRSTOV, G., VITCHEV, R. G., KUMAR, H., BLANPAIN, B., and VAN HUMBEECK, J., 2002. Biomaterials 23, 4863–4871.

FOHLISCH, A., WASSDAHL, N., HASSELSTROM, J., KARIS, O., MENZEL, D., MARTENSSON, N., NILSSON, A., 1998. Phys. Rev. Lett. 81, 1730.

FORSYTH, N. M., and COXON, P., 1994. Surf. Interface Anal. 21, 430.

FRANCA, L. H. G. et al., 2008. Update on Vascular Endoprostheses (Stents): from Experimental Studies to Clinical Practice," Jornal Vascular Brasileirovol 7, no. 4 Porto Alegre, 351–363.

FREYER, N., KISKINOVA, M., PIRUG, G., BONZEL, H.P., 1986. Surf. Sci. 166, 206.

GABASCH, H., KNOP-GERICKE, A., SCHLÖGL, R., BORASIO, M., WEILACH, C., RUPPRECHTER, G., PENNER, S., JENEWEIN, B., HAYEK, K., and KLOTZER, B., 2007. Phys. Chem. Chem. Phys. 9, 533-540.

GATES, B. C., KNOEZINGER, H., and JENTOFT, F., 2009. Advances in Catalysis, Academic Press.

GELIUS, U., WANNBERG, B., BALZER, P., FELLNER-FELLDEG, H., CARLSSON, G., JOHANSSON, C. G., LARSON, J., MUNGER, P., and VEGERFORS, G., 1990. J. Electron Spectrosc. Relat. Phenom. 52, 747.

GHOSAL, S., HEMMINGER, J. C., BLUHM, H., MUN, B. S., HEBENSTREIT, E.L.D., KETTELER, G., OGLETREE, D. F., REQUEJO, F. G., and SALMERON, M., 2005. Science 307, 563-566.

GIL, F. X., MANERO, J. M., and PLANELL, J. A., 1996. J. Mater. Sci.- Mater. Med. 7, 403.

GIMENEZ, A. A., RIAMBAU, V., SERRA-BALDRICH, E., and CAMARASA, J. G. A., 2000. Contact Dermatitis, 43(1), 35.

GRASS, M. E., ZHANG, Y., BUTCHER, D. R., PARK, J. Y., LI, Y., BLUHM, H., BRATLIE, K. M., ZHANG, T., SOMORJAI, G., and ANGEW, G. A., 2008. Chem. Int. Ed. 47, 8893-8896.

GRASS, M. E., KARLSSON, P. G., AKSOY, F., LUNDQVIST, M., WANNBERG, B., MUN, B. S., HUSSAIN, Z., and LIU, Z., 2010. Review of Scientific Instrumens 81, 053106.

GREGORATTI, L., MENTES, T. O., LOCATELLI, A., and KISKINOVA, M., 2009. J. Electron Spectrosc. Relat. Phenom. 170, 13-18.

GRUNZE, M., DWYER, D. J., NASSIR, M., and TSAI, Y., 1992. ACS Symposium Series 482, 169–182.

GURKER, N., EBEL, M. F., and EBEL, H., 1983. Surf. Interface Anal. 5, 13.

GURKER, N., EBEL, M. F., EBEL, H., MANTLER, M., HEDRICH, H., and SCHON, P., 1987. Surf. Interface Anal. 10, 242.

GÜNTHER, S., KAULICH, B., GREGORATTI, L., and KISKINOVA, M., 2002. Progress in Surf. Sci. 70, 187-260.

GÜNTHER, S., SCHEIBE, A., BLUHM, H., HAEVECKER, M., KLEIMENOV, E., KNOP-GERICKE, A., SCHLÖGL, R., and IMBIHL, R., 2008. J. Phys. Chem. C 112, 15382-15393.

HAGSTRÖM, S., NORDLING, C., and SIEGBAHN, K., 1964. Z. Pyhs. 178, 439.

HENRICH, V. E., and COX, P. A., 1994. The Surface Science of Metal Oxides. Cambridge University Press, Cambridge.

HENDRIKSEN, B. L. M., FRENKEN, J. W. M., 2002. Phys. Rev. Lett. 89, 046101.

HENDRIKSEN, B. L. M., BOBARU, S. C., and FRENKEN, J. W. M., 2004. Surf.Sci. 552, 229.

HELMER, J. C., and WEICHERT, N. H., 1968. Appl. Phys. Lett. 13, 266.

HENKE, B. L., 1961. Adv. X-ray Anal. 4, 244.

HENKE, B. L., 1962. Adv. X-ray Anal. 5, 285.

HENKE, B. L., 1963. X-ray Optics and Microanalysis. Academic pres, New York, USA, p. 157.

HIMPSEL, F. J., AKATSU, H., CARLISLE, J. A., TERMINELLO, L. J., HUDSON, E. A., JIA, J. J., CALLCOTT, T. A., PERERA, R. C., SAMANT, M. G., STOHR, J., EDERER, D. L., 1994. Core-Level Spectroscopy of Thin Oxides and Oxynitrides, Proceedings of the Electrochemical Society Symposium "Silicon Nitride and Silicon Dioxide Thin Insulating FiIms" San Francisco, California May 22-27.

HUSSAIN, Z., HUFF, W. R. A., KELLAR, S. A., MOLER, E. J., HEIMANN, P. A., MCKINNEY, W., PADMORE, H. A., FADLEY, C. S., and SHIRLEY, D. A., 1996. J. Electron Spectrosc. Relat. Phenom. 80, 401-404.

INNES, P. D., 1907. Proc. Roy. Soc. , Ser. A 79, 442.

JACKSON, J. D., 1962. Classical Electrodynamics, Third Edition Wiley, New York.

JACOBSEN, F. M., RAAEN, S., RUCKMAN, M. W., and STRONGIN, M., 1995. Phys. Rev. B 52, 11339.

JENKIN, J. G., LECKEY, R. C. G., and LIESEGANG, J., 1977. J. Electron Spectrosc. Relat. Phenom. 12, 1.

JENKIN, J. G., RILEY, J. D., LIESEGANG, J., and LECKEY, R. C. G., 1978. J. Electron Spectrosc. Relat. Phenom. 14, 477.

JIA, W., BEATTY, M. W., REINHARDT, R. A., PETRO, T. M., COHEN, D. M., MAZE, C. R., STROM, E. A., and HOFFMAN, M., 1999. J. Biomed.Mater. Res. Part B 48, 488.

JOYNER, R. W., ROBERTS, M. W., and YATES, K., 1979a. Surf. Sci. 87, 501-509.

JOYNER, R. W., and ROBERTS, M. W., 1979b. Chemical Physics Letters 60, 459-462.

KEENLYSIDE, M., and PIANETTA, P., 1990. J. Electron Spectrosc. Relat. Phenom. 66, 189.

KELLY, M. A., and TYLER, C. E., 1973. Hewlett-Packard Journal 24, 2.

KELLY, M. A., SHEK, M. L., PIANETTA, P., GÜR, T. M., BEASLEY, M. R., 2001. J. Vac. Sci. Technol. A 19, 2127- 2133.

KETTELER, G., OGLETREE, D. F., BLUHM, H., LIU, H., Hebenstreit E. L. D., and SALMERON M., 2005. J. Am. Chem. Soc. 127, 18269-18273.

KIM, K.-J., 1989. Characteristics of Synchrotron Radiation in Physics of Particle Accelerators, AIP Conference Proceedings 184, Amer. Inst. Of Physics, New York, 565-632.

KIM, K.-J., 1995a. Characteristics of Synchrotron Radiation-X-Ray Data Booklet, Center of X-Ray Optics, Lawrence Berkeley National Laboratory.

KIM, K.-J., 1995b. Optical and Power Characteristics of Synchrotron Radiation Sources. Opt. Engr. 34, 342.

KLEIMENOV, E., 2005. High-pressure X-ray Photoelectron Spectroscopy Applied to Vanadium Phosphorus Oxide Catalysts Under Reaction Conditions, Ph.D. Thesis, Technische Universität Berlin, Germany.

KNAPP, G. S., KEENLYSIDE, M., and GRIFFIN, C., 1990. Surf. Interface Anal. 15, 786.

KOVNIR, K., ARMBRUSTER, M., TESCHNER, D., VENKOV, T. V., JENTOFT, F. C., KNOP-GERICKE, A., GRIN, YU., and SCHLOGL, R., 2007. Sci. Technol. Adv. Mat. 8, 420-427.

KREBS, R. E., 1998. Platinum. The History and Use of our Earth's Chemical Elements. Greenwood Press. 124–127.

KRISCHER, K., EISWIRTH, M., ERTL, G., 1992. J. Phys. Chem. 96, 9161.

KRISHNAKUMAR, E., and SRIVASTAVA, S. K., 1992. Int. J. Mass. Spectrom. Ion Processes 113, 1.

KUCHEYEV, S. O., BUUREN, T. V., BAUMANN, T. F., SATCHER, J. H., WILLEY, T. M., MEULENBERG, R. W., FELTER, T. E., POCO, J. F., GAMMON, S. A., and TERMINELLO, L, J., 2004. Phys. Rev. B 69, 245102.

LEE, J. D., 1972. Rev. Sci. Instrum. 43, 1291.

LEE, J. D., 1973. Rev. Sci. Instrum. 44, 893.

LI, W. X., OSTERLUND, L., VESTERGAARD, E. K., VANG, R. T., MATTHIESEN, J., PEDERSEN, T. M., LAEGSGAARD, E., HAMMER, B., BESENBACHER, F., 2004. Phys. Rev. Lett. 93, 146104.

LIBRA, J., and MATOLIN, V., 2006. Surf. Sci. 600, 2317-2322.

LUSVARDI, V. S., BARTEAU, M. A., CHEN, J. G., ENG, J. Jr., FRUHBERGER, B., and TEPLYAKOV, A., 1998. Surface Science, 397, 237-250.

MARS, P., KREVELEN, D. W. V., 1954. Spec. Suppl. Chem. Eng. Sci. 3, 41.

MASSIES, J., and CONTOUR, J. P., 1985. J. Appl. Phys. 58, 806.

MCCASH, E. M., 2002. Surface Chemistry, Oxford University Press.

MOBERG, R., BOKMAN, F., BOHMAN, O., SIEGBAHN, H., 1991a. J. Chem. Phys. 94, 5226.

MOBERG, R., BOKMAN, F., BOHMAN, O., SIEGBAHN, H., 1991b. J. Am. Chem. Soc. 113, 3663-3667.

MOTT, N. F., 1939a. Trans. Faraday Soc. 35, 1175.

MOTT, N. F., 1939b. Trans. Faraday Soc. 39, 472.

MOTT, N. F., 1947. Trans. Faraday Soc. 43, 429.

MULLER, U., and HAUERT, R., 1996. Thin Solid Films, 290-292, 323-327.

NEMEC, L., GAEHRS, H. J., CHIA, L., DELAHAY, P., 1977. J. Chem. Phys. 66, 4450.

NIEUWENHUYS, B. E., PONEC, V., KOTEN, G. V., LEEUVEN, P. W. N. M. V., and SANTEN, R. A., 1993. Bonding and elementary steps in catalysis, Chapter 4 in Studies in Surface Science and Catalysis 79, Elsevier Science Publisher, B. V. Amsterdam.

NIST database, http://srdata.nist.gov.

NORDLING, C., SOKOLOWSKI, E., and SIEGBAHN, K., 1958. Arkiv Fysik 13, 483.

OGLETREE, D. F., 2000, Talk at 8th International Conference on Electronic Spectroscopy and Structure, Clark Kerr Campus, University of California, Berkeley, California, USA.

OGLETREE, D. F., BLUHM, H., LEBEDEV, G., FADLEY, C. S., HUSSAIN, Z., and SALMERON, M., 2002. Rev. Sci. Instrum. 73, 3872.

OGLETREE, D. F., BLUHM, H., HEBENSTREIT, E. D., and SALMERON, M., 2009. Nucl. Instrum. Methods Phys. Res., Sect. A 601, 151-160.

ORCHARD, A. F., 1977. Handbook of X-ray and Ultraviolet Photoelectron Spectroscopy, London UK, 49.

ÖSTERLUND, L., RASMUSSEN, P.B., THOSTRUP, P., LAEGSGAARD, E., STENSGAARD, I., BESENBACHER, F., 2001. Phys. Rev. Lett. 86, 460.

PANTFORDER, J., POLLMANN, S., ZHU, J. F., BORGMANN, D., DENECKE, R., and STEINRUCK, H. P., 2005. Rev. Sci. Instrum. 76, 014102-9.

PELTON, A. R., MEHTA, A., ZHU, L., TREPANIER, C., IMBENI, V., ROBERTSON, S., BARNEY, M., and MINOR, A., 2005. Solid-to Solid Transformations in Inorganic Materials, Vol 2: Phase Transformations in Novel Systems or Special Materials.

PETRUCCI, Ralph H., 2007. General Chemistry: Principles & Modern Applications, Nineth Edition, Prentice Hall. 606.

POWELL, C. J., 1974. Surf. Sci. 44, 29.

PURCELL, E. M., 1938. Phys. Rev. 54, 818.

RAMSIER, R. D., and YATES, J. T., 1991. Surf. Sci. Rep. 12, 246-378.

RIEPE, G., 2000. Proceedings of the International Conference on Shape Memory and Superelastic Technologies, 279-283.

ROBINSON, H., and RAWLINSON, W. F., 1914. Phil. Mag. 28, 277.

ROBERTSON, S. W., 2006. On the Mechanical Properties and Microstructure of Nitinol for Biomedical Stent Applications, Ph. D. Thesis.

ROBINSON, K. S., STREET, F. J., and DRUMMOND, I. W., 1993. Inst. Phys. Conf. Ser. 130, 169.

ROTERMUND, H. H., HAAS, G., FRANZ, R. U., TROMP, R. M., 1995. G. Ertl, Science 270, 608.

RUPPENDER, H. J., GRUNZE, M., KONG, C. W., and WILMERS, M., 1990. Surf. Interf. Anal. 15, 245-253.

RUPPRECHTER, G., and WEILACH, C., 2008. J. Phys. Condens. Mater. 20, 184019.

RUTHERFORD, E., 1914. Phil. Mag. 28, 305.

RUUS, R., KIKAS, A., SAAR, A., AUSMEES, A., NOMMISTE, E. AARIK, J., AIDLA, A., UUSTARE, T., and MARTINSON, I., 1997. Solid State Commun. 104, 199.

SACCHI, M., PANACCIONE, G., VOGEL, J., MIRONE, A., VAN DER LAAN, G., 1998. Phys. Rev. B 58, 3750–3754.

SALMERON, M., BREWER, L., SOMORJAI, G. A., 1981. Surf. Sci. 112, 207.

SALMERON, M., and SCHLOGL, R., 2008. Surf. Sci. Rep. 63, 169-199.

SOMORJAI, G. A., 1994. Introduction to Surface Chemistry and Catalysis, Wiley, New York.

SAR-EL, H. Z., 1996. Nucl. Instrum. Methods 42, 71.

SCHIER, V., MICHEL, H.-J., and HALBRITTER, J., 1993. Fres. J. Anal. Chem. 346 1–3, 227–232.

SCHRAM, B. L., HEER, F. J. D., WEIL, M. J. V. D., and KISTENMAKER, J., 1965. Physica 31, 94.

SCHNEIDER, W., MOLODTSOV, S. L., RICHTER, M., GANTZ, T., ENGELMANN, P., and LAUBSCHAT, C., 1998. Phys. Rev. B 57, 14930.

SCHOFILED, J. H., 1976. J. Electron Spectrosc.Relat.Phenom. 8, 129.

SEAH, M. P., 1972. Surf. Sci. 32, 703.

SEAH, M.P., and DENCH, W. A., 1979. Surf. Interf. Anal. 1, 2.

SEAH, M. P., and SMITH, G. C., 1988. Surf. and Interf. Anal. 11, 69-79.

SEAH, M. P., and WHITE, R., 2002. Surf. Interface Anal. 33 , 960.

SEILER, H. G., SIGEL, H., SIGEL, A., 1988. Handbook on Toxicity of Inorganic Compounds. Marcel Dekker, Inc.

SHABALOVSKAYA, S. A., and ANDEREGG, J. W., 1995. J. Vac. Sci. Technol. A 13 (5), 2624-2632.

SHABALOVSKAYA, S. A., 2002. Bio-Med. Mater. Eng. 12, 69.

SHABALOVSKAYA, S., ANDEREGG, J., and HUMBEECK, J. V., 2008. Acta Biomater. 4**,** 447–467.

SHABALOVSKAYA, S. A., TIAN, H., ANDEREGG, J. W., SCHRYVERS, D. U., CARROLL, W. U., HUMBEECK, J. V., 2009. Biomaterials 30, 468-477.

SHAM, T. K., and RIVERS, M. L., 2002. Reviews in Mineralogy and Geochemistry, 49; 1, p. 117-147.

SHEVCHENKO, N., PHAM, M. T., and MAITZ, M. F. 2004. Appl. Surf. Sci. 235, 126.

SHIRLEY, D. A., 1972. Phys. Rev. B 5, 4709.

SIEGHBELN, K., NORDLING, C., and SOKOLOWSKI, E., 1957. Proceedings of Rehoveth Conference on Nuclear Structure. North Holland, Amsterdam, The Netherlands, p. 291.

SIEGBAHN, K., NORDLING, C., FAHLMAN, A., NORDBERG, R., HAMRIN, K., HEDMAN, J., JOHANSSON, G., BERGMARK, T., KARLSSON, S. E., LINDGREN, I., and LINDBERG, B., 1967a. Nova ACTA Reg. Soc. Sci. Upsaliensis 20, 1.

SIEGBAHN, K., NORDLING, C., FAHLMAN, A., NORDBERG, R., HAMRIN, K., HEDMAN, J., JOHANSSON, G., BERGMARK, T., KARLSSON, S. E., LINDGREN, I., and LINDBERG, B., 1967b. ESCA: Atomic, Molecular and Solid State Structure by Means of Electron Spectroscopy. Almqvist and Wiksells, Uppsala, Sweden.

SIEGBAHN, K., NORDLING, C., JOHANSSON, G., HEDMAN, J., HEDEN, P.F., HAMRIN, K., GELIUS, U., BERGMARK, T., WERME, L. O., MANNE, R., BAER, Y., 1969. ESCA Applied to Free Molecules, North-Holland, Amsterdam.

SIEGBAHN, H., and SIEGBAHN, K., 1973. J. Electron Spectrosc. Relat. Phenom. 2, 319.

SIEGBAHN, H., and LUNDHOLM, M., 1982. J. Electron Spectrosc. Relat. Phenom. 28, 135.

SIEGBAHN, H., SVENSSON, S., and LUNDHOLM, M., 1981. J. Electron Spectrosc. Relat. Phenom. 24, 205-213.

SIEGBAHN, H., 1985. J. Phys. Chem. 89, 897.

SOKOLOWSKI, E., NORDLING, C., and SIEGBAHN, K., 1958. Phys. Rev. 110, 776.

SORIANO, L., ABBATE, M., VOGEL, J., FUGGLE, J. C., FERNÁNDEZ, A., GONZÁLEZ-ELIPE, A. R., SACCHI, M., and SANZ, J. M., 1993. Surf. Sci. 290, 427.

STEINHARDT, R. G., and SURFASS, E. J., 1951. Anal Chem. 23, 1585.

STEINHARDT, R. G., and SURFASS, E. J., 1953. Anal Chem. 25, 697.

STOLTZE, P., and NORSKOV, J. K., 1985. Phys. Rev. Lett. 55, 2502.

STOECKEL, D., PELTON, A., DUERIG, T., 2004, Eur. Rad. 14, 292-301.

STOHR, J., 1992. Nexafs Spectroscopy, Springer-Verlag, Berlin, New York

SU, X., CREMER, P. S., SHEN, Y. R., SOMORJAI, G. A., 1996. Phys. Rev. Lett. 77, 3858.

SWIFT, P.W., 1987. Surf. Interface Anal. 4, 47.

TANUMA, S., POWELL, C. J., PENN, D. R., 1994. Values of IMFP obtained from TPP-2M IMFP NiTi. Surface and Interface Anal. 21, 165.

TAO, F., GRASS, M. E., ZHANG, Y., BUTCHER, D. R., RENZAS, J. R., LIU, Z., CHUNG, J. Y., MUN, B. S., SALMERON, M., and SOMORJAI, G. A., 2008. Science 322, 932-934.

TEPE, G., SCHMEHL, J., WENDEL, H. P., SCHAFFNER, S., HELLER, S., GIANOTTI, M., CLAUSSEN, C. D., and DUDA, S. H., 2006. Biomaterials, 27(4), 643-650.

TESCHNER, D., PESTRYAKOV, A., KLEIMENOV, E., HÄVECKER, M., BLUHM, S. H., KNOP-GERICKE, A., SCHLOGL, R., 2005. J. of Catalysis 230, 186 -194 and 195-203.

TIAN H., SCHRYVERS D., SHABALOVSKAYA S. A., VAN HUMBEECK J., 2009. Microscopy and Microanalysis, 15, 62-7.

TIANA, H., SCHRYVERS, D., SHABALOVSKAYA, S., and VAN HUMBEECK, J., 2009. TEM study of the mechanism of Ni ion release from Nitinol wires with original oxides, Proc. ESOMAT-2009, 05027, 1-6.

TOLLEFSEN, H., and RAAEN, S., 2009. Journal of Applied Surface Science 105, 123501.

TREPANIER, C., TABRIZIAN, M. and YAHIA, L. H., 1998. J.Biomed. Mater.Res., 43(4), 433.

TREPANIER, C., ZHU, L., FINO, J., and PELTON, A. R., 2003. Corrosion Resistance of Oxidized Nitinol, Proc SMST-2003, 367-373.

TRIGWELL, S., HAYDEN, R. D., NELSON, K. F., and SELVADURAY, G., 1998. Surf Interface Anal 26, 483–489.

TURNER, D. W., PLUMMER, I. R., and PORTER, H. A., 1986. Anal. NY Acad. Sci. 483, 354.

VAN DER LAAN, G., 1990. Phys. Rev. B 41, 12366.

VAQUILA, I., PASSEGGI, M. C. G. Jr., and FERRON, J., 1996. Appl. Surf. Sci. 93, 247.

VAQUILA, I., PASSEGGI, M. C. G. Jr., and FERRÓN, J., 1997. Phys. Rev. B 55, 13925.

VASS, E.M., HAVERCKER, M., ZAFERIRATOS, S., TESCHNER, D., KNOP-GERICKE, SCHLOGL, A. R., 2008. J. Phys. Condens. Mater. 20, 184016.

VENUGOPALAN, R., TREPANIER, C., 2000. Min. Invas. Ther & Allied Technol, 9(2), 67.

VERGARA, L. I., PASSEGGI, M. C. G. Jr., and FERRON, J., 2002. Appl. Surf. Sci. 187, 199.

VERNER, D. A., and YAKOVLEV, D. G., 1995. Astr. Astroph. Suppl. Ser. 109, 125.

WANG, J. G., LI, W. X., BORG, M., GUSTAFSON, J., MIKKELSEN, A., PEDERSEN, T. M., LUNDGREN, E., WEISSENRIEDER, J., KLIKOVITS, J., SCHMID, M., HAMMER, B., ANDERSEN, J. N., 2005. Phys. Rev. Lett. 95, 256102.

WANG, R. M., CHU, C. L., HU, T., DONG, Y. S., GUO, C., SHENG, X. B., LIN, P. H., CHUNG, C. Y., and CHU, P. K., 2007. Applied Surface Science 253, 8507-8512.

WATANABE, I., FLANAGAN, J. B., DELAHAY, P., 1980. J. Chem. Phys. 73, 2057.

WIDU, F., DRESCHER, D., JUNKER, R., and BOURAUEL, C., 1999. J. Mater. Sci.- Mater. Med. 10, 275.

WINTER, B., WEBER, R., WIDDRA, W., DITTMAR, M., FAUBEL, M., HERTEL, I. V., 2004. J. Phys. Chem. A 108, 2625.

WINTER, B., WEBER, R., HERTEL, I. V., FAUBEL, M., JUNGWIRTH, P., BROWN, E. C., BRADFORTH, S. E., 2005. J. Am. Chem. Soc. 127, 7203.

XU, C. H., MA, X. Q., SHI, S. Q., and WOO, C. H., 2004. Mater. Sci. Eng. A371, 45.

YEH, J., and LINDAU, I., 1985. At. Dat. Nucl. Dat. Tabl. 32, 1-155.

YEUNG, K. W. K., LU, W. W., LUK, K. D. K., and CHEUNG, K. M. C., 2006. Spine 31, 2296.

ZHOU, S., GWEON, G. H., SPATARU, C., GRAF, J., LEE, D.-H., LOUIE, S., and LANZARA, A., 2005. Phys. Rev. B 71, 161403.

ZHU, L., FINO, J. M., and PELTON, A. R., 2003. Proceedings of the International Conference on Shape Memory and Superelastic Technologies, eds. A.R. Pelton and T. Duerig, 357-366.

ZUBAVICHUS, Y., FUCHS, O., WEINHARDT, L., HESKE, C., UMBACH, E., DENLINGER, J. D., and GRUNZE, M., 2004. Radiat. Res. 161, 346-358.

CURRICULUM VITAE

Funda AKSOY was born on January the 28th 1979 in Adana, Turkey. She graduated from Çağrı Bey High School, and continued her studies in Physics in Çukurova University receiving a BSc in Physics in 2002 with highest second grade and MSc in Physics in 2005 with highest first grade. She wrote a master thesis on the subject "Investigation of Electrical, Optical and Structural Properties of InP Thin Films Obtained by Spraying Payrolysis Method" under the supervision of Prof. Dr. Refik Kayalı. She continued her Ph.D. research under the supervision of Prof. Dr. Prof. Dr. Metin Özdemir. Her research was performed at the Lawrence Berkeley National Laboratory/Advanced Light Source in Berkeley CA, USA under the supervision of Dr. Zhi Liu. Her research was on Ambient Pressure X-ray Photoelectron Spectroscopy and its applications.

APPENDIX

Three Step Model:

The most commonly used model for the interpretation of photoemission spectra in solids. The basis of model is shown in figure. In the three-step model the photoemission process is broken up into three distinct and independent processes. These processes are:

1) Optical excitation of the electron in the solid. In this step photo-ionization take places: locally the photon is absorbed and an electron is excited.

2) Transport of the electron to the surface. The excited electron travels through the sample to the surface.

3) Escape of the electron into vacuum. The electron escapes through the surface into the vacuum where it is detected.

Three Step Model

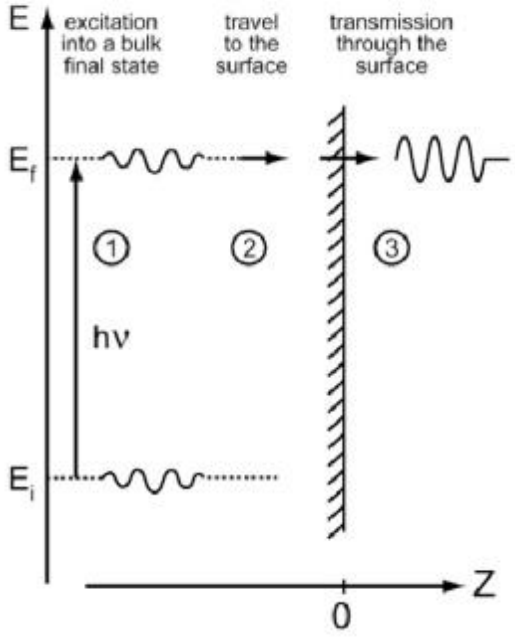

ALS Beamline 9.3.2

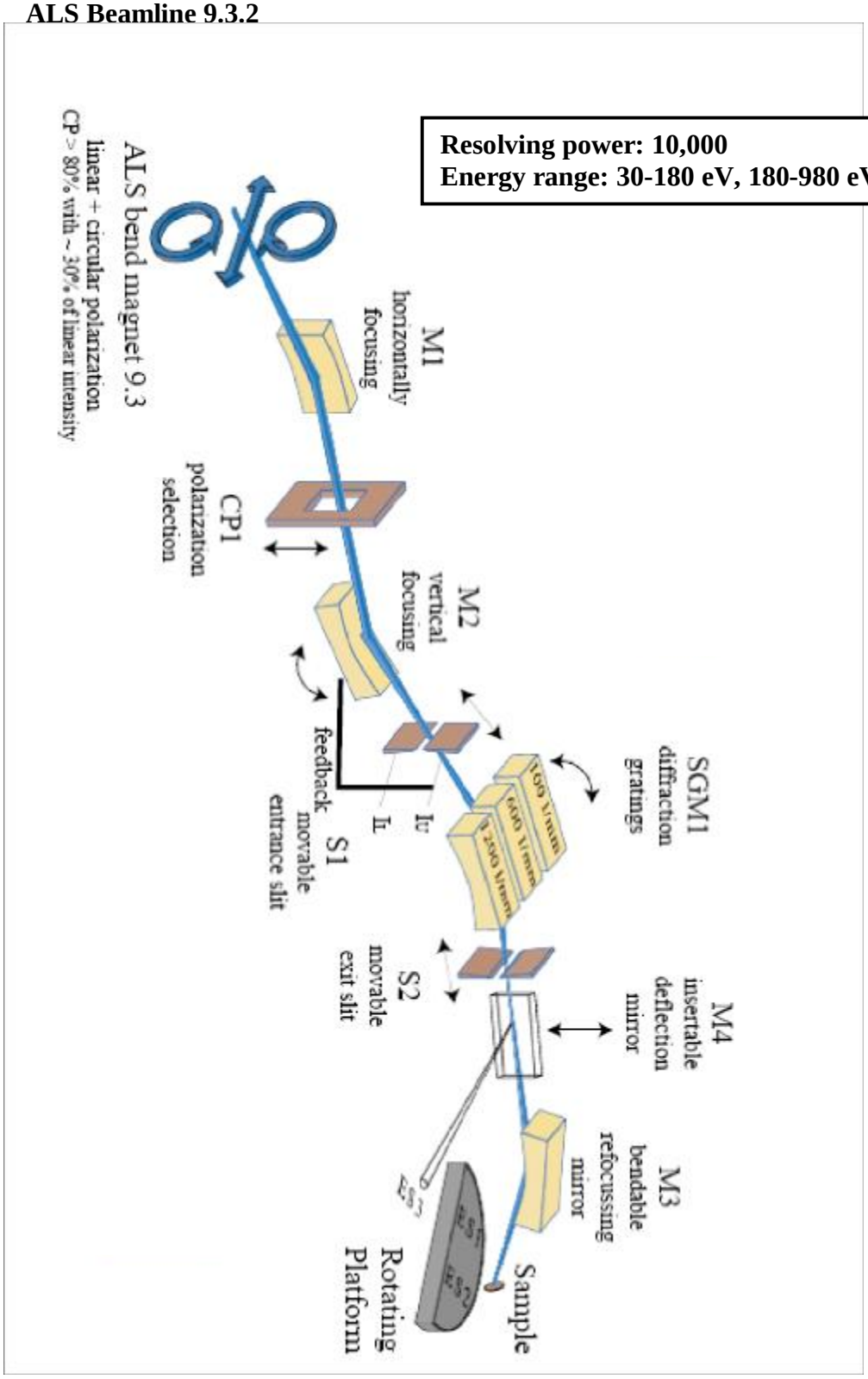

A Picture of Previous APXPS System at BL 9.3.2 at ALS

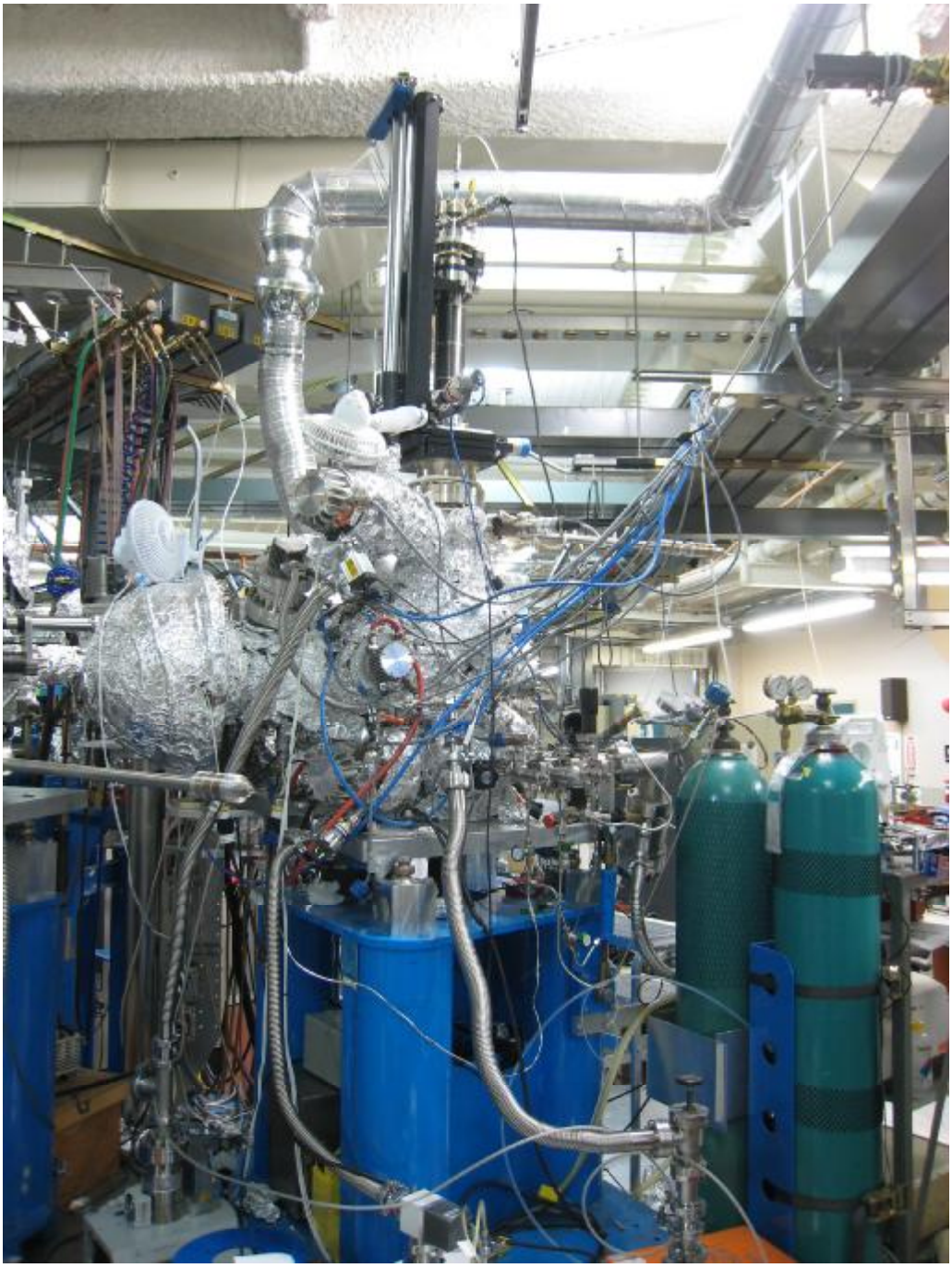

A Picture of Newly Designed APXPS System at BL 9.3.2 at ALS

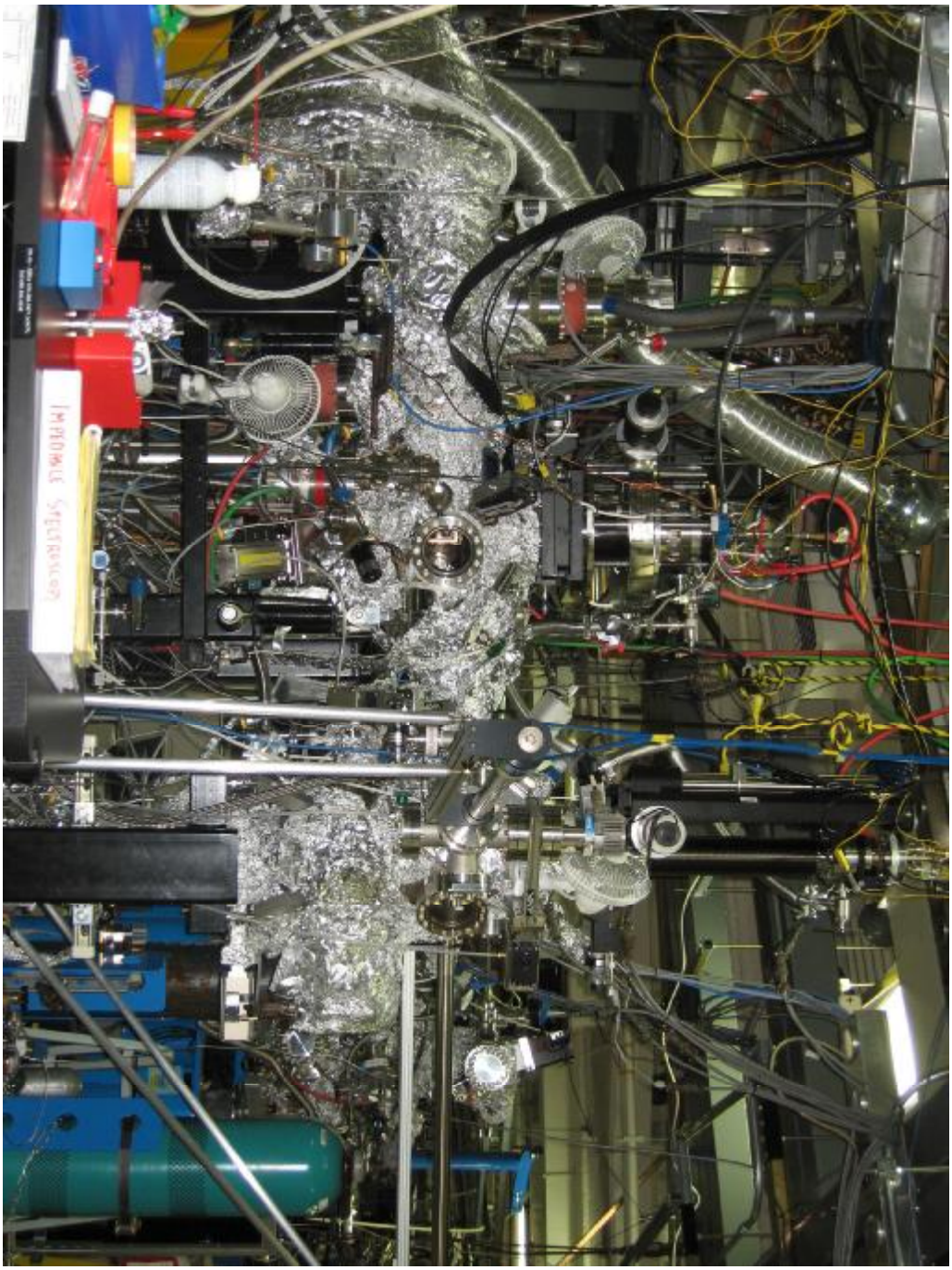

Scheme of Main Chamber with the Pumping Section and Preparation Chamber of Newly Designed APXPS System at BL 9.3.2 at ALS

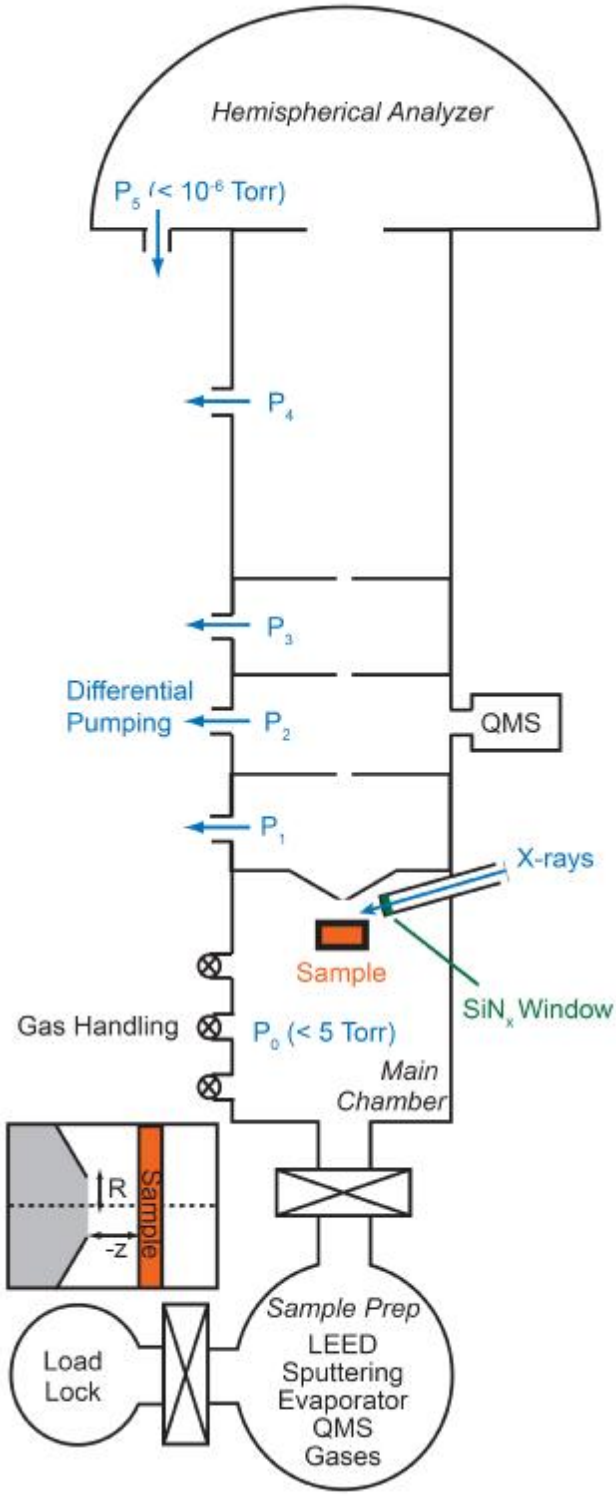

Scheme of Differential Pumping System of Newly Designed APXPS System at BL 9.3.2 at ALS

